ELECTRON INDUCED ALPHA PARTICLE EMISSION

Thesis

Submitted by

ALAN G. FLOWERS, B.Sc.

for the degree of

DOCTOR OF PHILOSOPHY

University of Edinburgh

AUGUST, 1980.

ABSTRACT

New data are presented on electron induced alpha particle emission using the University of Glasgow's Kelvin Laboratory 150 MeV electron linear accelerator and magnetic spectrometer. Energy spectra for alpha particles with energies in the range 4 MeV - 64 MeV are presented for the nuclei ^{27}Al, ^{56}Fe, ^{60}Ni, ^{68}Zn, ^{92}Mo, ^{94}Mo and ^{197}Au, following bombardment by electrons of 120 MeV energy. Additionally, alpha particle energy spectra resulting from 60 MeV and 33 MeV electrons on ^{60}Ni and 60 MeV electrons on ^{56}Fe are presented. Angular distributions are obtained at 8.2 MeV, 11.3 MeV and 15.7 MeV alpha energy for ^{56}Fe and ^{60}Ni at both 60 MeV and 120 MeV electron energy, and at 8.2 MeV and 11.3 MeV alpha energy for ^{60}Ni at 33 MeV electron energy. Angular distributions are also obtained for $\sim$30 MeV and $\sim$50 MeV alpha particles from natural nickel and gold bombarded by 120 MeV electrons. Cross sections for 8.2 MeV, 15.7 MeV, 20.3 MeV and 25.4 MeV alpha particles emitted from ^{60}Ni following bombardment by 19 MeV - 120 MeV electrons are presented in four electron energy dependent excitation functions.

The data are compared with the predictions of statistical (equilibrium) and pre-equilibrium particle decay models. Hauser-Feshbach statistical model calculations for giant dipole resonance decay give good quantitative agreement in the region of the peak of the alpha energy spectra for medium weight nuclei. Alpha decay contributions from other giant multipole resonances are discussed. An upper limit of 7% E2 sum rule is assigned to the giant quadrupole resonance alpha decay branch in ^{60}Ni. Higher energy alpha particles ($E_\alpha \gtrsim 12$ MeV) exhibit increasingly forward peaked angular distributions and cross sections several orders of magnitude above the statistical model predictions. The data are evaluated

ABSTRACT (contd.)

in terms of nuclear temperatures, mass dependences and angular distribution kinematics. These indicate that for medium weight and heavy nuclei at excitation energies above the resonance region the (e, α) reaction proceeds predominantly by a two step (e, N) - (N, α) process. In light nuclei a substantial equilibrium component may be present up to $\sim$ 100 MeV excitation energy. The pre-equilibrium exciton model can be appropriately applied to (e, α) reactions in medium weight and heavy nuclei. Calculations yield energy spectrum shapes in reasonable agreement with the data. Shortcomings in presently employed pre-equilibrium models, and the necessary improvements, are discussed. It is possible that a small component of the emitted alpha particles arises from a direct (one step) photoalpha process.

DECLARATION

The data presented in this thesis was obtained by a collaboration between Edinburgh and Glasgow University nuclear structure groups in which I undertook a major role. This thesis has been composed by myself. The data analysis and interpretation is entirely my own work.

ACKNOWLEDGEMENTS

I am pleased to acknowledge the extensive advice, encouragement and support provided throughout this thesis work by my two supervisors Dr. Alan Shotter and Dr. Derek Branford. Particular thanks are due to Alan Shotter whose enthusiasm for nuclear physics drew me into the subject and who had the foresight to suggest what has become the fruitful and topical subject of this thesis.

Thanks are due to all those who assisted with and supported the experimental work for this thesis. Dr. Owens of Glasgow University deserves special thanks for affording me the use of the Kelvin Laboratory spectrometer and charged particle detection system, together with providing me with the necessary instruction for the use of the system. Dr. McGeorge provided cheerful and enthusiastic assistance with all the acquisition of data for this thesis. I am grateful to Dr. Zimmerman, Dr. Pringle and Ms. Thorley for assistance with the latter stages of the experimental work. The hospitality of the respective directors of the Kelvin Laboratory, Professor J. Reid and Dr. Owens is gratefully acknowledged.

Advice on computing matters was willingly and helpfully supplied by Arrick Wilkinson, Alan Coles and Les Craig of the Kelvin Laboratory, together with the Edinburgh Regional Computing Centre (E.R.C.C.) advisory staff. Particular thanks are due to John Murison (E.R.C.C.) who provided the invaluable assistance which led to the successful implementation of the photonuclear cascade evaporation code, PICA.

The production of this thesis has been aided by the inclusion of some diagrams prepared by Mrs. Hamilton and Mrs. Taylor of Glasgow University and by Mrs. Hyslop of Edinburgh University. I have been

particularly fortunate to have secured the dedicated services of Mrs. Chester for the production of the typescript. Any failure of this thesis to attain the high standard of production for which she strives must be entirely attributed to myself.

I gratefully acknowledge the receipt of an Edinburgh University Science Faculty Scholarship during the preliminary stages of this work, and am grateful to the respective heads of the Physics Department, Professors Feather, Cochran and Cowley for affording me the hospitality and facilities of their department, and for their encouragement of this work.

My wife deserves particular thanks for supporting and caring for an often absent husband during the course of this research work, and by so doing enabling the completion of this thesis.

CONTENTS

C O N T E N T S (Contd.)

C O N T E N T S (Contd.)

C O N T E N T S (Contd.)

C O N T E N T S (Contd.)

CHAPTER 1

INTRODUCTION

1.1 Prologue

Photonuclear physics is now (1980) only a few years short of completing its first half century of development. This development has proceeded through three periods associated with different available photon sources. Early studies of photon induced nuclear reactions used γ-rays emitted from naturally occurring radioactive isotopes, and were limited to a maximum energy of only 2.62 MeV, from ^{208}Tl, in the thorium decay series. However, such photon energies were sufficient to allow the first observations of photodisintegration processes - those of the deuteron[1] and ^{9}Be [2] in 1934. The successful prediction of the observed Q-values for these reactions led to predictions of other photonuclear processes, including the (γ, α) reaction. Livingstone and Bethe noted[3] in 1936 that the threshold energies for light element alpha emission would be about 6-7 MeV, and would thus be a likely candidate for photonuclear reaction study with low energy photon sources. At that time the second period of photon source development was about to begin with the use of low energy proton, deuteron and alpha particle beams from the early cyclotrons, to provide particle capture γ-rays. The $^{7}Li(p, \gamma)$ reaction was used extensively up to the early 1950's to provide a source of γ-rays of up to 17.6 MeV energy, and with such a source numerous new photodisintegration processes were observed, and particle thresholds measured, using photographic emulsion or cloud chamber techniques. The photographic emulsion method of particle track observation was used by Hanni[4] in 1948 to make the first unambiguous observation of a photoalpha reaction. Emulsion plates were irradiated with the 17.6 MeV and 14.6 MeV γ-rays from the $^{7}Li(p, \gamma)$

reaction, and the $^{12}C(\gamma,3\alpha)$ reaction was observed.

In the period between the first suggestion of a (γ,α) reaction study, by Livingstone and Bethe, and Hanni's experimental observation of the process, rapid scientific progress took place associated with the Second World War. The development of high power radio frequency sources during this time and the building of low energy Betatrons during the early 1940's in both the U.S.A.[5] and Germany[6], paved the way for the launching of the period of pulsed electron accelerator photon sources, after the Second World War. By 1945 a 100 MeV Betatron[7] was available for photonuclear studies, and a year later Baldwin and Klaiber[8] published the results of cloud chamber and activation analysis studies of various photodisintegration processes. These included the observation of alpha particle cloud chamber tracks, but unlike the later Hanni experiment[3], these tracks could not be unambiguously identified with a particular reaction.

Initially only Betatrons were available, then later synchrotrons, and finally, by the mid 1950's, electron linear accelerators were introduced for use in nuclear structure studies. Machine developments were primarily associated with medical physics applications and thus early electron accelerators were produced to provide electron beams with the 25 MeV - 30 MeV energies required for photon and neutron production to irradiate patients to half-body thickness. These accelerators provided nuclear physicists with photon sources of sufficient energy to observe the phenomena of a "giant" photon absorption resonance above particle thresholds, with a maximum cross section at excitation energies of $\sim 80/A^{1/3}$ MeV, i.e. 13-23 MeV for mass numbers A = 235 - 40. Several laboratories undertook studies of photoalpha reactions with such accelerators as part of a programme of alpha particle cluster model and giant resonance studies.

In particular, at Harwell (Goward and Wilkins[9]), Zurich (Erdös and Stoll[10]), and at Saskatoon (Haslam and Taylor[11]), extensive programmes of photoalpha studies were carried out in the 1950's, at excitation energies up to ∿ 30 MeV.

A fourth period of photonuclear physics research is soon to begin as high duty cycle electron accelerators become available for coincidence (e, e'x) and (γ, γ'x) experiments[12] within and above the giant resonance region. However, despite the extensive acquisition of photoalpha data using pulsed electron accelerators, few data were acquired above the giant resonances, and prior to the initiation of this thesis work no (e,α) data had been published in the open literature[13]. Furthermore, several features of photoalpha data remained to be clarified. These features, and the historical development of photoalpha data, are considered in the next section. This thesis work therefore intends to provide new data on the hitherto poorly investigated (e,α) reaction process, and to use this data to make more exacting tests of current ideas on photonuclear reactions than has previously been possible. Particular attention is given to testing the present understanding of photonuclear reactions above the giant resonances. Thus, it is hoped to provide a firm basis for alpha emission studies in the forthcoming new period of photonuclear physics.

1.2 Historical Introduction to Bremsstrahlung and Electron Induced Alpha Emission Studies

The first quarter century of electromagnetically induced alpha particle emission studies was almost solely dedicated to bremsstrahlung (real photon) induced alpha emission at excitation energies below

$\sim$ 30 MeV. Following Hanni's observation of the $^{12}C(\gamma, 3\alpha)$ reaction, the increasing availability of Betatrons in the late 1940's, and interest in the alpha particle cluster model led to considerable activity in the study of alpha particle break up of light nuclei. In particular, ^{12}C, ^{14}N and ^{16}O were extensively studied. Indeed, prior to 1955 nearly 60% of publications on the (γ,α) process concerned at least one of the nuclei, ^{12}C, ^{14}N, or ^{16}O, and about half the remainder related to silver or bromine. The early interest in these nuclei reflects not only the interest in alpha particle cluster model effects, but also the ease of observing reactions on these nuclei, using photographic emulsions. As a measure of the activity in photoalpha reaction studies over the first quarter century of such research, the number of publications which include a photoalpha reaction study, are presented in Fig. 1.1 for each year from 1948-1977. The figure includes all (γ,α) references cited in Science Abstracts (1948-1955) and the National Bureau of Standards (U.S.A.), Photonuclear Reaction Data Index[13] (to 1977).

The distribution of photoalpha publications exhibits a dramatic rise in activity in the early 1950's, followed by a decrease and then a second period of activity in the early and mid 1960's, followed by an almost complete cessation of interest in the subject. The two periods of activity can be correlated with, firstly, the initial availability of 23-30 MeV Betatrons in the early 1950's, and secondly, the development of solid state semiconductor detectors in the early 1960's.

The first period of activity, in the early 1950's, included the first studies of (γ,α) reactions on medium and heavy nuclei. Since photographic emulsions were the principal detection medium, the first of these reactions to be studied were understandably $Ag(\gamma,\alpha)$ and $Br(\gamma,\alpha)$, in 1950[15]. In the following two years, Haslam, Taylor and co-workers at the University of Saskatchewan presented "activation

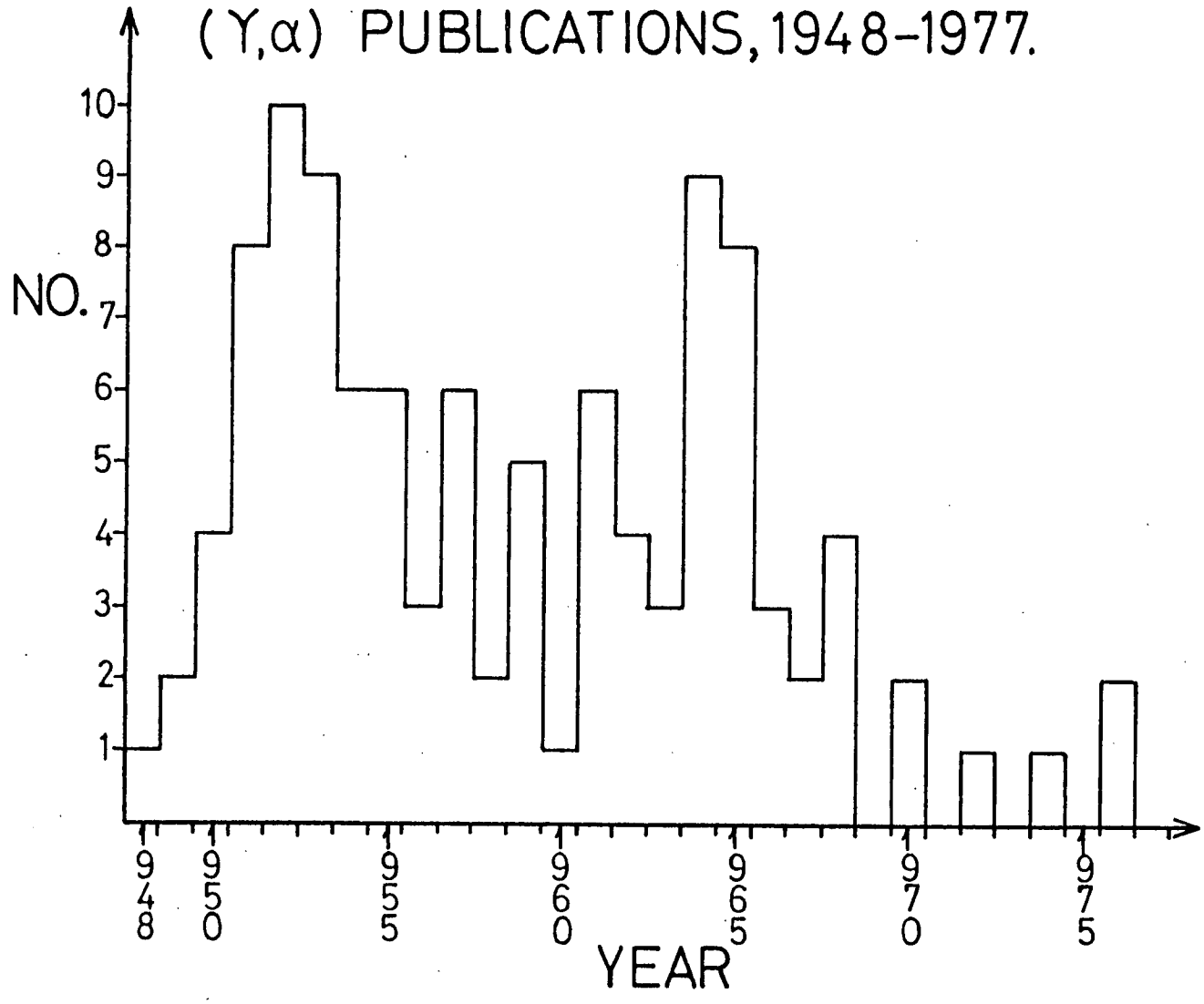

Fig. 1.1 Frequency of (γ,α) Publications 1948-1977.

curves" for the reactions $^{87}Rb(\gamma,\alpha)^{83}Br$ [16], $^{65}Cu(\gamma,\alpha)^{61}Co$ [17], $Ag(\gamma,\alpha)Rh$ [18] and $^{81}Br(\gamma,\alpha)^{77}As$ [18]. Betatron energies in the region 15-26 MeV were used, and a photon difference analysis technique[19] applied to yield a photon energy dependent total (γ,α) cross section. The cross sections obtained showed a pronounced resonance shape, centred at 20-24 MeV excitation energy, and the general form could be related to (γ,n) cross sections by applying the statistical model of nuclear reactions. It was therefore established, at an early stage, that together with the (γ,n) and (γ,p) reactions, the (γ,α) reaction exhibited a resonance phenomena in the region of 20 MeV excitation energy. Some measurements of photoalpha energy spectra were obtained to study the decay mechanism for this "giant resonance". The few early spectra obtained[14),18),21)] (using emulsion track range-energy relationships) were compared with the predictions of Blatt and Weisskopf's evaporation theory[22]. The difficulties associated with emulsion track studies of a low yield reaction led to poorly resolved energy spectra of low statistical accuracy, and thus only a crude test of evaporation theory was possible. However, on the basis of reasonable agreement between the predicted and observed forms of alpha energy spectra it was tentatively concluded that photoalphas from medium weight nuclei up to silver, arose from compound nucleus particle evaporation.

During the 1950's, effort in (γ,α) studies waned and was mostly directed towards obtaining photoalpha yield systematics, and comparisons of yields with statistical model calculations (e.g. Ref. 20). Sufficient yield data was acquired by 1954 to illustrate the general systematics of the (γ,α) reaction for 23 MeV[11] end point bremsstrahlung, and by 1957 Erdös, Scherrer and Stoll[10] were able to present a comprehensive review of the reaction to which little would be added in the next 15 years. Taking together data obtained by both emulsion techniques

and activation analysis, the photoalpha yield (see Fig. 1.2) was found to rise from that at $Z = 7$ to a maximum at $Z \sim 30$ and then decrease with increasing atomic number. These general features are understood as arising from the following combined effects on giant resonance alpha decay:

i) The giant resonance becomes narrower and its peak position lower in energy with increasing atomic number.

ii) The giant resonance total photon absorption cross section increases almost linearly with atomic number.

iii) The alpha particle Coulomb barrier increases with increasing atomic number.

Thus, in the region $Z = 20-30$ the alpha particle Coulomb barrier and Q-values combine to give effective alpha emission thresholds below the giant resonance, and hence the alpha yield increases as the photon absorption cross section increases with atomic number. Some fluctuations occur in the general trend due to the relative positions of the neutron and alpha thresholds, but in general the (γ,α) yield increases. Above $Z \sim 30$ the increasing Coulomb barrier rapidly suppresses giant resonance alpha decay and the alpha yield at $Z \sim 35$ is about a factor of ten below that at $Z \sim 30$. Above $Z \sim 35$ the alpha yield decreases with increasing atomic number due primarily to the reduction in the number of unsuppressed open channels by the increasing Coulomb barrier. At bremsstrahlung end point energies of $E_o \sim 32$ MeV, the increasing Coulomb barrier has a less pronounced effect and the alpha yield for $Z > 35$ is mainly dependent on the magnitude and relative positions of the alpha particle and neutron thresholds. Indeed, differing relative neutron and alpha Q-values produce large fluctuations in the alpha yields from nuclei of similar atomic number. In Figure 1.2, the $Z = 37$ data

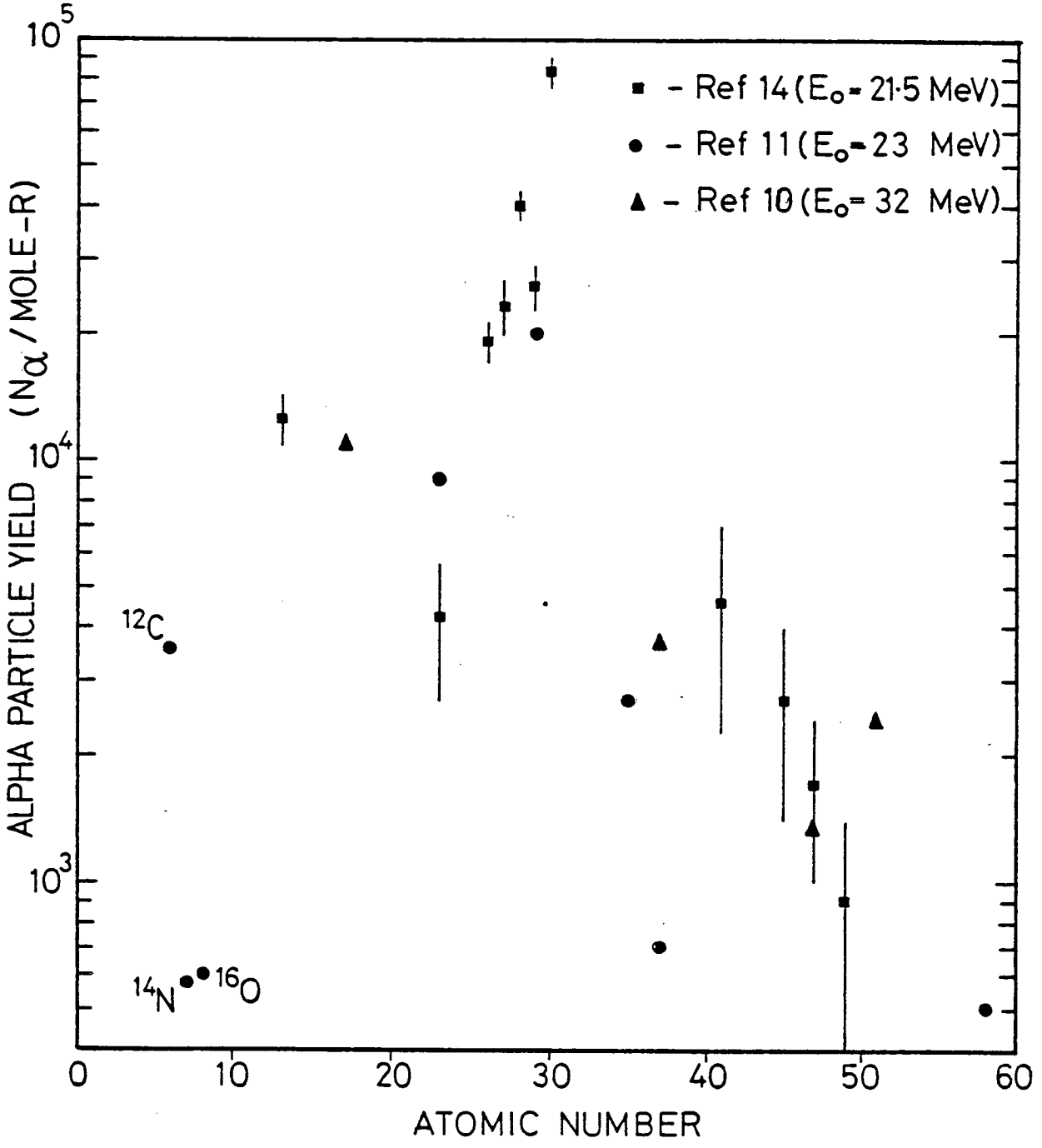

Fig. 1.2 Photoalpha yields from nuclei with Z = 6 - 58 irradiated by $E_o \leq 32$ MeV bremsstrahlung.

point (^{87}Rb) appears to be out of place in an otherwise systematic alpha yield decrease with increasing atomic number. The $^{87}_{37}$Rb yield is a factor 3.6 lower than that for $^{81}_{35}$Br (both yields obtained by the same authors). However, the alpha particle binding energy for ^{87}Rb is 1.5 MeV higher than that for ^{81}Br, whilst the neutron separation energies are almost identical. Thus the higher alpha yield for ^{81}Br is indicated by simple statistical model considerations of the available reaction channels. Some heavy nucleus alpha yields are not so easily explained. The 32 MeV bremsstrahlung induced total alpha yields from ^{203}Tℓ and ^{205}Tℓ are of a similar magnitude to nuclei around $Z \sim 40$, and in the ratio 2:5 respectively[10]. However, ^{203}Tℓ has the lower alpha threshold with respect to the neutron threshold, and the relative yields are therefore opposite to those expected from simple statistical model considerations. Hence, although the yields from medium weight nuclei could be reasonably explained using statistical considerations, neither the absolute nor relative yields for heavy nuclei were easily explained using compound nucleus decay models. As a consequence, a direct pre-formed alpha cluster knock-out process in heavy nuclei was proposed[23].

The availability of solid state semiconductor detectors, in the early 1960's, led to the second main period of activity in photoalpha studies, and several research groups[24) - 29)] used these to obtain photoalpha energy spectra, mainly from the high alpha yield medium weight nuclei, using up to 35 MeV end point bremsstrahlung. Although these studies in no way contradicted the earlier tentative conclusions in support of compound nucleus decay, some normalisation was generally required to bring theoretical predictions into agreement with the observations. Furthermore, experiments which considered heavy nuclei revealed yields and energy spectra incompatible with the results of

statistical model calculations and although a direct (γ,α) process was proposed, no calculations of energy spectra were attempted to allow quantitative comparison with the data.

Having reached a stage where total yields, (γ,α) total photodisintegration cross sections, and (γ,α) energy spectra had been studied extensively for high yield medium weight nuclei, photoalpha studies diminished to at most one or two publications per year, by the early 1970's. The early extensive work with light nuclei left little need for further low energy (γ,α) studies at that end of the periodic table. In contrast, the high yields and apparently non-evaporative energy spectra observed for heavy nuclei, remained unexplored. It is therefore one of the aims of this thesis to investigate the alpha emission process in heavy nuclei and compare it with that in medium weight nuclei.

Although interest in (γ,α) reaction studies waned, interest in the complementary (e,α) reaction increased in the early 1970's. Previously, attempts to study the (e,α) reaction had been discarded in favour of the (γ,α) reaction, with which much higher particle count rates can be obtained from a given nucleus if suitably thick bremsstrahlung radiators are placed in the electron beam. By the mid 1970's some research laboratories, which had carried out electron scattering and photonucleon experiments, began to employ magnetic spectrometers in order to permit the generally low count rate (e,α) experiments to be undertaken with reasonable ease despite the high radiation background associated with an electron beam. Two main factors motivated this work. Firstly, a belief that the theory of electron-nuclear interactions had reached the stage where meaningful information could be extracted about the photon multipolarities - and hence the giant resonance multipolarities involved in (e,α) and (γ, α)

reaction processes. Secondly, an interest in alpha particle clustering effects, and the possibility that such effects might be studied using (e,α) reactions.

After the initiation of this thesis study, in 1974, it was found that independent (e,α) reaction studies had been launched almost simultaneously at Saskatchewan University, Canada, and São Paulo, Brazil. The São Paulo work was soon continued at N.B.S., Washington, where earlier in the 1970's Dodge and Molen had carried out an extensive but unpublished (other than in a Conference Proceedings[30]) study of the Ag(e,α) and Au(e,α) reactions. Those studies which relate to the present work are discussed in more detail, where appropriate, in Chapters 3 and 4. Table 1.1 lists all (e,α) studies published up to 1979. The majority of these studies relate to giant resonance decay properties, and in particular ^{238}U and the nickel isotopes have been extensively studied. The ^{238}U and Ni studies partly arose following the suggestion of surprisingly large alpha decay widths for the giant quadrupole resonance[33),41)]. The authors of these suggestions concede that some of the originally published data was in error[40),45)], and thus, of the fourteen (e,α) studies published between 1975-1979, six are either erroneous work[33),41)] or efforts to correct such work[37),39),40),44)].

1.3 The Electron-Nucleus Interaction

1.3.1 Relation between Electrodisintegration and Photodisintegration of Nuclei

Photon-nucleus and electron-nucleus interactions are both electromagnetic and thus must be expected to have common general features. This was illustrated as early as 1939, when Guth and coworkers[46)] showed that for a given disintegration process, the electrodisintegration and

TABLE 1.1

Summary of (e,α) Publications

Year of Publication	Ref.	Location of Research Group	Nuclei Studied and Comments
1975	31	Saskatoon, Canada	^{16}O, ^{20}Ne; Magnetic Spectrometer; Energy Spectra, Angular Distributions.
1975	32	Sendai, Japan	^{26}Mg; Magnetic Spectrometer; Energy Spectra; Studied Giant Resonance Isospin Splitting; primarily an (e,p) study.
1976	33	São Paulo, Brazil	^{238}U; Activation Analysis; Excitation Function; Deduced large alpha decay width from Quadrupole Resonance at 9 MeV Excitation Energy.
1977	34	Saskatoon, Canada	^{63}Cu, ^{107}Ag, ^{159}Tb, ^{165}Ho, ^{169}Tm, ^{181}Ta; Magnetic Spectrometer; Energy Spectra, Angular Distributions. Studied reaction systematics.
1977	35	Sendai, Japan	^{44}Ca, ^{46}Ti; Magnetic Spectrometer; Energy Spectra; Studied Giant Resonance Isospin Splitting; primarily an (e,p) study.
1978	36	Edinburgh/Glasgow	^{60}Ni; Magnetic Spectrometer; Energy Spectra, Angular Distribution. First observation of pre-equilibrium (e,α) reaction in medium weight nuclei.
1978	37	Edinburgh/Glasgow	^{238}U; Activation Analysis, near beam Semiconductor Detectors; Energy Spectra; Concluded work of Ref. 33 was in error.

Continued on the following page.

TABLE 1.1 (Contd.)

Year of Publication	Ref.	Location of Research Group	Nuclei Studied and Comments
1978	38	Saskatoon, Canada	^{63}Cu, ^{92}Mo, ^{159}Tb, ^{162}Dy, ^{166}Er, ^{181}Ta, ^{197}Au; Magnetic Spectrometer; Energy Spectra, Angular Distributions; Direct (pre-equilibrium) reaction component indicated in medium weight and heavy nuclei.
1978	39	Illinois	^{238}U; Activation Analysis; Concluded work of Ref. 33 was in error.
1978	40	N.B.S., Washington	^{238}U; Magnetic Spectrometer; Energy Spectra; concluded work of Ref. 33 was in error.
1979	41	N.B.S., Washington	^{58}Ni, ^{60}Ni, ^{62}Ni; Magnetic Spectrometer; Excitation Functions; Deduced large alpha decay width from Giant Quadrupole Resonance.
1979	42	Edinburgh/Glasgow	^{27}Al, ^{NAT}Ni, ^{92}Mo, ^{94}Mo, ^{197}Au; Magnetic Spectrometer; Energy Spectra, Angular Distributions; Established systematics of high energy (e,α) reaction, and validit of a pre-equilibrium model description.
1979	43	Dubna, Russia	^{58}Ni; Studied alpha decay of giant resonances of ^{58}Ni.
1979	44	Edinburgh/Glasgow	^{NAT}Ni; Magnetic Spectrometer; Excitation Functions; Concluded work of Ref. 41 was in error.

photodisintegration thresholds are identical. Later, the yield curves obtained for reactions using electrons and bremsstrahlung were found to be of a similar form, indicating that both processes excited the giant resonances. The absolute yields for electron reactions, though, are of the order $\frac{1}{137}$ (fine structure constant) below those for real photon induced reactions.

The kinematics of the two reactions are compared in Figure 1.3. The mechanism for photodisintegration requires the absorption of an incident photon, followed by subsequent emission of a particle,

$$\gamma + {}^{N}_{Z}A \rightarrow {}^{N-N'}_{Z-Z'}(A-A') + {}^{N'}_{Z'}A' \quad .$$

A photon of energy E_γ, and momentum $\underline{k}_\gamma$, excites the nucleus to an energy $E_x = E_\gamma$ (neglecting the nucleus recoil energy). The momentum transferred to the nucleus, $\underline{q}$, is fixed for a given photon energy, since, by conservation of momentum,

$$\underline{k}_\gamma = \underline{q} \ ,$$

and hence, $\hbar c k_\gamma = E_\gamma = E_x = \hbar c q$. Such a process is described as "on-the-energy-shell". In contrast, an electron with initial momentum $\underline{k}_1$, may be scattered through any angle, θ, from $0^\circ - 180^\circ$, and may have any final momentum magnitude, k_2, from $0 - k_1$. The momentum transferred to the nucleus is then,

$$q = \left(k_1^2 + k_2^2 - 2 k_1 k_2 \cos\theta\right)^{\frac{1}{2}}, \qquad (1.1)$$

and the nuclear excitation energy will be,

$$\hbar c(k_1 - k_2) = E_x \ . \qquad (1.2)$$

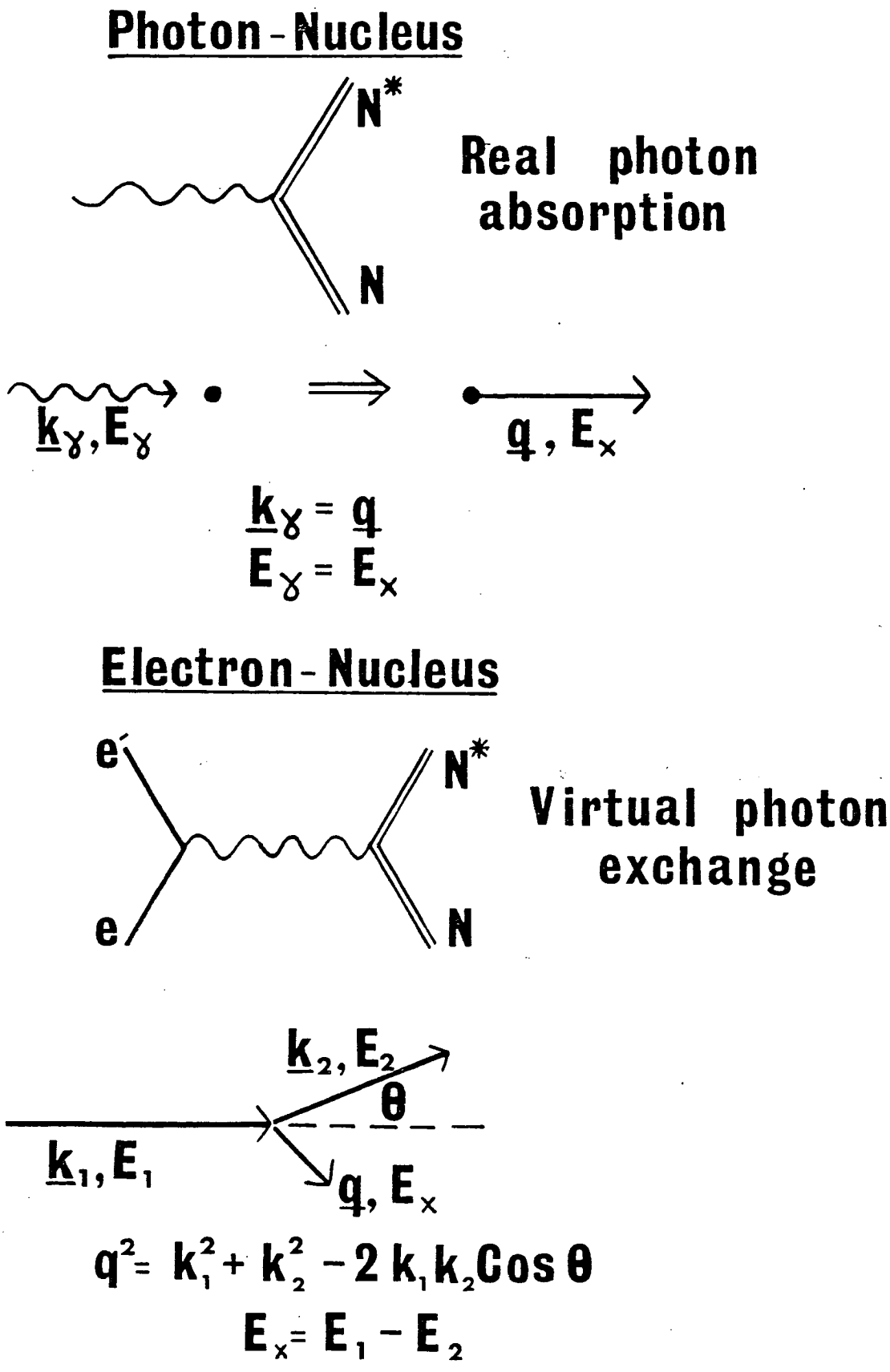

Figure 1.3 Comparison of Photon-Nucleus and Electron-Nucleus interaction kinematics.

Only when the forward scattering condition is met, i.e. at $\theta = 0^{\circ}$. does the reaction process have the "on-shell" energy relation for photoexcitation, i.e. $E_x = \hbar c q$. Thus, for a given nuclear excitation energy, momenta of $E_x/\hbar c$ upwards will be transferred in the electron-nucleus interaction, and consequently, differing forms of transition matrix elements and kinematic factors must be employed for the two interactions. Furthermore, whilst the electromagnetic field of the photon interacts with the nuclear current and magnetization density, the electron-nucleus interaction additionally includes a Coulomb interaction due to the Coulomb field around the electron. This Coulomb interaction introduces a longitudinal component into the interaction, which is not present in the purely transverse real photon electromagnetic field. The longitudinal field has similar types of multipole components to the transverse field but with the addition of an $L = 0$ multipole. Therefore, unlike photons, electrons may excite nuclei with a zero angular momentum transfer, e.g. by $0^+ \rightarrow 0^+$ transitions. Consequently, electrons are a useful tool with which to study monopole ($L = 0$) resonances.

Most electrodisintegration studies, including this thesis study, make no coincidence measurement between the inelastically scattered electron and the reaction products, but only make measurements on the products themselves. These experiments are termed "inclusive" and provide no energy, momentum, or other information, about the scattered electron. The observed reaction products arise from a range of excitation energies which extends up to the incident electrons' kinetic energy. Evidently a measure is required of the probability of exciting a nucleus to a given energy by a particular multipole transition. This is obtained by relating the electron-nucleus and photon-nucleus excitation mechanisms.

The relation between nuclear disintegration by electrons and by photons has been examined in many experimental studies[47) - 55)]. These studies mostly applied the Weizsäker[56)] and Williams[57)] description of the electron-nucleus interaction. This considers the interaction as due to an electromagnetic field decomposed into multipoles of type λ (electric or magnetic) and multipolarity L, each with an associated virtual radiation spectrum. These radiation spectra, or "virtual photon spectra", together with appropriate photon absorption cross sections, provide the nuclear excitation energy probability distribution required to describe inclusive electrodisintegration experiments. Calculations of these spectra indicate that the low multipolarity radiation flux is primarily associated with forward scattered electrons. The approximation, $\theta = 0^{o}$, (see equation (1.1)) can then be made, and $E_x = \hbar c q$, so the process becomes "on-shell" and the transition matrix elements become identical to those in photodisintegration, except for the presence of the longitudinal Coulomb term. However, at low momentum transfers, i.e. $qR << 1$, Seigert's Theorem[58)] can be applied to replace the longitudinal Coulomb matrix elements, by transverse electric matrix elements. The nuclear transition elements describing electrodisintegration then become identical with those describing the photodisintegration process, and thus the two processes can be related without the use of any model of nuclear charge and current.

The electron interaction is then considered as arising from "virtual photons", which differ from "real photons" by their dispersion relation, $E_\gamma = f(q)$, and by the presence of a longitudinal component. The virtual radiation spectra are used to calculate electrodisintegration cross sections, $\sigma_e(E_e)$ at electron energy E_e, from the appropriate photon absorption cross section, $\sigma_\gamma(E_\gamma)$, decomposed into multipolarities, λL, (λ = E or M, L = 1,2, ...),

$$\sigma_\gamma(E_\gamma) = \sum_{\lambda L} \sigma_\gamma^{\lambda L}(E_\gamma) \ . \qquad (1.3)$$

Then

$$\sigma_e(E_e) = \sum_{\lambda L} \int_0^{E_e - m_o} \sigma_\gamma^{\lambda L}(E_\gamma) \ \frac{N^{\lambda L}(E_e, E_\gamma)}{E_\gamma} \ dE_\gamma \ . \qquad (1.4)$$

where $N^{\lambda L}(E_e, E_\gamma)$ is the λL multipolarity virtual photon intensity at photon energy E_γ for electron energy E_e. This expression is analogous to that for the calculation of bremsstrahlung cross sections, $\sigma_{br}(E_e)$,

$$\sigma_{br}(E_e) = \sum_{\lambda L} \int_0^{E_e - m_o} \sigma_\gamma^{\lambda L}(E_\gamma) \ \frac{K(E_e, E_\gamma)}{E_\gamma} \ dE_\gamma \ , \qquad (1.5)$$

Here $K(E_e, E_\gamma)/E_\gamma$ defines the bremsstrahlung spectrum of real photons, which is identical for all photon multipolarities, and so the multipolarity decomposition is unnecessary for the real photon case. In contrast, the virtual photon spectra are enhanced for high multipolarity transitions. The differing multipolarity contributions in electron and photon reactions led to the comparison of these reactions in order to deduce the multipolarities present in photodisintegration processes[50) - 55)], and thus obtain nuclear structure information relating to giant resonance properties (see Section 1.4). However, such studies must ensure that the virtual photon formalism is only applied in those kinematic regions where the approximations discussed earlier, are valid. The limitations of commonly applied virtual photon calculations are discussed in the next section.

1.3.2 Development of the Virtual Photon Formalism

Theoretical approaches to the calculation of virtual photon spectra were initially simplified by the need to obtain only cross sections for

low energy electrons (E_e < 30 MeV), at low momentum transfers, on light, low Z nuclei. In such cases the point nucleus, long wavelength, and plane wave assumptions are valid. Consequently, the plane wave Born Approximation (P.W.B.A.) was applied in several early studies[59) - 60)], and later by Guth and Mullin[62) - 64)], who by 1952 had developed the P.W.B.A. virtual photon formalism to the stage at which it became the basis of electrodisintegration calculations for nearly two decades. However, this approach evidently omits the nuclear Coulomb field distortion on the incoming and outgoing electron wave and so is valid only in the limit $Z \to 0$. Furthermore, a point nucleus was assumed, and thus the finite nuclear size was neglected. Such simplifications were known to lead to serious discrepancies for high Z nuclei and for electron energies where the long wavelength approximation, $qR \ll 1$, breaks down. Limiting $qR < 0.2$, requires electron energies below $\sim$ 30 MeV, at A = 240, and therefore the long wavelength approximation was valid for most work carried out with the early, low energy, electron accelerators.

Difficulties with the plane wave formalism soon became evident when plane wave virtual photon spectra appropriate to electric dipole (E1), electric quadrupole (E2), and magnetic dipole (M1) transitions were used to calculate electrodisintegration cross sections for comparison with measurements[49) - 54)]. A confusing picture emerged, with the results indicating that photon absorption comprised, for light and medium weight nuclei, a mixture of E1 with up to 12% E2 contribution, and for heavy nuclei an E2 contribution of the same magnitude as E1, or higher. These results were surprising, since it was expected that photon absorption would proceed primarily by a dipole excitation process, and hence efforts were directed towards applying corrections to the plane wave calculations. Initially

these were limited to estimating the magnitude of finite nuclear size effects[52),53)] since these could be estimated within the framework of the existing plane wave theory. The corrections were negligible below $E_e \sim 30$ MeV, and indicated a greater, rather than lesser, mixture of multipoles other than E1. It was therefore concluded that the plane wave spectra were in error for heavy (high Z) nuclei, and that the Coulomb field produced a significant distortion of the incoming and outgoing electron partial waves. This was supported by measurements of the cross section ratios for positron, σ^+, and electron, σ^-, nuclear disintegration. The ratios, σ^-/σ^+, for low ($E_e \sim 27$ MeV) electron energies were found to increase with the nuclear charge, Z[65)], in accord with that expected if Coulomb distortion effects were significant on electrons, which pass closer to the nucleus than positrons of equivalent energy.

In 1971 a distorted wave treatment of virtual photon theory was published by Gargaro and Onley[66)]. At low electron energies ($E_e < 50$ MeV) this treatment accounted for the observed electron to positron nuclear disintegration cross section ratios[67)], and related $\sigma(e,n)/\sigma(\gamma,n)$ and $\sigma(e,2n)/\sigma(\gamma,2n)$ data, without the inclusion of multipoles other than E1. Additionally, a test of the D.W.B.A. theory for the $^{238}U(e,n)$ reaction, for $E_e = 7 - 25$ MeV, indicated a systematic discrepancy of only 3% between the data and calculations based on solely E1 transitions[68)]. Such tests have not, however, been possible for higher multipoles, and thus up to the present only the D.W.B.A. calculation for the E1 multipole has been tested experimentally.

A comparison of the E1 and E2, P.W.B.A. and D.W.B.A. virtual photon spectra is shown in Fig. 1.4, for Z = 28 and Z = 79, at 50 MeV total electron energy. This illustrates the importance of employing the D.W.B.A. calculation to describe reactions on medium and heavy

Fig. 1.4 E1 and E2 Virtual Photon Spectra calculated in P.W.B.A. and D.W.B.A. for Z = 28 and Z = 79.

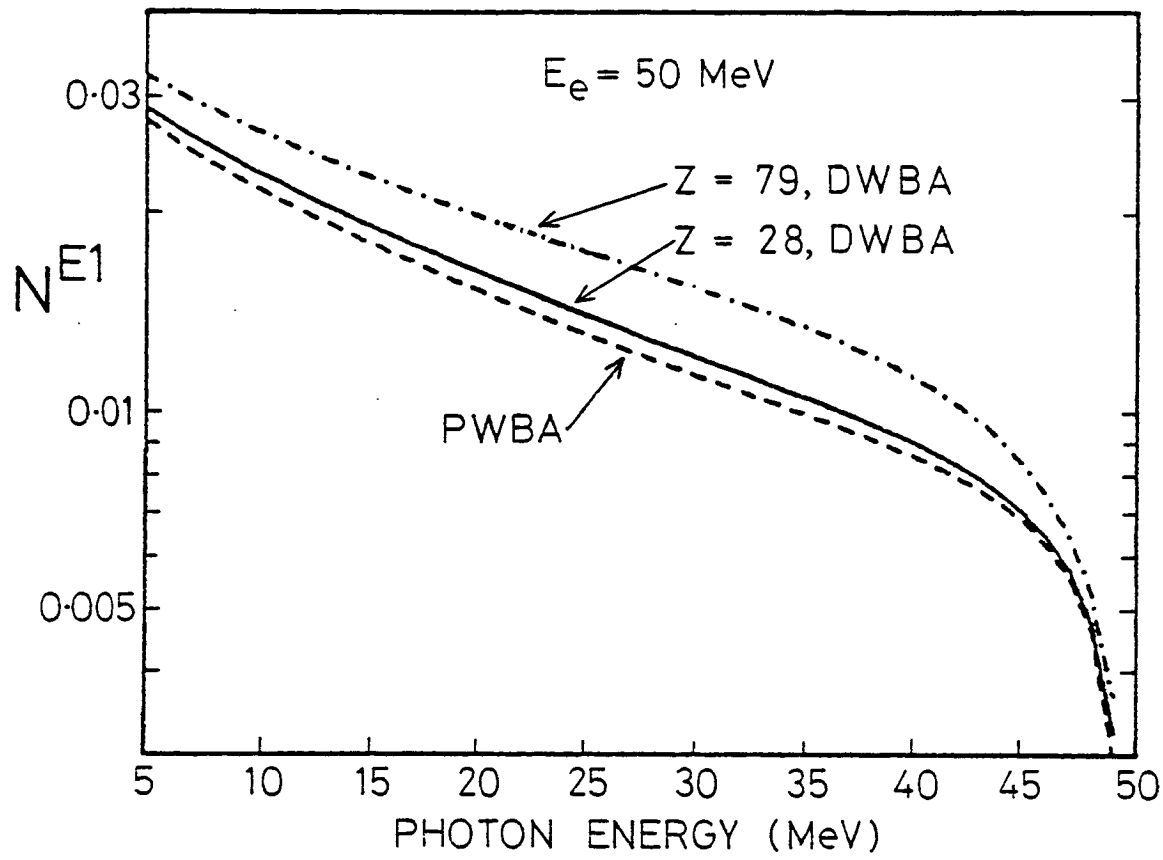

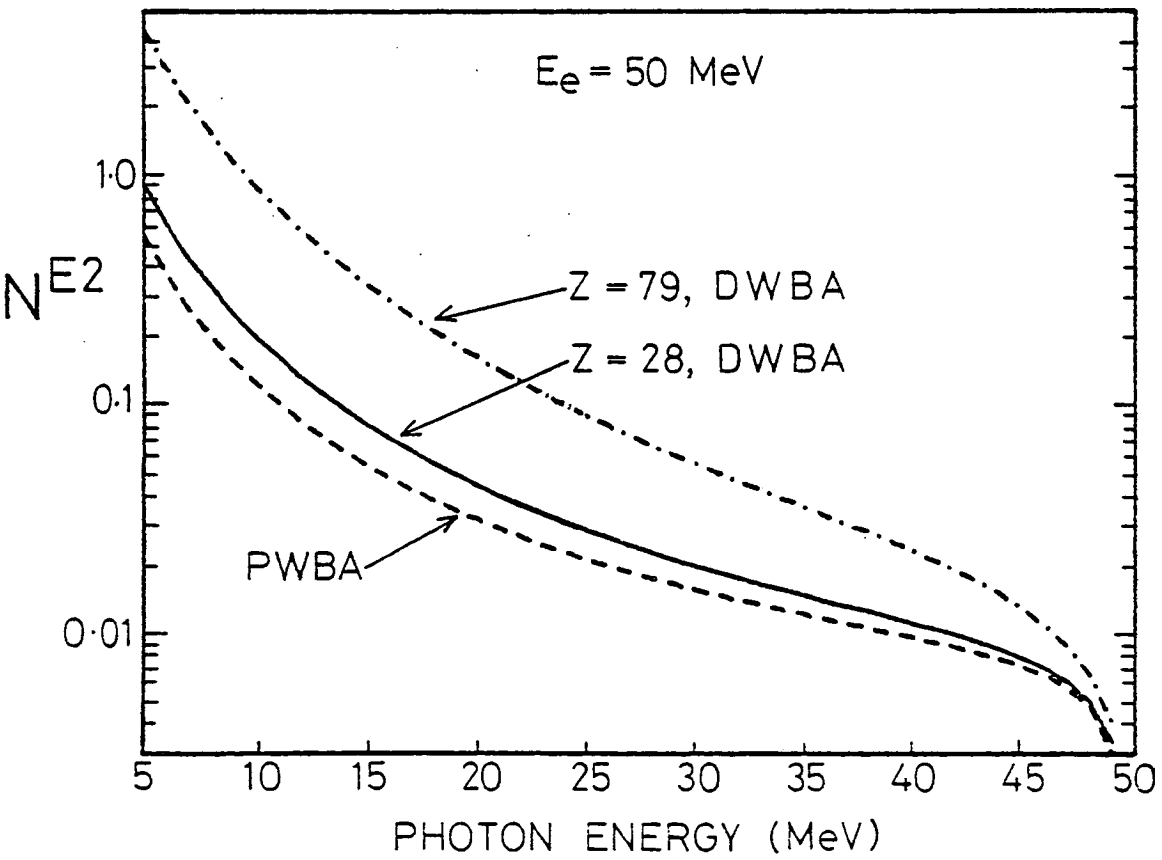

nuclei, particularly if higher (e.g. E2) multipolarities are considered. Since Coulomb distortion effects must reduce as $Z \to 0$, the D.W.B.A. results must approach those of P.W.B.A. in this limit, and this provides another test of the D.W.B.A. calculations. Unfortunately, the initial formulation of the D.W.B.A. theory required lengthy computer calculations. In particular, the E1 spectra had a very slowly converging partial wave sum for their calculation, and the numerical techniques employed were susceptible to computational rounding errors. These difficulties were avoided by the development of an analytic expression for the E1 virtual photon spectra, which agreed with the D.W.B.A. calculations to within 6% for $E_e < 50$ MeV[67]. This formulation has been used extensively in this thesis, and is found to agree reasonably with the D.W.B.A. calculation (e.g. to within 10% in the giant resonance region for $Z \sim 28$, at $E_e = 120$ MeV). Agreement becomes worse at higher atomic numbers, and the full D.W.B.A. calculation must be applied when applications demand accurate virtual photon spectra.

Recently, it has been noted[69] that the Coulomb distortion of the electron partial waves affects only the first few of these partial waves, and thus the difference between the plane wave result and the distorted wave result, for a given sum of partial waves, becomes constant early in the partial wave sum. By adding this difference, once it has converged, to the analytic plane wave result, a considerable reduction in computation time is achieved, and reliable E1 D.W.B.A. virtual photon spectra can now be calculated rapidly. Fast calculations can also be undertaken for E2, E3 and M1 virtual photon spectra, though the results must be treated with caution in the absence of any experimental tests. Furthermore, these D.W.B.A. calculations still assume that the nuclear charge is located at a point, and consequently they must be applied with caution for electron energies above $E_e \sim 30$ MeV.

Recently, Shotter has estimated the effects of a finite nuclear size by using the P.W.B.A. theory together with the Helm model description of nuclear transition charge and current densities[70]. Only a small effect (< 3% intensity reduction at E_e = 100 MeV) was indicated for the E1 spectra (at giant resonance excitation energies), but a dramatic suppression occurs for E2 virtual photon intensities (a factor of five reduction for A = 240, E_e = 100 MeV and E_γ = 10 MeV). In both cases the longitudinal components of the virtual photon spectra are those most strongly influenced by corrections for finite size effects. However, the transverse component dominates the E1 spectra whilst the longitudinal component dominates the E2 spectra, hence the differing response for these two multipoles. From these results it becomes apparent that a single calculation is needed which takes account of both Coulomb distortion and penetration of the nuclear surface. Onley and Wright are presently trying to extend their D.W.B.A. calculations to account for these effects by including a suitable model of nuclear charge and currents. Until this is done, no reliable description will be available for multipole excitations, other than E1, by the electron-nucleus interaction at energies above $\sim$ 30 MeV.

In summary, the tests of E1 spectra described above, together with Shotter's estimates of small finite nuclear size effects on these calculated spectra, indicate that the present D.W.B.A. virtual photon formalism[69] for E1 transitions is valid for the electrons of energies up to $\sim$ 120 MeV considered in this thesis. Consideration of the nuclear photon absorption process shows that electric dipole transitions dominate all other multipolarities, up to the pion threshold (see Section 1.4), hence an accurate description is available of the electron-nucleus interaction in the inclusive experiments described in this thesis.

1.3.3 Selection Rules for Electromagnetic Transitions

1.3.3.1 Angular Momentum

The angular momentum selection rules which apply to real photon transitions can be extended to virtual photon induced transitions by including consideration of a longitudinal Coulomb component. Whereas real photon transitions require an angular momentum transfer, $L \geq 1$, virtual photon electric transitions may include the case, $L = 0$, due to the Coulomb component. Magnetic transitions must transfer angular momentum, $L \geq 1$, as for both real and virtual photons.

The parity and angular momentum selection rules for electromagnetic transitions of type λ (here $\lambda = 1$ for electric, $\lambda = 0$ for magnetic) and angular momentum transfer L, between an initial nuclear state $|J_i\ \pi_i>$ and a final state $|J_f\ \pi_f>$ are,

1) $$|J_i - J_f| \leq L \leq |J_i + J_f|$$

2) $$\pi_f = \pi_i (-1)^{\lambda+L+1} \quad .$$

Consequently, electric dipole or electric quadrupole excitation of a 0^+ ground state nucleus, leads to only 1^- or 2^+ excited states, respectively. Since dipole excitation dominates the photon absorption process, states of high excitation energy, but of low angular momentum, are reached in electromagnetic interactions. This contrasts with hadron induced reactions, in which states of high excitation energy are reached with a range of angular momentum transfers, often up to 10 - 100$\hbar$. The analysis of electromagnetic reactions is therefore simplified by the restriction to only low angular momentum ($J_f \sim 1$) excited states.

1.3.3.2 Isospin

Evidence for the charge independence of nuclear forces led to consideration of the proton and neutron as two states of the nucleon, and to the introduction of an 'isospin' quantum number to distinguish between these states. Nucleons are assigned a total isospin $T = \frac{1}{2}$, and depending on the convention applied, the neutron and proton are assigned to either the "spin up" or "spin down" state ($T_Z = \frac{1}{2}$ and $T_Z = -\frac{1}{2}$). The isospin projection, T_Z, for a nucleus of Z protons and N neutrons is defined as $T_Z = (N - Z)/2$. In general, the ground state isospin, T_o, is given by $T_o = T_Z$, and higher states may occur with $T_i = T_Z + 1$, $T_Z + 2$, etc.

Isospin selection rules for electromagnetic transitions have been discussed in detail by several authors[72) - 75)]. Assuming nuclear force charge independence, the selection rules for change of isospin, ΔT, are:-

1) Multipoles other than E1 and M1:

$$\Delta T = 0, \pm 1.$$

2) E1 Transitions:

$$\Delta T = 0, \pm 1 \quad \text{when} \quad T_Z \neq 0$$

$$\Delta T = \pm 1 \quad \text{when} \quad T_Z = 0.$$

3) M1 Transitions:

$$\Delta T = 0, \pm 1 \quad \text{when} \quad T_Z \neq 0$$

$$\Delta T = 0 \text{ inhibited}, \quad \Delta T = \pm 1 \quad \text{when} \quad T_Z = 0.$$

Coulomb forces in the nucleus and the neutron-proton mass difference lead to isospin mixing of nuclear states. Forbidden transitions may thus proceed between such mixed states and so the selection rules are only an indication of likely inhibited transitions. The selection rules are most applicable to low Z nuclei, and have been applied successfully to the (γ,α) reaction in light self-conjugate nuclei[74)]. Furthermore, the

rules for E1 and M1 transitions are derived in the long wavelength approximation, and will therefore break down for electromagnetic processes in which high order terms in qR become important, such as large angle electron scattering. Isospin "forbidden" transitions are therefore less inhibited for electrodisintegration than photodisintegration.

Coulomb forces in medium and heavy weight nuclei are expected to lead to substantial isospin mixing and thus the isospin selection rules are expected to have limited validity for these nuclei. Application of the selection rules to the nuclei studied in this thesis (all have $T_Z \neq 0$) indicates that all multipoles will lead to states of total isospin $T = T_o$ ($T_<$) or $T = T_o + 1$ ($T_>$). The allowed channels for particle emission to ground states or low lying levels of neighbouring nuclei are illustrated in Fig. 1.5. The extent to which such selective decays occur and the evidence for isospin mixing in medium weight nuclei is discussed in Chapter 4.

1.4 Giant Resonances

1.4.1 The Giant Dipole Resonance

Early photoneutron studies[76] showed the existence of a "giant" resonance in the photon absorption cross section, a few MeV above the neutron threshold. This was soon interpreted by Goldhaber and Teller[77] as arising from collective dipole motions of neutrons with respect to protons. Their postulated collective motions included,

i) density vibrations of neutron and proton 'fluids' against each other, with the surface fixed,

and

ii) vibration of a fixed volume proton sphere against a fixed volume neutron sphere.

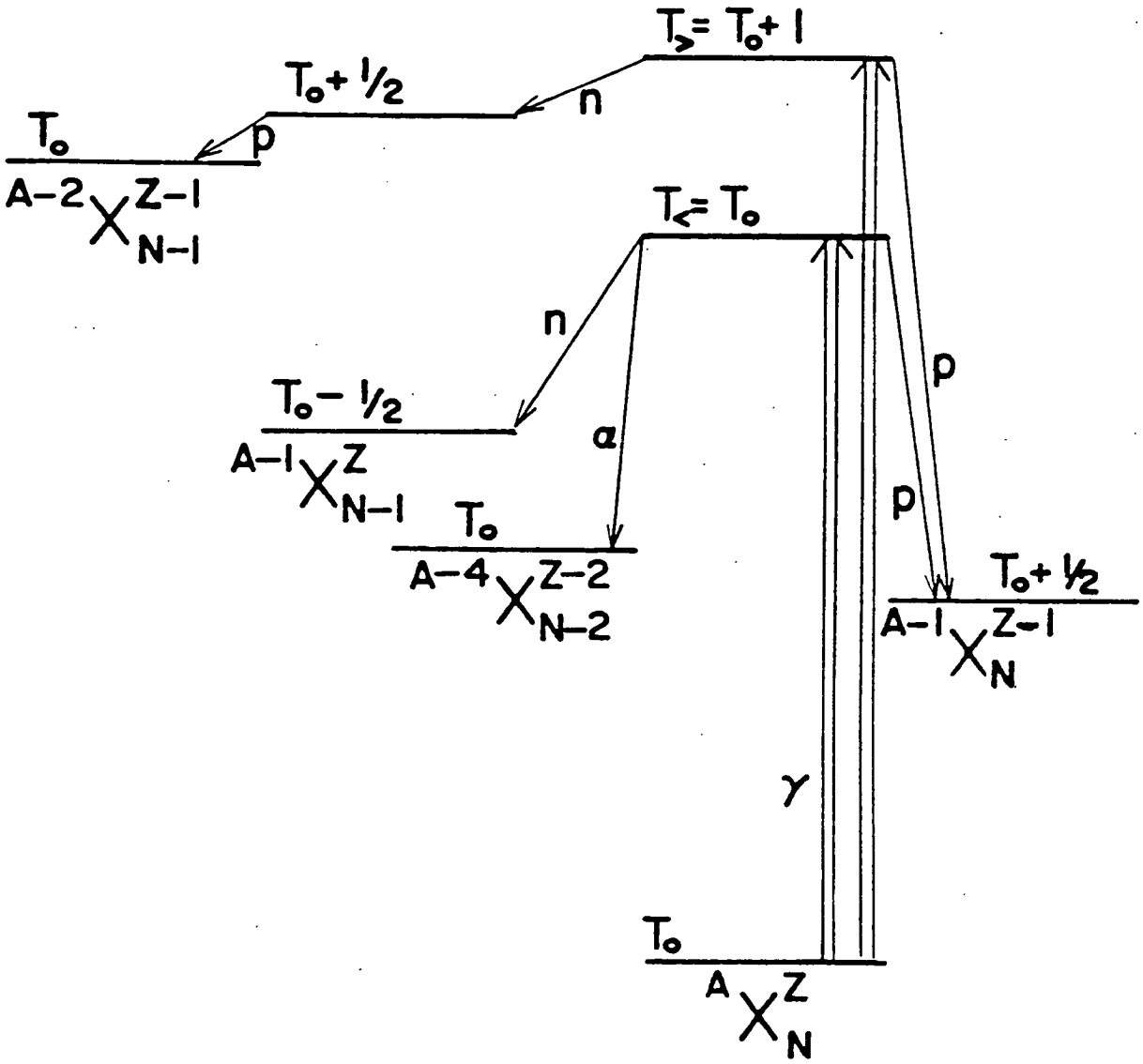

Figure 1.5 Isospin allowed particle decays of the $T_<$ and $T_>$ GDR components in $N \neq Z$ nuclei.

The former model was elaborated by Steinwedel and Jenson, and is associated with their names ("SJ mode"), whilst the latter model, which was discussed in some detail in the original Goldhaber-Teller paper, has become associated with these names ("GT mode"). The SJ mode leads to the correct prediction of the roughly $A^{-1/3}$ dependence of the resonance centroid energy, for $A \gtrsim 80$, and has received considerably more attention than the GT mode, which predicts an $A^{-1/6}$ dependence. Recently, the giant dipole resonance (GDR) has been treated by unifying these two extreme modes[78] and accurate predictions have been obtained for the form of the resonance centroid energy over almost the entire nuclear mass range (Fig. 1.6). This model indicates that the GT mode is important in light nuclei, with the SJ mode becoming significant, but never dominant, with increasing mass number. The centroid energy of the GDR varies smoothly without evidence of shell effects and may be estimated to within $\sim$ 5% using $E_c \sim 80/A^{1/3}$, for $A > 80$.

The width of the GDR varies from 4 - 7 MeV for $A = 50 - 240$, and shows a slight systematic decrease with increasing mass number. In contrast to the centroid energies the GDR widths do exhibit shell effects. The resonance is narrowest ($\sim$ 4 MeV) for spherical nuclei near the shell closures at $A = 40$, 90, 120 and 208. Larger widths ($\sim$ 7 MeV) are found in regions of highly deformed nuclei or where isospin effects are important. The broad double peaked resonances at $A \sim 60$ are ascribed to isospin splitting of the GDR into $T_<$ and $T_>$ components, whilst resonances of a similar form in the mass region $A \sim 160$ are explained in terms of the splitting of the centroid energy into degenerate components with energies inversely proportional to the nuclear axes lengths.

Above $A \sim 50$ the GDR is smooth and can be fitted well by a single or double Lorentz curve. At lower masses the resonance becomes

Figure 1.6 Giant resonance centroid energy mass dependence. The solid line results from the model of ref. 78, the squares are data from Ref. 147.

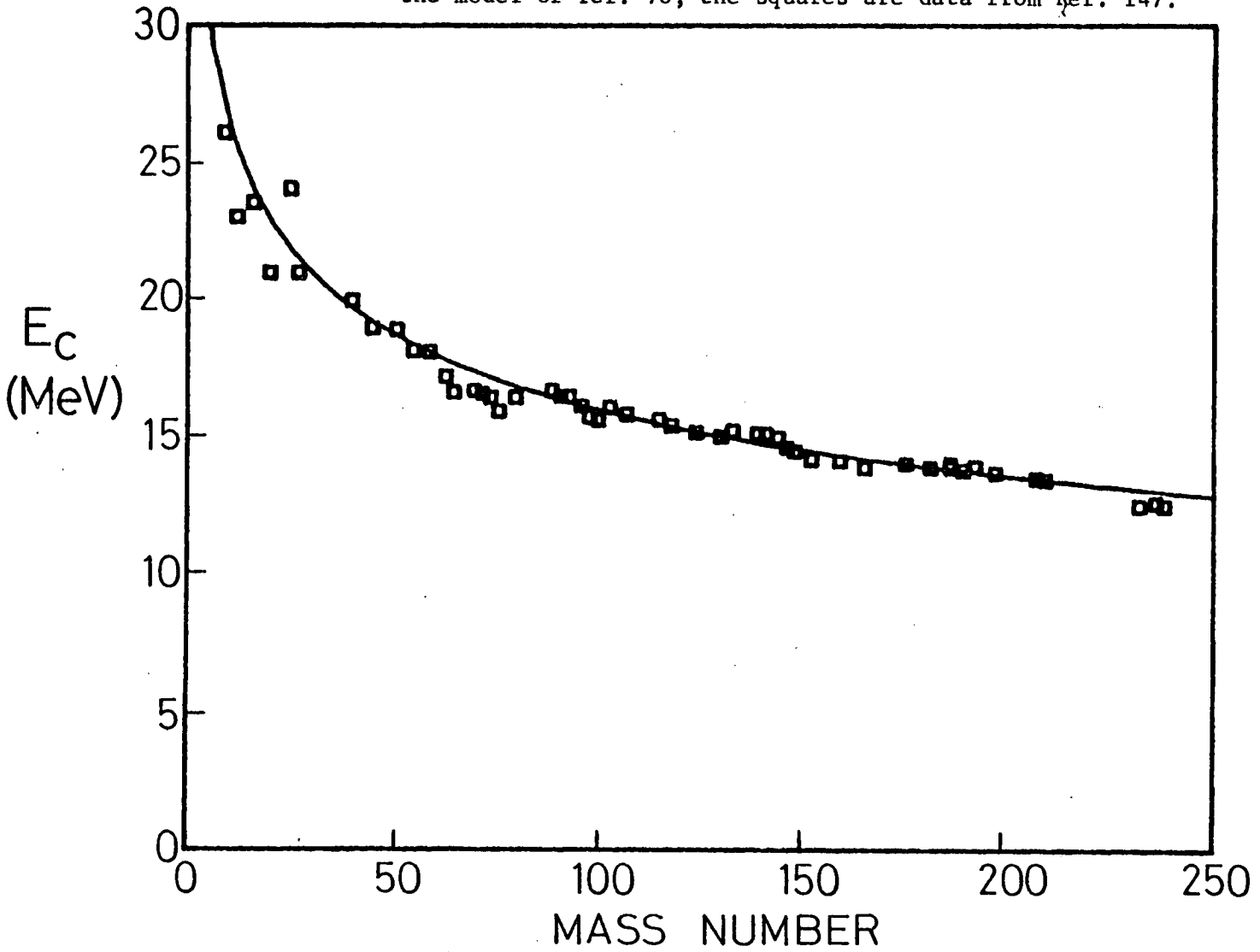

structured and broader, and begins to exhibit less collective characteristics. The varied features of the GDR, as displayed by total photoneutron cross sections, are illustrated in Fig. 1.7.

1.4.2 Multipole Resonances

In the early 1970's the existence of multipole resonances other than the GDR was experimentally confirmed, first by inelastic electron scattering[79),80)] and soon after by inelastic proton scattering[81)] and in a reanalysis[82)] of (p,p') data obtained in the late 1950's[83)]. These data indicated the existence of resonances of generally lower energy than the GDR which could be associated with monopole, quadrupole and octupole collective vibrations. Since then, broad peaks have been observed below the GDR at $E_x \sim 60/A^{1/3}$ in many nuclei, with inelastic proton[84)], deuteron[85)], ^{3}He[86)] and α [87),88)] scattering. These peaks are associated with a giant electric quadrupole vibration, and thus considered to be giant quadrupole resonances (GQRs). Of all possible collective resonances other than the GDR, it is the GQR which (because of its strength) has received the most attention in recent years.

The hydrodynamic picture of the monopole ($\lambda = 0$), dipole ($\lambda = 1$), and quadrupole ($\lambda = 2$) nuclear vibrations is illustrated in Fig. 1.8, in which the resonances are classified by their angular momentum, λ. The constituents of the nuclear 'fluid' comprise spin up and spin down neutrons and protons, hence these vibrations must be further classified according to how the constituents oscillate against each other (Fig. 1.9)[93)]. The electric modes ($E\lambda$) comprise oscillations of neutrons and protons without any spin differentiation, whilst the magnetic modes comprise spin oscillations. The electric vibrations are further termed isoscalar ($\Delta T = 0$), or isovector ($\Delta T = 1$) according to whether neutrons and protons oscillate in phase, or out of phase respectively, and for the

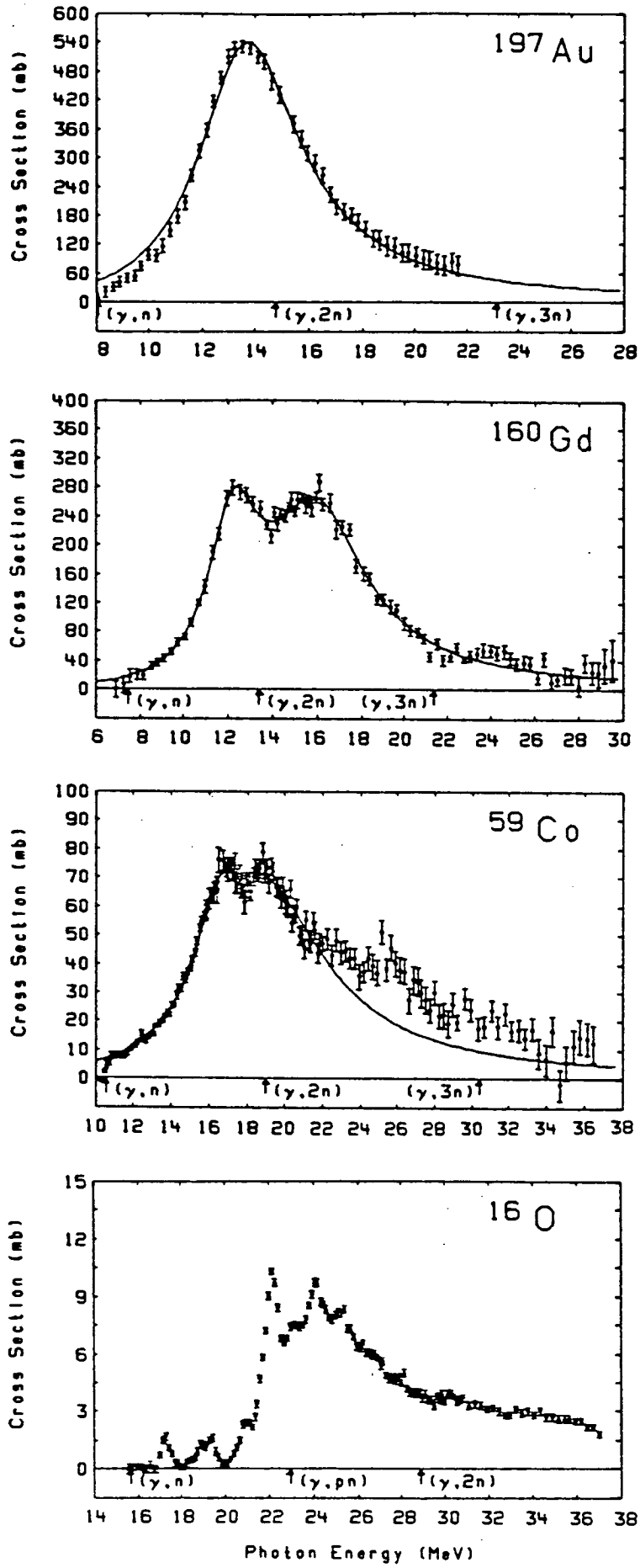

Figure 1.7 Total photoneutron cross sections for ^{16}O, ^{59}Co, ^{160}Gd and ^{197}Au (from Ref. 147).

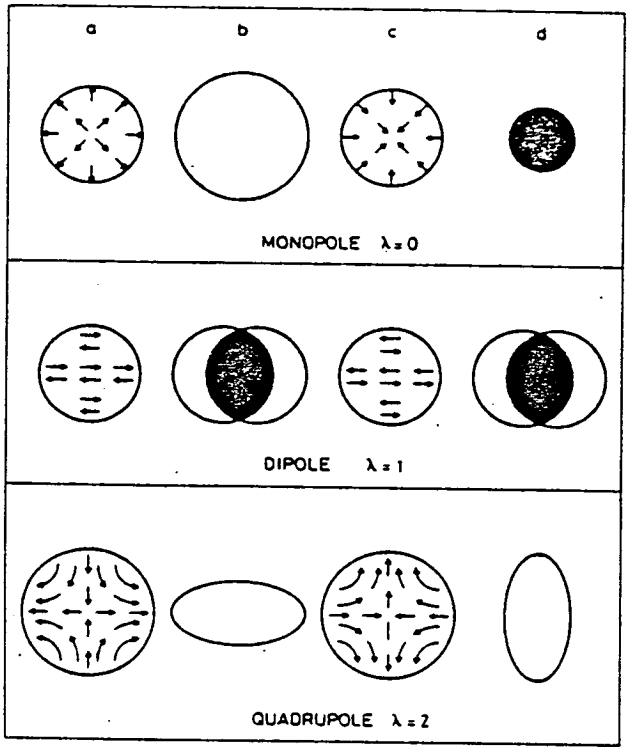

Figure 1.8 Hydrodynamic picture of the time evolution of the monopole, dipole and quadrupole nuclear collective vibrations. The velocity fields in the equilibrium configurations (a) and (c) are represented by arrows, (b) and (d) are the shapes of maximum distortion (from Ref. 92).

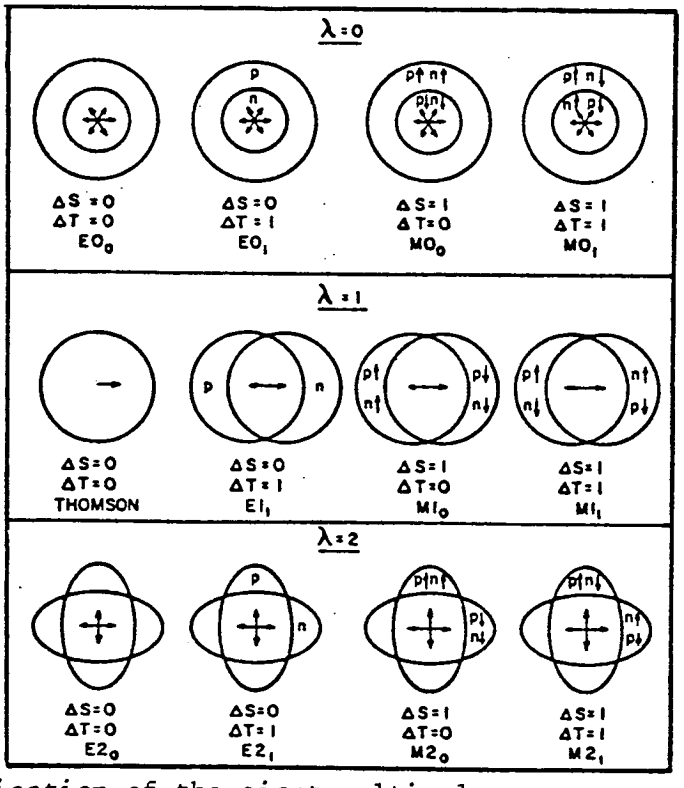

Figure 1.9 Classification of the giant multipole resonances according to angular momentum λ, spin ΔS and isospin ΔT quantum numbers (from Ref. 93).

magnetic vibrations these terms refer to whether the protons and neutrons oscillate together with spins aligned ($\Delta T = 0$) or unaligned ($\Delta T = 1$).

The MO modes cannot be excited by photon absorption or electron scattering since no longitudinal magnetic $L = 0$ components exist in the electromagnetic fields for either process. Furthermore, electromagnetic transitions only weakly excite the isoscalar M1 and M2 resonances. Hadron scattering also leads to only weak excitation of the magnetic resonances by the weak spin-spin interaction. Consequently, the magnetic resonances have received considerably less attention compared to the extensively studied electric resonances. Only for the isovector M1 resonance has any substantial strength been observed, with all other magnetic resonances either weak, fragmented or comprising groups of states with little collective character. The M1 resonance strength has been studied by electron scattering[89] and is found mainly in clusters of low lying states at excitation energies, $E_x = (35 - 45)/A^{1/3}$. The expectation that the magnetic resonances contribute little to electrodisintegration or photodisintegration cross sections is borne out by the few electrodisintegration experiments which attempt to decompose the total photodisintegration cross section into multipole components including M1 [90),91)]. At most, the M1 resonance may require consideration in the analysis of threshold photonuclear reactions. In this thesis, the magnetic resonances are given little further consideration, due to the dominance of the electric resonances in photonuclear reactions.

The properties of the low multipolarity electric resonances are summarised in terms of their centroid energies and sum rule strengths, in Table 1.2. The photon absorption cross sections for these resonances are indicated by the energy weighted sum rule appropriate to the electric transition of multipolarity, λ, for $\lambda \geq 1$,

$$\int \frac{\sigma(E)dE}{E^{2\lambda-2}} = \pi^2 \left(\frac{e^2}{\hbar c}\right) \frac{\lambda+1}{[(2\lambda+1)!!]^2} \frac{\hbar^2}{M} \cdot \frac{f(\Delta T)\cdot\langle r^{2\lambda-2}\rangle}{(\hbar c)^{2\lambda-2}}$$

where

$$f(0) = \frac{Z^2}{A} \qquad \text{(isoscalar mode)}$$

$$f(1) = \frac{NZ}{A} \qquad \text{(isovector mode)}$$

and $\sigma(E)$ is the photon absorption cross section at photon energy E for a nucleus comprising nucleons of mass M at radii r. Assuming a spherically symmetric nucleus of radius $R(R = r_o A^{1/3}, \; r_o = 1.2 \text{ fm})$ with isotropic nucleon distribution, yields

$$\langle r^n \rangle = \frac{3}{(n+3)} R^n \; .$$

Table 1.2 includes illustrative examples of the resonance centroid energies and photon absorption cross sections calculated for ^{60}Ni and ^{197}Au assuming the transitions localised at the appropriate centroid energy. In both medium weight and heavy nuclei only the dipole and quadrupole resonances contribute significantly to photonuclear processes, with the isovector dipole dominant. The isoscalar dipole 'resonance' is omitted from Table 1.2 since it corresponds (in the GT model) to a linear translation of the nucleus (Thomson scattering) and hence is not a collective nuclear excitation. The electric monopole resonances have also been omitted since these can have no photon absorption sum rule, though strengths can be expressed instead, in terms of reduced transition probabilities, B(E0). The isoscalar monopole resonance has been detected in the isovector GDR region at $\sim 80/A^{1/3}$ by electron[94], alpha[95),96)] and deuteron[96] scattering on heavy nuclei. This resonance may be excited in electrodisintegration reactions, though not in photodisintegration. It is further

Table 1.2 Electric Giant Resonances

Resonance	$E_c \cdot A^{1/3}$	$\int \frac{\sigma dE}{E^{2\lambda-2}}$
E1 - Isovector	80	$60 \frac{NZ}{A}$ mb - MeV
E2 - Isoscalar	63	$0.22\ Z^2/A^{1/3}$ μb/MeV
E2 - Isovector	130	$0.22NZ/A^{1/3}$ μb/MeV
E3 - Isoscalar	∼ 30	$0.31Z\ A^{1/3}$ pb/MeV^3
E3 - Isovector	∼110	$0.31NZA^{1/3}$ pb/MeV^3

	^{60}Ni		^{197}Au	
Resonance	Centroid Energy E_c (MeV)	Strength $E_c^{2\lambda-2} \int \frac{\sigma dE}{E^{2\lambda-2}}$ (MeV - mb)	Centroid Energy E_c (MeV)	Strength $E_c^{2\lambda-2} \int \frac{\sigma dE}{E^{2\lambda-2}}$ (MeV - mb)
E1(ΔT=1)	20.4	896	13.7	2840
E2(ΔT=0)	16.1	11.4	10.8	27.5
E2(ΔT=1)	33.2	55.5	22.3	175
E3(ΔT=0)	7.7	0.0033	5.2	0.0082
E3(ΔT=1)	28.1	0.68	18.9	0.215

commented upon in Chapter 4.

Above the giant dipole resonance collective nuclear excitation may proceed through the isovector monopole, quadrupole or octupole resonances, though these modes are expected to be dominated by a dipole photon absorption process on a correlated neutron-proton pair ("quasi-deuteron" photon absorption). This latter process is discussed in more detail in Chapter 5. The photon absorption process at energies between the giant dipole resonance and pion threshold (20 - 140 MeV) is presently poorly understood. The extent of collective or 'direct' photon absorption processes, and the significant transition multipolarities, still remain to be ascertained. Thus, it is one of the principal aims of this thesis to study the electrodisintegration reaction mechanism at excitation energies above the GDR.

1.4.3 Microscopic Model of Giant Resonances and their Decay Properties

Giant resonance decay provides an important example for studying how nuclei dispose of energy stored in a collective mode of excitation. Consequently much recent interest in the giant resonances has been directed towards the decay properties of the giant dipole and isoscalar quadrupole resonances, and the examination of their particle decay channels. A dominant direct particle emission channel indicates stable collective motion whilst dominant statistical decay indicates rapid dissipation of the coherent resonance energy among all the nucleons, i.e. thermalisation. Examination of giant resonance particle decay contributes to the understanding of the damping process in deep-inelastic collisions[97], the behaviour of large-amplitude oscillations in heavy ion reactions and the possibility of high excitation energy second harmonic giant resonances[98].

An understanding of giant resonance decay mechanisms requires consideration of the microscopic properties of the resonances. In the microscopic particle-hole model, giant resonances arise from a coherent superposition of all possible particle-hole states which give rise to the required angular momentum and parity for the given resonance. The single particle excitations which give rise to the monopole, dipole and quadrupole resonances in ^{40}Ca, are illustrated in Figure 1.10. Dipole resonance excitation arises through the excitation of particles from the last occupied harmonic oscillator shell into the first unoccupied shell above the Fermi surface. This requires an energy equivalent to the harmonic oscillator shell spacing, i.e. $\hbar\omega_o = 41/A^{1/3}$, and hence the GDR centroid energy mass dependence is reproduced, though the absolute excitation energy is too low. Elliot and Flowers[99] showed that the inclusion of an interaction between the excited particle and the hole it left behind brought the resonance energy into agreement with observations. Furthermore, it is this "residual interaction" which gives rise to the formation of a collective state from the coherent single particle states[100].

The giant resonance excitation and decay process can now be understood as proceeding through the stages:

i) The creation of a one particle - one hole (1p - 1h) state.

ii) Decay of the 1p - 1h state either by particle emission, with width $\Gamma^{\uparrow}$, or, by the creation of a 2p - 2h state and then successive particle-hole configurations until thermalisation (statistical equilibrium) occurs.

iii) Either, pre-equilibrium particle decay during the equilibration stage, or statistical particle decay at equilibrium, with total width $\Gamma^{\downarrow}$.

Nucleon emission from giant dipole resonance states has provided

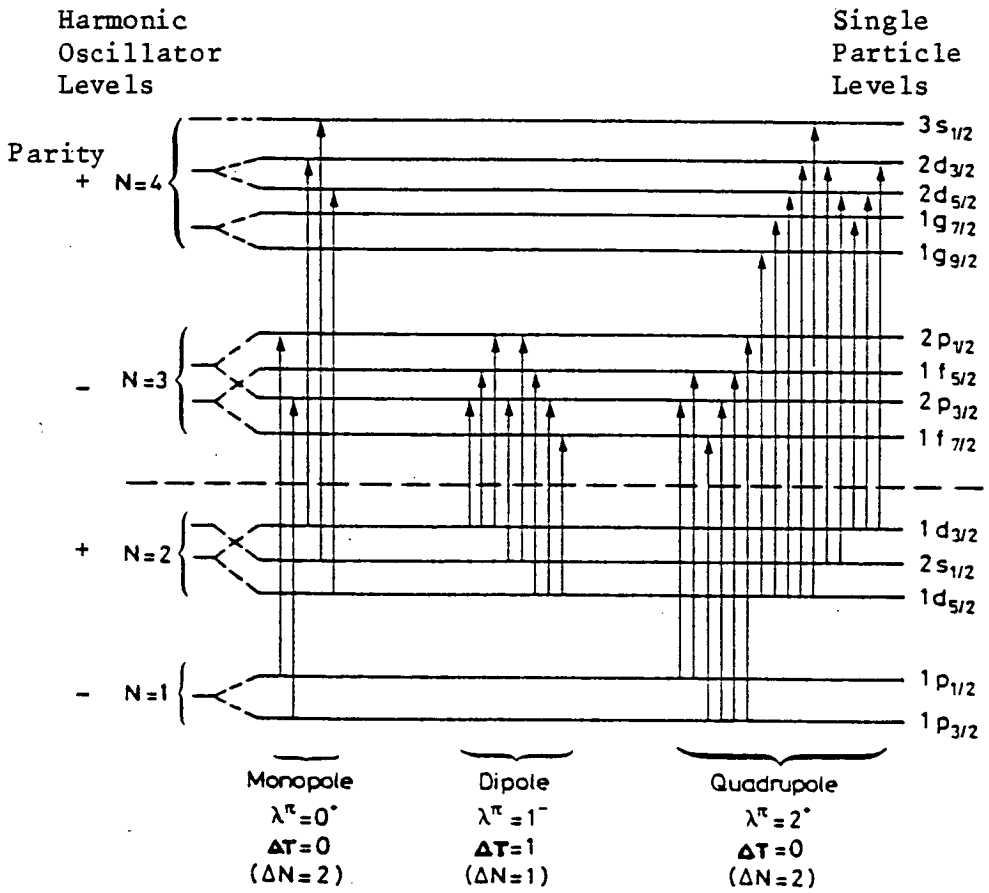

Figure 1.10. Particle-hole excitations for the monopole, dipole and quadrupole collective modes in ^{40}Ca (from Ref. 148).

extensive information on the relative magnitude of $\Gamma^{\uparrow}$ and $\Gamma^{\downarrow}$. In light nuclei $\Gamma^{\uparrow} >> \Gamma^{\downarrow}$ and direct nucleon emission is dominant, whilst in heavy nuclei $\Gamma^{\downarrow} >> \Gamma^{\uparrow}$ and equilibrium, or pre-equilibrium nucleon emission is important[101]. There is evidence that direct particle decay from the GDR is still a significant channel for nuclei up to ^{40}Ca [102], though heavier nuclei exhibit a dominant evaporative component. The alpha decay channel is of particular interest since unless the initial 1p - 1h state strongly overlaps with α-cluster states this channel must be associated with the $\Gamma^{\downarrow}$ resonance width (pre-equilibrium or equilibrium decays). Consequently, only if the giant resonance energy is rapidly dissipated into a compound nucleus state, and $\Gamma^{\downarrow} >> \Gamma^{\uparrow}$, will the alpha decay channels be well described by statistical compound nucleus decay. Non-statistical giant resonance alpha decay would generally indicate a slow thermalisation process.

During the course of this thesis study coincidence hadron scattering experiments on a wide range of nuclei have yielded information on the decay properties of the GQR. As for the GDR, dominant direct particle emission in light nuclei gives way to statistical particle emission in medium weight and heavy nuclei. Furthermore, a direct GQR alpha emission channel is important in light nuclei and has recently been explained[103] as arising from the large overlap of the GQR 1p - 1h states with α-cluster wave functions. The observation of direct alpha decay from giant resonances in heavier nuclei would therefore provide a useful tool for studying alpha clustering effects in such nuclei.

The electron-nucleus interaction enhances GQR excitation compared to photo-excitation and hence the (e, α) reaction may be a useful tool for studying the GQR decay properties, in addition to those of the GDR. Consequently (e, α) reaction studies have been undertaken in view of

the importance of unambiguously determining the decay properties of these resonances. This study has proved timely in the light of recent erroneous publications[33),41)] on (e, α) giant resonance studies which might otherwise have led to considerable confusion in the subject.

1.5 Thesis Objectives and Structure

The need to obtain data relating to alpha decay properties of giant resonances and photonuclear processes above the giant resonances is identified. A study of the (e, α) reaction at electron energies up to 120 MeV fulfils both these needs in addition to providing data on a hitherto poorly studied reaction. The early (γ, α) experiments indicated high alpha yields from medium weight nuclei about mass ∿60, consequently the nuclei ^{56}Fe and ^{60}Ni are selected for the detailed study of giant resonance alpha decay. To establish the systematics of the (e, α) reaction at higher excitation energies a range of nuclei from $^{27}Aℓ$ to ^{197}Au are studied. Such studies involve detecting low cross section ($1.0 - 10^{-4}$ μb/MeV.sr) charged particle emission in the presence of a high background. After initial tests with near-beam semiconductor detectors the necessity to use a well shielded magnetic spectrometer was established. The experimental system is discussed in detail in Chapter 2.

The data analysis procedure is discussed, and all data acquired is presented, in Chapter 3. There the general features of the data are also discussed and related to comparable studies.

In Chapter 4 the features of the data relating to giant resonance decay of medium weight nuclei are compared with the expected energy spectra and angular distributions for statistical GDR decay. Alpha decay of the GQR is briefly considered in Section 4.4.

Non-statistical decay effects observed in the acquired (e, α) data

are discussed in Chapter 5 with particular reference to current pre-equilibrium decay models. The systematics of the non-statistical (e, α) energy spectra and angular distributions are presented and used to deduce the properties of the reaction process. A summary of the conclusions of Chapters 4 and 5 is presented in Chapter 6, together with proposals for future experimental and theoretical studies of (e, α) and (γ, α) reactions. Where appropriate, cumbersome experimental or mathematical detail has been consigned to appendices.

CHAPTER 2

THE EXPERIMENTAL SYSTEM

2.1 Summary of Experimental System

All the experimental work is undertaken using the University of Glasgow's 150 MeV pulsed electron linear accelerator[104]. Electron beams of energies between 19 MeV and 120 MeV are used. After leaving the accelerator the electrons enter an energy compression system (E.C.S.) which decreases their momentum spread, prior to entering the beam deflection room. Here the beam is bent through 90°, by two 45° bending magnets, and energy analysed by energy defining slits placed between these two magnets. Thereafter the electron beam passes into a heavily shielded experimental area ('Igloo'). The pulsed electron current is monitored by passing the beam through a toroidal core placed around the beam, immediately in front of the scattering chamber. Signals induced by the electron beam, in windings around the core, are proportional to the electron beam current, and are electronically analysed to give a measure of it. After passing through the toroid the beam enters the scattering chamber and is intercepted by the photonuclear target, after which it leaves the scattering chamber and traverses about 2 metres through air prior to entering the beam dump. Charged particles emitted from the target are analysed according to their magnetic rigidity (momentum ÷ charge of particle) by a magnetic spectrometer. They are detected in the spectrometer focal plane using ten surface barrier semiconductor detectors. Signals from these detectors are carried by coaxial cables to the control room, where they

are pulse height analysed. The pulse height spectra are then stored in a computer from which they can be read out at the end of each run prior to data analysis.

2.2 Electron Accelerator

The electron linear accelerator is of the pulsed r.f. travelling wave (S-band) type, designed and constructed by Vickers-Armstrong Ltd., Swindon. An upgrading of the accelerator took place between the early and later stages of this thesis programme. This improved the efficiency of operation, and increased the maximum available energy from 120 MeV to approximately 160 MeV. Initially the accelerator consisted of three sections each with four 1.5m lengths of cylindrical wave guide powered by 20 MW klystrons with an operating frequency of 2.8562 GHz. Each klystron imparted an energy of approximately 40 MeV to the electron beam in each section. On upgrading, the third accelerator section was changed to four 2m lengths, and three 25 MW klystrons are now used to power the accelerator sections. An electron beam of 160 MeV acquires approximately 40 MeV from each of the first two sections and 80 MeV from the third section. A maximum beam energy of 164 MeV has been recorded, which yielded a mean electron current of 3 μa after 0.5% energy analysis.

The accelerator is pulsed at 100 p.p.s., with beam pulse lengths of 3.5 μsec prior to upgrading, and 3.25 μsec after upgrading, yielding a present duty factor of 3.25×10^{-4}. The early experimental runs employed accelerator peak pulsed currents of typically 120 - 150 ma, which, with the 0.75% energy analysis then used, yielded mean currents on target of $\sim$ 12-15 μa, i.e. $\sim (7.5 - 9.4) \times 10^{13}$ electrons/sec. The upgraded accelerator can provide such beam currents on target with no more than

80 ma peak current in the accelerator, even with an improved energy analysis of 0.5%.

Although pulse lengths shorter than 3.2 μsec could be obtained, they were not used since the data acquisition involved neither any timing nor fast count rates with any substantial dead time problems.

Operating at 100 p.p.s. requires the accelerator to be set with the klystron and electron gun power supplies all locked in phase. This is essential since the voltage pulses applied across the klystrons are charged from 3 phase rectified 50 Hz power supplies which, although smoothed, still have a 300 Hz ripple on their outputs. Additionally the electron gun is supplied with rectified and smoothed 3 phase 50 Hz A.C. which still has some 300 Hz ripple. This produces a modulation of the electron beam energy if the phases of the firing pulses are not always the same. Such a problem results in the production of an electron beam with almost two distinct energies of electrons, one of which will generally suffer an undesirable substantial current loss in the energy analysis system.

Changes in beam energy are made by attenuating the r.f. power in some of the sections, or by changing the relative phases of the r.f. power in the three sections. However, the latter approach results in reduced beam currents as the phases are moved off optimum setting. To obtain energies below $\sim$ 80 MeV it might appear necessary to operate with one "dead" accelerator section, with no r.f. power, through which the beam would have to drift freely. This is avoided by "back-phasing" one of the latter two accelerator sections, e.g. at an energy of $\sim$ 60 MeV the beam will be accelerated in section one, decelerated in a back-phased section two, and then accelerated to the final energy, in section three. The decelerating section ensures beam stability throughout all the accelerating sections. Such methods of beam energy variation provide electron beams of energies between 19 MeV and 120 MeV at mean

currents rarely below 7 μa on target.

During this thesis programme an energy compression system (E.C.S.) was installed at the accelerator exit. This reduced the momentum spread of the beam prior to entering the beam handling system. Although the E.C.S. was commissioned to provide an improved energy resolution for certain electron scattering experiments, it also facilitated the experimental work described here. It automatically corrects small changes in the electron beam energy and hence provides improved beam stability after energy analysis. The improved energy resolution provided by the E.C.S. assists beam handling to the target and allows the transmission of higher currents through the beam handling system, with a lower associated background.

2.3 Energy Compression and Beam Handling Systems

An energy compression system reduces the momentum spread of the electron beam, as produced by the accelerating sections, and thus acts as a matching device for the beam handling system. The operation of such systems has been fully described by Kaiser[105] hence only a summary is presented here. The linac emittance is schematically represented in Fig. 2.1 by a rectangle (I), in the longitudinal phase space, of width b (the electron bunch length) and length δp_1 (the electron bunch momentum spread). In reality the emittance approximates more closely to an ellipse. The electron beam is passed through three dipole magnets. A schematic plan view of these is presented in Fig. 2.2. The action of these magnets causes low energy electrons to take a longer route through the system than higher energy electrons, resulting in the sharply bunched beam being transformed into the "sheared" area II of Fig. 2.1. There now exists a linear relationship between the momentum of an electron and its

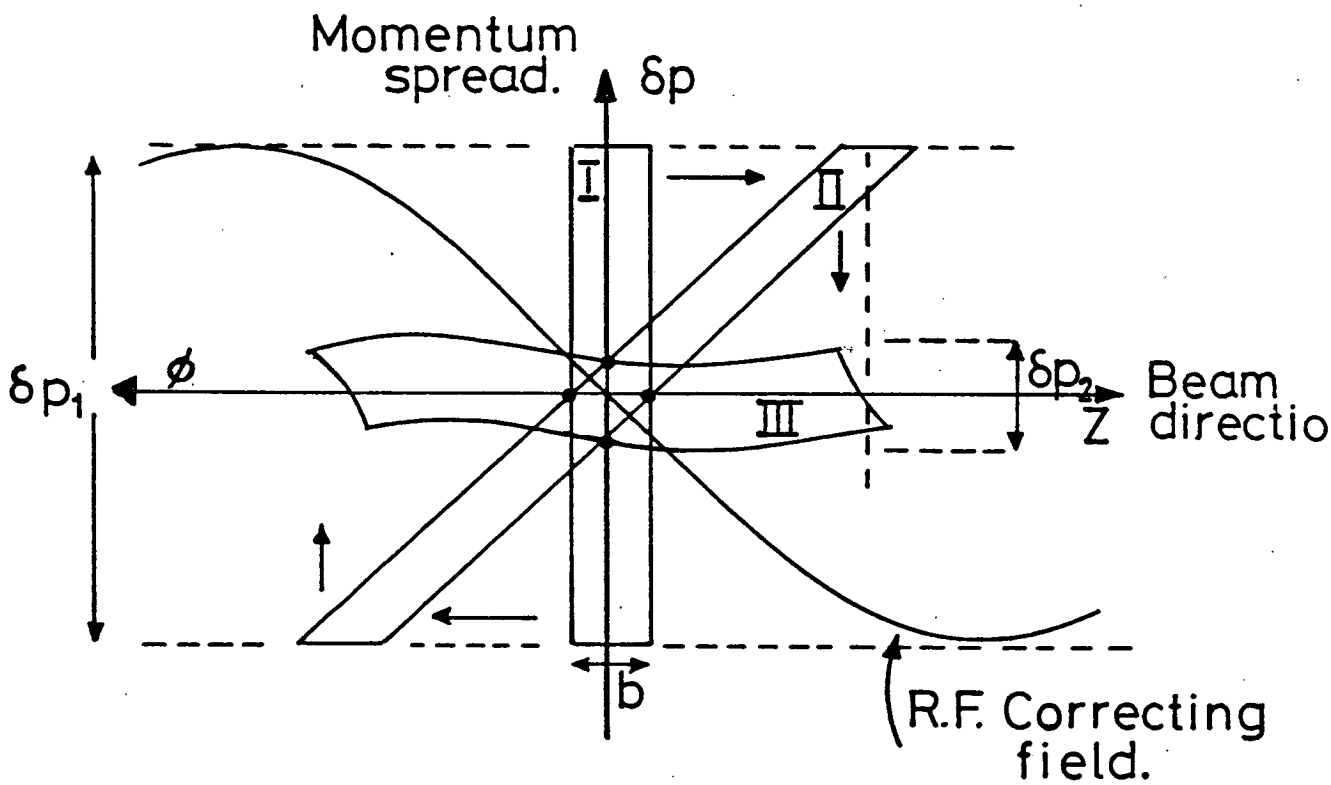

Figure 2.1. Schematic variation of beam emittance through the E.C.S. Area I - entry to E.C.S. Area II - exit from magnets and prior to entering R.F. correcting field. Area III - on exit from R.F. cavity.

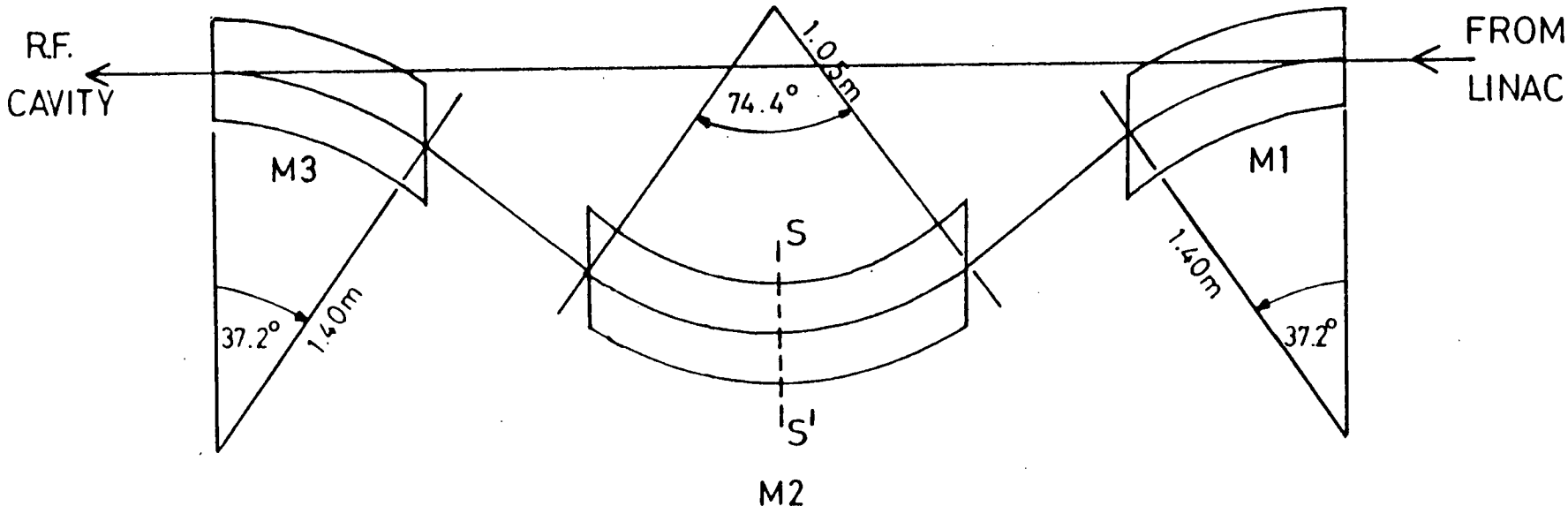

Figure 2.2. GEOMETRY OF E.C.S.

position in the bunch. This bunch is then passed through a short section of powered wave guide in which the r.f. field is adjusted to decelerate the higher energy electrons at the head of the bunch and accelerate the lower energy electrons at the tail of the bunch. The resulting beam bunch (illustrated by phase area III in Fig. 2.1) now has an increased electron bunch length, but decreased momentum spread, and has a slightly distorted emittance due principally to the inherent non-linearity of the sinusoidal field in the r.f. section. The bunch now has a momentum spread δp_2, whereas on entering the system it had a spread δp_1. The momentum is therefore compressed by a factor,

$$F_c = \frac{\delta p_1}{\delta p_2} .$$

This factor is typically about 10.

The E.C.S. also compensates small drifts in beam energy. If the centroid of phase area I drifted slightly off the momentum axis, the action of the r.f. field would hold the centroid of phase area III fixed on the Z axis, providing the maximum r.f. phase angle (ϕ) utilised does not become too large ($\gtrsim 50^{\circ}$).

The compressed beam enters the beam handling and energy analysis system shown in Fig. 2.3. Quadrupoles H1 and H2 focus the beam at the rectangular collimating aperture C1,C2. This aperture is the focal point of the energy analysis system, comprising magnet D1 and the energy defining slit, C3. Slit C3 in turn acts as the object for the second 45° magnet D2, a mirror image of D1. Quadrupoles H4 and H5 produce an approximately parallel beam which travels along approximately 2.5m of beam pipe, surrounded by concrete shielding, before entering the experimental area. There, using steering magnets S5, S6 and quadrupoles H6, H7, the beam is finally steered and focussed on to the target.

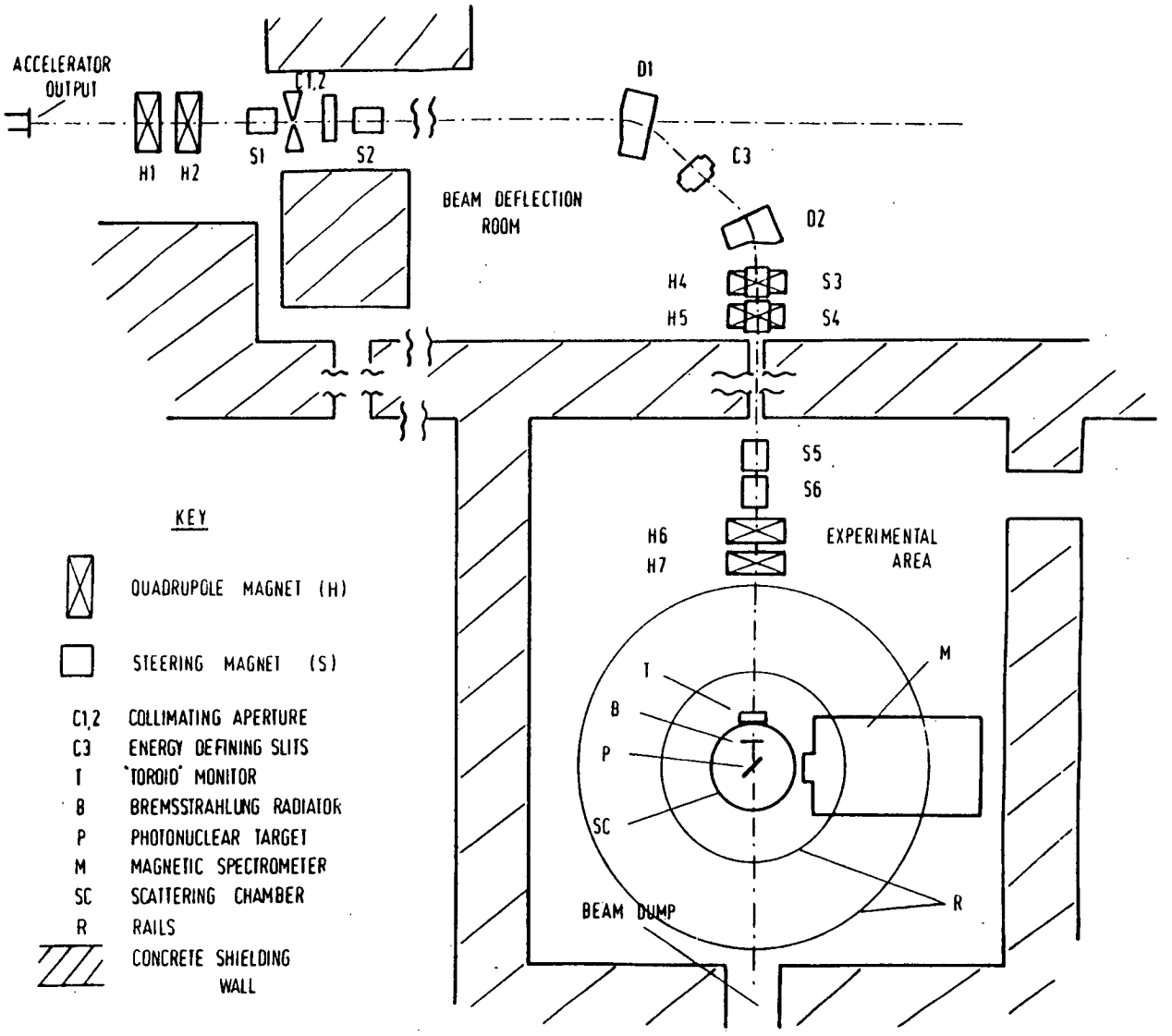

Figure 2.3 Beam handling, energy analysis and experimental areas.

The beam energy is obtained from a measurement of the magnetic field in the bending magnet D1. This magnetic field is monitored using a Nuclear Magnetic Resonance (N.M.R.) probe positioned between the pole pieces. The frequency of the N.M.R. radio frequency oscillator at resonance gives a measure of the magnetic field in which the probe is situated. This measurement is displayed in digital form by a Spectromagnetic N.M.R. Gaussmeter Model 5300. The beam energy calibration and measurement is described in Appendix 1.

2.4 Charge Monitor

A non-intercepting beam current integrator[106] is employed to monitor the electric charge incident on the photonuclear target. A toroidal current transformer is situated immediately before the scattering chamber, and thus approximately 30 cms from the target. The electron beam acts as a "primary" winding in the transformer and a 20 turn winding round the mu-metal core forms the "secondary" in which the beam current induces a current pulse. Figure 2.4 shows the circuit arrangement and associated electronics.

The signal from the "secondary" winding of the current transformer is amplified by a low ($\sim 7\Omega$) input impedance preamplifier. This is a.c. coupled to both the toroid and gating electronics to avoid problems associated with d.c. drift. The preamplifier is mounted close to the toroid winding and is therefore shielded with lead to avoid damage to its transistors by the high radiation intensities experienced near the electron beam. The input current pulse to the preamplifier is typically a 1 - 2 ma negative rectangular pulse, with a very small trailing edge droop and undershoot. The preamplifier is designed specifically to preserve the linearity of the current pulse, and has a pulse rise time of $\sim$ 6ns. The output from the preamplifier passes to the remaining

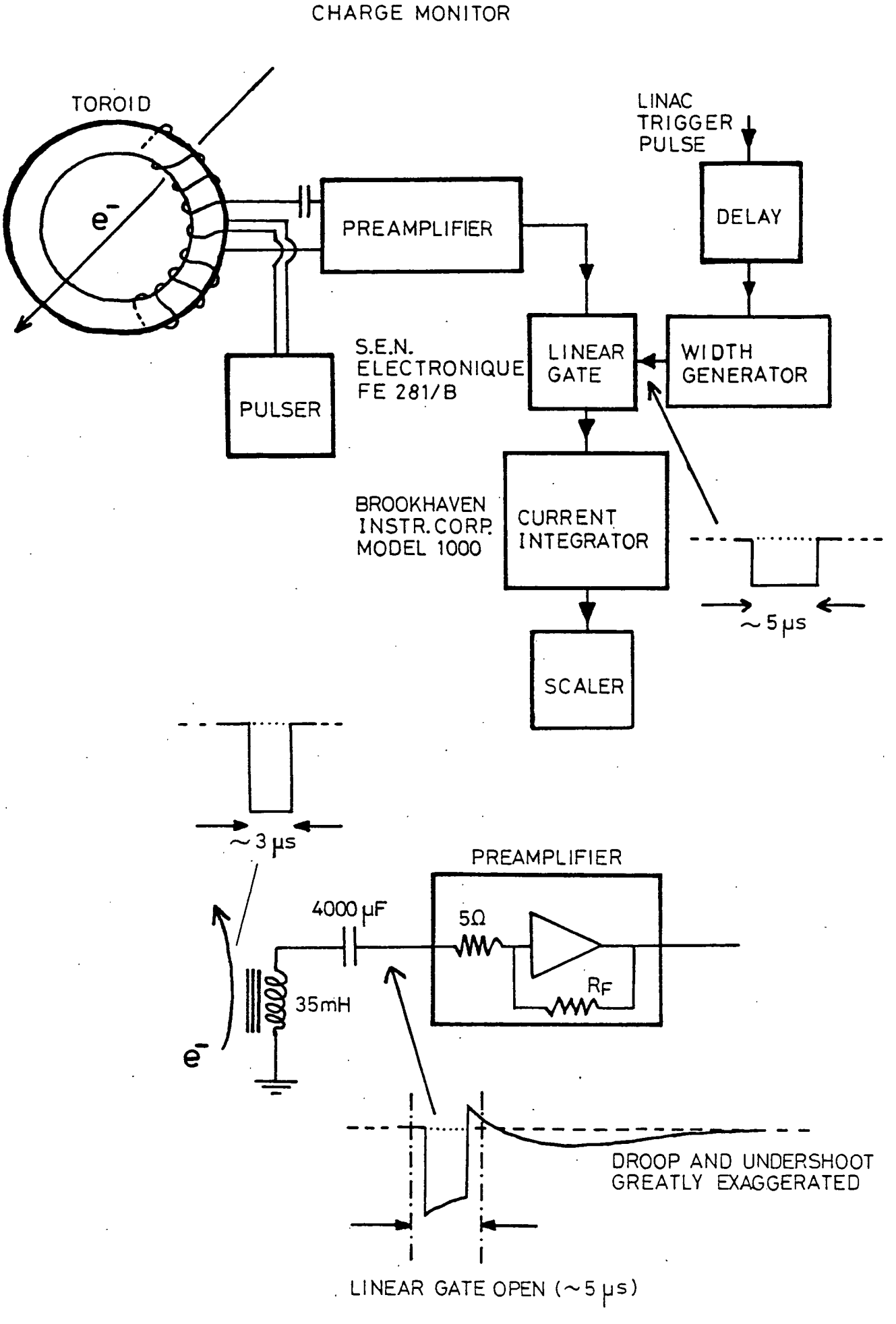

Figure 2.4 Charge monitor circuit and electronics.

electronics, situated in the experimental control room. To avoid signal pick-up from the 2.8 GHz klystrons near the control room the toroid pulses are passed along double shielded coaxial cable. Pick-up in the outer surface of the cable shields is attenuated by winding the cable about 7 turns through a mu-metal toroidal core, to form a "choke".

The toroid pulse signals are passed to a current integrator through a linear gate, which is held open for approximately 5 μs after the gate receives an accelerator trigger pulse. This allows the toroid current pulse induced by each beam pulse to pass to the integrator but avoids any spurious pick-up reaching the current integrator between beam pulses, and of course removes the undershoot component of the toroid pulse. The current integrator provides an output pulse to a scaler after a preset quantity of charge is received. A measure of the charge incident on the target is provided by the scaler reading. An automatic stop facility in this scaler produces an output pulse when a preset count is reached. This output pulse is used to inhibit further data acquisition and thus ensure that each experimental run is performed with the required preset charge delivered to the photonuclear target. Typical mean currents delivered to the target were $\sim$ 12 μa, and experimental runs were generally stopped after 10^5 output pulses had been counted from the integrator, equivalent to $\sim 3 \times 10^{-2}$ coulombs of charge delivered on target.

It is essential to ensure that the toroid charge monitoring system is operated in a region of linearity, and that any preamplifier saturation is avoided. Checks on linearity, using a Faraday Cup, show the system to be linear within $\sim$ 0.5% over the range of mean currents 1 - 15μa. Above 15μa preamplifier saturation effects are evident. The stability of the system is monitored regularly by feeding pulses from a precision pulse generator directly to a single turn wound around the toroidal current transformer. The response obtained provides an indication

of any changes in the circuit properties, and can be used to correct any preamplifier gain shifts. Details of the toroid monitor calibration and linearity checks are given in Appendix 2.

2.5 Scattering Chamber

The scattering chamber contains a five position target ladder and provision for a bremsstrahlung radiator, as illustrated in Fig. 2.5. This cylindrical aluminium chamber is 10" in height and 18" diameter with windows set at 15^{o} intervals, starting at 15^{o} from the beam on one side, and $7\frac{1}{2}^{o}$ from the beam on the other side. Provision is made for vacuum coupling the spectrometer to the chamber at 18 angle settings with $7\frac{1}{2}^{o}$ intervals. Vacuum coupling is ideal since it eliminates energy losses in the chamber windows and in a spectrometer-chamber air gap. However, the spectrometer could hold a vacuum of only about 10^{-3} Torr and thus had to be vacuum isolated from the chamber and beam pipe vacuum of approximately 10^{-6} Torr. This was accomplished by fitting a 200 $\mu gm/cm^2$ Al foil inside a spectrometer-chamber couple. This coupling procedure resulted in alpha particle energy losses of less than 0.15 MeV over the range of energies studied.

The target ladder could be operated remotely from the control room and included an $\sim$60 mg/cm^2 beryllium oxide scintillator in one position. The targets are observed through a $\sim\frac{1}{4}$" thick perspex window, and are viewed remotely with the aid of a television system. Thus when the scintillator is placed in beam, the electron beam position and focus can be viewed and controlled remotely.

The electron beam passes out of the target chamber through a 0.025 cm aluminium exit port and through $\sim$2 metres air until reaching the entrance of the beam dump. The entrance aperture is $\sim$1 metre square and leads

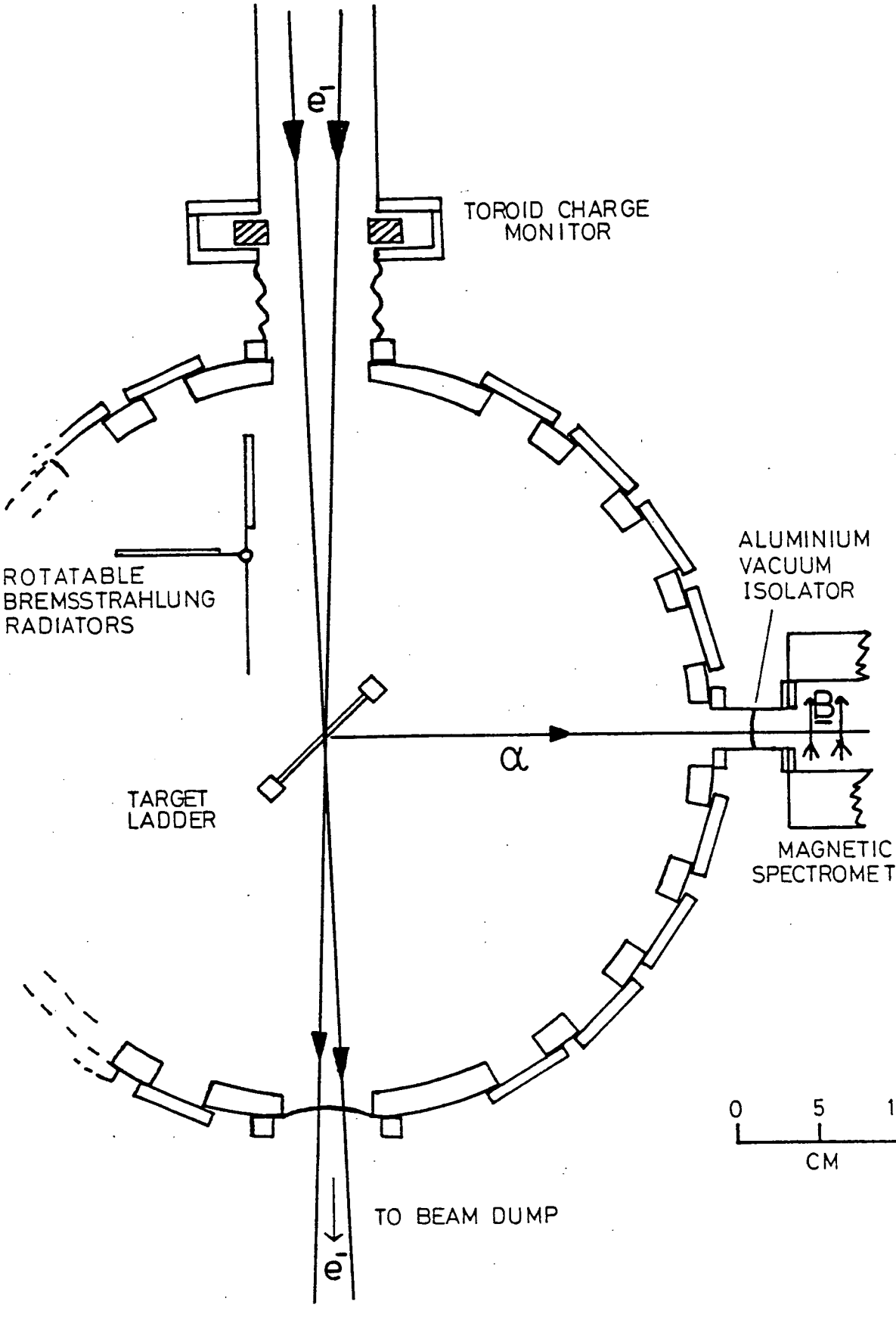

Figure 2.5 Scattering chamber.

into a concrete shielded tunnel ∿5 metres long. This tunnel minimises the return of background neutrons to the target and spectrometer focal plane detectors.

2.6 Targets

The targets are supported on aluminium frames mounted in a five position target ladder situated in the centre of the scattering chamber. The ladder could be raised and lowered pneumatically to select any one of the targets, or a blank position used for the determination of background count rates.

The selection of target thickness is a compromise between acceptable alpha energy losses and adequate counting rates to obtain data with sufficiently low statistical errors in reasonable times. Target thicknesses are selected to ensure alpha energy losses, $\Delta E_\alpha < 0.05E_\alpha$. The targets selected are isotopically enriched, or of high isotopic purity, with one exception. Thick natural nickel targets were employed as a substitute for ^{60}Ni and ^{58}Ni in certain high energy alpha emission studies requiring thick targets. This substitution is reasonable since data has been obtained for $20 < E_\alpha < 30$ MeV showing the cross sections for ^{60}Ni and ^{NAT}Ni targets to be equivalent within the experimental accuracy. The targets used for the data acquisition are listed in Table 2.1 together with their thickness and isotopic purity.

Two methods of target thickness measurement were applied. Targets thicker than ∿ 1 mg/cm^2 were simply weighed and their area measured to give a mass per unit area thickness. Lower target thicknesses were obtained by measuring alpha particle energy losses in the target. Accurate energy loss measurements were carried out using a thin ^{238}Pu alpha source and the Kelvin Laboratory magnetic spectrometer, with its associated focal

Table 2.1 - Targets

Target	Purity[e] %	10^{18} Thickness Atoms/cm^2
^{27}Aℓ	99.99[c]	246 ± 7.6
^{27}Aℓ	99.99[c]	950 ± 28.5
^{56}Fe	99.95[a]	13.70 ± 0.75
^{60}Ni	99.6 [a]	10.23 ± 0.61
^{60}Ni	99.6 [a]	54 ± 2.0
^{NAT}Ni	99.9 [b]	8.13 ± 0.41
^{NAT}Ni	99.9 [b]	44.98 ± 1.35
^{NAT}Ni	99.9 [b]	83.14 ± 1.66
^{NAT}Ni	99.9 [b]	163.7 ± 3.3
^{NAT}Ni	99.9 [b]	580.4 ± 23.2
^{68}Zn	> 97.0 [a]	10.45 ± 0.438
^{92}Mo	> 98.0 [d]	389.2 ± 18.5
^{94}Mo	> 98.0 [d]	435.4 ± 4.4
^{197}Au	99.9 [c]	90.8 ± 3.63

a) Isotopic purity quoted by Stable Isotope Unit, Harwell.

b) Atomic purity quoted by Chromium Corp. of America.

c) Isotopic purity quoted by Goodfellow Metals, Ltd.

d) Isotopic purity quoted by R.P. Singhal, private communication.

e) All quoted purities exclude gaseous impurities.

plane detectors. The small ^{238}Pu source could be placed close to a target in the ladder, on the opposite side from the spectrometer. The uniformity and thickness of a target could be estimated by placing different regions of the target in front of the α-source, and measuring the transmitted alpha energies, from which an energy loss could be deduced. Using energy loss tables[107),108)] a measure of the target thickness can be derived. Such measurements result in a systematic error of ∿5%, arising principally from the uncertainty in the tabulated stopping power data used.

2.7 Spectrometer

The Kelvin Laboratory, $n = \frac{1}{2}$ double-focussing, magnetic spectrometer is used for momentum (actually, momentum ÷ charge of particle) analysis of charged particles emitted from the photonuclear target, prior to detection by solid state semiconductor detectors, in the spectrometer focal plane. The spectrometer parameters are listed in Table 2.2, the spectrometer geometry is illustrated in Fig. 2.6. The measurements of the spectrometer parameters were made using a small ^{238}Pu α-source, and are described in Ref.109.

The spectrometer magnet windings are water cooled and provided with current from a highly stabilised (3 parts in 10^5) 170V, 700A power supply. This power supply can provide safe operating currents to the windings which allow the spectrometer to analyse alpha particles of momentum to 700 MeV/c (i.e. $E_\alpha \sim 65$ MeV). Whereas many electron accelerators have spectrometer systems designed primarily for electron scattering studies, and thus with momentum acceptances close to the highest momenta provided by the accelerator, the Kelvin Laboratory spectrometer was installed with due consideration for charged particle work, in particular photoproton studies. The dominant photon absorption process above the giant

Table 2.2

Magnetic Spectrometer Characteristics

	Spectrometer Parameters	
	Theoretical	Measured[109]
Field index n	0.5	-
Field index β	0.25	-
Radius	80 cm	-
Deflection angle	169.8°	-
Image distance for object distance = 65.28 cm	65.28	65.49 ± 0.25 cm
Vertical (along focal plane) Magnification	-1.00	0.95 ± 0.02
Horizontal magnification	-1.00	-1.02 ± 0.02
Dispersion	4.00	4.02 ± 0.06
Focal plane angle	$33^{\circ}29'$	$34^{\circ}27' \pm 1^{\circ}36'$
Intrinsic resolution	0.02%	< 0.05%

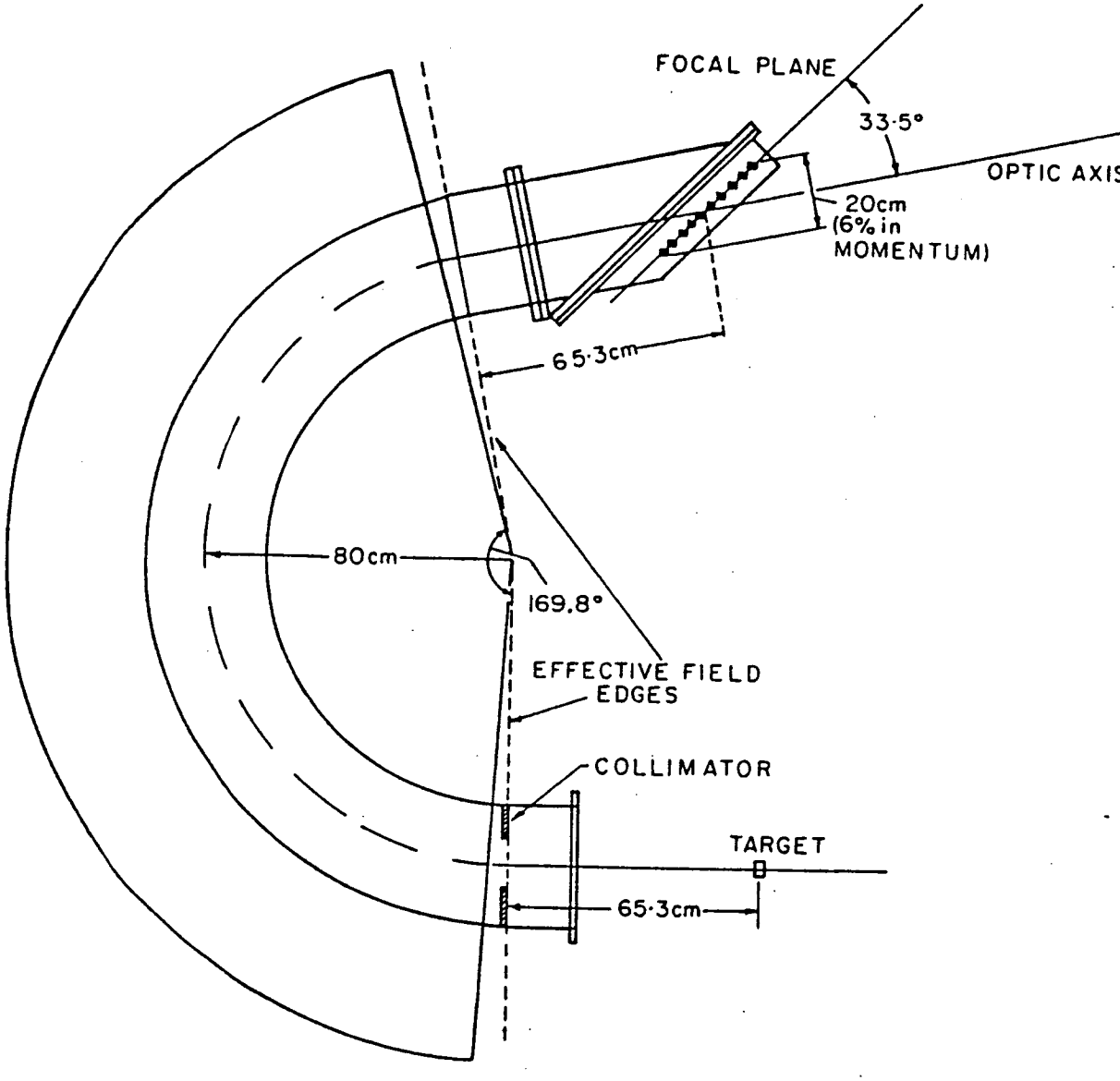

Figure 2.6. Magnetic spectrometer and charged particle detector array.

resonance region is quasi-deuteron photon absorption, whereby the photon energy is shared by the proton and neutron in a correlated pair. Thus, for an accelerator design energy of 130 MeV, it was considered adequate to have a charged particle detection facility which would accept protons up to half the machine energy, i.e. E_p = 65 MeV, $P_p \sim 350$ MeV/c. These considerations resulted in the provision of a unique combination of electron accelerator and spectrometer, which enabled much of the original electron induced alpha emission studies, described in this thesis, to be undertaken up to alpha energies, E_α = 65 MeV.

The spectrometer pole faces form part of the vacuum enclosure in which pressures down to 10^{-3} Torr can be reached. Such pressures minimise particle energy losses, scattering, and atomic electron capture (e.g. $^{++}$He converting to $^{+}$He) such that particle losses due to these factors are negligible even for the lowest alpha particle energies considered ($E_\alpha \sim 3.5$ MeV).

The angular position of the spectrometer could be varied by moving the spectrometer round two concentric rails by use of a motor driven carriage on which the whole assembly is mounted. Since the couple between the spectrometer and scattering chamber did not incorporate a sliding seal, angle changes involved letting the scattering chamber up to air and sealing off the spectrometer vacuum enclosure before decoupling the spectrometer prior to moving to the next angle.

The spectrometer focal plane contains a detector ladder which covers ∿6% momentum bite (12% energy bite) with respect to the central detector particle momentum (energy). Ten detectors are mounted in the ladder, each having a maximum possible momentum bite, with no collimation, of ∿.45%, and with the spacing between one detector and the next, centre to centre, of 0.6% momentum.

The spectrometer subtends a solid angle at the target of 10.00 millisteradians, defined by a brass collimator placed at the effective pole edge of the magnet. It has been experimentally verified[109] that considerably less than 1% of charged particles are lost between the collimator and the two detectors nearest to the centre of the focal plane. However, detectors at the ends of the focal plane receive a particle flux depleted by collisions with the pole faces and the effect of the field distributions near the pole faces causing aberrations of the image on the focal plane. This depletion is significant but can be corrected by measuring the relative efficiencies of the detectors relative to the centre of the focal plane. (See Appendix 3).

The magnetic field is measured using a Rawson-Lush rotating coil gaussmeter, with the probe situated near the outer edges of the pole pieces. This probe reduces the effective spectrometer solid angle from 10.00 to 9.94 millisteradians.

The energy calibration of the spectrometer (magnetic rigidity as a function of magnetic field) is described in Appendix 4. The calibration shows that the relationship between the measured spectrometer magnetic field and the magnetic rigidity of particles incident on the centre of the focal plane, was slightly non-linear at high momenta (e.g. $\sim$ 4% non-linearity at $p_\alpha \sim 700$ MeV/c). The non-linearity is due to saturation of the pole piece iron, which will be particularly evident near the outer edges of the poles where the probe is situated.

2.8 Detectors

An array of ten silicon surface barrier detectors is arranged in the focal plane of the spectrometer as shown in Fig. 2.7. The detectors were manufactured by Philips and have the specifications listed in

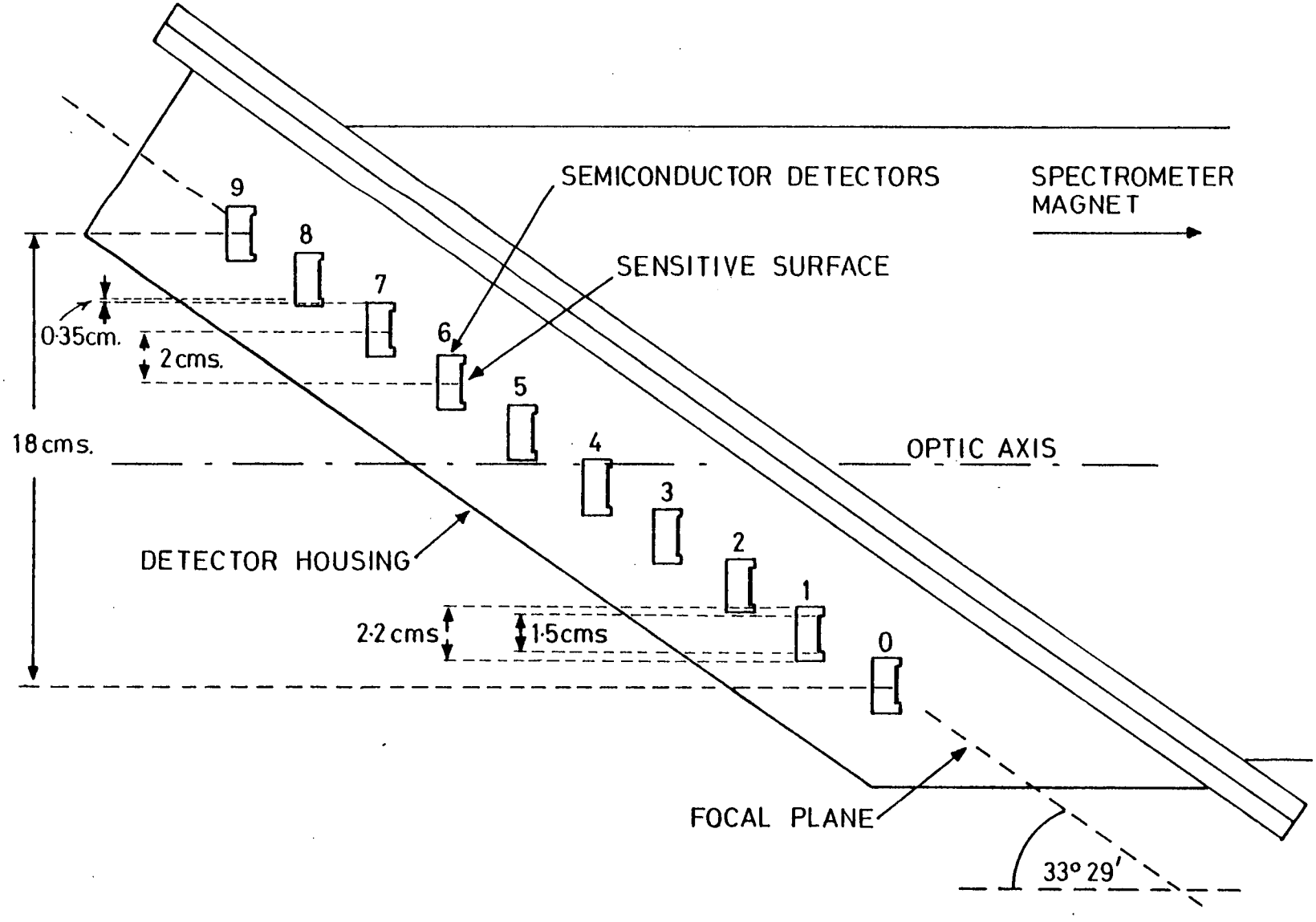

Figure 2.7. Charged particle detector array.

Table 2.3. The detector depletion layer thickness was controlled by variation of the applied bias voltage since,

$$d \approx 0.5\ (\rho_n V)^{\frac{1}{2}}$$

where d = depletion (sensitive) depth in μm.

ρ_n = resistivity of silicon (n-type here) in Ω- cm.

V = applied bias (across detector) in volts.

The maximum depletion depth for the detectors is reached when about 200 volts bias is applied across them. In general, voltages considerably below 200 volts are employed, for two principal reasons. Firstly, since the spectrometer focusses alpha particles and protons of identical energies at the same position in the focal plane, some procedure must be applied to separate the arrival of a proton or an alpha particle in the detector. Since these particles have greatly differing stopping powers it is possible to set depletion depths for which an alpha particle will deposit its total kinetic energy, whilst a proton will deposit only a fraction of its kinetic energy in the detector. Since the output voltage pulse height from a suitable charge sensitive preamplifier connected to the detector, will be proportional to the energy deposited in the detector, subsequent pulse height analysis will yield a clear separation of the proton and alpha particle peaks. Thus, when setting a detector bias appropriate for the energy of the alpha particles being examined, careful consideration has to be given to the range and stopping powers of the charged particles incident on the detectors. Using an "energy loss" technique, as described above, protons and alpha particles down to 3 MeV kinetic energy can be satisfactorily separated prior to pulse height analysis.

A second reason for employing as thin a depletion layer as possible

Table 2.3

Silicon Surface Barrier Detector Parameters

Sensitive area	-	nominal 16 mm × 40 mm
	-	minimum 15 mm × 38 mm
Silicon wafer	-	n type
	-	resistivity 4000 - 6000 ohm cm
	-	thickness 500 ± 2 microns
Resolution	-	40 keV or better
Leakage current	-	less than 2 microamps
Case	-	dimensions 55 mm × 22 mm × 12 mm
Plug	-	Microdot type 0033-0036 on 12 mm × 22 mm side

is to reduce events due to background charged particles or background neutron induced reactions in the sensitive volume of the detector. The considerable shielding placed around the detectors and around the various sources of background radiation, together with the small sensitive volume of the detectors employed, reduces the background to negligible proportions. Around the counters themselves is placed approximately 4" of lead and 12" of borated paraffin wax. Substantial shielding is also placed around three other sources of background radiation; firstly, scattered radiation associated with the beam, where it enters the experimental area through steering and quadrupole magnets; secondly, scattering when the beam passes through the photonuclear target in the scattering chamber about 4' directly below the spectrometer focal plane; and thirdly, radiation from the beam dump.

Many detectors had poor charge collection properties near their edges. This was manifest by a substantial low energy tail observed in pulse height spectra obtained during tests with α calibration sources. The removal of such low energy tails is preferable in order to ensure that the detector absolute efficiency can be determined such as to be applicable to the total counts obtained from analysis of the pulse height spectra. Detectors which produce low energy tails in pulse height spectra make the reproducible assignment of a "lower bound" of the peaks difficult. Strips of 0.0055" photographic film were attached to the edge of the detectors in order to collimate incident particles into a sensitive detector region no nearer than 1.5mm from the detector edge. Such an arrangement entirely removes any substantial low energy tail.

The collimated detectors have a 1.2 cm sensitive width, compared to 1.5 cm for an uncollimated detector. The detectors are placed every 2 cm along the ladder, thus giving a minimum ratio of detector

bite to detector spacing of $\sim \frac{1.2}{2.0} = \frac{3}{5}$. Since the relative momenta seen by two adjacent detectors, at their centres, as determined by the α-calibration, is ∿0.6% in momentum - a collimated detector momentum bite will be $0.6 \times \frac{3}{5} = 0.36\%$.

The ten detectors are placed symmetrically with respect to the optic axis of the spectrometer, and are numbered J = 0 - 9 inclusive, with detector 0 "seeing" the lowest energy particles at a given spectrometer field. The efficiency of each detector is considered as having two components, an absolute and relative efficiency. The detector absolute efficiency, which involves consideration of multiple scattering and inelastic nuclear interactions in the detector, is discussed in Appendix 5, where it is shown to be essentially 100% for each detector. The relative efficiency derives from the spectrometer properties and is a function of the detector position (J) in the focal plane. It is considered in Appendix 3. As referred to in Section 2.7, there is no significant loss of charged particles between the spectrometer entrance collimator and the centre of the focal plane. Thus a detector at the centre of the focal plane (J = 4.5) has a relative efficiency of 100%.

2.9 Signal Processing Electronics

The charge pulse from each detector is accepted by the input capacitor of a charge sensitive preamplifier placed immediately outside the detector ladder vacuum box, and inside the spectrometer focal plane shielding. The preamplifier integration and differentiation time constants (τ_i and τ_d) are carefully chosen to produce a voltage pulse to suit the operation of the successive circuit elements, and in particular to match the input characteristics of the pulse digitiser later

in the circuit. Values of $\tau_i = \tau_d = 500$ ns were selected, yielding an output voltage pulse from the preamplifier as shown in Fig. 2.8. Thereafter the voltage pulse is transmitted by a doubly screened coaxial cable to amplifiers in the control room. All ten signal cables are wound around toroidal cores, at the experimental area and control room ends, to produce a radio frequency choke.

The signal processing circuit following each preamplifier is illustrated schematically in Fig. 2.9. Ten such identical channels are used, one for each detector in the spectrometer focal plane. The signal pulse is first amplified in a fixed gain (×10) fast amplifier, prior to further amplification in a variable gain fast amplifier. At this stage the signal path divides into a gating signal, and a linear signal ready for analogue to digital conversion. The gating signal then passes through a further variable gain amplifier prior to entering a network of discriminators which set the criterion for allowing a gate pulse to reach the digitiser. This second variable gain amplifier can be used to vary the pulse height reaching the discriminator network, and thus provides a simple means of varying the magnitude of the linear signal which may be provided with a gate pulse at the digitiser. The first discriminator has a threshold set to remove small background pulses. This discriminator thus provides an output pulse for each "acceptable" input. This output pulse could be used to gate the digitiser if "acceptable pulse" rates and digital processing times were such that no dead time would arise. However the overall process of digitising can take up to $\sim$ 20 μsec, nearly 7 times the actual beam pulse time. Thus only one "acceptable pulse" from each detector may be processed per beam pulse. A measure of the dead time (or lost "acceptable" pulses) is therefore necessary.

A measure of dead time is provided by employing two further

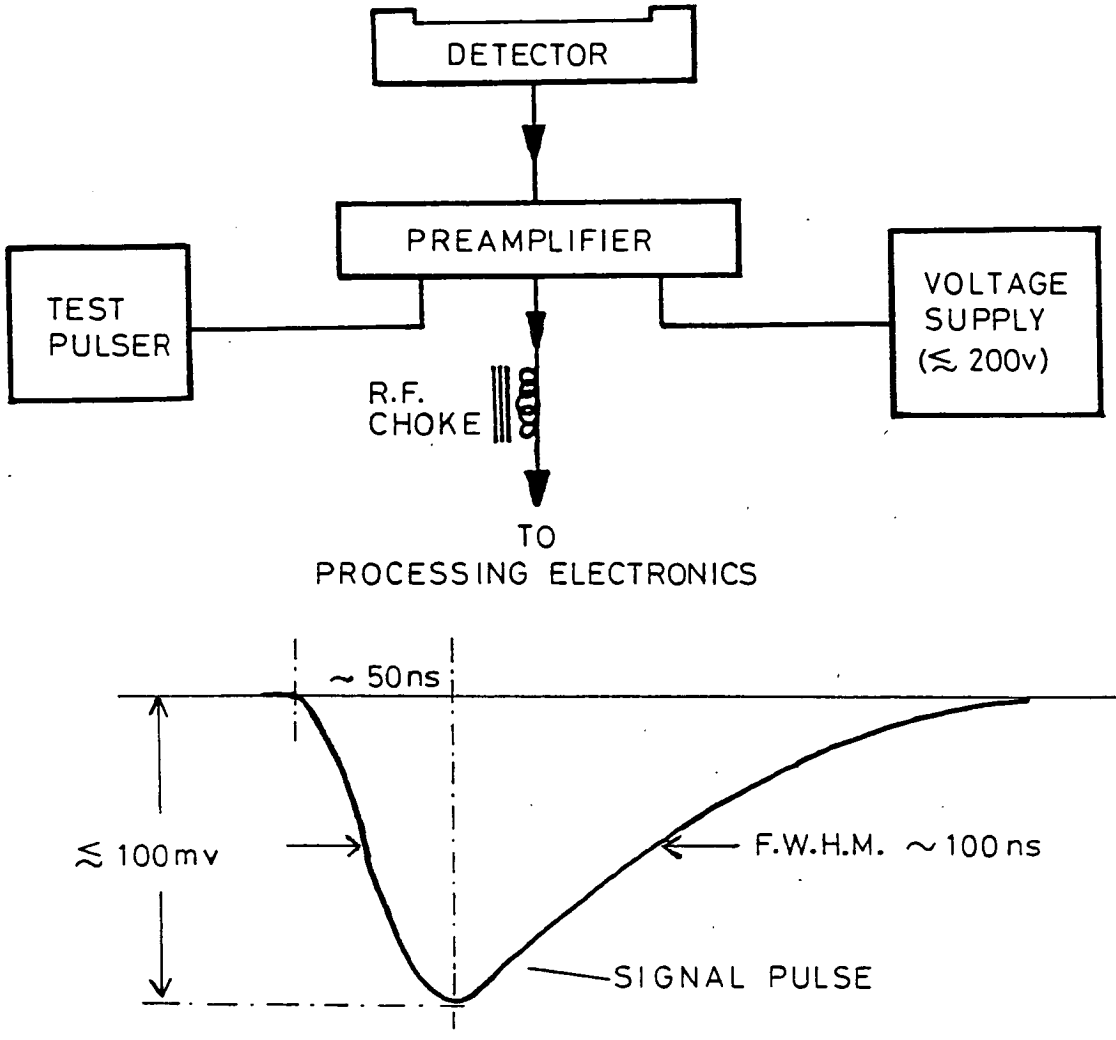

Figure 2.8 Detector electronics and preamplifier output voltage pulse.

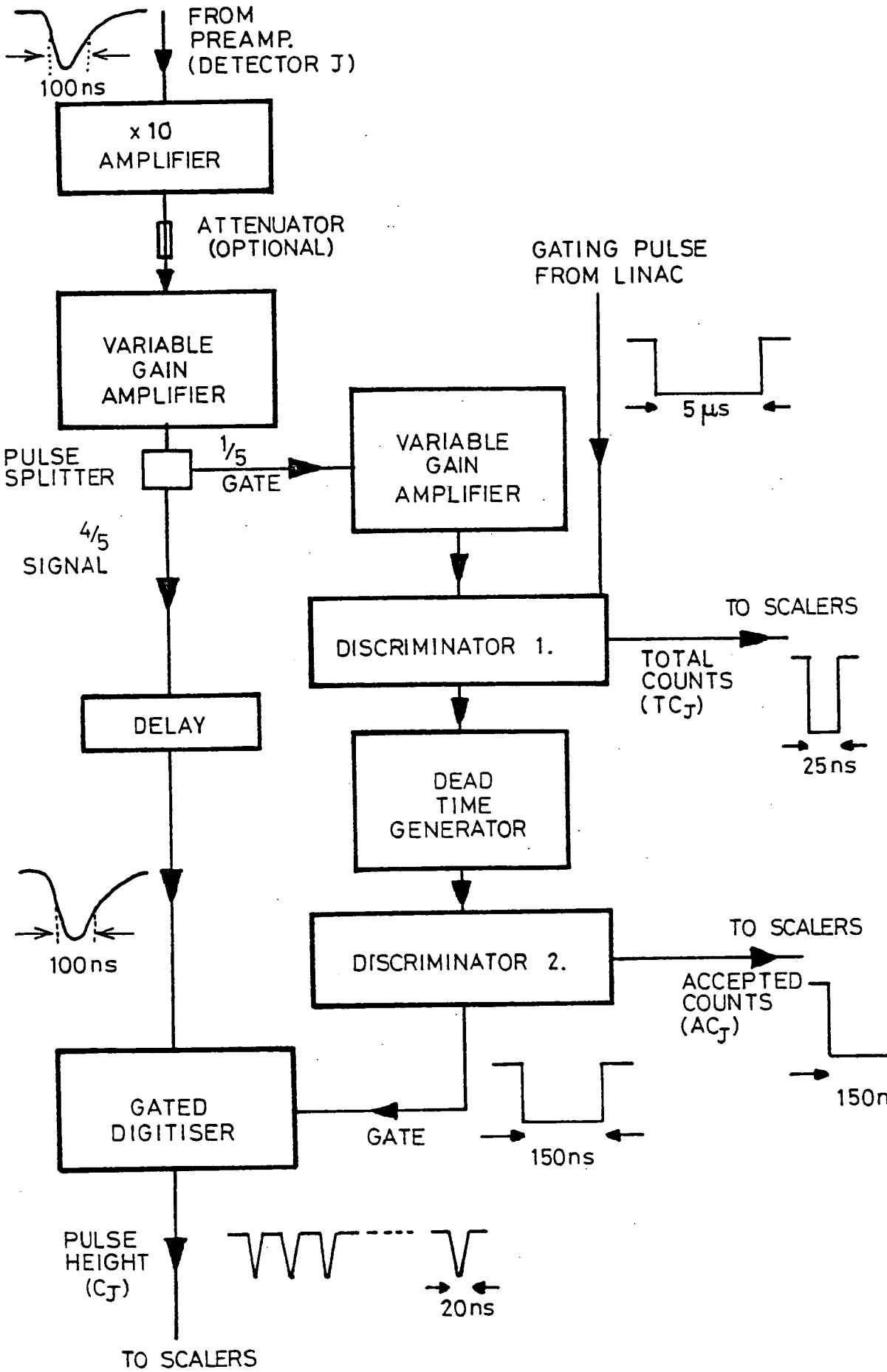

Figure 2.9. Signal processing electronics.

discriminators, the first of which produces at its output a replica of the short pulse applied to its input if a similar pulse was not present in the previous 50 μsec. This discriminator is referred to as a "Dead Time Generator". The last discriminator merely provides two logic pulses. One pulse ensures that the digitiser is gated for long enough (∿ 150 ns) to allow only one linear pulse to pass when the gate is open - the other is counted to provide a measure of the number of finally accepted pulses (AC_J) which can be compared with the total "acceptable pulses" (TC_J) output from the first discriminator in the series of three. Thus the percentage dead time for each counter is given by:-

$$D_J = \left(\frac{TC_J - AC_J}{TC_J}\right) \times 100\% \quad .$$

The discriminators themselves are gated by accelerator beam pulses, such that "acceptable pulses" are only produced during beam bursts. This avoids the collection of background pulses produced after a beam burst.

The linear signal passes through a delay, which is set to ensure its arrival at the digitiser during the period when its corresponding gate pulse would arrive if all the criteria set by the discriminators are met. This delay compensates for the delay encountered by the gate pulse whilst passing through the second variable gain amplifier, the discriminators and dead time generator.

The digitiser produces a train of up to 200 logic pulses. The number of these is proportional to the height of the counter pulse.

The electronic signal processing produces three digital outputs per beam pulse for each of the ten channels:

1) A number proportional to the height of the pulse (C_J)

$$C_J = 1 - 200 \quad (J = 0, - 9).$$

2) Total number of acceptable counts (TC_J)

$$TC_J = 0, 1, 2, \ldots\ldots .$$

3) Accepted Number of Counts (AC_J)

$$AC_J = 0, 1 .$$

A physically realistic deadtime requires $TC_J \geq AC_J$, else negative deadtimes are obtained. Such deadtime provides an immediate indication of a discriminator or scaler malfunction.

The thirty numbers output following signal processing are stored in a Lecroy type 150 scaling system, prior to reading and storage by a computer, as described in the next section.

2.10 Computer Data Storage

2.10.1 Computer Interface

The computer interface electronics is illustrated in schematic form in Fig. 2.10. The interface consists of two interface stages - a Lecroy/CAMAC* interface and CAMAC/P.D.P. 8 interface. The Module for Interfacing the Lecroy Camac (data) Highway (MILCH) is the only non-commercial unit used. It enables control of the Lecroy Scalers to be passed either to the Lecroy controller or the CAMAC controller.

Prior to each beam burst the scalers are clear and control is passed to the Lecroy controller. The output pulses from the electronic signal processing, as described in Section 2.9, are counted in the

---

* CAMAC is officially not an acronym, but is an invented palindrome that symbolises the interface looking in two directions, towards the computer and towards the peripherals or modules. Coincidentally, CAMAC is an acronym for Computer Aided Measurement And Control.

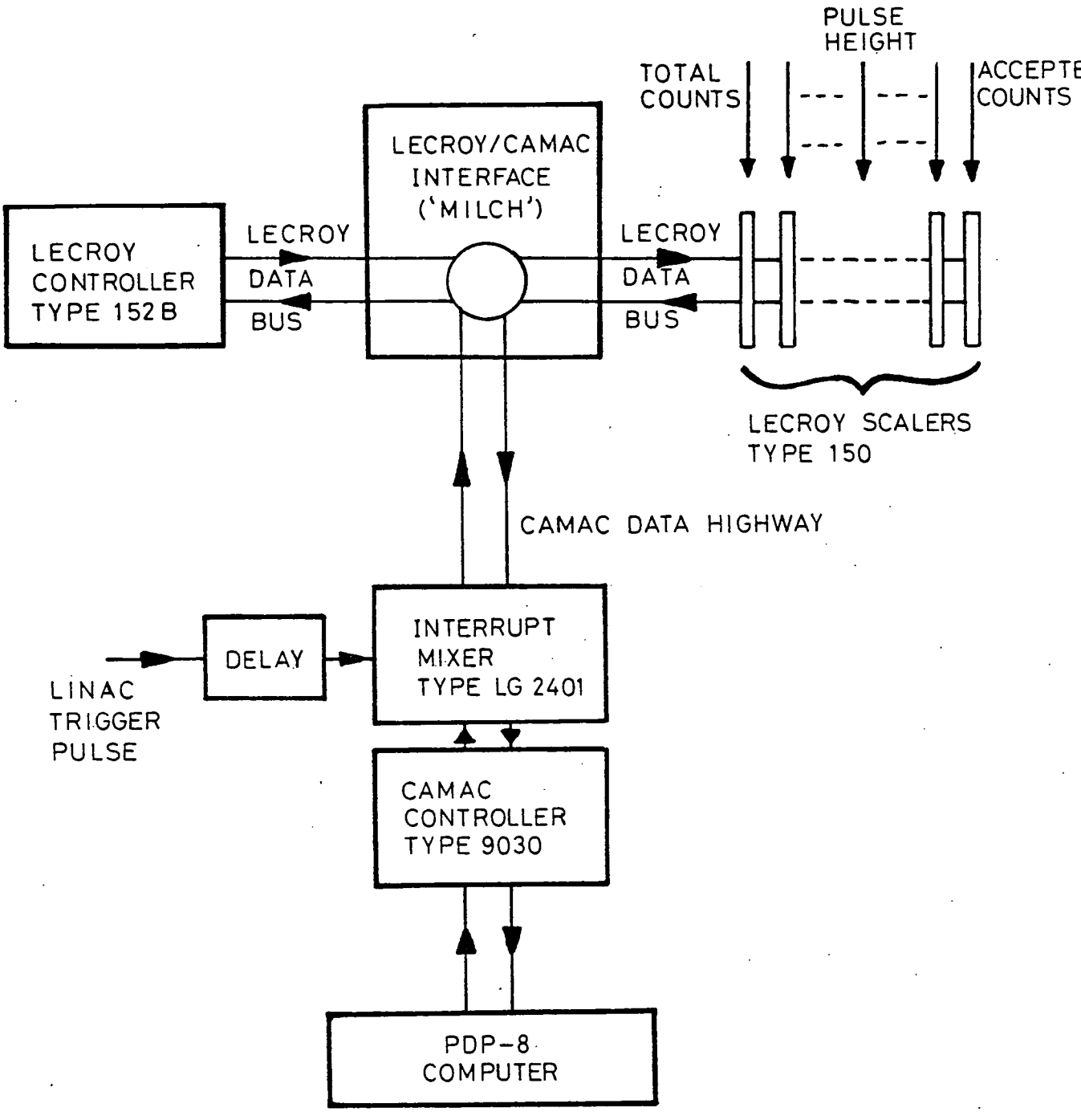

Figure 2.10 Computer interface electronics.

Lecroy scalers during each beam pulse. After the pulse the intercept mixer receives a delayed linac trigger pulse, sends an interrupt to the P.D.P. 8 computer, and switches control of the scalers to the CAMAC controller. The scalers are then inhibited and the contents of each scaler are sent to the Lecroy data bus and read by computer. When all the scalers have been read they are cleared and control is returned to the Lecroy controller.

The Lecroy controller in turn receives control from the scaler accumulating the counts derived from the toroidal charge monitor. This scaler is equipped with an automatic stop facility enabling it to stop when a preset count has been reached. Use of the scaler inhibit line will stop all other scalers in use. This line is also used to inhibit the Lecroy controller. Thus when the toroid charge scaler is stopped, no data accumulation in the computer may take place. The data acquisition process is thus controlled by the start and stop controls on one scaler, and will cease when that scaler reaches a predetermined count, i.e. when a set quantity of charge has been passed through the target.

2.10.2 P.D.P. 8 Computer Programme and Data Storage

Data acquisition and storage was carried out on line using a D.E.C. P.D.P. 8 computer (loaded with a modified version of a standard D.E.C. kicksorting programme). During data acquisition this programme may be switched between a mode for reading the Lecroy scalers and updating computer memory locations, and a display mode for on-line viewing of the accumulating pulse height spectra.

The Lecroy scalers are read in response to an interupt from the CAMAC/P.D.P.8 interface, which causes the computer to jump out of its

display routine. The total and accepted counts received during the preceding beam pulse are then added to the two appropriate pairs of 12-bit word locations used for the storage of each of these numbers, for each detector. Two 12-bit locations are used instead of one since for most data acquisition runs the total and accepted counts for each detector will exceed $2^{12} = 4096$. The second 12-bit location is used as an overflow counter from the first location.

The remaining scalers hold a number representing the pulse height corresponding to any accepted pulse received during the previous beam pulse. This number corresponds to a channel in a 200 channel pulse height spectrum, and for each detector the computer memory location containing the contents for the channel whose number is stored in the scaler, will be increased by one. In the event of a memory location exceeding the maximum storage of 4096 counts, overflows are counted in the location corresponding to channel 1 of the pulse height spectrum. The overflows from all channels are summed in this location, hence care has to be taken at the stage of pulse height spectrum analysis, to ensure that the appropriate portion of the spectrum has a number of counts added to it equal to 4096 multiplied by the number of overflows. This system of overflow storage precludes the acquisition of spectra in which more than one peak may acquire a channel with over 4096 counts. At no time in the course of the present work is a spectrum encountered in which the allocation of the overflow numbers to a particular peak is ambiguous.

At the end of every data acquisition run, ten pulse height spectra are stored in the memory, along with the corresponding accepted and total count summations. This data can be rapidly transferred to disk storage on a D.E.C. P.D.P.10, using a fast computer link, and thereafter stored on magnetic tape and analysed. Additionally the spectra are written on DEC-tape, and the facilities exist for type out on a teletype, or punch out on paper tape.

CHAPTER 3

DATA ANALYSIS AND PRESENTATION

3.1 Analysis Procedure

All pulse height spectra are analysed by the same general procedure. The aim of the procedure is to obtain alpha particle double differential cross sections ($d^2\sigma/dE_\alpha d\Omega$) per incident electron, sorted into energy spectra ($d^2\sigma/dE_\alpha d\Omega$ v.s. E_α), angular distributions ($d^2\sigma/dE_\alpha d\Omega$ v.s. θ_α) or excitation functions ($d^2\sigma/dE_\alpha d\Omega$ v.s. E_e), where an alpha particle of laboratory frame energy E_α is detected at an angle θ_α to an electron beam of energy E_e.

The following procedure was followed and is described in detail in this chapter:

1. identification of pulse height spectra peaks with particle types incident on the detector;
2. determination of alpha peak areas from the pulse height spectra accumulated in the on-line computer;
3. calculation of the cross section from the peak areas and various electron beam, spectrometer, detector and target variables which parameterise a particular experimental run.

3.2 Assignment of Pulse Height Spectrum Peaks

Examples of pulse height spectra obtained from a ^{60}Ni target for 3 different spectrometer field settings are shown in Fig. 3.1. In this work the peak in the pulse height spectrum corresponding to alpha particles incident on a detector must be unambiguously identified. Given a

Figure 3.1

Figure 3.1 Charged particle spectra obtained from spectrometer focal plane detectors.

(a) 8 MeV alpha particles stopped in an ∿220 μm depletion depth detector are in channel 160. The peak at channel 50 arises from 8 MeV unstopped protons. 4 MeV (stopped) deuterons are just visible in channel 80.

(b) Peaks at channels ∿120, ∿60 and ∿40 correspond to 13.4 MeV alphas, 6.7 MeV deuterons and 4.46 MeV tritons, respectively, all stopped in an ∿220 μm depletion depth detector. The 17.9 MeV ^{3}He incident on the detector have a range a few microns above the depletion depth and are unstopped.

(c) 30 MeV alpha particles, 40 MeV ^{3}He and 15 MeV deuterons, all unstopped in an ∿400 μm depletion depth detector. Only the 10 MeV tritons are stopped. Note that the ^{3}He peak has now passed below the alpha peak.

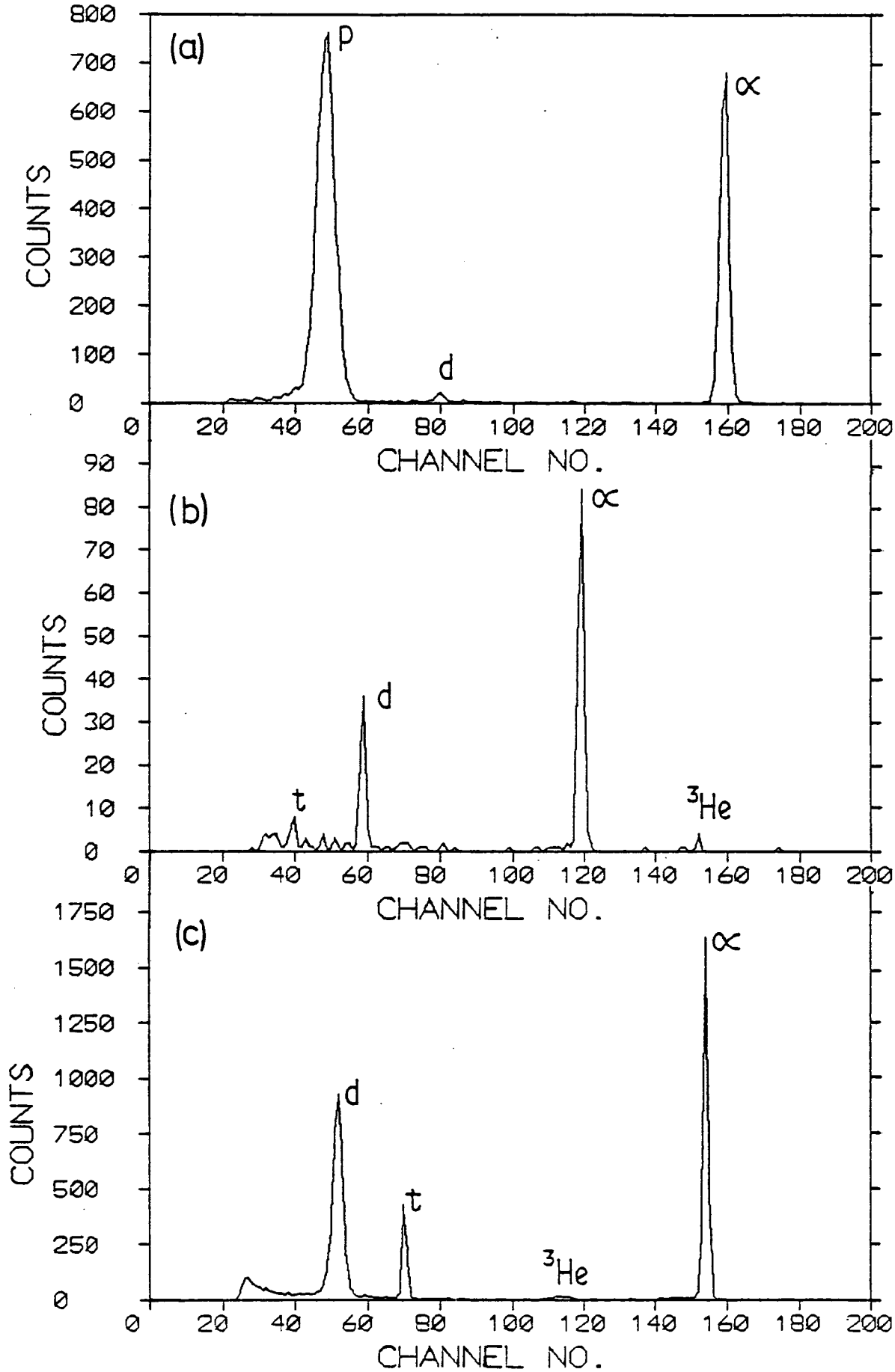
(a)
p
d
α
COUNTS
CHANNEL NO.
(b)
α
d
t
³He
COUNTS
CHANNEL NO.
(c)
α
d
t
³He
COUNTS
CHANNEL NO.

Figure 3.1

fixed magnetic field in the spectrometer, the energy E_x, of particle type x, incident on a detector in the focal plane, is related to its charge Z_x, and mass A_x by,

$$E_x \propto \frac{Z_x^2}{A_x} \quad .$$

Thus the energies of tritons, deuterons, alpha particles, protons and ^{3}He incident on a given detector will be in the ratio, 0.33 : 0.5 : 1.0 : 1.0 ; 1.33 respectively. If all these particles are stopped in the detector the channel number of their corresponding spectrum peaks will also be in these ratios. Since alpha particles and protons enter the detector at the same energy it is essential that the detector depletion depths are set (as discussed in Section 2.8) such that protons only deposit a fraction of their energy. Noting the energies at which various charged particles will cease to deposit their full energy in a detector with a given bias voltage, the ratios of the "stopped" peaks can be simply employed to rigorously determine the charged particles from which they are derived. Such a procedure is appropriate for $E_\alpha \lesssim 20$ MeV on 500 μm silicon surface barrier detectors, for which tritons and ^{3}He of the same magnetic rigidity are easily stopped. Above $E_\alpha \sim 20$ MeV care has to be taken that the ^{3}He peak does not sum with the α peak as ^{3}He particles begin to deposit only a fraction of their energy. Careful choice of detector bias voltage allows detector depletion layer thicknesses to be selected such that any accidental summing of ^{3}He peaks with α particle peaks is avoided. In all instances the α peak is unambiguously determined from the ^{3}He peak, being substantially larger in magnitude, and better resolved.

At high energies, i.e. $E_\alpha \gtrsim 30$ MeV, the alpha particles can no longer be stopped in the available depletion layer thicknesses.

Consequently the alpha particle pulse height peak becomes relatively broader compared to the deposited energy, and diminishes in channel number location. However, for all targets considered at $E_x \gtrsim 30$ MeV, alpha particles corresponded to the highest pulse height spectrum peak. Thus over the whole range of alpha particle energies considered ($3.0 \text{ MeV} \leq E_\alpha \leq 65 \text{ MeV}$), the alpha particle peak could be separated from other particles and clearly identified.

3.3 Determination of Alpha Peak Area

The alpha peak area is determined by summing all counts in the pulse height spectrum channels over which the alpha peak is defined, and subtracting an appropriate background contribution determined from the background observed above and below the alpha particle peak. In general, the alpha peak is well defined over a range of about 10 channels, and the background contribution is negligible. It is particularly important that the two central detectors ($J = 4$ and 5) provide a well defined peak, since the other detectors' relative efficiencies are normalised to the mean relative efficiency of detectors 4 and 5. The mean relative efficiency of detectors 4 and 5 is taken to correspond to the relative efficiency for a detector in the centre of the focal plane (on the optic axis) and is set to unity. (See Appendix 3). If the alpha peak areas for detectors $J = 4$ and 5 are well determined then the relative efficiencies of all other detectors will correct for any loss of alpha particle counts due to cutting off low energy tails in the alpha peak or any other peak integration inaccuracies. This, however, is only true if the upper and lower bounds of the peak are to be defined in a constant manner relative to the centroid of the peak, which must remain

stable with time. In particular the alpha peaks from which relative efficiencies are obtained must be integrated in as close a fashion as possible to the data for each detector.

Background subtraction is only significant in the cases where low alpha particle energies are considered, and a small alpha peak has to be summed while sitting on a rising "background" proton peak (it being difficult to reduce the proton peak any more relative to the alpha peak). However the same subtraction technique applying to this case is used for the determination of all background contributions, however small.

Two "fitting" regions are defined above and below the peak and a function is fitted through both these regions simultaneously. The function obtained provides an interpolation of the background under the peak, which is then subtracted to obtain a true alpha peak area. The functions fitted (B(x)) are sums of Legendre Polynomials up to order n,

$$B(x) = a_o P_o(x) + a_1 P_1(x) + a_2 P_2(x) + \ldots + a_n P_n(x)$$

where a_n are coefficients obtained in the fit. The spectrum channels $I = 0 \rightarrow 200$ are mapped on to the region $x = -1.0 \rightarrow 1.0$ by the simple transformation

$$x = \frac{I}{100} - 1.0 \quad .$$

This transformation is made to make use of, a) the orthogonality of Legendre Polynomials in the interval $\left[-1, +1\right]$, and b) the form of the lowest order Legendre Polynomials about $x = 0$, which approximate well in shape to the worst background encountered, and will thus provide good background fits for peaks near the centre of the spectrum (about channel 100), where alpha peaks are placed using appropriate

gain settings. In all cases the maximum order of Legendre Polynomial used is $n = 2$.

The fitting and integration procedure is carried out using the on-line interactive graphics facilities of a D.E.C. P.D.P. 10 computer. The pulse height spectrum for each detector in turn is displayed on a Tektronix storage oscilloscope and the channels between which the peak is to be summed and the background fitted, are chosen by a cursor mechanism. The background fit is then drawn over the spectrum and the calculated χ^2 is displayed. If the fitted curve is seen to be a sensible interpolation of the background the next detector is considered, otherwise a change in the fitted region is made in order to produce an improved fit.

This apparently subjective method of fitting and integrating by eye was tested against a peak search and integration computer code, based on the pulse height analysis programme used interactively. The peak search code had fixed criteria for the selection of the upper and lower peak bounds and the background fitting regions. Thus the search code can only be used for cases when the alpha peak is well separated from other peaks. Comparison of peak areas obtained by on-line "visual" integration, with areas obtained by the rigorously fixed criteria in the peak search code shows differences to be less than 5%. Comparisons of areas determined on-line by different people, show similar differences. In all cases the differences in peak areas obtained by different methods of summation are less than the statistical error assigned to the area.

Areas obtained by on-line visual determination of the peak defining channels, and background fitting regions are used in preference to those from automatic peak search and integration techniques. This ensures

that appropriate background subtractions are applied in all cases, and that any peaks close to the alpha peak are allowed for in the area and background determination.

Dead time corrections, obtained as discussed in Section 2.9, are applied at this stage in the analysis. The peak areas obtained are multiplied by the appropriate correction for each detector.

Detector effects such as multiple scattering and inelastic nuclear interactions, for which corrections to the peak area may have to be applied, are considered in Appendix 5, where they are shown to be negligible.

3.4 Determination of Reaction Cross Section

Each experimental run results in the acquisition of a set of alpha particle peak areas, C_J, where $J = 0,1, \ldots, 9$, corresponding to each detector in the focal plane. The general expression for the double differential cross section in alpha energy and solid angle, per incident electron, $d^2\sigma/dE_\alpha d\Omega$ (in units of barns per MeV per steradian per incident electron) is given by

$$\frac{d^2\sigma}{dE_\alpha d\Omega} = \frac{C_J}{\Delta E_J \Delta\Omega_J N_e N_t \varepsilon_J} \cdot D(E_J, E_J')^{-1} \qquad (3.4.1)$$

Here ΔE_J and $\Delta\Omega_J$ are the energy interval and solid angle subtended by detector J, N_e is the number of electrons incident on the target (see Appendix 2), N_t is the number of nuclei the electrons may traverse per unit area (accounting for the angle of incidence of the electron beam to the target), and ε_J is the detector absolute efficiency discussed in Appendix 5. The quantity $D(E_J, E_J')$ is an energy dilatation

factor which accounts for the differing energy intervals at the detector (ΔE_J) and in the target ($\Delta E_J'$) due to particle energy loss in the target and the vacuum isolator dilating the energy spectrum. The determination of this factor, and the treatment applied to the calculation of particle energy loss is given in Appendix 6.

The only non trivial factor in expression 3.4.1 is the energy interval - solid angle product, $\Delta E_J \cdot \Delta\Omega_J$. This is different across the focal plane of the spectrometer due to magnification, dispersion, and edge field distortion effects. The momentum at each detector can be determined from the momentum of a particle along the spectrometer optic axis ($\bar{p}(R)$), for a given magnetic field setting, R *, and from the function F(J) determined from the spectrometer alpha calibration, by,

$$p(R, J) = F(J)\bar{p}(R).$$

Hence

$$\Delta p(R, J) = \frac{dF(J)}{dJ} \cdot \bar{p}(R)\, \Delta J \quad .$$

For relativistic particles, it can be shown that

$$\Delta E = \frac{pc^2 \Delta p}{E + m_o c^2} \quad ,$$

where E is the particle kinetic energy.

Hence,

$$\Delta E_J = \frac{(\bar{p}(R))^2 c^2}{E_J + m_o c^2} \cdot F(J) \cdot \frac{dF(J)}{dJ} \cdot \Delta J$$

or alternatively,

---

* The symbol 'R' is used here instead of the customary 'B' since in practice the magnetic field is derived directly from a Rawson-Lush gaussmeter N.M.R. probe, and the numerical field setting, R, of this probe is in practice termed a "Rawson Setting". $B \simeq 2R$ gauss.

$$\Delta E_J = \frac{2\bar{E}\left(1 + \frac{\bar{E}}{2m_o c^2}\right)}{\left(1 + \frac{E_J}{m_o c^2}\right)} \cdot F(J) \cdot \frac{dF(J)}{dJ} \cdot \Delta J \qquad (3.4.2)$$

However, due to the non-linear effects noted above, the quantity $\frac{dF(J)}{dJ}$ will not be constant across the focal plane. The relative efficiency, r_J, determined in Appendix 3, accounts for all such differences in properties between detectors across the focal plane, i.e.

$$r_J = \frac{F(J) \cdot \frac{dF(J)}{dJ} \cdot \Delta J \cdot \Omega_J}{\left(F(J) \cdot \frac{dF(J)}{dJ} \cdot \Delta J \cdot \Omega_J\right)_{J = 4.5)}} ,$$

where the parameter $J = 4.5$ is defined as corresponding to a detector placed on the spectrometer optic axis, then, $\Omega_{4.5}$ is the spectrometer solid angle (Ω), $F(4.5) = 1$ (by definition), $\Delta J_{4.5}$ is the mean of the detector width to spacing ratio for detectors $J = 4$ and 5 (3/4 for uncollimated detectors), and $(dF(J)/dJ)_{4.5} = 0.00621$ from Appendix 4. The quantity $\Delta E_J \Delta\Omega_J$ can now be expressed as,

$$\Delta E_J \Delta\Omega_J = \frac{2\bar{E}\left(1 + \frac{\bar{E}}{2m_o c^2}\right)}{\left(1 + \frac{E_J}{m_o c^2}\right)} \cdot \Omega \cdot 0.00621 \cdot \Delta J_{4.5} \cdot r_J \qquad (3.4.3)$$

The principal uncertainties in the calculation of cross section arise from the target thickness error ($\lesssim 6\%$), and the statistical error on the peak area, varying from 4% upwards, although generally less than 10%. All other quantities have relative errors less than 2%.

The absolute error in the cross section is compounded from standard

errors (e.g. error on particle counts) and assigned measurement errors (e.g. error on detector width to detector spacing ratio , ΔJ). A standard error, σ, is a statistical quantity derived on the assumption that measurements are normally distributed about a "true" value. On this assumption there is a 67% probability that the "true" value is within $\pm \sigma$ of the measured value, x. In contrast, an assigned measurement error, δx, defines an interval $\pm \delta x$ about a measurement within which, ideally, there is a 100% probability of the "true" value occurring. Assignment of error to a product requires that relative standard errors, σ/x, are summed in quadrature, and relative measurement errors, $\delta x/x$, are summed linearly. Here, the errors on quantities in the cross section product comprise both forms, and the resultant relative error from all the statistically obtained quantities is summed linearly with the relative measurement errors. This procedure yields an absolute cross section error which defines an interval about the measured cross section within which there is more than 67% but less than 100% probability of the "true" value occurring.

The cross section is obtained in sets of ten particle energies, each energy separated by 1.2% from the next. Such resolution is unnecessary for the mostly unstructured energy spectra studied here. Hence in many cases the cross sections from all ten detectors are summed and averaged to simplify the presentation of the data. When this is done the absolute statistical errors for each detector are combined in the cross section error by summing in quadrature. All angular distribution and excitation function data are presented in this manner.

The alpha energy spectrum from ^{68}Zn, at 90°, for 120 MeV electrons is presented in Figs. 3.2a and 3.2b, allowing comparison of the

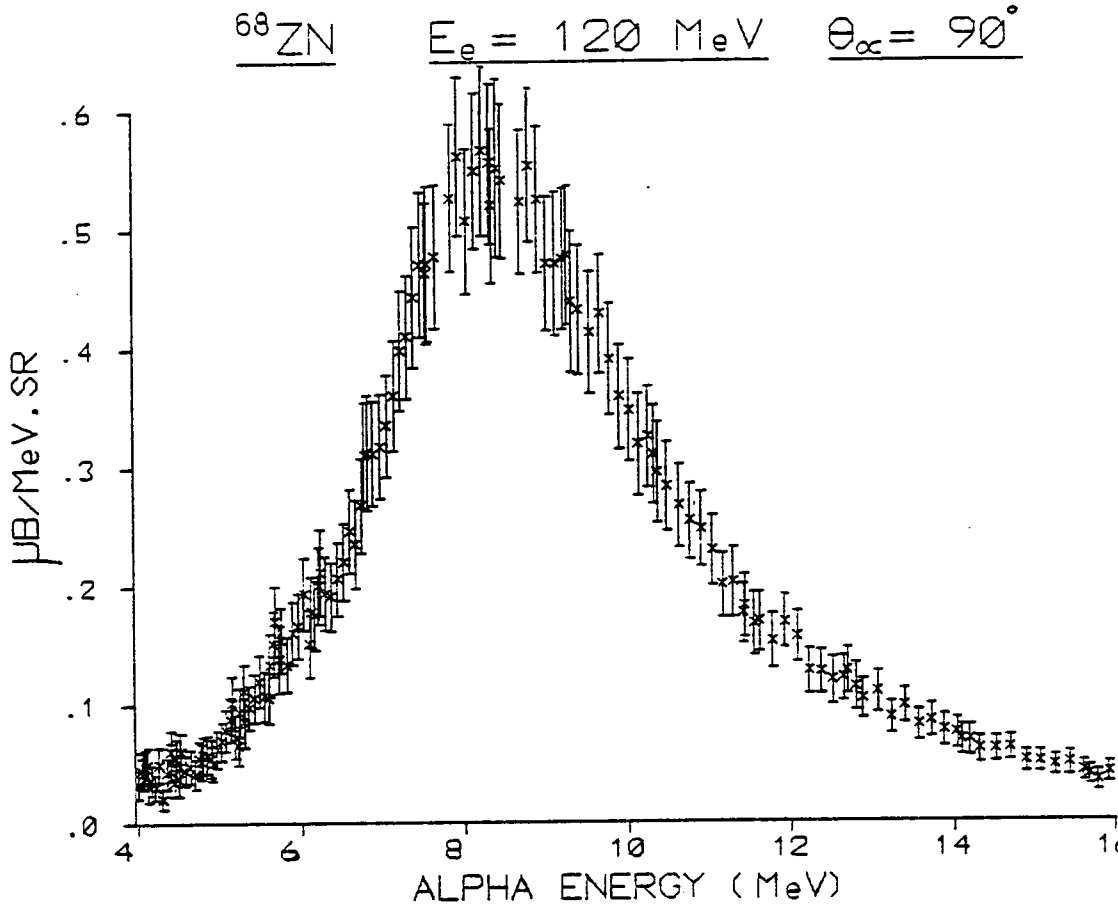

Figure 3.2a. Cross sections presented for each detector pulse height spectrum obtained. Absolute errors shown.

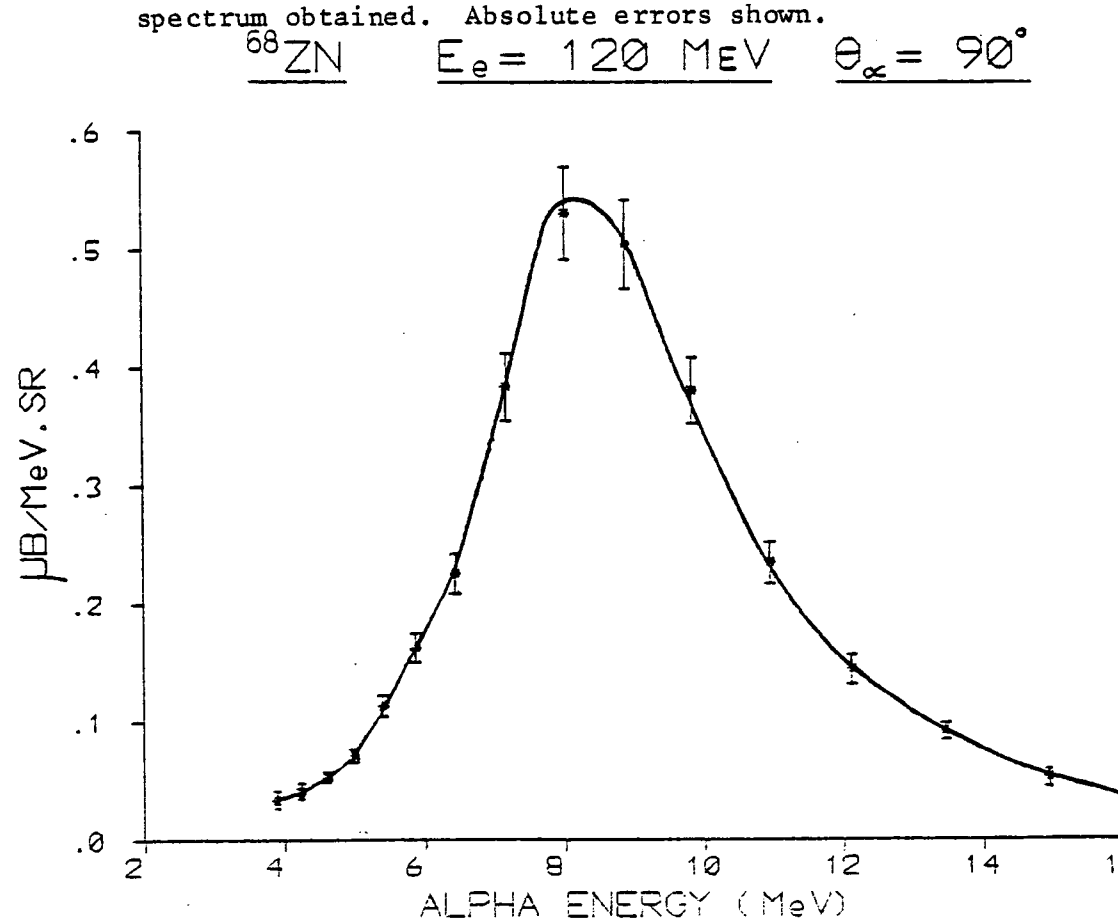

Figure 3.2b. Cross sections presented after averaging over all ten spectrometer focal plane detectors. Absolute errors shown.

two methods of presentation, and illustrating the form of the data contributing to each "averaged" cross-section.

3.5 Experimental Data

3.5.1 Tabulation of Acquired Data Sets

The sets of experimental data obtained are listed in Table 3.1. A data set is parameterised by the target, particle energy (E_α), spectrometer angle (θ_α) and electron energy (E_e) for which it was obtained. All angles and particle energies refer to the laboratory reference frame. The complete set of experimental data obtained during this thesis work is presented in Figs. 3.3 to 3.16. The solid lines in these figures are merely a guide to the eye. A key to these figures is included in Table 3.1.

The figures comprise groups of data extensive enough to form angular distributions, energy spectra and excitation functions of use in the detailed discussion and analysis of Chapters 4 and 5. In the remainder of this chapter a general discussion of the experimental data is presented, together with comparison of other relevant work.

3.5.2 Energy Spectra and Angular Distributions (E_α < 20 MeV)

Alpha energy spectra for the medium weight nuclei ^{56}Fe, ^{60}Ni and ^{68}Zn are presented in Figs. 3.3 - 3.6. The spectra for ^{56}Fe and ^{68}Zn show no significant structure, whereas the ^{60}Ni spectra exhibit a pronounced "cusp" at $E_\alpha \sim 4.5$ MeV, for all electron energies considered (data for E_α < 6 MeV, at E_e = 60 MeV has been omitted in Fig. 3.4, to allow clarification between the E_e = 33 and 120 MeV data). Other than this feature the ^{60}Ni spectra are qualitatively similar to those

TABLE 3.1

(e, α) Data Acquired during this Thesis Work

Target	Alpha Energy (E_α) (MeV)	Angle to Electron Beam (θ_α) (Degs)	Electron Energy (E_e) (MeV)	Fig. No.
^{27}Al	$16 < E_\alpha < 57$	30°	120	3.15
^{56}Fe	$3.8 < E_\alpha < 21.5$	90°	60, 120	3.3
^{56}Fe	8.2, 11.3, 15.7	$30^\circ < \theta_\alpha < 150^\circ$	60	3.7
^{56}Fe	8.2, 11.3, 15.7	$30^\circ < \theta_\alpha < 150^\circ$	120	3.8
^{60}Ni	$4 < E_\alpha < 30$	90°	120	3.4,3.5
^{60}Ni	$6 < E_\alpha < 21$	90°	60	3.4
^{60}Ni	$6 < E_\alpha < 14$	90°	33	3.4
^{60}Ni	$5 < E_\alpha < 36.5$	45°	120	3.5
^{60}Ni	8.2, 11.3	$30^\circ < \theta_\alpha < 150^\circ$	33	3.9
^{60}Ni	8.2, 11.3, 15.7	$30^\circ < \theta_\alpha < 150^\circ$	60	3.10
^{60}Ni	8.2, 11.3, 15.7	$30^\circ < \theta_\alpha < 150^\circ$	120	3.11
^{60}Ni	$4.1 < E_\alpha < 5.2$	30°, 90°	120	3.12
^{60}Ni	8.2	45°	$19 < E_e < 120$	3.13
^{60}Ni	15.7	45°	$27 < E_e < 120$	3.13
^{60}Ni	20.3	45°	$33 < E_e < 120$	3.13
^{60}Ni	25.4	45°	$55 < E_e < 120$	3.13
^{NAT}Ni	$4 < E_\alpha < 64$	30°	120	3.14,3.15
^{NAT}Ni	31, 50	$30^\circ < \theta_\alpha < 150^\circ$	120	3.16
^{68}Zn	$4 < E_\alpha < 29$	30°, 90°	120	3.2,3.6
^{92}Mo	$27 < E_\alpha < 64$	30°	120	3.15
^{94}Mo	$27 < E_\alpha < 64$	30°	120	3.15
^{197}Au	$16 < E_\alpha < 64$	30°	120	3.15
^{197}Au	31, 49	$30^\circ < \theta_\alpha < 150^\circ$	120	3.16

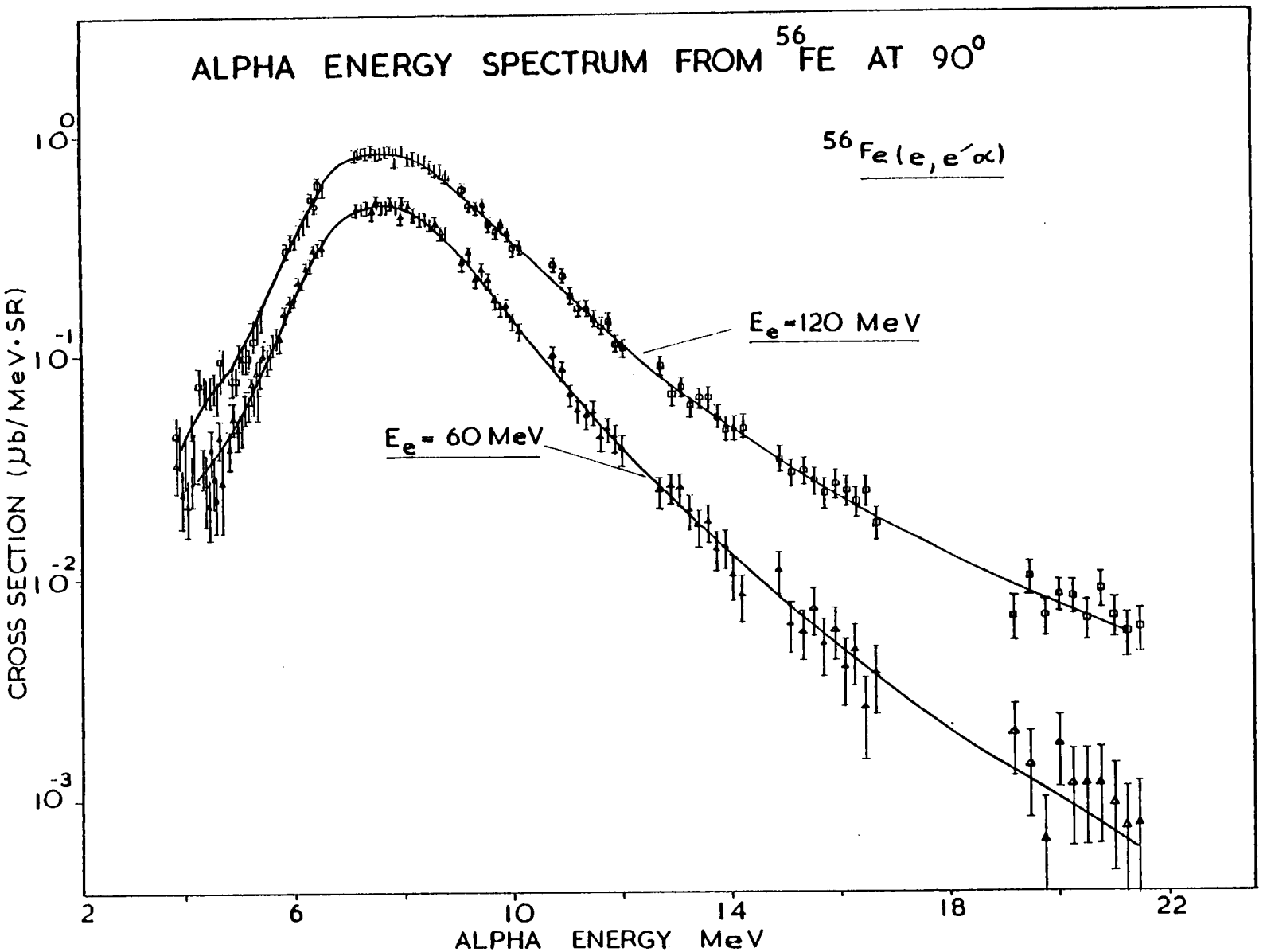
ALPHA ENERGY SPECTRUM FROM 56FE AT 90°
56Fe(e,e'α)
Ee=120 MeV
Ee= 60 MeV
CROSS SECTION (μb/MeV·SR)
10⁰
10⁻¹
10⁻²
10⁻³
2
6
10
14
18
22
ALPHA ENERGY MeV

Figure 3.3.

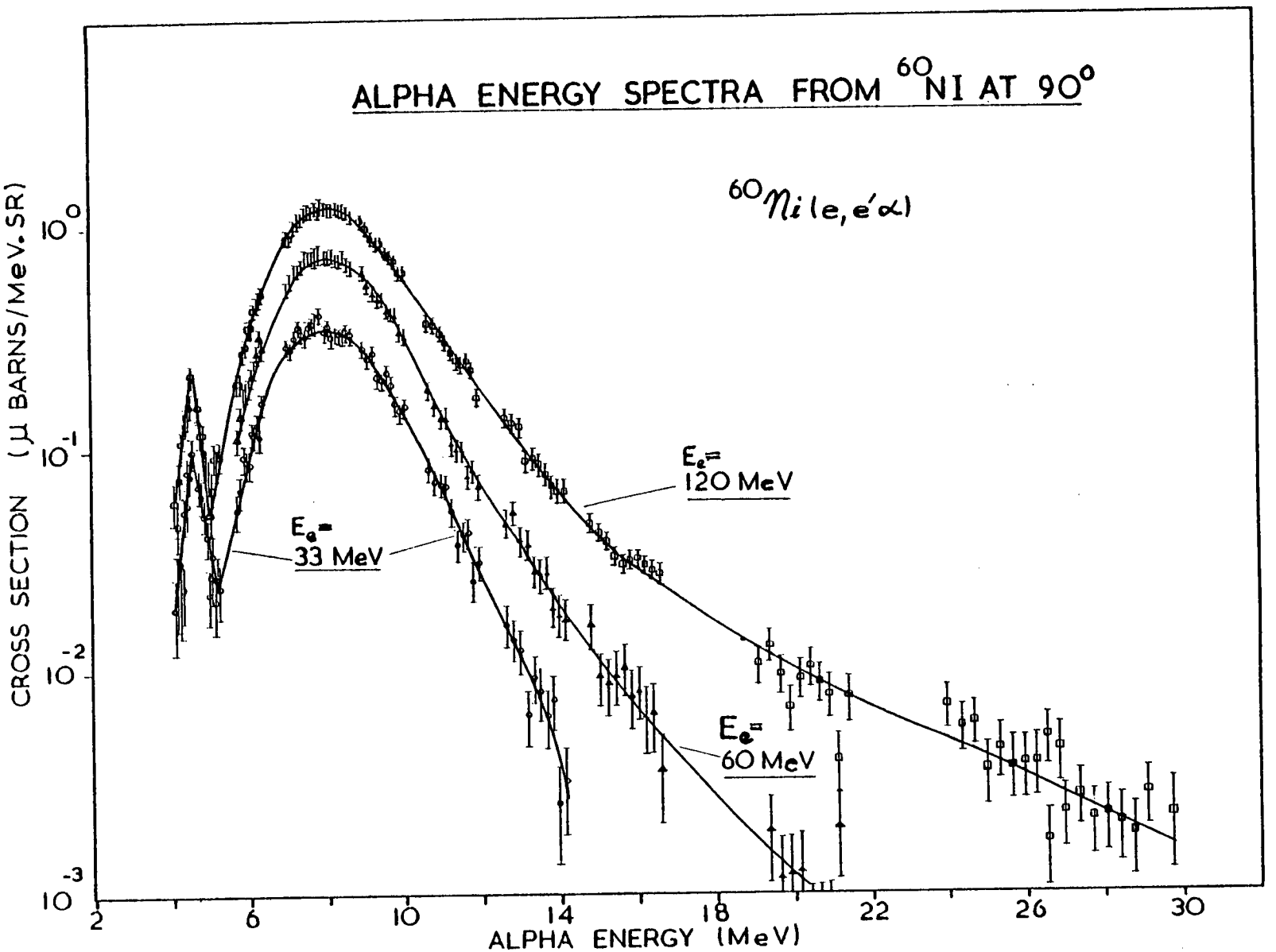
ALPHA ENERGY SPECTRA FROM ^{60}NI AT 90°
$^{60}Ni(e,e'\alpha)$
CROSS SECTION (μ BARNS/MeV.SR)
ALPHA ENERGY (MeV)
E_e= 120 MeV
E_e= 60 MeV
E_e= 33 MeV
10^{0}
10^{-1}
10^{-2}
10^{-3}
2
6
10
14
18
22
26
30

Figure 3.4.

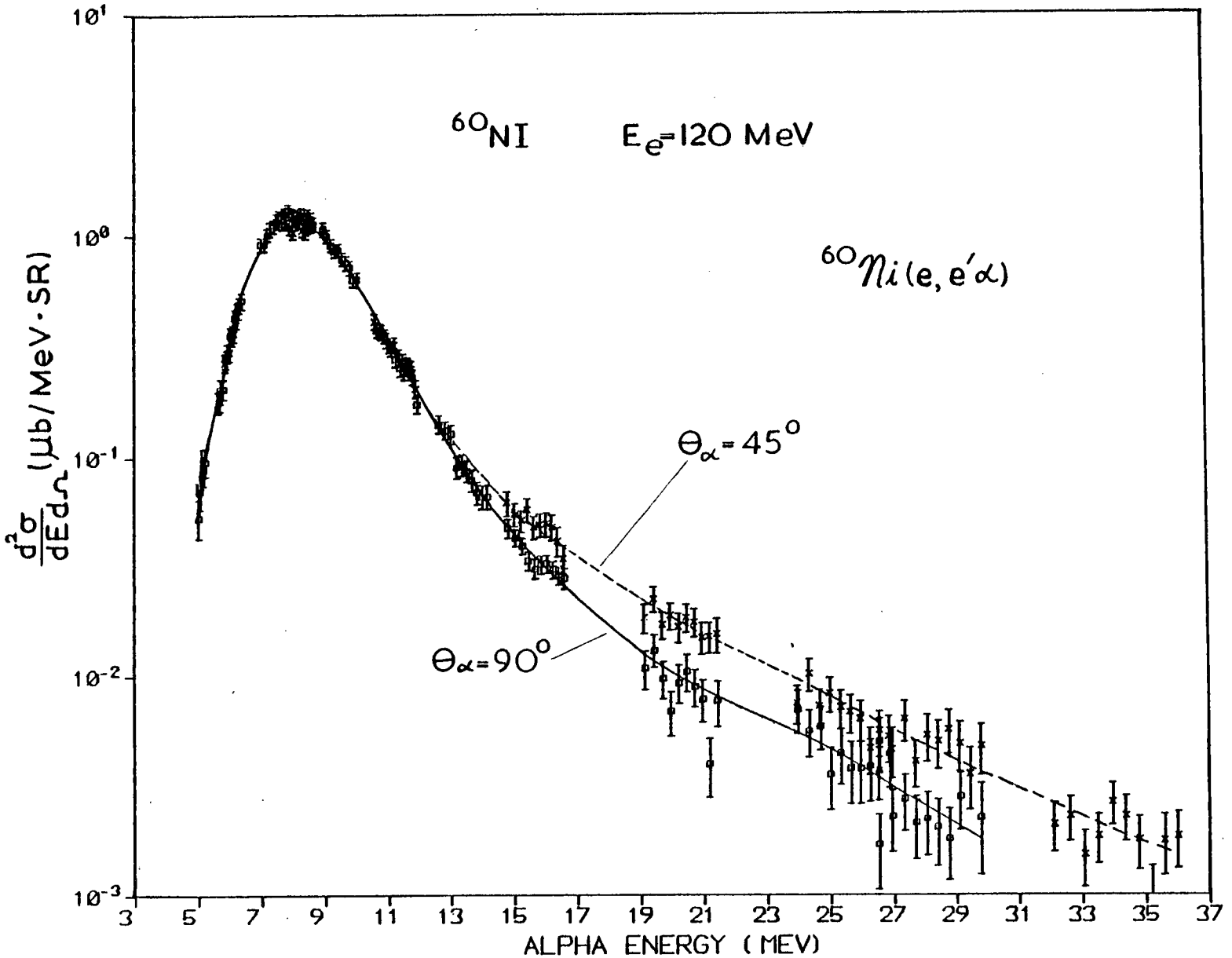
^{60}NI E$_e$=120 MeV
^{60}Ni(e, e'α)
Θ$_α$=45°
Θ$_α$=90°
$\frac{d^2\sigma}{dEd\Omega}$ (μb/MeV·SR)
ALPHA ENERGY (MEV)
10^1
10^0
10^{-1}
10^{-2}
10^{-3}
3 5 7 9 11 13 15 17 19 21 23 25 27 29 31 33 35 37

Figure 3.5.

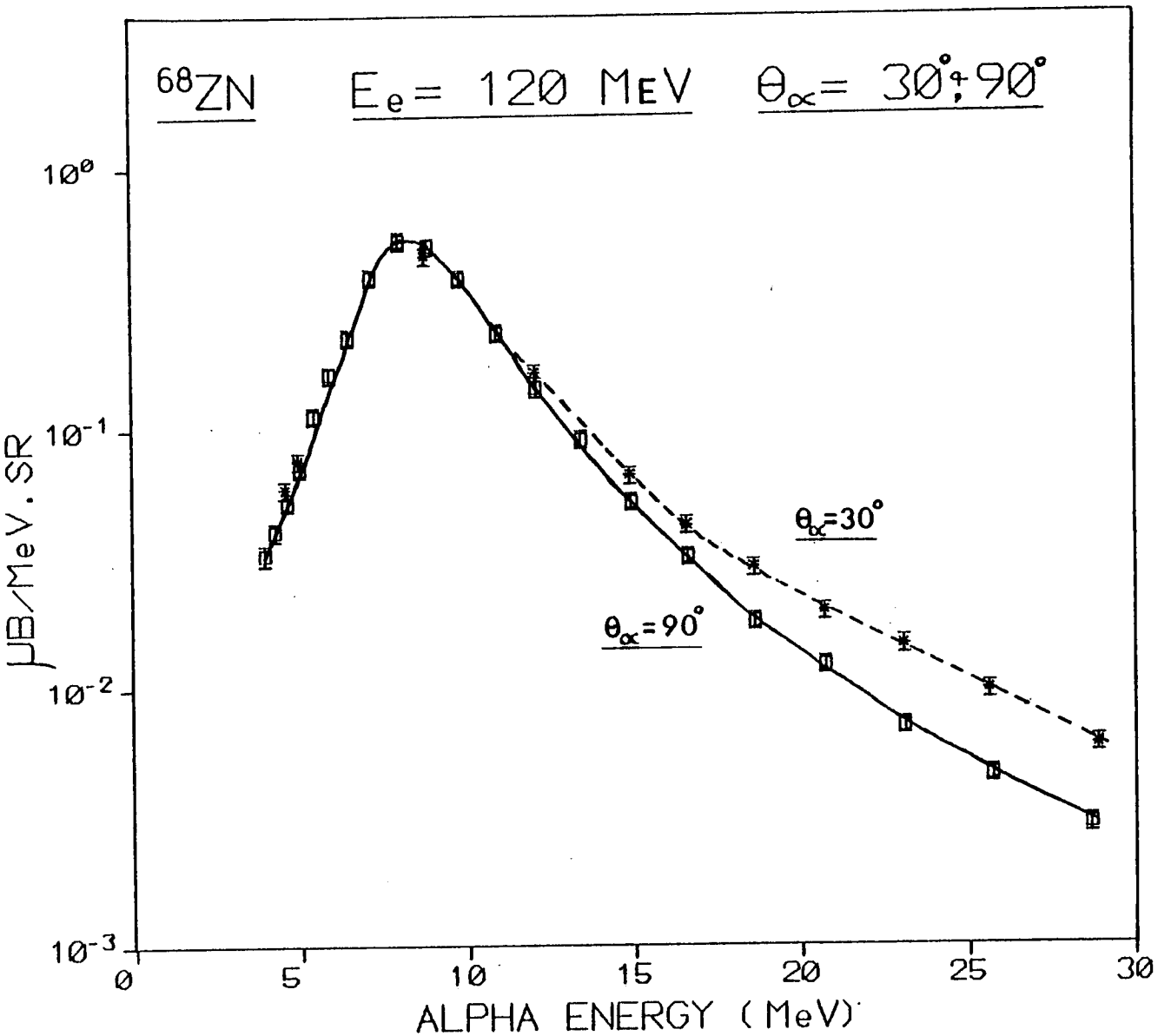
^{68}ZN
E_e = 120 MeV
θ_α = 30°; 90°
10^0
10^{-1}
10^{-2}
10^{-3}
μB/MeV.SR
θ_α=30°
θ_α=90°
0
5
10
15
20
25
30
ALPHA ENERGY (MeV)

Figure 3.6.

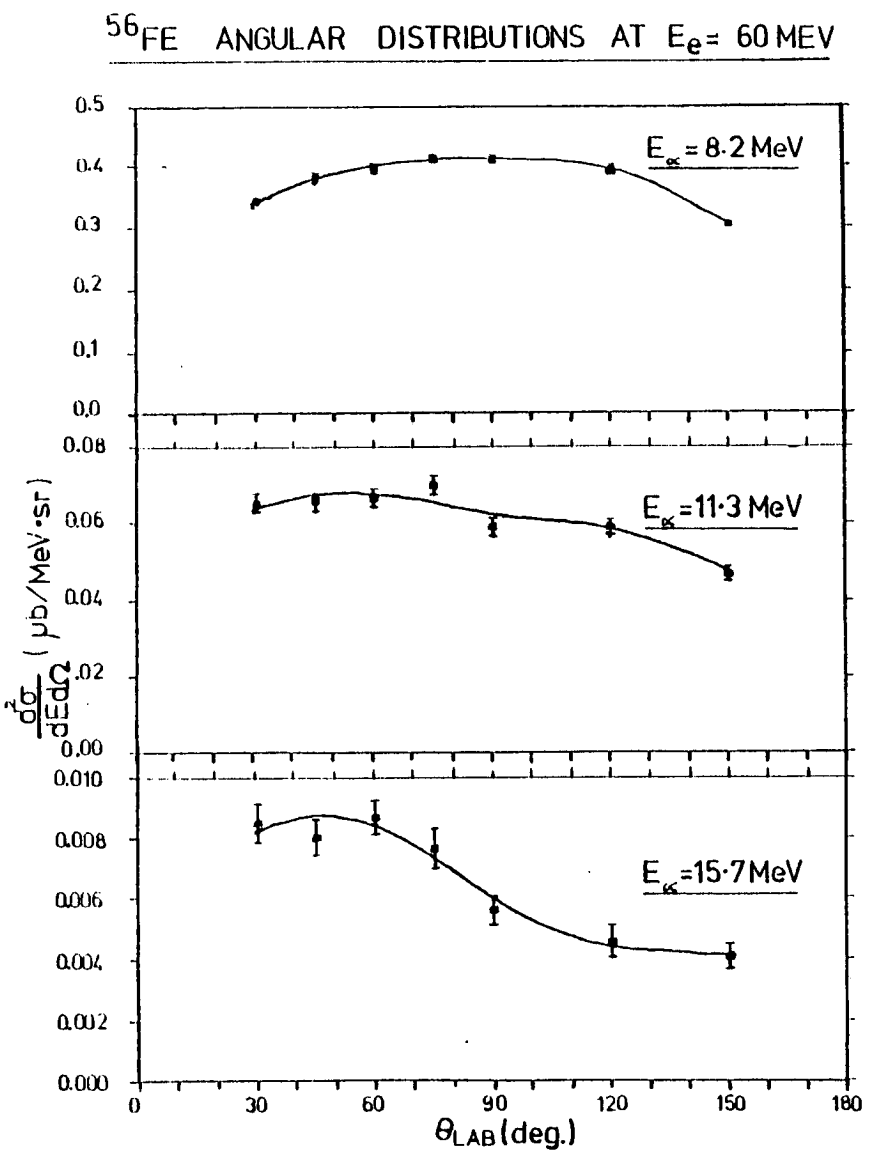

Figure 3.7.

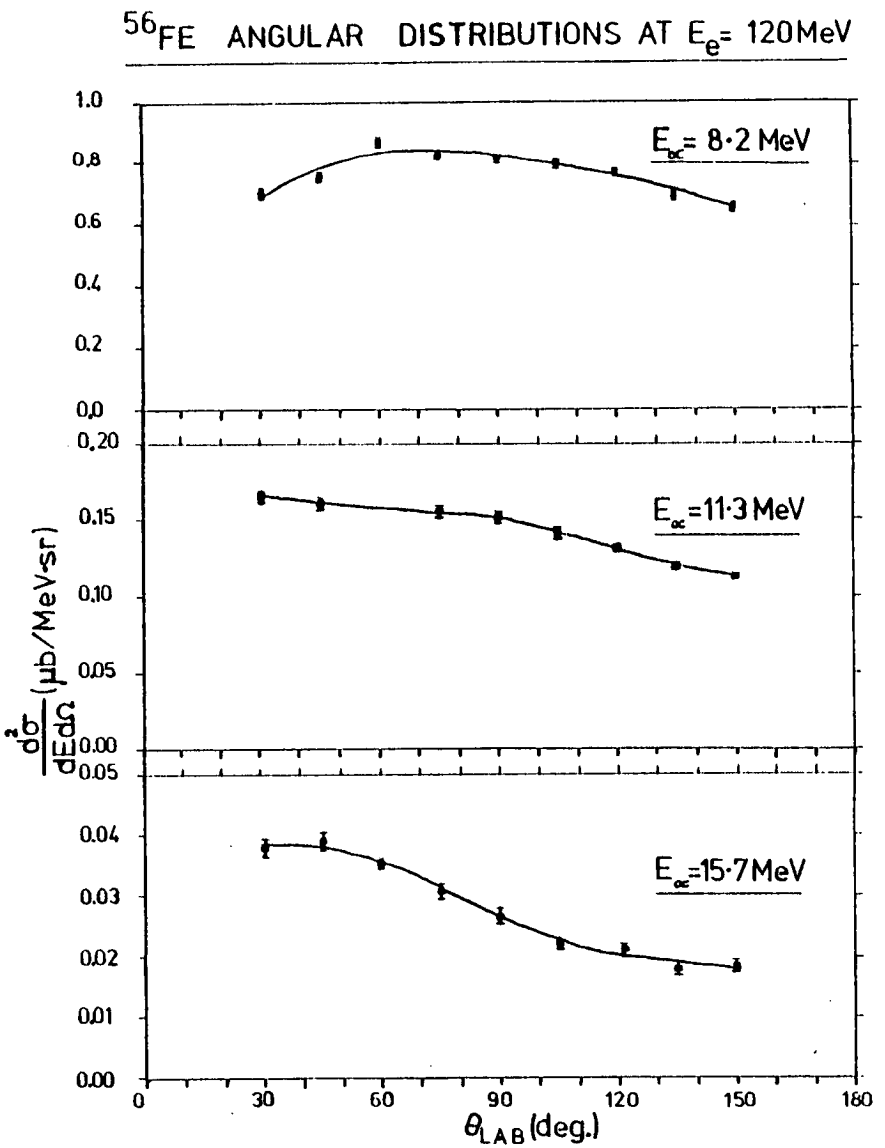

Figure 3.8.

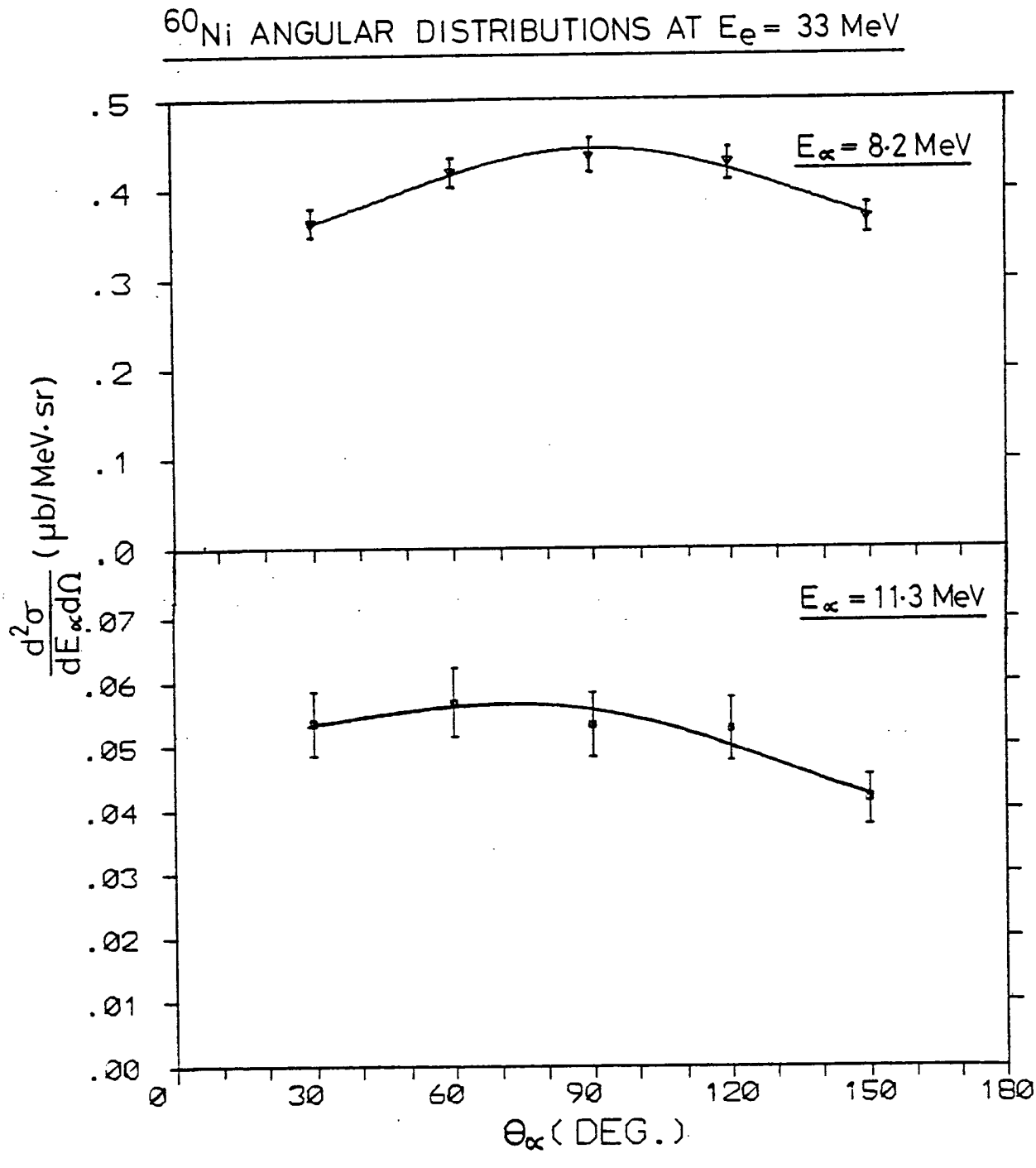
^{60}Ni ANGULAR DISTRIBUTIONS AT E_e = 33 MeV
E_α = 8·2 MeV
E_α = 11·3 MeV
$\frac{d^2\sigma}{dE_\alpha d\Omega}$ (μb/MeV·sr)
.5
.4
.3
.2
.1
.0
.07
.06
.05
.04
.03
.02
.01
.00
0
30
60
90
120
150
180
θ_α (DEG.)

Figure 3.9.

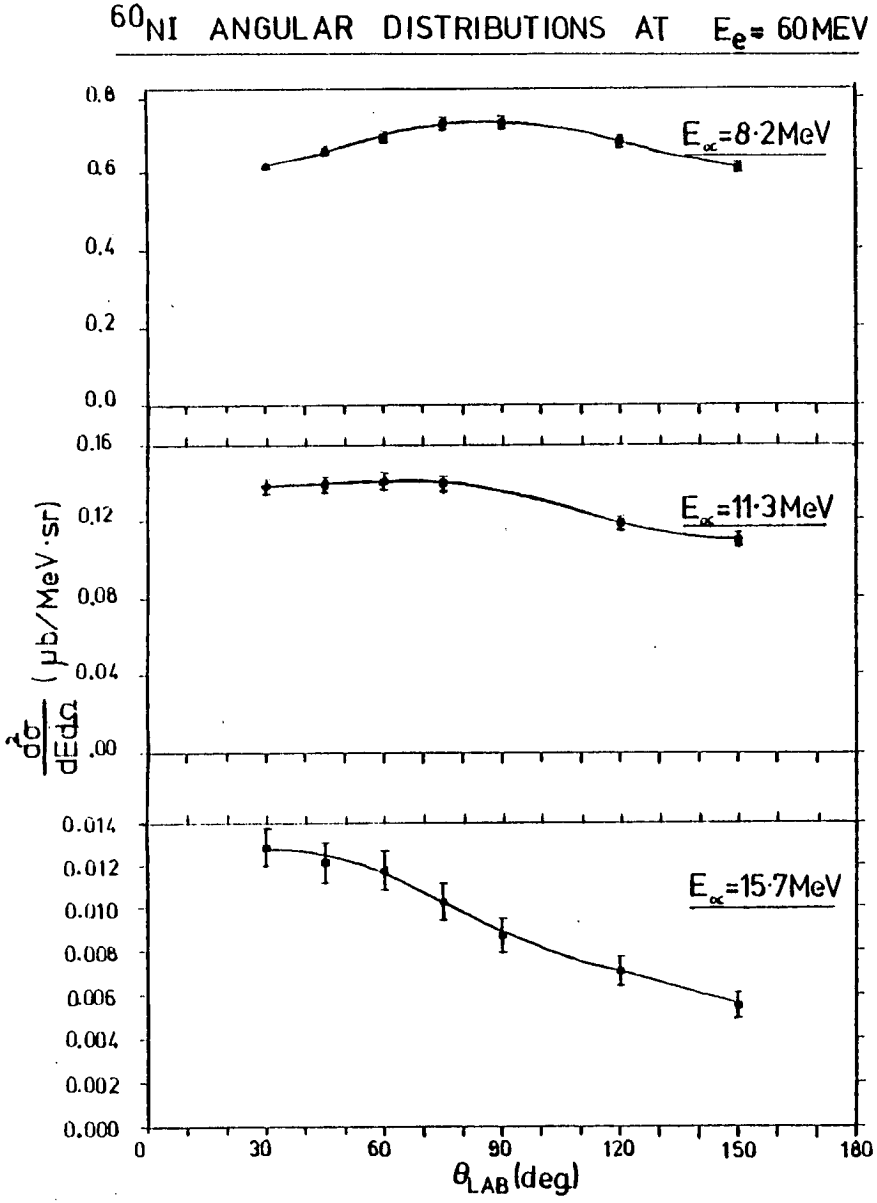

Figure 3.10.

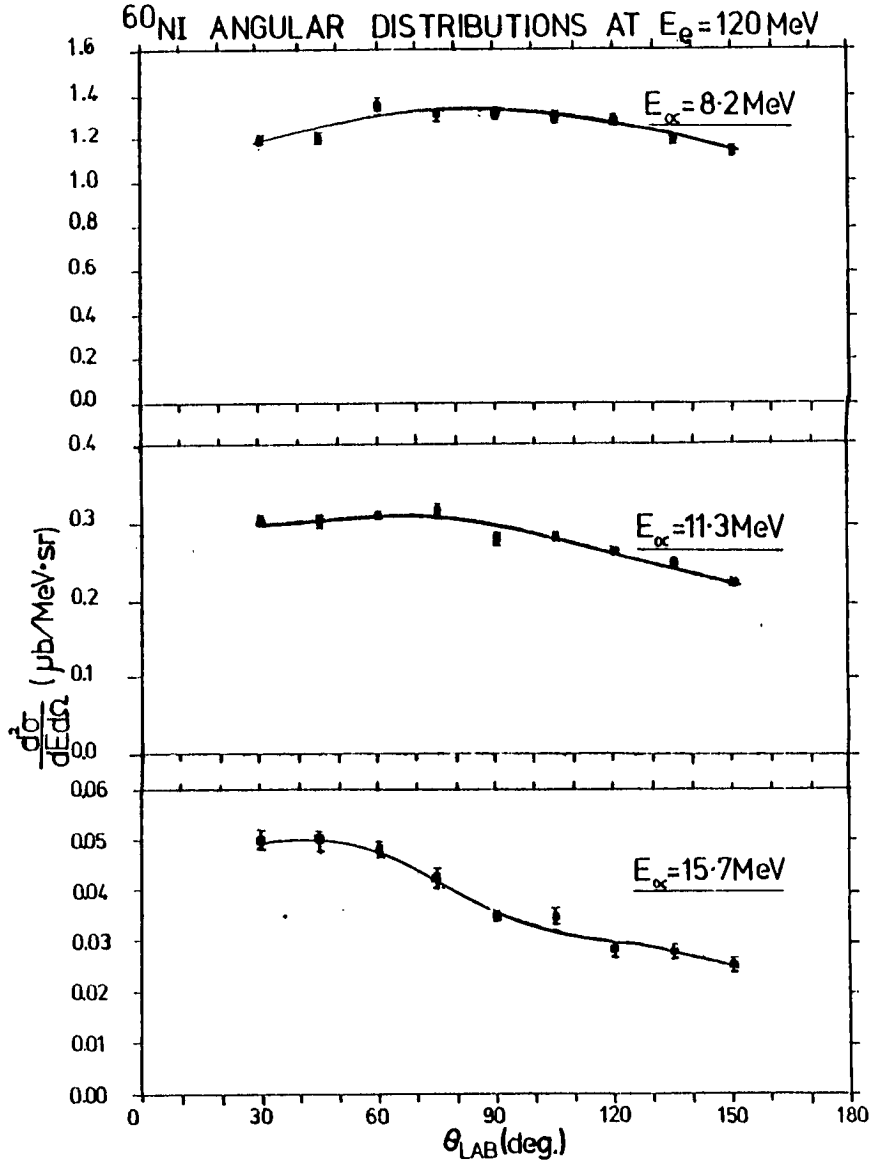

Figure 3.11.

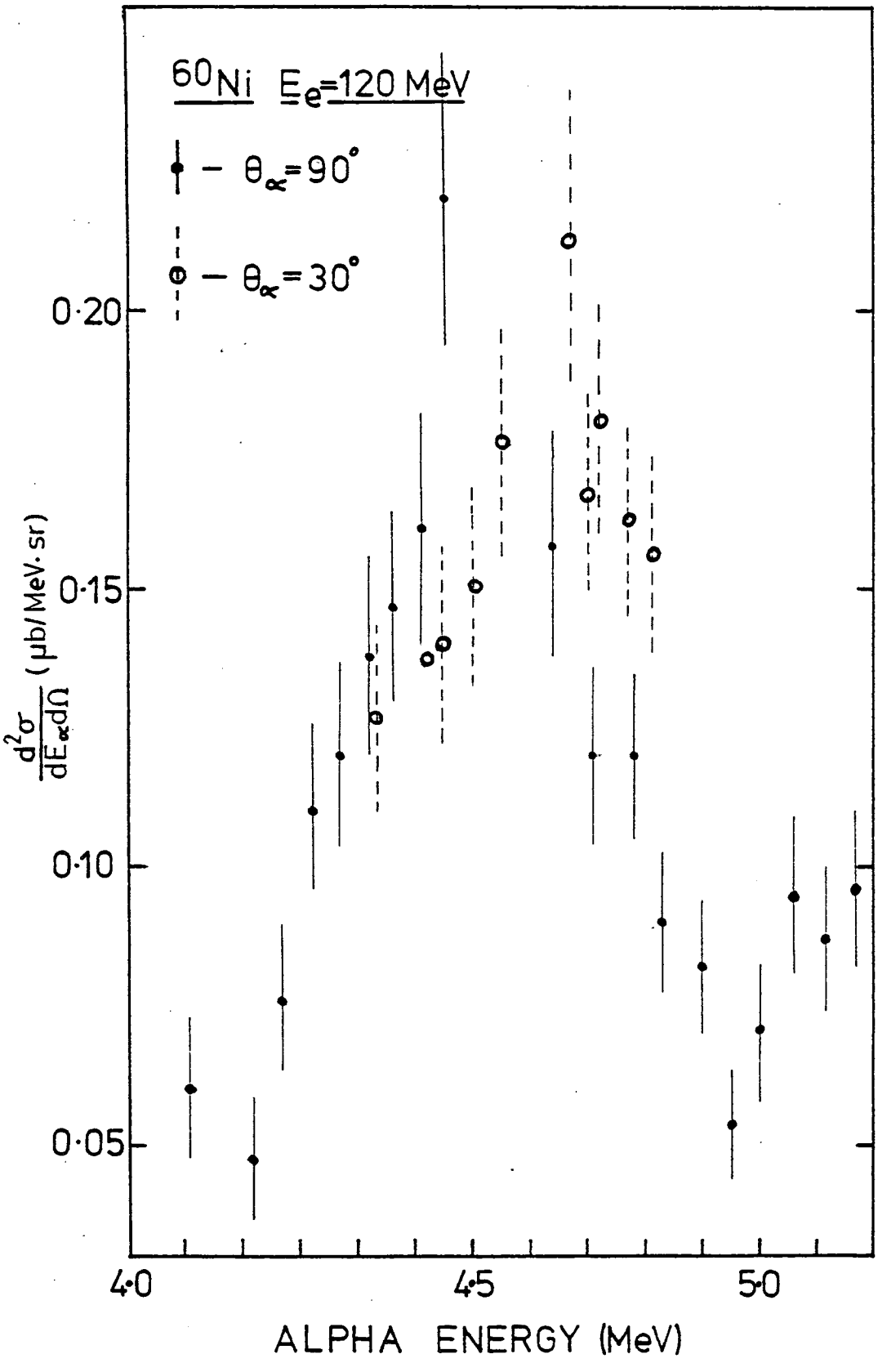
60Ni Ee=120 MeV
θα=90°
θα=30°
0·20
0·15
0·10
0·05
d²σ/dEα dΩ (μb/MeV·sr)
4·0
4·5
5·0
ALPHA ENERGY (MeV)

Figure 3.12.

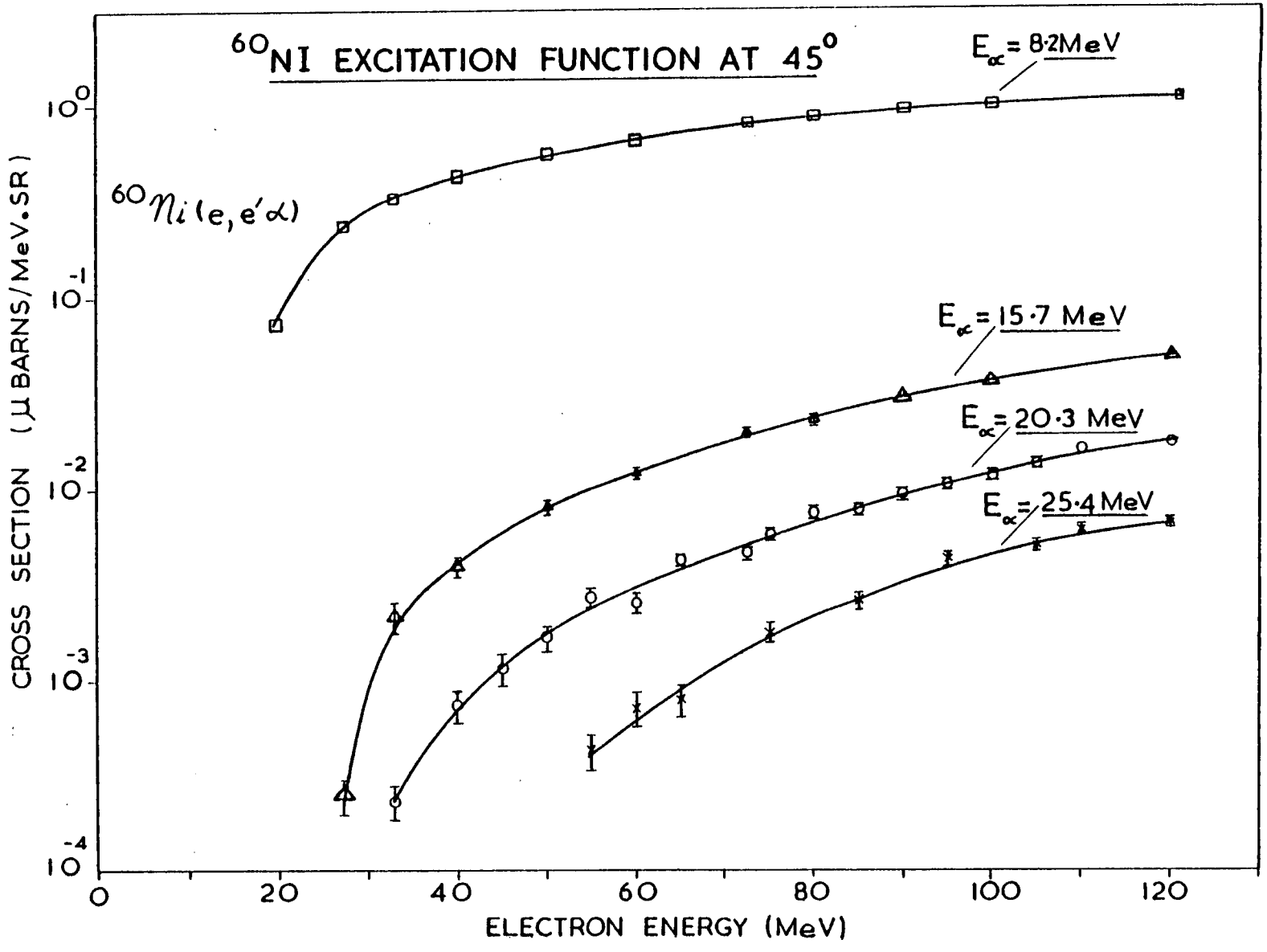
60NI EXCITATION FUNCTION AT 45°
Eα = 8·2MeV
60Ni(e,e'α)
Eα = 15·7 MeV
Eα = 20·3 MeV
Eα = 25·4 MeV
CROSS SECTION (μ BARNS/MeV.SR)
10^0
10^-1
10^-2
10^-3
10^-4
0
20
40
60
80
100
120
ELECTRON ENERGY (MeV)

Figure 3.13.

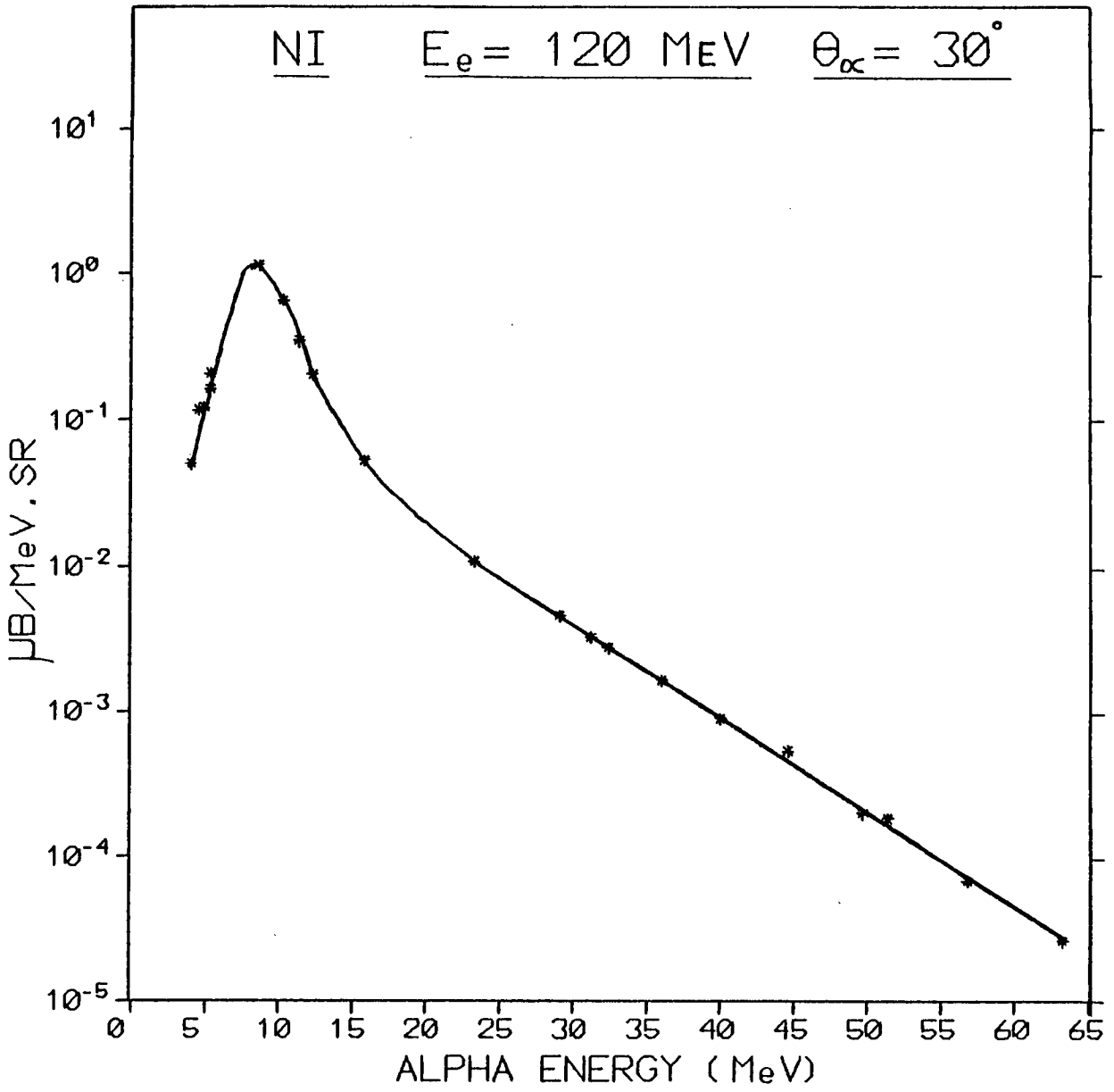
NI E_e= 120 MeV θ_α= 30°
10^1
10^0
10^{-1}
10^{-2}
10^{-3}
10^{-4}
10^{-5}
μB/MeV.SR
0 5 10 15 20 25 30 35 40 45 50 55 60 65
ALPHA ENERGY (MeV)

Figure 3.14.

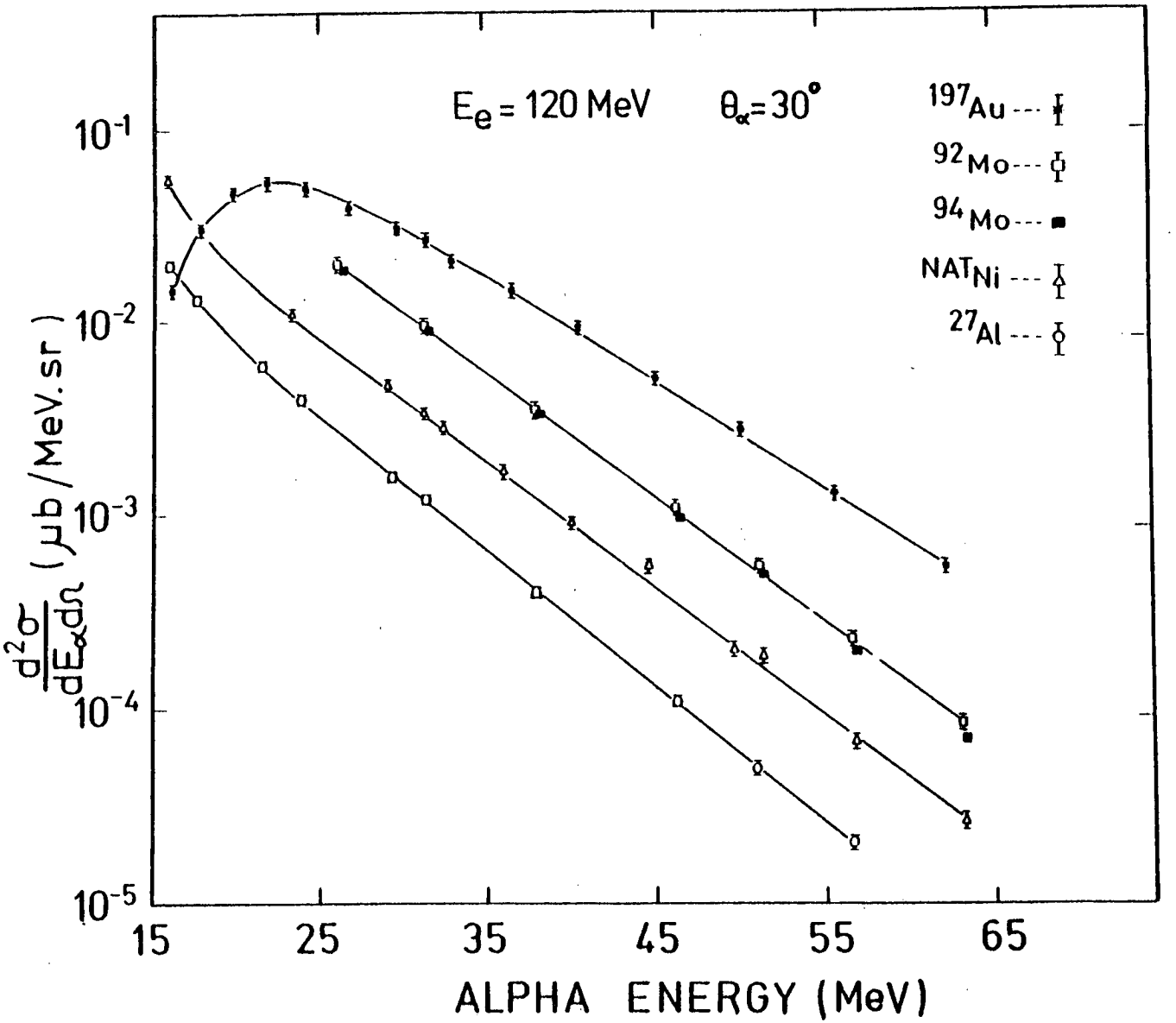
E_e = 120 MeV
θ_α=30°
^{197}Au
^{92}Mo
^{94}Mo
NAT$_{Ni}$
^{27}Al
$\frac{d^2\sigma}{dE_\alpha d\Omega}$ (μb/MeV.sr)
10^{-1}
10^{-2}
10^{-3}
10^{-4}
10^{-5}
15
25
35
45
55
65
ALPHA ENERGY (MeV)

Figure 3.15.

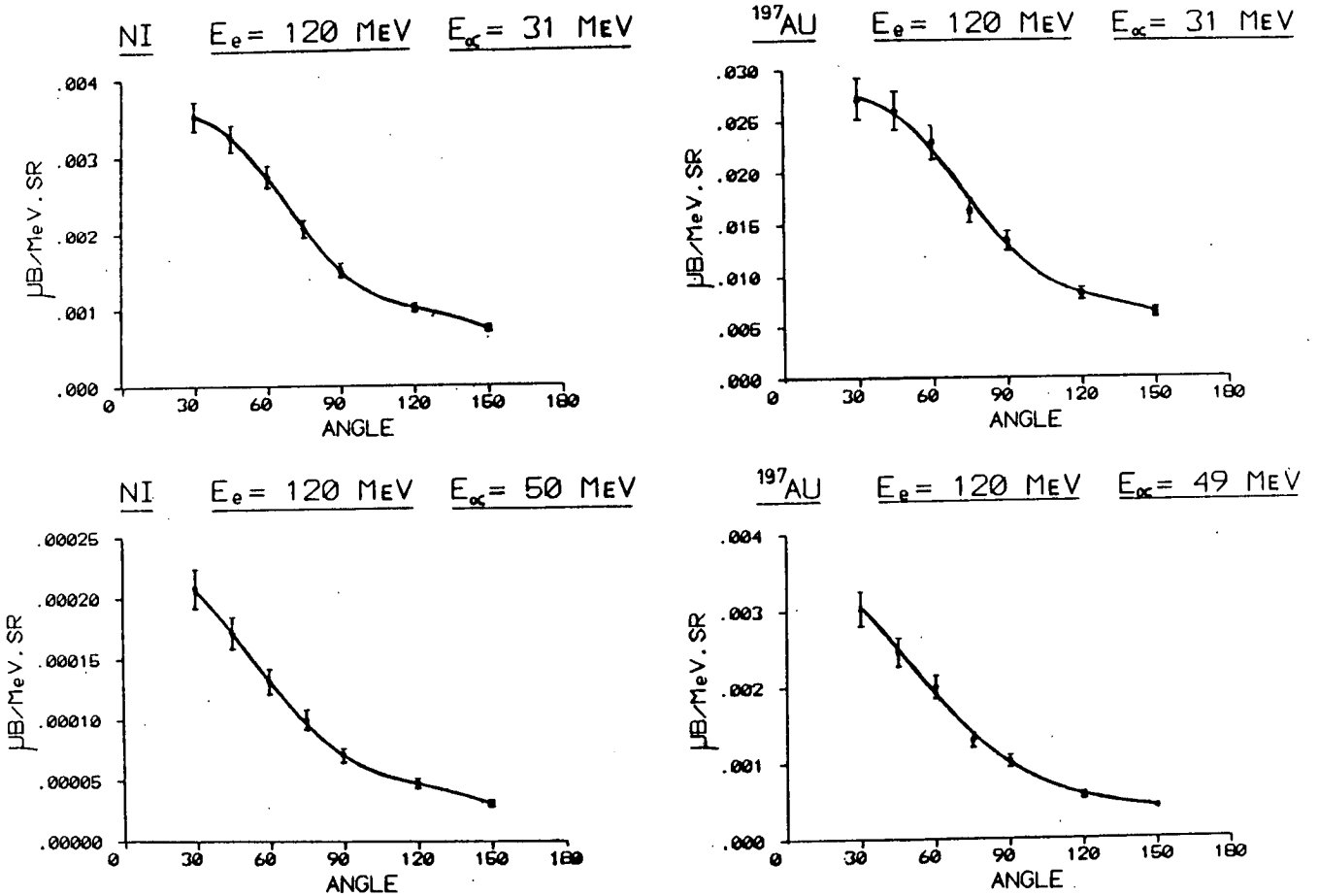
NI E_e= 120 MeV E_α= 31 MeV
μB/MeV.SR
.004
.003
.002
.001
.000
0 30 60 90 120 150 180
ANGLE
^{197}AU E_e= 120 MeV E_α= 31 MeV
μB/MeV.SR
.030
.025
.020
.015
.010
.005
.000
0 30 60 90 120 150 180
ANGLE
NI E_e= 120 MeV E_α= 50 MeV
μB/MeV.SR
.00025
.00020
.00015
.00010
.00005
.00000
0 30 60 90 120 150 180
ANGLE
^{197}AU E_e= 120 MeV E_α= 49 MeV
μB/MeV.SR
.004
.003
.002
.001
.000
0 30 60 90 120 150 180
ANGLE

Figure 3.16.

for ^{56}Fe and ^{68}Zn - exhibiting a broad peak centred about E_α = 8 - 9 MeV whose position shifts upwards in energy with nucleus mass number. Further discussion of the "Nickel Cusp" is postponed until Section 3.5.3. The cross sections in the peak region increase with increasing electron energy - higher energy alphas showing the most increase in cross section. Both ^{60}Ni and ^{68}Zn energy spectra taken at forward angles, show an increase in cross section over the 90° data for E_α > 12 MeV (Figs. 3.5 and 3.6), indicating an increasing anisotropy with increasing alpha energy. The form of this anisotropy is shown by the angular distributions of Figs. 3.7 - 3.11. Above E_α = 8 MeV, the angular distributions become increasingly forward peaked with increasing alpha particle energy. The angular distributions of the alphas at the energy spectrum peak ($E_\alpha \sim 8$ MeV) are symmetric, but increasingly anisotropic with decreasing electron energy.

Few data exist for comparison with the data presented here. During this thesis work energy spectra and angular distributions were published for the Cu(e, α) reaction at E_e = 100 MeV, in two publications by Murphy et al.[34), 38)]. In Ref. 34 an alpha energy spectrum, for $6 < E_\alpha < 18$ MeV from natural copper, is shown with a similar shape and magnitude to the spectra of Figs. 3.3 - 3.6, - peaking at E_α = 8.5 MeV with a peak cross section of $d^2\sigma/dE_\alpha d\Omega = 0.85 \pm 0.05$ μb/MeV.sr at $\theta_\alpha = 50°$. Cu(e, α) angular distributions were shown to be isotropic for $6 < E_\alpha < 13$ MeV, at E_e = 100 MeV in Ref. 34 and forward peaked for $15 < E_\alpha < 17$ MeV[38)]. The data presented here shows similar features for ^{56}Fe and ^{60}Ni, but with the angular asymmetry increasing more smoothly than suggested by the data of Murphy et al. In both references 34 and 38 there is no attempt to provide a quantitative explanation of the observed angular distributions. A good fit to the Cu(e,α) energy spectrum of Ref. 34 is achieved by using the evaporation shape,

$$\frac{d^2\sigma}{dE_\alpha d\Omega} \propto E\sigma(E)e^{-E/\theta}$$

where E is the α-particle energy, $\sigma(E)$ is the capture cross section and θ is the nuclear temperature.

Alpha energy spectra and angular distributions for ^{58}Ni, ^{60}Ni and ^{62}Ni (e, α) at E_e = 16 -50 MeV have been acquired at the United States' National Bureau of Standards (N.B.S.) for a recent publication considering total cross section excitation function data [41]. The actual energy spectra and angular distributions have not yet been published, however data at $5 < E_\alpha < 12$ MeV for ^{60}Ni at E_e = 50 MeV, has been received [45], and this is compared with the data of the present work in Fig. 3.17. Allowance must be made for the different electron energies, which should cause the present E_e = 60 MeV data to be slightly greater in cross section than that of N.B.S. at E_e = 50 MeV. Allowing for this, agreement in both the shape and absolute magnitude of the cross section is very good.

Comparable (γ, α) data has been obtained by Keller and McConnell [29] for seven elements in the region Z = 22 - 30, using bremsstrahlung end point energies up to E_o = 32 MeV. The data is qualitatively similar to the present (e, α) data - exhibiting broad energy spectra which peak at $E_\alpha \sim 8$ MeV, and symmetric, anisotropic angular distributions in the spectrum peak region. The (γ, α) angular distributions for even-even nuclei peak at 90° in common with those observed here for the even-even nuclei, ^{60}Ni and ^{56}Fe.

The data presented here considerably extends the known (e, α) reaction studies, and where comparison is possible there is good agreement with the existing work.

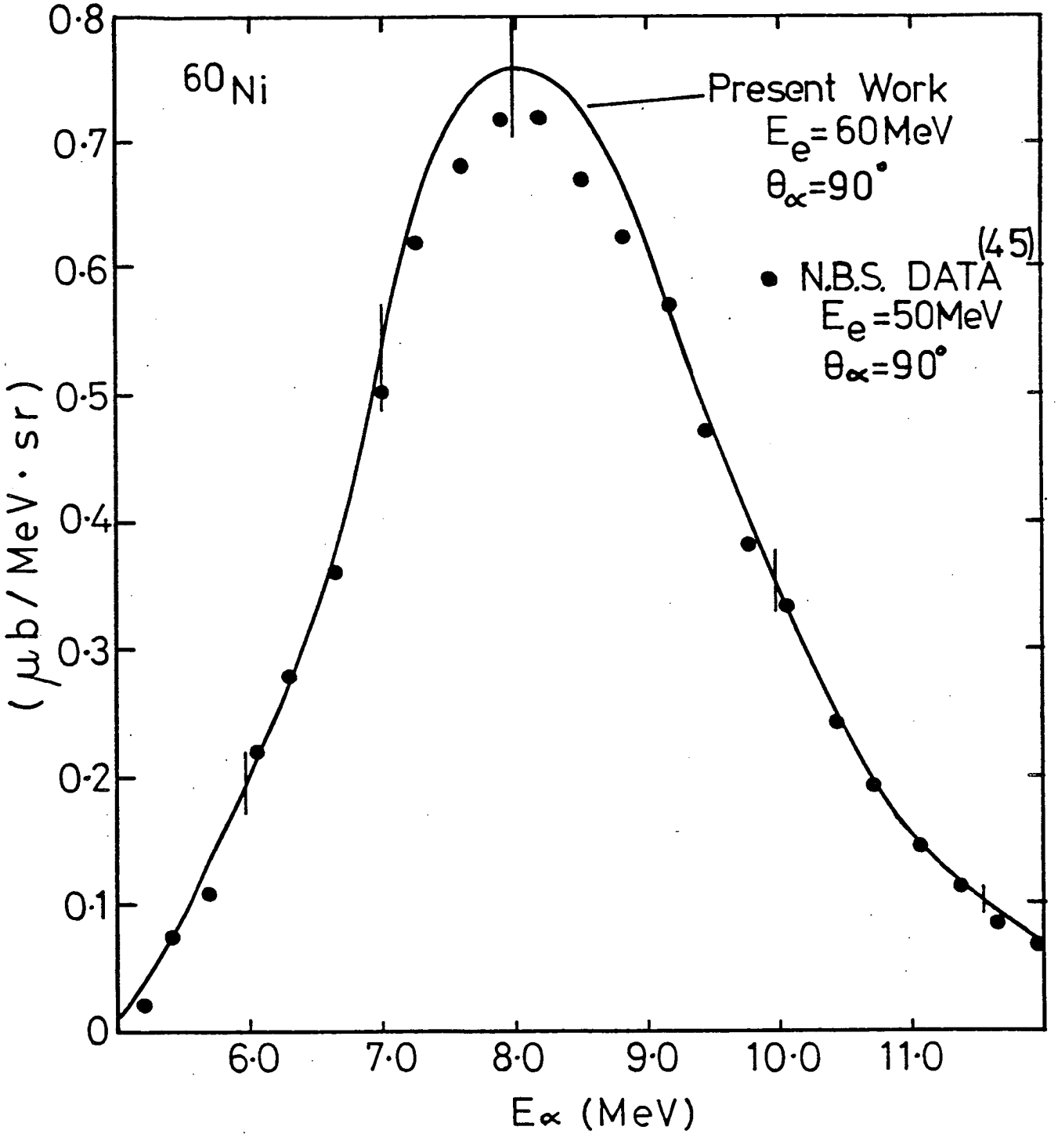

Figure 3.17. Comparison of ^{60}Ni (e,α) energy spectra acquired at N.B.S., Washington and in the present work.

3.5.3 The Nickel-60 "Cusp"

The prominent peak present in Fig. 3.4, for alpha particles of energy $E_\alpha \sim 4.5$ MeV, is considered to have two possible origins:

a) a rapid decrease in the alpha emission cross section above the neutron threshold,

b) light element target contamination.

In this section the evidence relating to these two possibilities is discussed.

Below the ^{60}Ni neutron threshold, at 11.4 MeV, the alpha and proton channels are open, and proton emission, with $Q_p = -9.5$ MeV, is strongly inhibited by the Coulomb barrier, whereas alpha emission ($Q_\alpha = -6.3$ MeV) may proceed less inhibited by barrier effects for a short energy range below $E_\alpha^{LAB} = 4.75$ MeV (the laboratory frame alpha particle energy at which neutron emission becomes allowed). These effects are reflected in the form of the alpha particle emission branching probability, Γ_α/Γ, as illustrated for the region about the neutron threshold, in Fig. 3.18. The sharp decrease in the alpha emission probability at the neutron threshold, together with the rapid decrease in Coulomb barrier penetration with decreasing particle energy, combine to form a "competition cusp". Such a process was considered in 1948 by Wigner[110], who dismissed it as being of little theoretical interest. More recently, several particle capture experiments have been carried out in medium weight nuclei which show spectacular cusps in (p, γ) and (p, α_o) excitation functions[111),112)] at neutron thresholds. In particular a pronounced cusp has recently been observed in the ^{56}Fe$(\alpha, \gamma)^{60}$Ni reaction[113)], at the (α, n) threshold.

In contrast to particle capture reactions, in the (e, α) reaction excitation occurs for all energies up to the electron end-point energy. Thus, while competition cusps are clearly observed in (particle, γ) reactions, it is not obvious that the inverse reaction will show a cusp

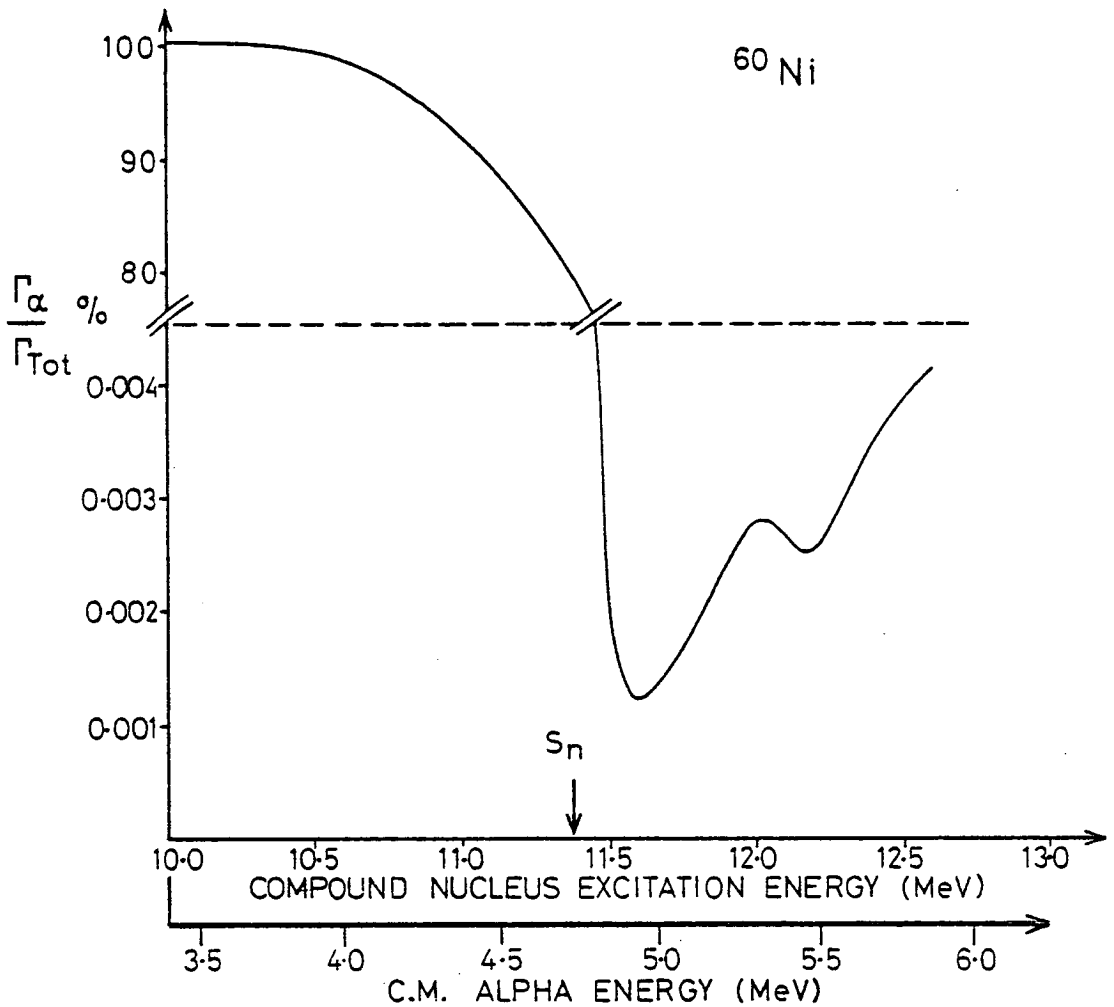

Figure 3.18. ^{60}Ni alpha particle branching ratio at the neutron threshold.

since substantial low energy particle emission will arise from excitation energies above the neutron threshold, for an electron energy $E_e > -Q_n$. Consequently any structure in the cusp region will tend to be smoothed over, particularly in view of the smaller photon absorption cross section near the neutron threshold compared to that in the higher energy, giant resonance region. It is therefore surprising that such a pronounced cusp is observed. Consequently, attempts have been made to observe similar cusps in other medium weight nuclei. The criterion for possible observation of alpha emission below the neutron threshold is for the sum of the neutron separation energy, S(n), and alpha Q value, Q(α), to be large and positive - together with a lower value of S(n) + Q(p). Several medium weight nuclei, for which this is the case, are listed in Table 3.2, together with their neutron separation energies and alpha and proton Q values. It is evident that ^{68}Zn should yield a cusp at a similar alpha energy to the ^{60}Ni cusp, yet no cusp is observed for $E_\alpha^{LAB} > 4$ MeV, despite a cusp being observed in the ^{64}Ni(α, γ)^{68}Zn reaction[114]. Furthermore, neither of the expected cusps for ^{56}Fe at $E_\alpha^{LAB} < 3.4$ MeV, and natural nickel (containing ^{58}Ni), at $E_\alpha^{LAB} < 5.4$ MeV are observed. A natural nickel target did, however, yield a cusp at the same peak energy as that observed with ^{60}Ni, yet with ~50% of the ^{60}Ni peak cross section. The presence of a cusp in targets containing ^{60}Ni, yet none of the other medium weight nuclei considered, suggests the possible presence of contaminants in the nickel targets.

Light element contamination may result in observation of a low energy alpha peak, due to the lower Coulomb barrier. In particular, oxygen contamination is likely since the target material is prepared from reduced nickel oxide, prior to rolling in air. Furthermore, large E1 resonances exist in ^{16}O at E_x = 12.44 and 13.1 MeV [115]. Since Q_α = -7.2 MeV for ^{16}O, alpha particles emitted from the 13.1 MeV

TABLE 3.2

Nuclide	S(N) (MeV)	S(P) (MeV)	Q(α) (MeV)	S(n)+Q(α) (MeV)	S(p)+Q(α) (MeV)
$^{42}_{20}Ca$	11.5	10.3	-6.25	5.25	4.05
$^{56}_{26}Fe$	11.2	10.2	-7.6	3.6	2.6
$^{58}_{28}Ni$	12.2	8.2	-6.4	5.8	1.8
$^{60}_{28}Ni$	11.4	9.5	-6.3	5.1	3.2
$^{64}_{30}Zn$	11.9	7.7	-4.0	7.9	3.7
$^{68}_{30}Zn$	10.2	10.0	-5.3	4.9	4.7
$^{70}_{32}Ge$	11.5	8.5	-4.1	7.4	4.4

resonance have E_α^{LAB} = 4.4 MeV, close to the observed laboratory frame peak energy, E_α^{LAB} = 4.6 MeV, at $\theta_\alpha = 90^o$. Alpha particles of energy $E_\alpha^{LAB} \sim 4.5$ MeV, at $\theta_\alpha = 90^o$, from ^{16}O, have a laboratory frame energy kinematic shift of +0.15 MeV when observed at $\theta_\alpha = 30^o$. Such a shift of the cusp is evident in Fig. 3.12, indicating the likelihood that the observed alpha emission arises from nuclei about mass number 16.

An analysis of ^{60}Ni foil from the same isotope batch used for the ^{60}Ni targets has been carried out using two independent techniques. Activation analysis yielded an ^{16}O: ^{60}Ni ratio (by parts) of 1 : 40, and destructive testing yielded 1 : 60 [116]. Such a contamination, taken together with the $^{12}C(\alpha, \gamma_o)^{16}O$ cross section [115] at E_γ = 13.1 MeV, is found to yield a predicted (e, α) cross section of at most only ~5% of that observed. This result casts doubt on the postulate that the observed cusp arises from oxygen contamination. However, the kinematic behaviour of the cusp is consistent with light element alpha emission and thus possibly casts doubt on the correctness of either the measured oxygen contamination or the $^{12}C(\alpha, \gamma_o)^{16}O$ cross section measurements. Other light element contamination is considered to be negligible. In particular, the target activation analysis showed no significant ^{19}F contamination, and measured ^{12}C(e, α) cross sections show no pronounced cusp at $E_\alpha^{LAB} \sim 4.5$ MeV [117].

Given the contradictory evidence relating to the nature of the observed Nickel-60 cusp, no definite conclusion can yet be made as to its origin. The substantial discrepancy between the measured oxygen contamination, and the observed cross section calculated assuming the presence of oxygen, requires further detailed investigation outwith the scope of this thesis work. In the absence of any definitive conclusions as to its true origin, all data obtained from the ^{60}Ni target with $E_\alpha^{LAB} < 5$ MeV is omitted from all further consideration. Measurements

of $^{12}C(\alpha, \gamma_0)$ cross sections [115] and $^{16}O(e, \alpha)$ cross section[31] indicate that even if the observed cusp arises from ^{16}O contamination only a negligible contaminant contribution would be present in the energy spectra for $E_\alpha > 5$ MeV.

3.5.4 $^{60}Ni(e, \alpha)$ Excitation Functions

Excitation functions at four alpha particle energies have been acquired for ^{60}Ni, to provide information on the distribution of the photoalpha cross section over excitation energies from threshold to 120 MeV. Excitation functions for alpha particles of energies 8.2 15.7, 20.3 and 25.4 MeV, for $19 < E_e < 120$ MeV are shown in Fig. 3.13. The cross sections displayed are averaged over the spectrometer energy bite corresponding to each of the alpha energies considered. Since the spectrometer has a 12% energy bite with respect to the energy of particles along the optic axis, the cross sections are therefore averaged over the alpha particle energy intervals $E_\alpha \pm 0.06E$. The cross sections for $E_\alpha = 8$ MeV are in good agreement with similar data obtained by an N.B.S. group (Fig. 3.19) [41]. No comparable data exists for the higher alpha particle energies considered here.

The excitation functions for $E_\alpha = 8$ and 15.7 MeV rise rapidly above their respective reaction thresholds, indicating a substantial cross section for particle emission near threshold, compared to several MeV above threshold, where the excitation functions level off to a more gentle increase with electron energy. At $E_\alpha = 20.3$ and 25.4 MeV there is a less dramatic rise near threshold and the cross section continues to rise more rapidly than for the lower alpha energy excitation functions. This is likely to result from an

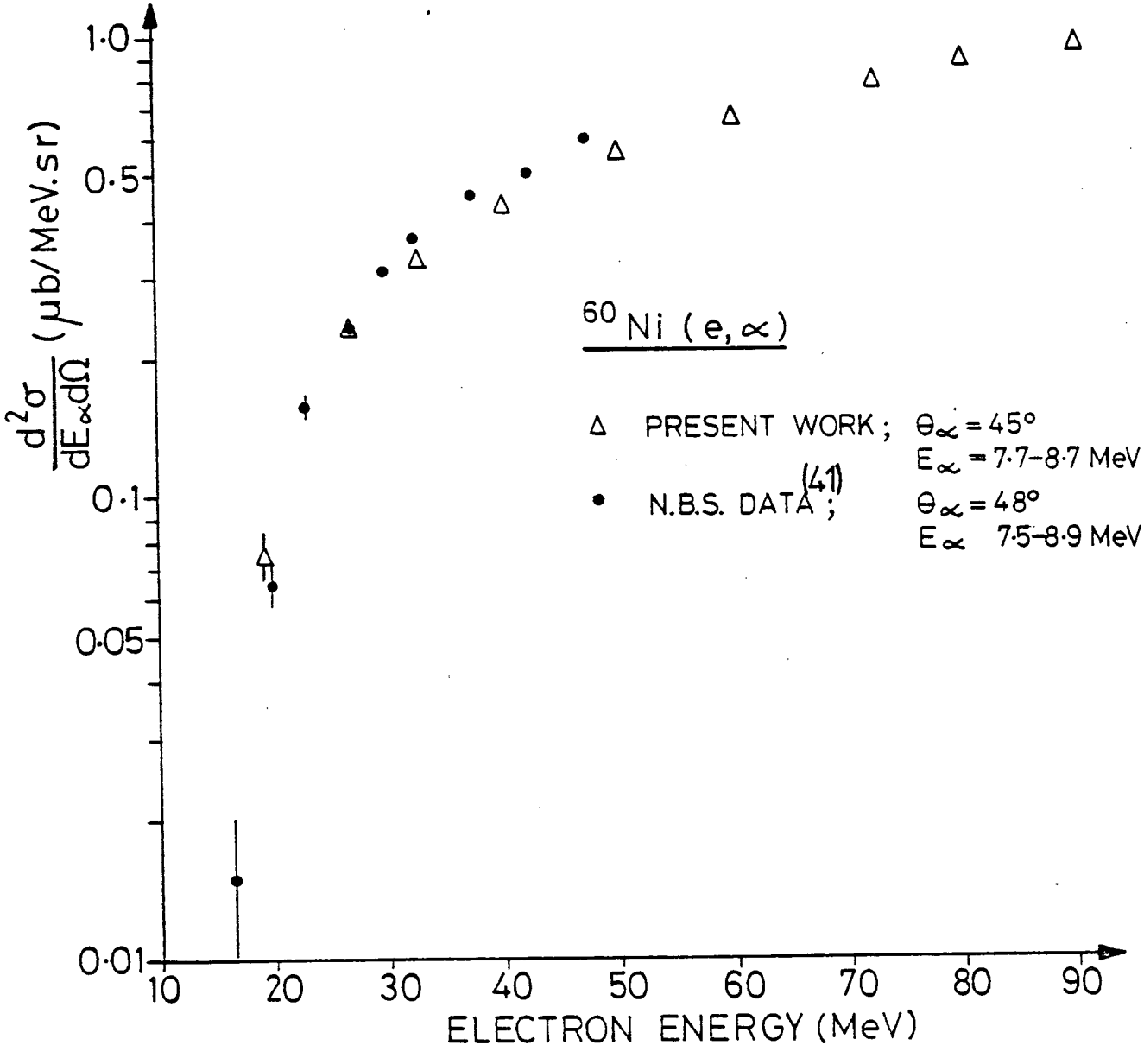

Figure 3.19 Comparison of ^{60}Ni(e, α) excitation functions acquired at N.B.S., Washington, and in the present work.

alpha emission cross section which is spread out over a wide range of excitation energies. However, definite conclusions arising from excitation function data cannot be made without considering the variation of virtual photon intensities, with electron energy.

3.5.5 Energy Spectra and Angular Distributions (E_α > 20 MeV)

The energy spectra of Fig. 3.3 - 3.6 exhibit a change in their slope above the peak alpha energy, around $E_\alpha \sim 16$ MeV, for ^{56}Fe, ^{60}Ni and ^{68}Zn at $E_e = 120$ MeV. The alpha particle energy spectrum for ^{NAT}Ni at $E_e = 120$ MeV, $\theta_\alpha = 30^\circ$ over $5 < E_\alpha < 65$ MeV is shown in Fig. 3.14. The sharp fall in cross section above the peak becomes less steep and exponentially decreasing for $E_\alpha > 20$ MeV. Similar energy spectra are observed for alpha particles from ^{27}Al, ^{92}Mo, ^{94}Mo and ^{197}Au (Fig. 3.15). The cross sections for ^{92}Mo and ^{94}Mo show no significant differences for $E_\alpha > 25$ MeV, indicating the unimportance of shell effects, or differing Q values, in the high energy alpha emission process.

Angular distributions for $E_\alpha = 31$ MeV and $\sim$50 MeV, for both nickel and gold are forward peaked and of similar form, though different magnitudes, at each alpha energy, as shown in Fig. 3.16. Alpha particle angular distributions obtained by Murphy et al. [34), 38)], for the (e, α) reaction with $E_e = 100$ MeV, show similar forward peaking. Murphy et al. considered these to arise from a direct alpha emission process, though no qualitative analysis was undertaken.

No comparable (e, α) energy spectra are known - most (γ, α) and (e, α) reaction studies yield energy spectra cut off at $E_\alpha < 22$ MeV. Two high energy bremsstrahlung (γ, α) experiments, with $E_o = 450$ MeV [118)] and $E_o = 500$ MeV [119)], have obtained alpha energy

spectra up to E_α = 50 MeV, using semiconductor detector telescopes. Energy spectra obtained in reference 118 for alpha particles from ^{40}Ca, ^{93}Nb and ^{197}Au, and in reference 119 for ^{197}Au, exhibit exponentially decreasing cross sections above $E_\alpha \sim 15$ MeV for ^{40}Ca and ^{93}Nb, and above $E_\alpha \sim 20$ MeV for ^{197}Au. These spectra are therefore qualitatively similar to those observed here, though pose a more complex analysis problem, since in these cases the alpha particles are likely to arise from all excitation energies up to 450 MeV, whereas here the excitation region is limited to below the pion threshold region.

CHAPTER 4

STATISTICAL GIANT RESONANCE DECAY

4.1 Introduction

The form of energy spectra for alpha particles emitted by medium weight nuclei excited by real photons strongly suggests a statistical (or evaporative) decay of the excited nucleus[24) - 29), 120)]. Additionally, the observed evaporation spectra of neutrons and protons from photon induced reactions provides convincing evidence that the photonuclear reaction proceeds predominantly through the compound nucleus in a statistical manner[121)]. Comparison of the energy spectra presented in Figs 3.2 - 3.6 with (γ, α) studies shows the expected similarity in the forms of (e, α) and (γ, α) energy spectra.

Despite the resemblance of photoalpha energy spectra to the forms expected for statistical particle decay, the calculation of these spectra has met with limited success. Carver [120)] calculated the ratio $\sigma(\gamma,\alpha)/\sigma(\gamma,n)$ for ^{51}V and found excellent agreement with the experimental ratio. However, no attempt was made to calculate absolute (γ, α) cross sections. Meneghetti and Vitale[26)] did attempt such calculations and they obtained excellent fits to the shape of the energy spectra for medium weight nuclei, but the absolute normalisation was incorrect by a factor of three for copper and nine for silver. Even greater disagreement between experimental and theoretical results was found in heavy nuclei. Evaporative yields predicted for indium and gold were respectively factors of 30 and 200 below the observed yields and disagreed markedly with the observed energy spectra shapes. These results led to the suggestion that direct effects were present in the (γ, α)

reaction on heavy nuclei. Keller and McConnell[29] also attempted statistical model calculations for a range of medium weight nuclei and found poor agreement with the shape and magnitude of the experimental photoalpha cross sections. Recently Murphy et al.[34), 38] deduced that (γ, α) spectra for nuclei in the range $Z = 29 - 79$ arise from evaporative processes, on the basis of fitting an evaporative shape to their energy spectra.

The analysis of photoalpha data has only been partially successful since many of the calculations were performed before the advent of high speed computers and thus took simplifying steps in the calculations, particularly with regard to the energy level density parameterisation. It is of interest, therefore, to test the application of a full Hauser-Feshbach statistical model calculation to the decay of giant resonances excited in inelastic electron scattering.

In the next two sections the statistical decay of the giant dipole resonance is discussed, and all other multipole resonances are initially neglected on the basis of the considerations in Section 1.4.2. The extent of observable alpha decay from any other multipole resonances is returned to in more detail in Sections 4.3 and 4.4.

4.2 Hauser-Feshbach Calculation

4.2.1 Application of Hauser-Feshbach Theory to the (e, α) Reaction

The Hauser-Feshbach expression for the reaction cross section $\overline{\sigma}_{cc'}$ averaged over compound nucleus fluctuations, for an entrance channel c and exit channel c' is given by,

$$\overline{\sigma}_{cc'} = \frac{\pi}{k_c^2} \sum_{J\pi} \left\{ \frac{(2J+1)}{(2J_c+1)(2j+1)} \cdot \{ \sum_{s\ell} T_\ell(c) \} \cdot \frac{\sum_{s'\ell'} T_{\ell'}(c')}{\sum_{s''\ell''} T_{\ell''}(c'')} \right\} \quad (4.1)$$

where the unprimed quantities refer to the incoming channel, c, single primed quantities to the outgoing channel of interest, c', and double primed quantities to all possible outgoing channels c". The quantum numbers of each channel c are given by

$c = (\alpha, J_c, j, s, \ell, J, M_J, \pi)$ where α labels the pair of particles in their state of excitation. J_c and j are intrinsic spins of the particles (e.g. target nucleus and projectile), s is the channel spin ($\underline{s} = \underline{J_c} + \underline{j}$), J the total angular momentum ($\underline{J} = \underline{\ell} + \underline{s}$), M_J its components (assumed to be averaged over) and π is the total parity. The wave number of the incident channel is given by k_c, and T_ℓ are transmission coefficients calculated as described in Section 4.2.4. The assumptions which lead to expression (4.1), and its applicability to alpha particle decay channels, are fully discussed in reference 122.

The assumption by Bohr that the formation and decay of the compound nucleus are independent processes has been well tested experimentally (e.g. Ref. 123). The $\bar{\sigma}_{cc'}$ for each compound nucleus state of spin J and parity π can be factorised into

$$\bar{\sigma}^{J\pi}_{cc'} = \bar{\sigma}^{J\pi}_{CN}(c) \frac{\sum_{s'\ell'} T_{\ell'}(c')}{\sum_{s''\ell''} T_{\ell''}(c'')} \qquad (4.2)$$

where $\bar{c}^{J\pi}_{CN}(c)$ is the cross section for the formation of the compound nucleus. The second term is a branching ratio which gives the probability that the compound nucleus will decay by channel c'.

In the case of alpha particle decay following GDR excitation by photons in even-even target nuclei, only $J^\pi = 1^-$ compound nuclear states will be excited, and expression (4.2) can be applied for this case. The compound nucleus formation cross section is then simply the GDR total photon absorption cross section, $\bar{\sigma}_{CN}(\gamma)$, (assuming no direct or pre-equilibrium GDR decays). However, this has only been measured

for a few light nuclei, and so it is preferable to base the calculation on the more extensively measured photoneutron cross section. Taking excitation of $J^{\pi} = 1^{-}$ states to be understood, equation (4.2) yields,

$$\bar{\sigma}_{\gamma,n} = \bar{\sigma}_{CN}(\gamma) \frac{\sum_{s'\ell'} T_{\ell'}(n)}{\sum_{s''\ell''} T_{\ell''}(c'')} .$$

Consideration of a similar expression for $\sigma(\gamma, \alpha)$, yields

$$\bar{\sigma}_{\gamma,\alpha} = \bar{\sigma}_{\gamma,n} \frac{\sum_{s'\ell'} T_{\ell'}(\alpha)}{\sum_{s''\ell''} T_{\ell''}(n)} .$$

From this it can be directly seen that the alpha emission cross section differential in energy can be derived from the energy dependence of the alpha particle transmission coefficients, $T_{\ell'}(\alpha)$, i.e.

$$d\bar{\sigma}_{\gamma,\alpha}(E_{\gamma}, E_{\alpha}) = \bar{\sigma}_{\gamma,n}(E\gamma) \frac{\sum_{s'\ell'} T_{\ell'}(E_{\gamma},E_{\alpha})}{\sum_{s''\ell''} T_{\ell''}(n)} dE_{\alpha} \qquad (4.3)$$

The (e, α) differential cross section is then computed using the analytical E1 virtual photon spectrum of reference 67 , $N^{E1}(E_e,E_{\gamma})$, following the assumption of a pure dipole resonance excitation process,

$$d\sigma^{E1}_{e,\alpha}(E_e,E_{\alpha}) = \int_{-Q_n}^{33} d\bar{\sigma}_{\gamma,\alpha}(E_{\gamma},E_{\alpha}) N^{E1}(E_e,E_{\gamma}) \cdot E_{\gamma}^{-1} \, dE_{\gamma} \qquad (4.4)$$

The calculation of the alpha energy spectra is carried out up to a photon energy (excitation energy) of 33 MeV, - corresponding to the lowest electron beam energy for which an alpha particle energy spectrum is presented in Chapter 3. Additionally, the cross section for photon

absorption leading to compound nucleus formation is uncertain above ∿30 MeV, and difficulties also arise with the validity of level density formulae at high excitation energies. Hence the questionable validity of calculations for a compound nucleus at excitation energies above ∿30 MeV further led to a cut off for the statistical model calculations at 33 MeV excitation. This energy corresponds with a reasonable upper limit of the giant resonance region in medium weight and heavy nuclei, hence the calculated alpha energy spectra relate only to particle decays from the giant resonance region. In light nuclei the giant dipole resonance extends up to higher excitation energies and the application of (4.4) would then require an alteration of the integral upper limit.

The calculation of $d\sigma_{e,\alpha}(E_e,E_\alpha)$ using relations (4.3) and (4.4) reduces to a determination of the transmission coefficients, T_ℓ, the selection of a measured photoneutron cross section, and the calculation of electric dipole virtual photon intensities. Calculations are carried out for two even-even nuclei, ^{56}Fe and ^{60}Ni (both with $J_c^\pi = 0^+$) and for ^{197}Au, with $J_c^\pi = \frac{3}{2}^+$. In the case of ^{197}Au consideration must be given to dipole excitation leading to $\frac{1}{2}^-$, $\frac{3}{2}^-$ and $\frac{5}{2}^-$ levels of the compound nucleus.

4.2.2 Isospin Effects on the Hauser-Feshbach Calculation

Excitation of the GDR results in an isospin change of $\Delta T = 1$ for self-conjugate nuclei ($N = Z$), and a change of $\Delta T = 0, \pm 1$ for $N \neq Z$. (See Section 1.3.1). The GDR will therefore comprise both isospin states $T_< = T_o$ and $T_> = T_o + 1$, for the $N > Z$ nuclei considered here, where $T_o = (N - Z)/2$. The isospin allowed transitions from the GDR of a $T_o \neq 0$ nucleus, to low lying levels of residual nuclei, are illustrated in Fig. 1.5. Alpha particles have

$T = 0$, so alpha decays from $T_>$ states to low lying levels in the residual nucleus will be isospin forbidden, and in general, the isospin allowed decays to the higher lying $T_o + 1$ states in the residual nucleus will be energetically forbidden. Neutrons have $T = \frac{1}{2}$, so their decays from $T_>$ states to low lying levels in the residual nucleus are also isospin forbidden. However, transitions to $T_o + \frac{1}{2}$ states are generally energetically allowed, hence both the $T_<$ and $T_>$ giant resonance states may neutron decay by isospin allowed transitions. A consideration of isospin effects is therefore necessary if the (γ, α) and (γ, n) channels are to be related as in expression (4.3).

The inclusion of isospin selection rules in statistical calculations has been considered by Grimes et al.[124], who substantially modified the conventional Hauser-Feshbach expressions. Fowler[125] has further modified the expressions to include various fractions of isospin mixing. Despite their availability, these modifications have been seldom applied, principally because of substantial evidence for almost complete isospin mixing of GDR states in medium weight and heavy nuclei, and the observation of isospin forbidden decays in these nuclei. Alpha capture studies of $N \neq Z$ nuclei show low (γ, α_o) cross sections in the $T_>$ region which can be reasonably explained by Hauser-Feshbach calculations neglecting isospin[126), 127]. Furthermore, statistical model analyses of (α,γ), (α, n), (p,γ), (p,n) and (p,α) data in the region of neutron thresholds have indicated essentially complete isospin mixing between $T_>$ and $T_<$ states in medium weight nuclei[112) - 114]. These features can be understood in terms of the substantial overlapping of GDR levels which must occur in medium weight (and also heavy) nuclei. Consequently the conclusions here cannot be extended to lighter nuclei near shell closures where separated GDR levels occur, e.g. ^{16}O and ^{40}Ca.

In summary, the isospin selection rules suggest that the (γ, α) channel for decays to low lying residual nucleus states should be related only to a (γ, n) channel applicable to the $T_<$ part of the giant resonance. However, substantial isospin mixing of the $T_<$ and $T_>$ giant resonance states indicates that the total (γ, n) cross section may be applied in expression (4.3) for medium weight and heavy nuclei. The statistical model calculations in this thesis are therefore carried out on the assumption of complete isospin mixing.

4.2.3 Values adopted for $\bar{\sigma}_{\gamma,n}$

The values of $\bar{\sigma}_{\gamma,n}$ used for each nucleus considered here are shown in Fig. 4.1, and referenced there accordingly. For ^{60}Ni and ^{197}Au the (γ,n) cross sections are approximated by using the single photoneutron cross sections, $\sigma(\gamma, 1n)$ which includes both (γ, n) and (γ, pn) reactions, i.e. $\sigma(\gamma, 1n) = \sigma(\gamma, n) + \sigma(\gamma, pn)$. This approximation is reasonable since in the low energy region considered in our calculation, $\sigma(\gamma, pn)$ are small compared with $\sigma(\gamma, n)$. In the absence of any single photoneutron measurements for ^{56}Fe, the $^{56}Fe(\gamma, n)$ cross sections are approximated by $\sigma(\gamma, xn)$ for natural iron. The use of data for a natural isotopic mixture is not a great deficiency since natural iron is comprised of $\sim$92% ^{56}Fe. In using the $\sigma(\gamma, xn)$ cross sections allowance was made for $\sigma(\gamma, 2n)$ cross sections comparable with those observed for ^{60}Ni, - the nearest $T = 2$ nucleus for which data is available.

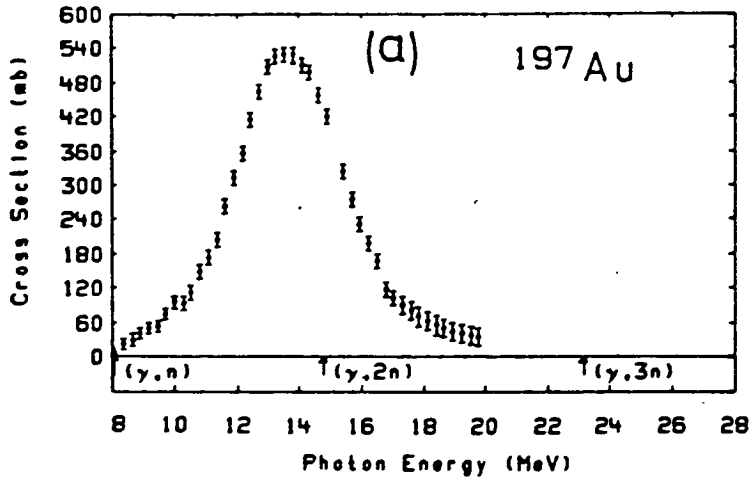

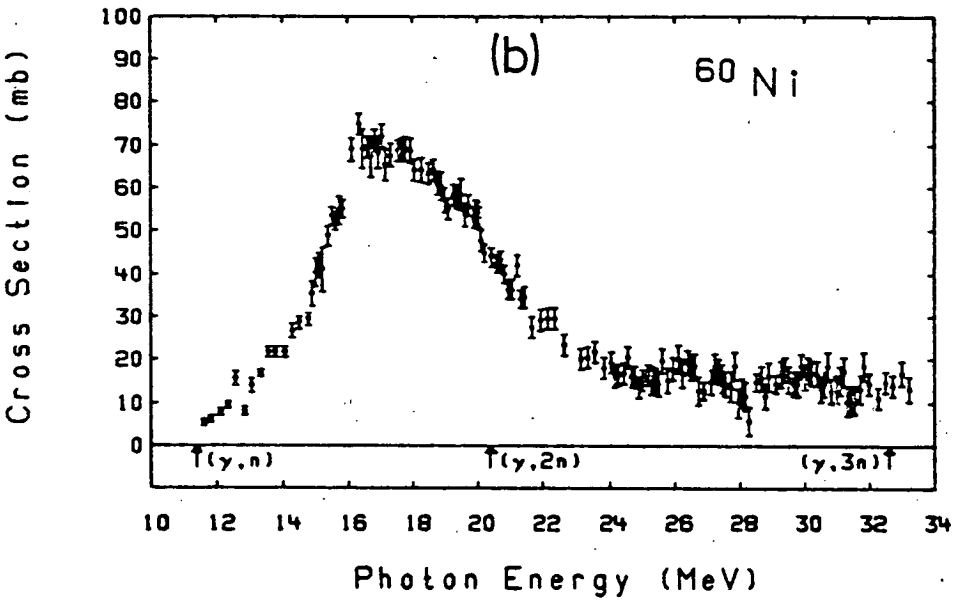

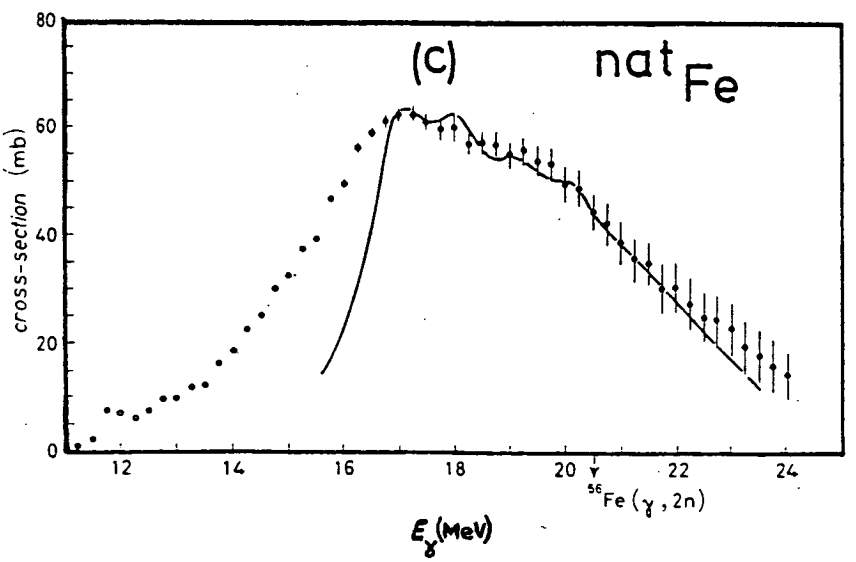

Figure 4.1 Values adopted for $\overline{\sigma}_{\gamma,n}$. (a) and (b) are from Ref. 147 and (c) is from Ref. 149. The solid line in diagram (c) is the sum of calculated dipole strengths.

4.2.4 Calculation of Transmission Coefficients

The transmission coefficients $T_\ell(E_\gamma, E_\alpha)$ are calculated using a version of the computer code HAUSER[128] for the case of a reaction proceeding through a single compound nucleus state of given J^π. The transmission coefficient is derived from the optical model phase shift parameter, δ_ℓ, calculated for the optical potential appropriate to the channel under consideration,

$$T_\ell = 1 - \left| e^{2i\delta_\ell} \right|^2 .$$

The optical potential used is of the form

$$V_{OPT}(r) = -Vf(r) - i\left(Wf(r) + 4a_D W_D \frac{df(r)}{dr}\right) - \text{central potential}$$

$$+ \left(\frac{\hbar}{m_\pi c}\right)^2 \frac{V_{SO}}{r}(\underline{\sigma}\cdot\underline{\ell}) \frac{df(r)}{dr} - \text{Spin Orbit Potential}$$

$$+ \begin{cases} \dfrac{ZZ'e^2}{2R_C}\left(3 - \dfrac{r^2}{R_C^2}\right), & r \leq R_C \\ \dfrac{ZZ'e^2}{r}, & r > R_C \end{cases} - \text{Coulomb potential} \qquad (4.5)$$

where V is the depth of the real optical potential;

W is " " " " imaginary volume potential;

W_D is " " " " imaginary surface potential;

V_{SO} is " " " " spin orbit potential;

R_C is the Coulomb radius $(= r_o A^{1/3})$;

Z, Z' are the charge of target and projectile, respectively.

$f(r)$ is the Saxon-Woods form factor,

$$f(r) = \left[1 + \exp\left(\frac{r - r_o A^{1/3}}{a}\right)\right]^{-1}$$

where a and r_o are the diffuseness and radius parameters, which may be different for real, imaginary and spin orbit potentials.

$\left(\frac{\hbar}{m_\pi c}\right)^2 \simeq 2.0$ fm^2, where m_π is the pion mass.

$\underline{\sigma} \cdot \underline{\ell}$ is the spin orbit operator, given by

$$\underline{\sigma}\cdot\underline{\ell} \equiv \tfrac{1}{2}\Big(j(j+1) - \ell(\ell+1) - s(s+1)\Big)$$

where $\underline{j} = \underline{\ell} + \underline{s}$

$\underline{\sigma}\cdot\underline{\ell} \equiv 0$ for alpha particles

$$\underline{\sigma}\cdot\underline{\ell} \equiv \begin{cases} \ell & - \text{ spins parallel} \\ -\ell-1 & - \text{ spins anti-parallel} \end{cases} \quad \text{for neutrons.}$$

The parameters for neutrons are taken from Wilmore and Hodgson[129], who give generalised energy dependent real and imaginary surface potentials. At the suggestion of Perey[130], a neutron spin orbit potential V_{SO}, of 7 MeV is applied. The alpha particle parameters for ^{56}Fe and ^{60}Ni alpha decay are those of Lemos[131], determined from alpha particle elastic scattering data for ^{52}Cr and ^{56}Fe at 21 MeV alpha energy. The parameters for ^{197}Au alpha decay are derived by considering the values from alpha scattering on hafnium, tungsten and gold at 24.7 MeV alpha energy. The parameters employed are tabulated in Table 4.1.

4.2.5 Branching Ratios for Alpha and Neutron Channels

The ratio of the transmission coefficient sums in equation (4.3) yields the alpha particle to neutron branching ratio, i.e.

$$\frac{\Gamma_\alpha(E_\gamma,E_\alpha)dE_\alpha}{\int\Gamma_n(E_\gamma,E_n)dE_n} = \frac{\sum_{s'\ell'} T_{\ell'}(E_\gamma,E_\alpha)dE_\alpha}{\sum_{s''\ell''} T_{\ell''}(n)} \quad . \qquad (4.6)$$

Table 4.1

Optical Model parameters used to calculate the transmission coefficients for alpha particles and neutrons. Notation as in equation (4.5).

Parameter	Neutrons	Alphas		
		^{56}Fe	^{60}Ni	^{197}Au
V (MeV)	$47.01 - 0.267E - 0.0018E^2$	189.3	182.3	192
r_r (fm)	$1.322 - 7.6A\times10^{-4} + 4A^2\times10^{-6}$	1.36	1.37	1.42
a_r (fm)	0.66	0.57	0.55	0.55
W (MeV)	0	24.9	23.0	30
W_D (MeV)	$9.52 - 0.053E$	0	0	0
r_i (fm)	$1.266 - 3.7A\times10^{-4} + 2A^2\times10^{-6}$ $-4A^3\times10^{-9}$	0.57	0.55	0.55
a_i (fm)	0.48			
V_{SO} (MeV)	7.0	0	0	0
r_{SO} (fm)	1.25	0	0	0
a_{SO} (fm)	0.66	0	0	0

The calculation of this branching ratio requires the summation of the alpha particle transmission coefficients, $T_{\ell'}$, over all possible decay channels with channel spin s' and orbital angular momentum ℓ', for a given alpha energy, E_α, and photon energy, E_γ (= compound nucleus excitation energy). This sum is divided by the sum of the neutron transmission coefficients, $T_{\ell''}(n)$, taken over all possible decay channels for a given photon energy. The possible decay channels are only those allowed by the angular momentum and parity selection rules (Fig. 4.2), and must be energetically allowed. No allowance is made for isospin selection rules following the conclusions of Section 4.2.3.

An ideal calculation of the required transmission coefficients would require knowledge of the energies, spins and parities of all levels in the residual nuclei after neutron or alpha emission from the compound nucleus. However, since details of the level schemes of most nuclei are only known up to a few MeV excitation energy, the remaining levels' properties must be estimated using excitation energy, E, and spin, J_R, dependent level density formulae, $\rho(E,J_R)$. The formulae of Gilbert and Cameron[132] are used as described in Appendix 7. Assuming that the properties of the residual nucleus final states are known up to some excitation energy, U, the neutron transmission coefficient sum is given by,

$$\sum_{s''\ell''} T_{\ell''}(n) = \sum_{i=0}^{N} \sum_{s''\ell''} T_{i\ell''}(n) + \sum_{k=0} \sum_{s''\ell''} T_{k\ell''}(n) \cdot \cdot \rho\left[U + (k+\tfrac{1}{2})\Delta E,\ J_R\right] \cdot \Delta E_k \qquad (4.7)$$

where the sum over i is taken over all the known discrete levels up to the N^{th} excited state in the residual nucleus, at excitation energy

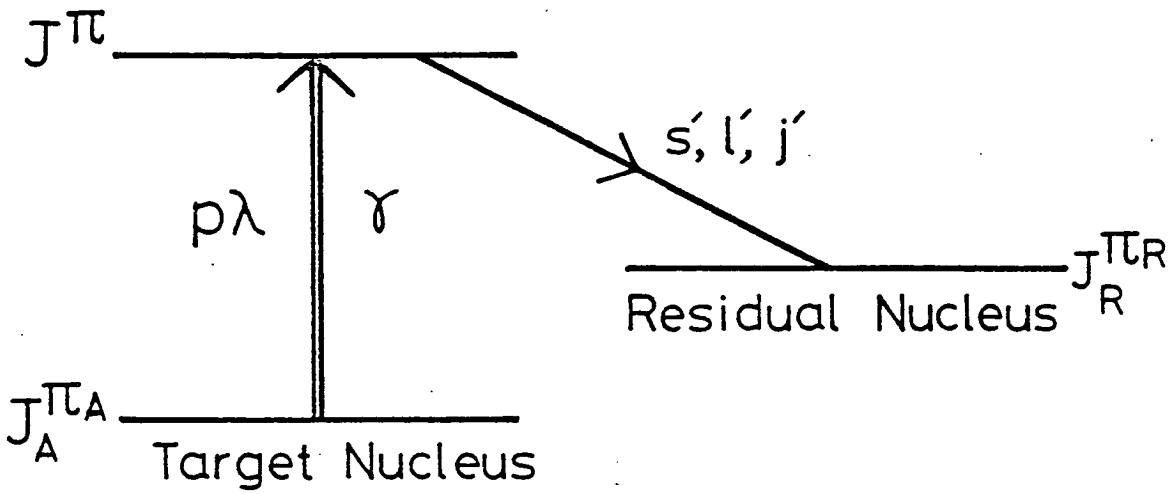

Notation:

s'	Channel spin for outgoing particle channel.
ℓ'	Particle orbital angular momentum.
j'	Particle spin $(j_\alpha' = 0)$.
$J_R^{\pi_R}$	Spin and parity of residual nucleus level
J^{π}	Spin and parity of target nucleus excited state.

Selection Rules:

1. $|J_R - j'| \leq s' \leq J_R + j'$
2. $|J - s'| \leq \ell' \leq J + s'$
3. $\pi_R = \pi(-1)^{\ell'}$

Example: $J^{\pi} = 2^+$; $J_R^{\pi_R} = 3^+$; $j' = 0$

1. $\Rightarrow$ $s' = 3$
2. $\Rightarrow$ $\ell' = 1, 2, 3, 4, 5,$
3. $\Rightarrow$ $\ell' = 2, 4$

$\therefore$ Allowed Channels - $(s', \ell') = (3,2), (3,4)$.

Figure 4.2. Angular momentum and parity selection rules for outgoing particle channel.

U. Thereafter the transmission coefficients are weighted as appropriate with the number of available levels of spin J_R in the interval ΔE_k, over which the transmission coefficients are assumed constant. In all cases the level density calculations were carried out with $\Delta E_k = 200$ keV. The summation over the level density bin index, k, ceases when an energetically forbidden residual nucleus excitation energy is reached.

The alpha energy dependence of the alpha channel transmission coefficients is retained by omitting the summations over residual nucleus levels. Thus,

$$\begin{aligned}\sum_{s'\ell'} T_{\ell'}(E_\gamma, E_\alpha^c) &= \sum_{s'\ell'} T_{i\ell'}(E_\gamma, E_\alpha^c) \\ &\quad -(E_\gamma + Q_\alpha > E_\alpha^c > E_\gamma + Q_\alpha - U) \\ &= \sum_{s'\ell'} T_{k\ell'}(E_\gamma, E_\alpha^c) \cdot \rho\left[U+(k+\tfrac{1}{2})\Delta E_k, J_R\right] \cdot \Delta E_k \\ &\quad - (E_\gamma + Q_\alpha - U > E_\alpha^c > 0)\end{aligned} \tag{4.8}$$

where E_α^c is the decay channel alpha particle energy in the centre of mass (uncorrected for recoil effects) and the symbols k, N, U and $\rho(E, J_R)$ are as for expression (4.7), though now relate to the residual nucleus after alpha decay. At an appropriate stage in the calculation of expression (4.3) the transmission coefficient sum calculated according to (4.8) is further summed into one MeV wide channel energy bins. The form of $\sum_{s'\ell'} T_{\ell'}$ thus defines the shape of the alpha energy spectrum at each excitation energy considered. Examples of this function are shown in Figs. 4.3, 4.4 and 4.5, for alpha decay from ^{60}Ni, $J^\pi = 1^-$ compound nucleus states at excitation energies 16, 20 and 25 MeV, and a $J^\pi = 2^+$ state at 16 MeV. Comparison of the spectra at $E_x = 20$

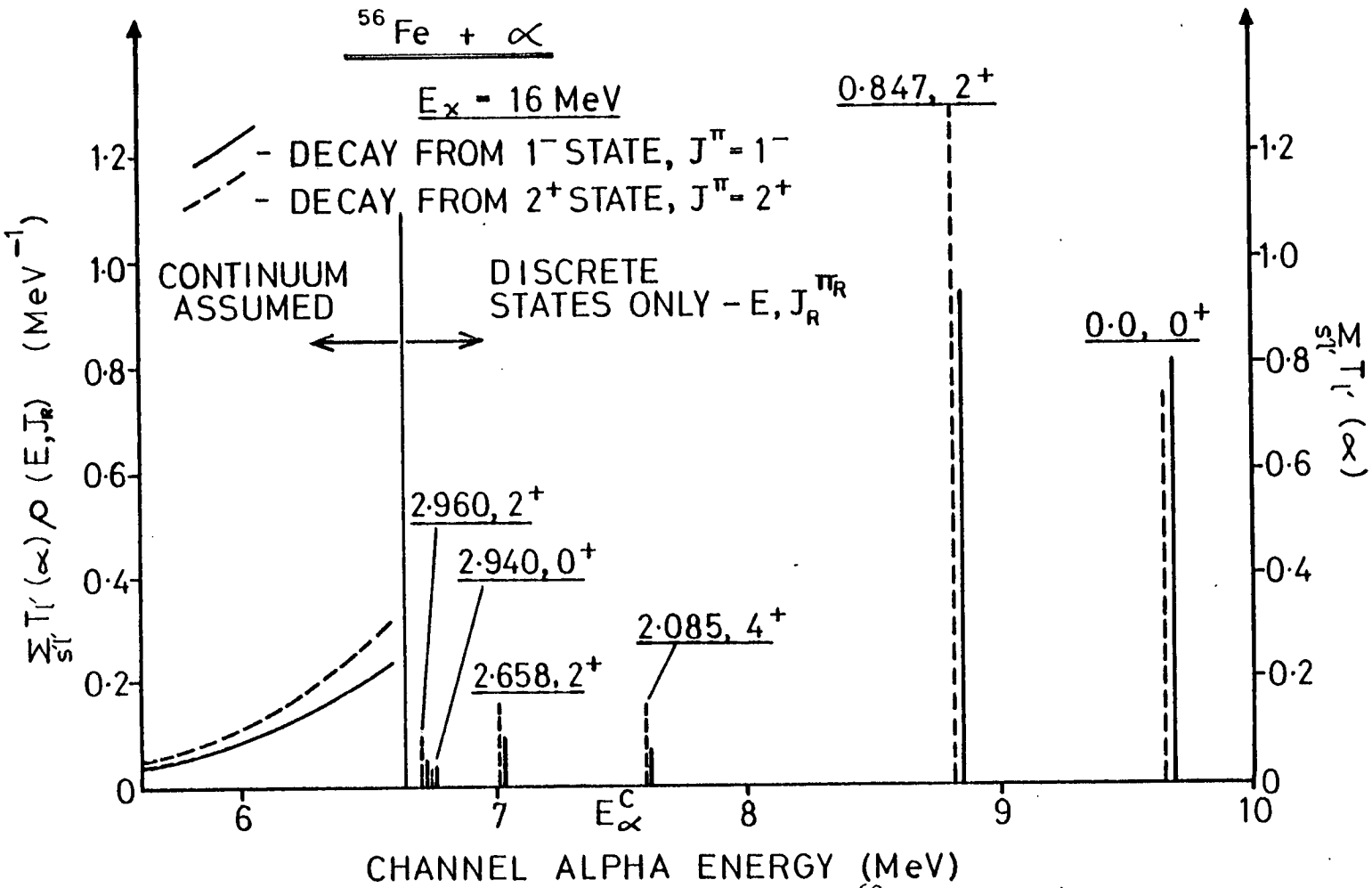

Figure 4.3 Summed transmission coefficients for alpha decay of ^{60}Ni 1^- and 2^+ levels at 16 MeV excitation energy.

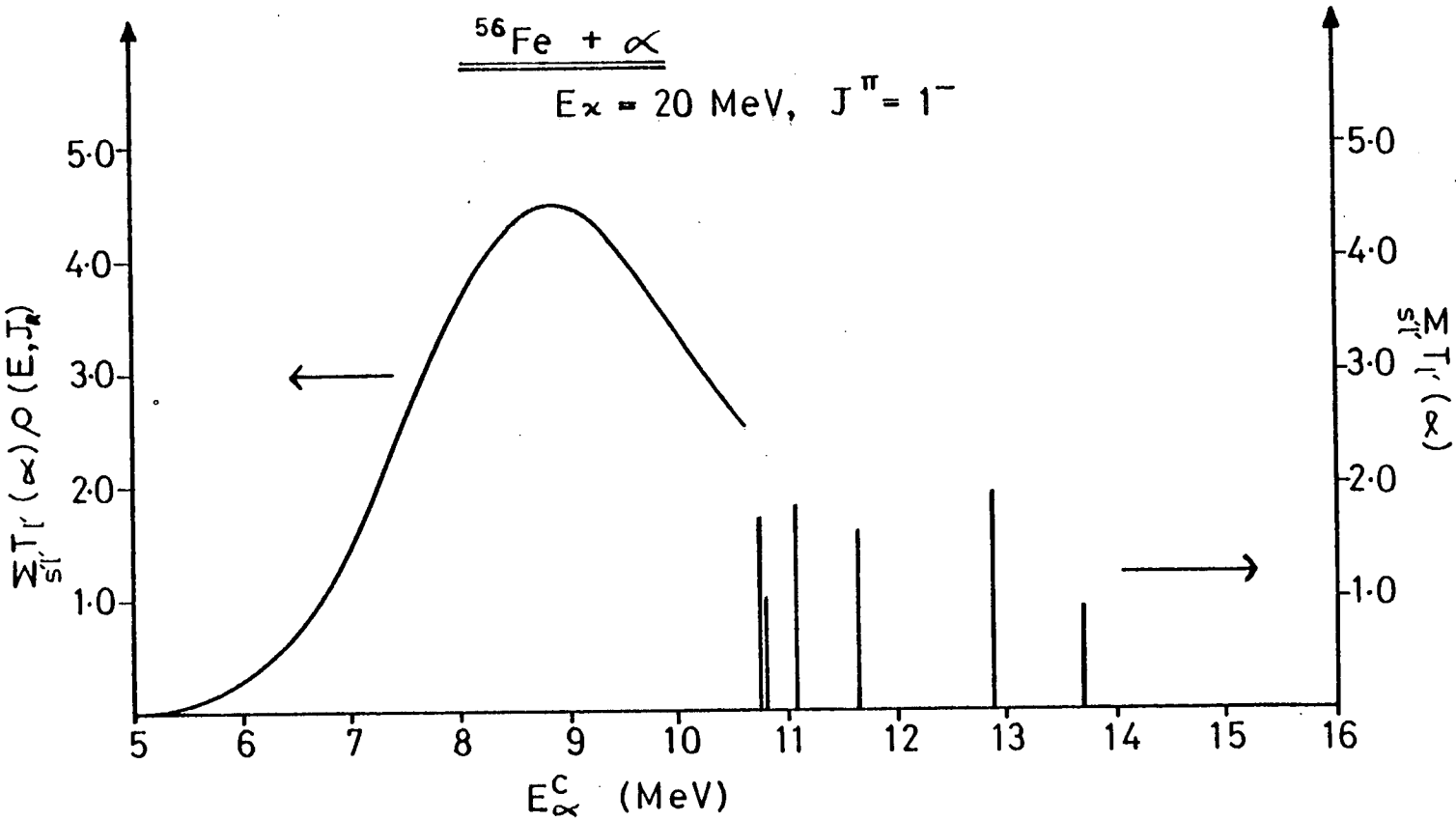

Figure 4.4 Summed transmission coefficients for alpha decay of a ^{60}Ni 1^{-} level at 20 MeV excitation energy.

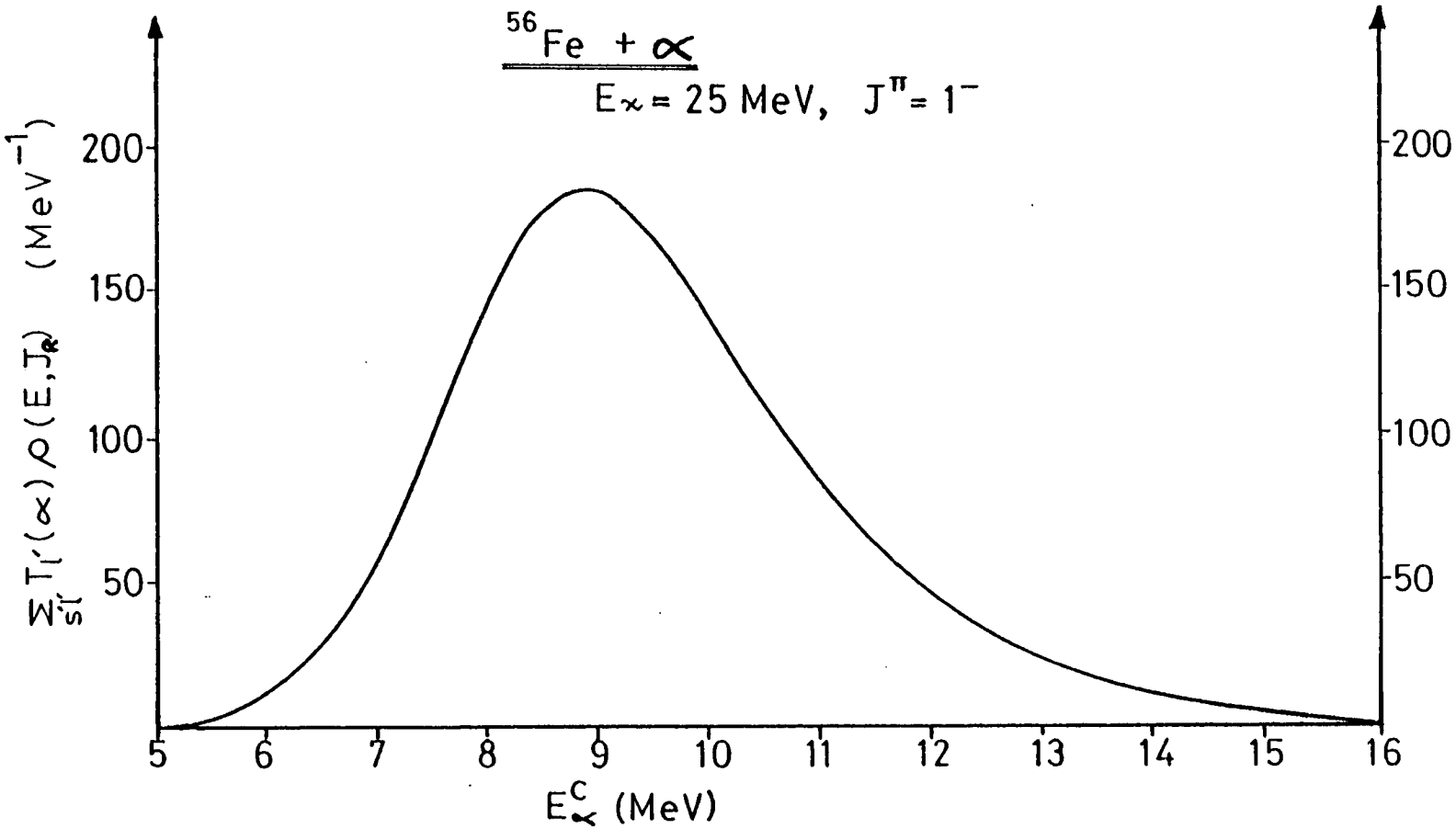

Figure 4.5 Summed transmission coefficients for alpha decay of a ^{60}Ni 1^{-} level at 25 MeV excitation energy.

and 25 MeV shows the near constancy of the peak position derived from the continuous level density part of the calculation at such excitation energies.

The calculation of $d\sigma(e, \alpha)$ is carried out in practice by obtaining the alpha to neutron branching ratio at 1 MeV excitation energy intervals and integrating expression (4.4) numerically. Alpha decays to discrete low lying states in the residual nucleus are found to be an important contribution to $d\sigma(e, \alpha)$, emphasising the importance of considering discrete low lying levels rather than using crude level density formulae, as in earlier calculations of this type.

In all cases the calculated energy spectra are divided by 4π to enable comparison with the experimentally obtained double differential energy spectra. The (e, α) angular distributions are considered in detail in Section 4.3.

4.2.6 Statistical Giant Resonance Decay Energy Spectra

4.2.6.1 Medium Weight Nuclei, ^{56}Fe and ^{60}Ni

Comparisons of the calculated (e, α) energy spectra with experimental data for ^{56}Fe and ^{60}Ni, at several electron energies, are shown in Figs. 4.6 and 4.7. The statistical model calculations are seen to give good agreement with the magnitude and position of the peak of the alpha energy spectra at all electron energies considered. In particular, in the range $E_\gamma = 6 - 12$ MeV discrepancies are no greater than ± 50%, which is within the inherent uncertainty of the calculation due to uncertainties in optical model and level density parameters. Above $E_\alpha = 12$ MeV, comparison of the measured and calculated energy spectra shows dramatic differences. These differences are further illustrated for ^{60}Ni in Fig. 4.8 which shows the variation of the ratio of the

Figure 4.6.

Figure 4.6. Alpha particle energy spectra for ^{60}Ni at $\theta_\alpha = 90^\circ$, for $E_e = 120$ MeV (curve A, upper left-hand scale), $E_e = 60$ MeV (curve B, right-hand scale), and $E_e = 33$ MeV (curve C, lower left-hand scale). Errors shown are absolute. The solid lines are the results of a statistical model calculation assuming photon absorption below $E_\gamma = 33$ MeV. The dashed lines mark the mean energies of the angular distributions presented in Figures 3.9 - 3.11.

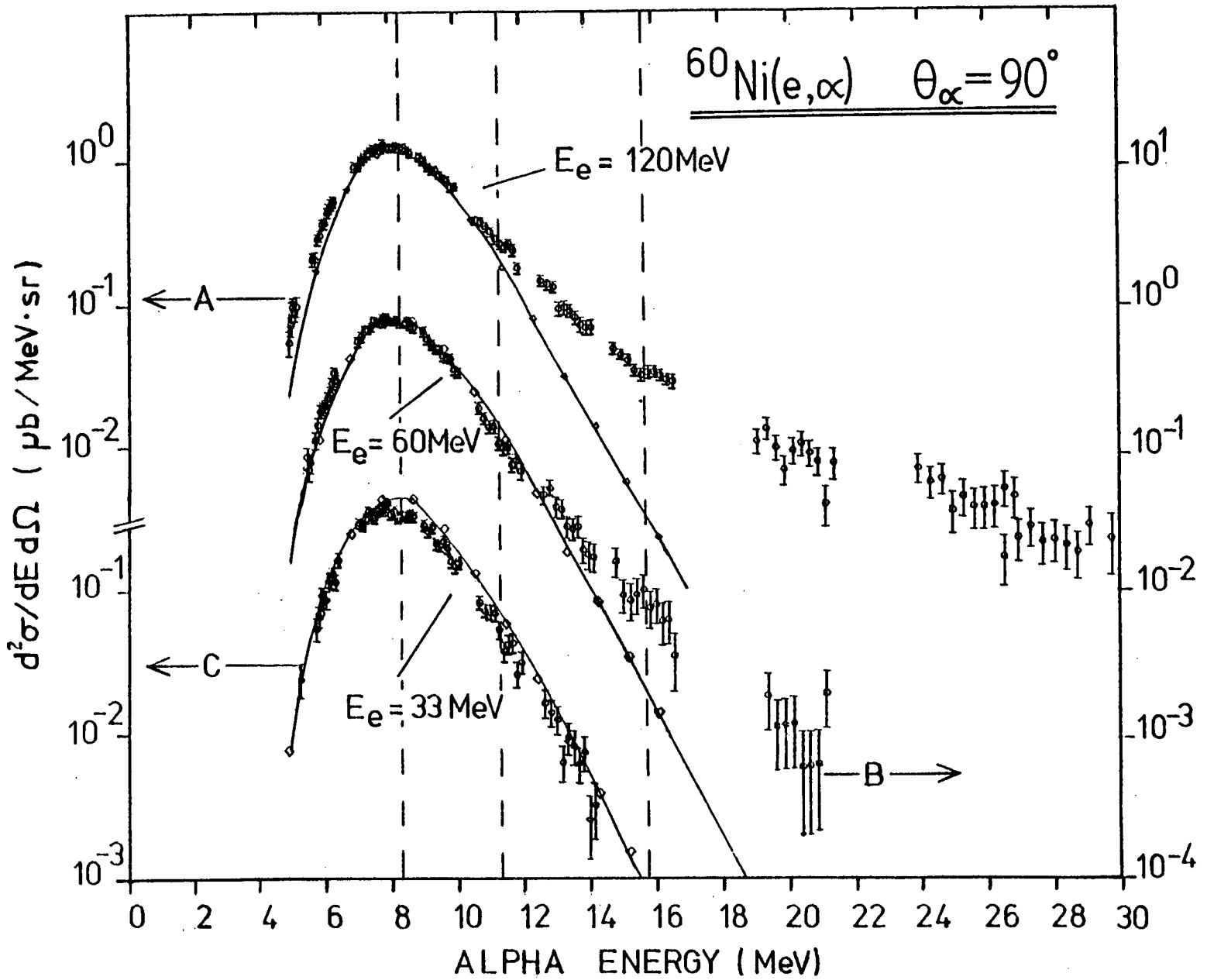
^{60}Ni(e,α) θα=90°
Ee = 120MeV
Ee= 60MeV
Ee = 33 MeV
A
B
C
d²σ/dE dΩ (μb / MeV·sr)
ALPHA ENERGY (MeV)

Figure 4.6.

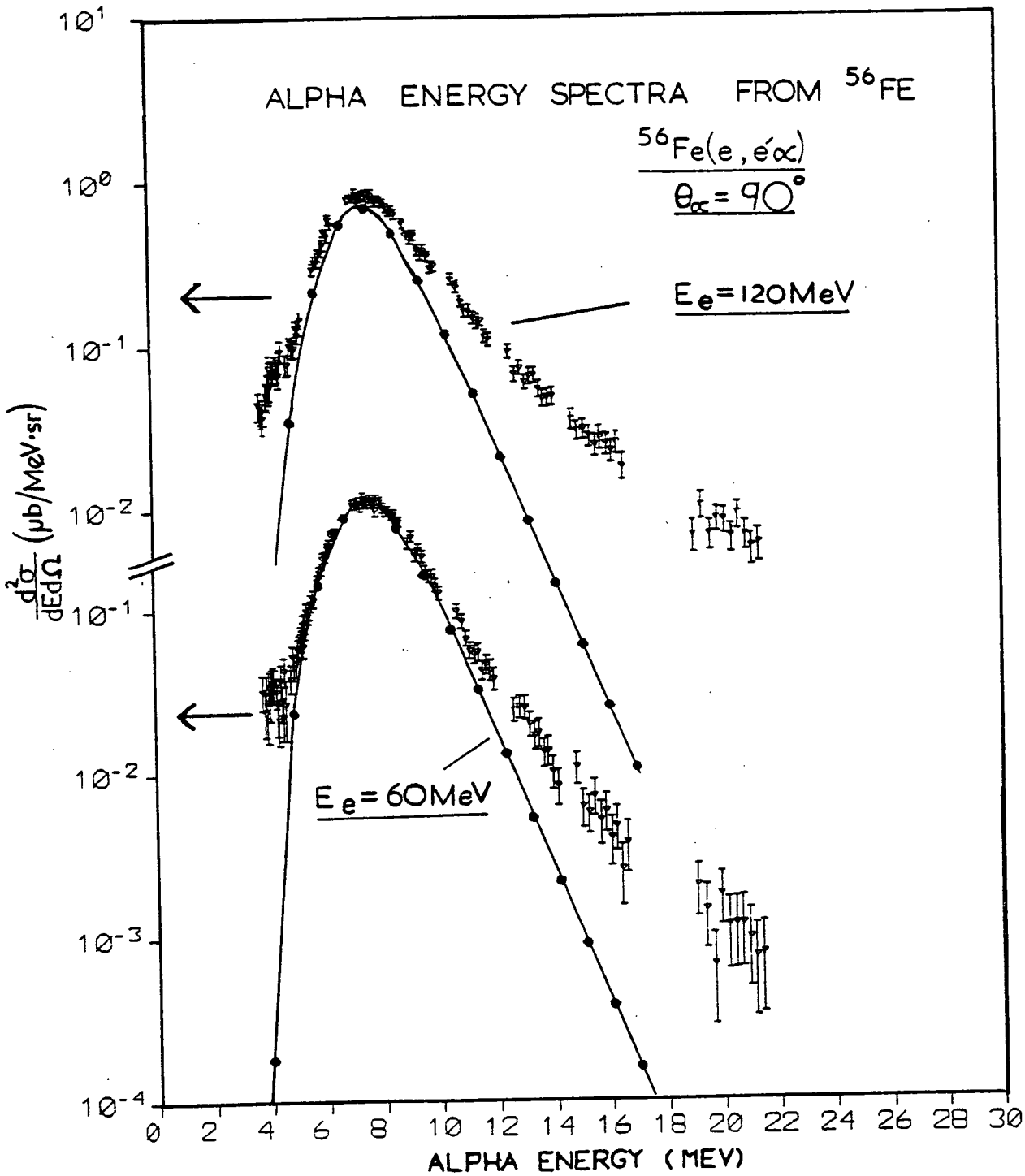

Figure 4.7. Alpha particle energy spectra for ^{56}Fe at $\theta_\alpha = 90^\circ$, for $E_e = 120$ MeV (upper curve and upper left-hand scale) and for $E_e = 60$ MeV (lower curve and lower left-hand scale). Errors shown are absolute. The solid lines and dots are the results of a statistical model calculation assuming photon absorption below $E_\gamma = 33$ MeV.

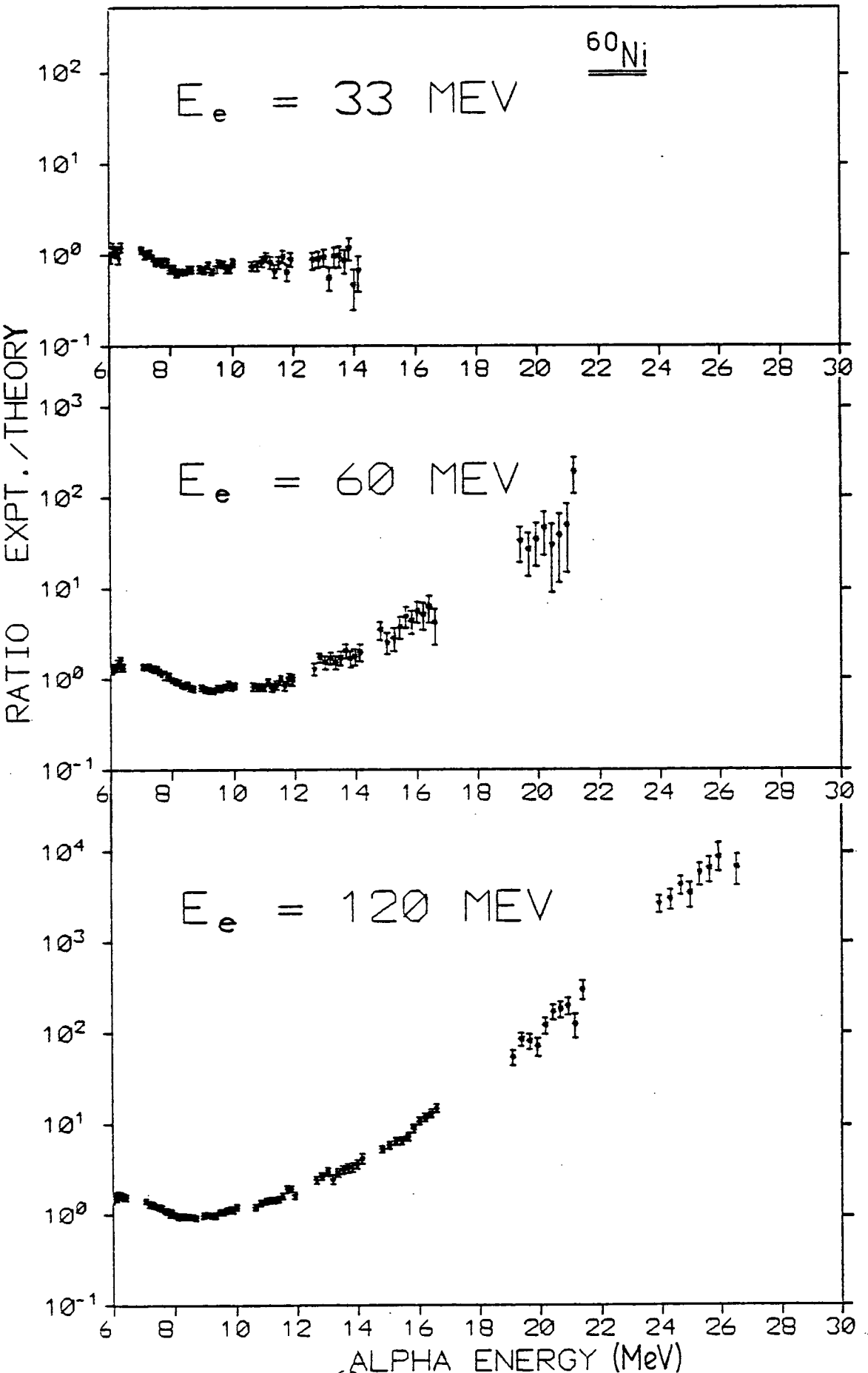

Figure 4.8. Ratio of measured ^{60}Ni alpha emission cross sections to calculated statistical alpha decay cross sections.

measured to calculated cross sections, "Expt./Theory", with increasing alpha energy. A high energy tail in the energy spectra becomes systematically larger compared to the statistical calculation, as the electron energy is increased. Whereas the observed high energy component agrees with the calculation at E_e = 33 MeV, it exceeds it by several orders of magnitude at E_e = 120 MeV. Although slight changes in the calculation input parameters would improve agreement of the absolute magnitude of the cross section in the 6 - 12 MeV region, such a procedure would not cause any significant improvement above $E_\alpha \sim 12$ MeV.

The (e, α) reaction in medium weight nuclei evidently contains a further component in addition to the evaporative part resulting from excitation of the target by photons of energy $E_\gamma \lesssim 33$ MeV. A full understanding of the (e, α) reaction process in medium weight nuclei therefore requires further consideration of the two most likely sources of this component;

(i) Direct or pre-equilibrium processes in the giant resonance region.

(ii) Alpha decay from levels at excitation energies above E_x = 33 MeV.

Consideration (i) is treated in Section 4.3, and consideration (ii) is deferred until Chapter 5.

Two significant assumptions regarding the nature of the reaction process for $E_\gamma < 33$ MeV are inherent in the calculations;

(a) The reaction proceeds only through giant dipole resonance states.

(b) The giant resonance $T_<$ and $T_>$ states fully isospin mix.

Assumption (b) has already been justified in Section 4.2.2. It is now

evident that the excellent reproduction of the spectrum shape over the energy range E_α = 6 - 12 MeV, particularly for the ^{60}Ni E_e = 33 MeV spectrum, could not have been achieved with the omission of isospin forbidden decays from the $T_>$ portion of the GDR. Alphas of energies $E_\alpha \gtrsim$ 11 MeV must substantially arise from any $T_>$ portion of the ^{60}Ni GDR, and these are certainly not overestimated here by assuming isospin mixing.

Assumption (a) has been discussed in general terms in Section 1.4 and is now considered in relation to the evidence for magnetic dipole (M1), electric monopole (E0) or electric quadrupole (E2) resonances in medium weight nuclei. Higher multipolarity resonances are unlikely to contribute to the reaction process since they are either located below the alpha threshold, for the nuclei considered here, or are expected to have sum rule strengths so low (see Section 1.4.2) that these would have to be exhausted many times over by the alpha channel alone to produce observable contributions to the measured cross sections.

Magnetic dipole strength has been observed[89), 133)], at excitation energies 11 - 14 MeV in medium weight nuclei and hence occupies a region from which alpha particles of energy $E_\alpha \lesssim$ 7 MeV would be observed. The M1 resonance region corresponds to the low energy tail of the GDR where low photonucleon cross sections are observed. No substantial alpha decay from these low lying M1 states is evident here, since a discrepancy between the observed and calculated low energy alpha spectra would then be expected. Further evidence that little M1 strength is present is obtained from a consideration of the angular distributions in Section 4.3.

The isoscalar monopole resonance is expected to appear at about 16 - 20 MeV in medium weight nuclei[134), 135)], and some weak evidence

has been obtained for its presence at these energies[80), 87)]. However, this resonance is difficult to identify since it is expected to appear at similar energies to the isoscalar GQR, and E0 and E2 strengths are difficult to separate in both hadron and electron scattering studies. Consequently, the existence of an E0 resonance in medium weight nuclei is unconfirmed. Since an estimate of the isoscalar monopole sum rule strength[136)] yields $\int \sigma dE \sim 11$ mb. MeV for an E0 resonance localised at 16 MeV in ^{60}Ni, it is necessary to consider the electron energy dependence of the (e, α) cross section arising from monopole transitions. An estimate of this has been made using calculated[137), 138)] monopole transition matrix elements and assuming a purely "on-shell" electro-excitation process. This indicates that the monopole cross section will increase more rapidly with electron energy than the dipole (e, α) cross section. A rapid increase with electron energy in the observed alpha emission cross section for low energy alphas ($E_\alpha \sim 8$ MeV) might therefore be indicative of isoscalar monopole excitation. The observed energy spectra at $E_e = 33$ MeV, 60 MeV and 120 MeV evidently agree with the general form of electron energy dependence expected for dipole resonance emission of $\sim$8 MeV alpha particles, and so show no large enhancement of the cross section over the dipole prediction which could be ascribed to monopole excitation. Alpha particle decay from the isoscalar monopole resonance is therefore considered to be unobserved in the present (e, α) data.

The isoscalar electric quadrupole resonance has been identified in a range of medium weight nuclei at about 16 MeV excitation energy[139)]. Therefore, it is likely that the observed alpha energy spectra comprise some fraction of alpha decays from the GQR. An estimate of the upper limit of GDR sum rule strength exhausted by the alpha particle channel in ^{60}Ni can be obtained by assuming that all the observed low

energy alphas arise from decay of a GQR localised at E_x = 16 MeV. In this extreme case approximately 75% of the E2 sum rule strength is exhausted. A statistical calculation of the alpha particle branching ratio for decay of a 2^+ state E_x = 16 MeV in ^{60}Ni indicates an $\sim$ 3% total alpha branch. Thus, a GQR exhausting 100% of its sum rule and decaying statistically would only be expected to contribute $\sim$ 4% of the observed cross section. Evidence for a substantially greater contribution of GQR alpha decays would indicate either a severe violation of the GQR sum rule estimate or highly non-statistical alpha decay. Although both these possibilities seem unlikely, and the present assumption of essentially 100% statistical GDR decay appears valid, the extent of the GQR contribution is considered in more detail in Section 4.4 in order to obtain an unambiguous conclusion about its decay properties.

4.2.6.2 The Heavy Nucleus, ^{197}Au

The statistical model calculation for 120 MeV electrons on ^{197}Au is compared with the experimental data in Fig. 4.9. In this case the (e, α) cross section arises almost entirely from the decay of states above the giant resonance region, and the statistical component from the giant resonance region is a negligible part of the total (e, α) cross section for 120 MeV electrons. This conclusion is in accord with that of Meneghetti and Vitale[26] who obtained a ^{197}Au(γ, α) cross section for 35 MeV maximum bremsstrahlung energy, which peaked at $E_\alpha \sim$ 23 MeV, and calculated an evaporation spectrum which peaked at $E_\alpha \simeq$ 17 MeV with a yield over two orders of magnitude below the experimental yield. Both these conclusions are at variance with Murphy et al.[38] who fitted their ^{197}Au(e, α) data using an evaporation

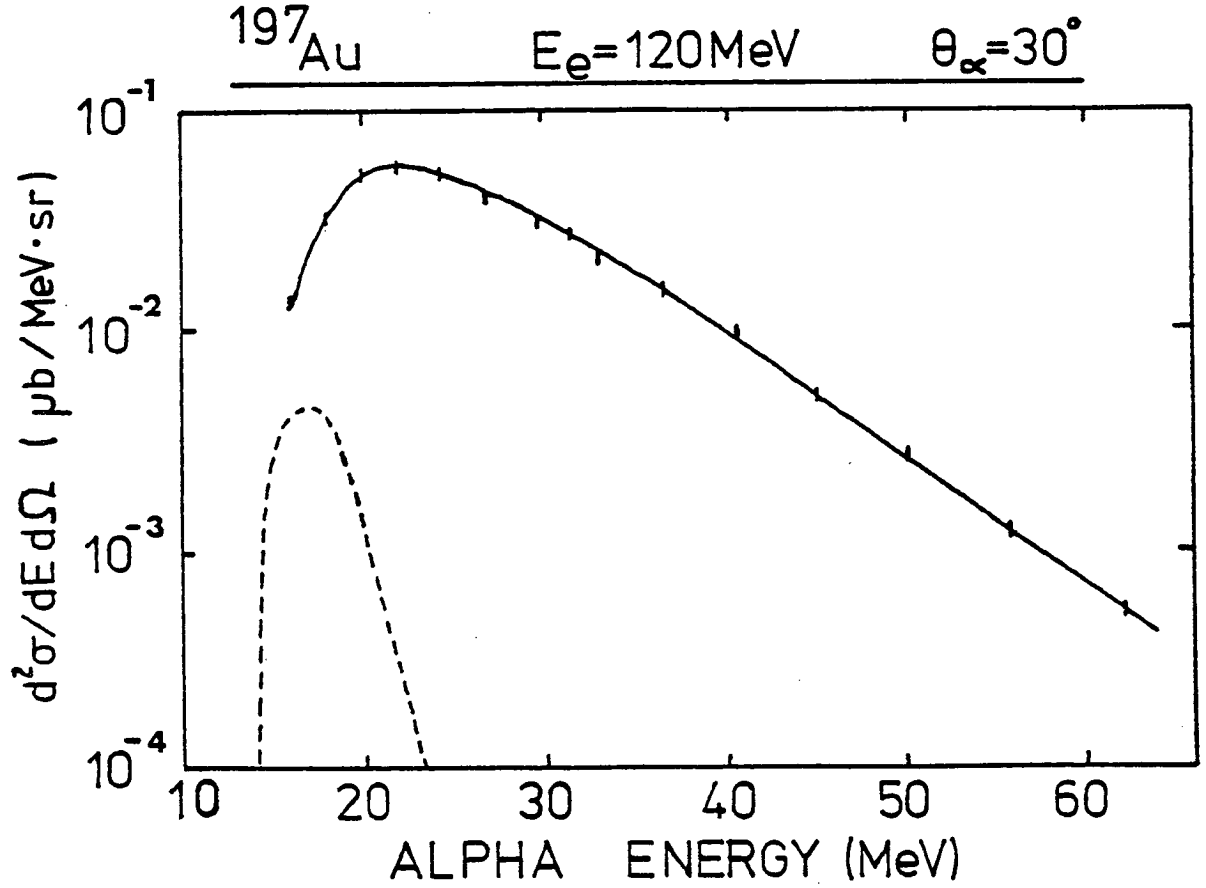

Figure 4.9 Alpha particle energy spectrum for ^{197}Au at θ_α = 30° for E_e = 120 MeV. Errors shown are absolute. The data are represented by the solid line. The dashed line is the result of a statistical model calculation.

spectrum shape with free temperature and Coulomb barrier parameters and concluded that the (e, α) process for E_e = 100 MeV is purely evaporative. This could only be reconciled with the other conclusions if alpha decays from levels above the giant resonance region were primarily statistical in nature with a higher peak energy than the GDR decay alphas. However, the forward peaked angular distributions presented in Fig. 3.16 are more indicative of a direct or pre-equilibrium process at high excitation energies. Such alpha decay mechanisms at excitation energies above the resonance region are considered in Chapter 5.

4.2.7 Conclusions from Hauser-Feshbach Calculations of Alpha Energy Spectra

The comparison of Hauser-Feshbach statistical model calculations with (e, α) data for ^{56}Fe, ^{60}Ni and ^{197}Au has shown:

a) Medium Weight Nuclei, A ∿ 60.

(i) The observed (e, α) energy spectra are well reproduced by assuming statistical decay of the GDR with full isospin mixing.

(ii) High energy, $E_\alpha \gtrsim 12$ MeV, alpha emission occurs from states above the giant resonance region.

(iii) The total (e, α) cross section for $E_e \lesssim 120$ MeV is dominated by alpha decay from the giant dipole resonance.

b) Heavy Nuclei, A ∿ 200.

(i) The Coulomb barrier inhibits alpha decay from the giant dipole resonance.

(ii) The total (e, α) cross section for 35 MeV $\lesssim E_e \lesssim$ 120 MeV is dominated by alpha decay from states excited to energies above the giant resonance region.

Two important questions are raised by the discussion in this section:

a) What is the magnitude of the GQR alpha decay channel?

b) What is the reaction process leading to the observed high energy alpha particles?

The first question is dealt with in Section 4.4 of this chapter, and the second is the subject of Chapter 5.

4.3 Low Energy Alpha Particle Angular Distributions

The angular distribution for alpha particles of energy $E_\alpha \sim 8.2$ MeV from ^{60}Ni, in the peak of the energy spectrum, are symmetric about 90° for E_e = 33, 60 and 120 MeV (Figs. 3.9 - 3.11), as expected for particle emission proceeding through compound nucleus states. The distributions for ^{56}Fe (Figs. 3.7, 3.8) are similar, though possibly indicate a small forward peaked component. These angular distributions all exhibit a maximum in the region of $\theta_\alpha = 90^\circ$, and thus when fitted with Legendre polynomials of up to fourth order, yield a non zero (negative) coefficient for the second order polynomial. In this section an attempt is made to understand these features by extending the Hauser-Feshbach calculations to include angular correlations and thus make deductions about the multipolarity of the giant resonance states excited. The symmetry of the low energy alpha particle angular distributions indicates an absence of interference terms. Consequently all interference terms are omitted in the development of the formalism.

4.3.1 Statistical Model Angular Distributions - Interference Terms Omitted.

The general theory of statistical model angular distributions is included in the original work of Hauser and Feshbach[140]. Expressing the double differential cross section from that work in terms of the Z coefficients introduced by Blatt and Biedenharn[141] (defined and discussed in Appendix 8) gives,

$$\frac{d^2\bar{\sigma}_{cc'}}{dE_\alpha d\Omega} = \frac{1}{4k_c^2,} \cdot \sum_L \sum_{s\ell} T_\ell(c) \sum_{s'\ell'} \left\{ \frac{T_{\ell'}(c')}{\sum_{s''\ell''} T_{\ell''}(c'')} \right\}$$

$$\times \; Z(\ell J \ell J; sL) Z(\ell' J \ell' J; s'L)$$

$$\times \; i^{-L} \cdot (-1)^{s-s'} \cdot P_L(\cos\theta) \qquad (4.9)$$

The notation is that of expression (4.1) with $P_L(\cos\theta)$ the L^{th} order Legendre polynomial. This expression must be modified for the case of photon induced reactions since the Z coefficients are calculated for all magnetic substates allowed, including $m = 0$. In E1 photoreactions only the substates $m = \pm 1$ are allowed, and for E2 the substates $m = \pm 1$, $m = \pm 2$ are allowed. This is accounted for by amending (4.9) to include the Z_γ coefficients and the phase factors of Morita et al.[142]. Furthermore the presence of only 2 allowed magnetic substates for E1 excitation requires $(2j+1)$ to be replaced by the factor 2. Then, setting $J_c = J_A$,

$$\frac{d^2\bar{\sigma}^{E1}}{dE_\alpha d\Omega} = \frac{1}{8k_c^2,} \cdot \frac{1}{(2J_A+1)} \cdot \{\sum_{s\ell} T_\ell(c)\} \cdot \sum_L \sum_{s'\ell'} \left\{ \frac{T_{\ell'}(c')}{\sum_{s''\ell''} T_{\ell''}(c'')} \right\}$$

$$\cdot \; Z \; Z' \; i^{-L} (-1)^{s'-J_A-1} \; P_L(\cos\theta) \qquad (4.10)$$

To relate the $(e, \alpha|$ cross section to the (γ, n) as in Section 4.2.1 it is noted that

$$\bar{\sigma}^{El}_{\gamma,n} = \frac{\pi}{k_c^{2'}} \cdot \frac{(2J+1)}{2(2J_A+1)} \cdot \left\{ \sum_{s\ell} T_\ell(c) \right\} \frac{\sum_{s'\ell'} T_{\ell'}(n)}{\sum_{s''\ell''} T_{\ell''}(c'')}$$

and hence expression (4.10) reduces to

$$\frac{d^2\bar{\sigma}^{El}}{dE_\alpha d\Omega} = \bar{\sigma}^{El}_{\gamma,n} \cdot \frac{1}{4\pi(2J+1)} \cdot \sum_L \sum_{s'\ell'} \frac{T_{\ell'}(\alpha)}{\sum_{s''\ell''} T_{\ell''}(n)} \cdot C_{tL} \cdot P_L(\cos\theta) \qquad (4.11)$$

Here the single primed outgoing channel parameters refer to the alpha particle channel, and the double primed parameters refer only to the neutron channel. The C_{tL} are related to the Z coefficients and are defined and tabulated for the cases of interest in this thesis, in Appendix 8. Expression (4.11) can be generalised to other multipoles by applying the appropriate multipole components of the total photoneutron cross section and calculating the transmission coefficients and angular correlation coefficients for the corresponding compound nucleus spins and parities.

The ratio of transmission coefficients in (4.11) is identical to that used for calculating energy spectra, thus the extension of the statistical model calculations from energy spectra with assumed angular isotropy to those in which angular correlations are included reduce to the inclusion of the C_{tL} coefficients from Appendix 8. Expression (4.11) can be checked for consistency with the earlier result for isotropy by noting that $C_{t0} = (2J+1)$ (see Appendix 8) and using expression (4.3) for $d\bar{\sigma}_{\gamma,\alpha}/dE_\alpha$. An isotropic angular distribution (i.e. $C_{tL} = 0$; $L > 0$) leads to the expected trivial relation,

$$\frac{d\bar{\sigma}^{J^\pi}}{dE_\alpha d\Omega} = \frac{1}{4\pi} \cdot \frac{d\bar{\sigma}^{J^\pi}_{\gamma,\alpha}}{dE_\alpha} \quad .$$

At a given compound nucleus excitation energy, the terms in (4.11) which define the form of an alpha particle angular distribution are,

$$\sum_L \sum_{s'\ell'} T_{\ell'}(\alpha)\, C_{tL}\, P_L(\cos\theta) \quad .$$

These are obtained by summing the products of the alpha particle transmission coefficients, $T_{\ell'}(\alpha)$, and angular distribution coefficients, C_{tL}, over all allowed decay channels. Ideally the angular distributions should be calculated using levels in the residual nuclei of known spin and parity. However, the lack of such information restricts these ideal calculations to low excitation energies (e.g. $E_x \lesssim 18$ MeV in ^{60}Ni).

The form of alpha particle angular distributions is calculated for decay of $J^\pi = 1^-$, 2^+ and 1^+ compound nucleus states (corresponding to E1, E2 and M1 multipole excitation respectively) at 16 MeV in ^{60}Ni, and presented in Fig. 4.10. These distributions are obtained by summing all alpha decays to the first four excited states in ^{56}Fe. The relative intensity of the alpha decay channels assuming the same compound nucleus formation probability for $J^\pi = 1^-$, 2^+ and 1^+ can be compared in Fig. 4.10. The distributions illustrated are qualitatively identical to all (γ, α) angular distributions expected for 0^+ ground state nuclei decaying to residual nucleus ground states or excited states with $J^\pi_R = 0^+, 2^+, 4^+$ ... etc. Comparison of Fig. 4.10 with the observed angular distributions shows that for the three cases considered, only E1 excitation yields angular distributions qualitatively similar to those observed for $E_\alpha \sim 8$ MeV.

The (e, α) angular distributions are given by,

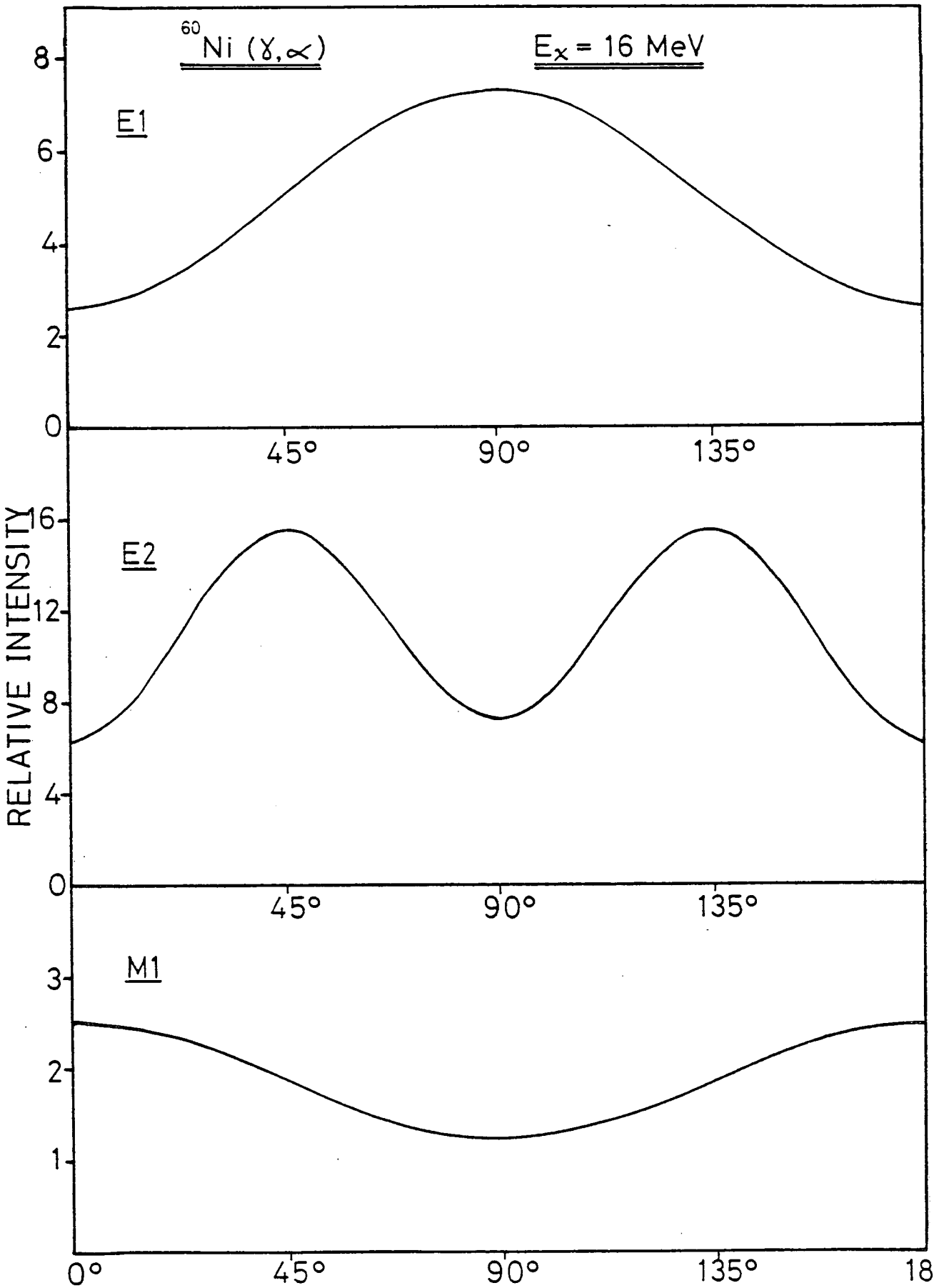

Figure 4.10. ^{60}Ni alpha particle angular distributions calculated for decays of 1^- (top), 2^+ (centre) and 1^+ (bottom) levels at 16 MeV excitation energy.

$$\frac{d^2\sigma^{J^\pi}(e,\alpha)}{dE_\alpha d\Omega} = \int_{Thr}^{E_e} \frac{N^{P\lambda}}{E_\gamma}(E_\gamma, E_e) \cdot \frac{d^2\sigma^{J^\pi}(E_\gamma)dE_\gamma}{dE_\alpha d\Omega} \qquad (4.12)$$

for virtual photons of type P and multipolarity λ exciting compound nucleus states of spin and parity J^π. Since the calculation requires consideration of residual nucleus levels with unknown spins and parities, spin dependent level density formulae must be used. It is assumed that odd and even spins of both parities are present with the probability given by these formulae (see Appendix 7). This is a reasonable assumption at high excitation energies; however, it may not be valid over the first few MeV for which level density formulae are applied. Since the assumed spin and parity distributions lead to a near isotropic angular distribution, whereas the presence of purely even spin positive parity residual nucleus levels leads to angular distributions as illustrated in Fig. 4.10, it is evident that at the excitation energy at which the calculations change from use of discrete known levels to level density formulae (i.e. at $E_x = U$), there will be a change from anisotropic to nearly isotropic calculated angular distributions. Angular distributions calculated using level density formulae are not completely isotropic since, for example, decays from $J^\pi = 2^+$ states to $J_R^{\pi_R} = 0^+$, 1^+ or 1^- levels, and decays from $J^\pi = 1^-$ states to $J_R^{\pi_R} = 0^+$ levels, all produce strong angular anisotropies. Furthermore, decays to a level of given J_R in the residual nucleus, with both parities assumed equally probable still yields $\sum_\ell T_\ell C_{tL} \neq 0$, summing over all the partial waves allowed for the transition $J^\pi \rightarrow J_R^{\pi_R}$. The C_{tL} coefficients themselves sum over the allowed orbital angular momenta to yield $\sum_\ell C_{tL} = 0$ (for $L > 0$, excluding the case of $J^\pi = 2^+$ or 1^-, for the examples quoted above), however the differing T_ℓ combine to yield non zero coefficients for the even order Legendre polynomials. It is

therefore important that any quantitative calculation of angular distributions includes correctly evaluated transmission coefficients rather than, for example, use of the sharp cut-off approximation (i.e. $T_\ell = 1.0, \quad \ell \leq \ell_c; \quad T_\ell = 0.0, \quad \ell > \ell_c, \quad \ell_c$ = cut-off partial wave orbital angular momentum). Most of the contribution to the anisotropy arises from alpha decay to the lower lying residual nucleus levels and therefore those $\sim$ 8 MeV alpha particles which result from decay of ^{60}Ni excited states at $E_x \sim 16 - 17$ MeV provide a good indication of the general form of the angular distribution expected.

The expected alpha angular distribution arising from 1^- compound nucleus levels is calculated using expression (4.12). At $E_e = 33$ MeV the ratio of the zeroth and second order Legendre polynomial coefficients has an experimental value of -0.17 ± 0.02. This compares well with the calculated value of -0.14. As expected, the predicted distribution is slightly more isotropic than observed, indicating the need to include better residual nucleus level information than the six discrete levels used in the present calculation. The inclusion of decays from 2^+ or 1^+ compound nucleus states would not improve the agreement since these would yield a more positive A_2/A_o ratio. The form of the low energy ($E_\alpha \sim 8$ MeV) angular distributions indicates dominant dipole resonance decay rather than magnetic dipole or GQR decay. Thus, further evidence is provided that GDR excitation is the dominant mechanism leading to the observed low energy alpha emission.

4.3.2 Alpha Energy Dependence of (e,α) Angular Distributions

The ^{56}Fe(e,α) and ^{60}Ni(e,α) angular distributions at $E_\alpha = 8.2$, 11.5 and 15.7 MeV, for incident electron energies $E_e = 60$ and 120 MeV, illustrated in Figs. 3.7, 3.8, 3.10 and 3.11, are fitted with Legendre

polynomials of up to fourth degree to allow comparison of these coefficients with those expected for statistical compound nucleus decay. The angular distributions are parameterised by the coefficients A_L and Q_L,

$$\frac{d^2\sigma}{dE_\alpha d\Omega} = \sum_{L=0}^{4} A_L \, Q_L \, P_L(\cos\theta) \quad ,$$

where the Q_L are angular distribution attenuation coefficients[143] which account for the smearing effect on the angular distribution by the finite spectrometer solid angle. Here, the Q_L are negligible,

$$1.0 - Q_L < 0.01, \qquad L = 1 - 4.$$

In all cases A_3/A_o and A_4/A_o were small ($\lesssim 0.1$), and in general were zero to within the experimental uncertainties. The ratios A_1/A_o and A_2/A_o yield the dominant terms and are illustrated in Figs. 4.11 and 4.12. These parameters further illustrate the increasing angular asymmetry observed with increasing particle energy at both E_e = 60 and 120 MeV. The A_1/A_o coefficient increases from zero, and A_2/A_o increases from a negative value to near zero.

The behaviour of the A_2/A_o term is understood by extending the considerations in Section 4.3.1 to higher energy alpha particles. The higher channel energies lead to larger transmission coefficients for a given orbital angular momentum and so higher angular momentum partial waves must be considered (see Fig. 4.13). Consequently, the probability of alpha decay to high spin residual nucleus states increases relative to decays to the low spin states J_R = 0, 1 which yield the angular anisotropy in the statistical calculation. Alpha particles of increased energy therefore arise from an increased number of channels which yield isotropic angular distributions on the assumption of non-interference

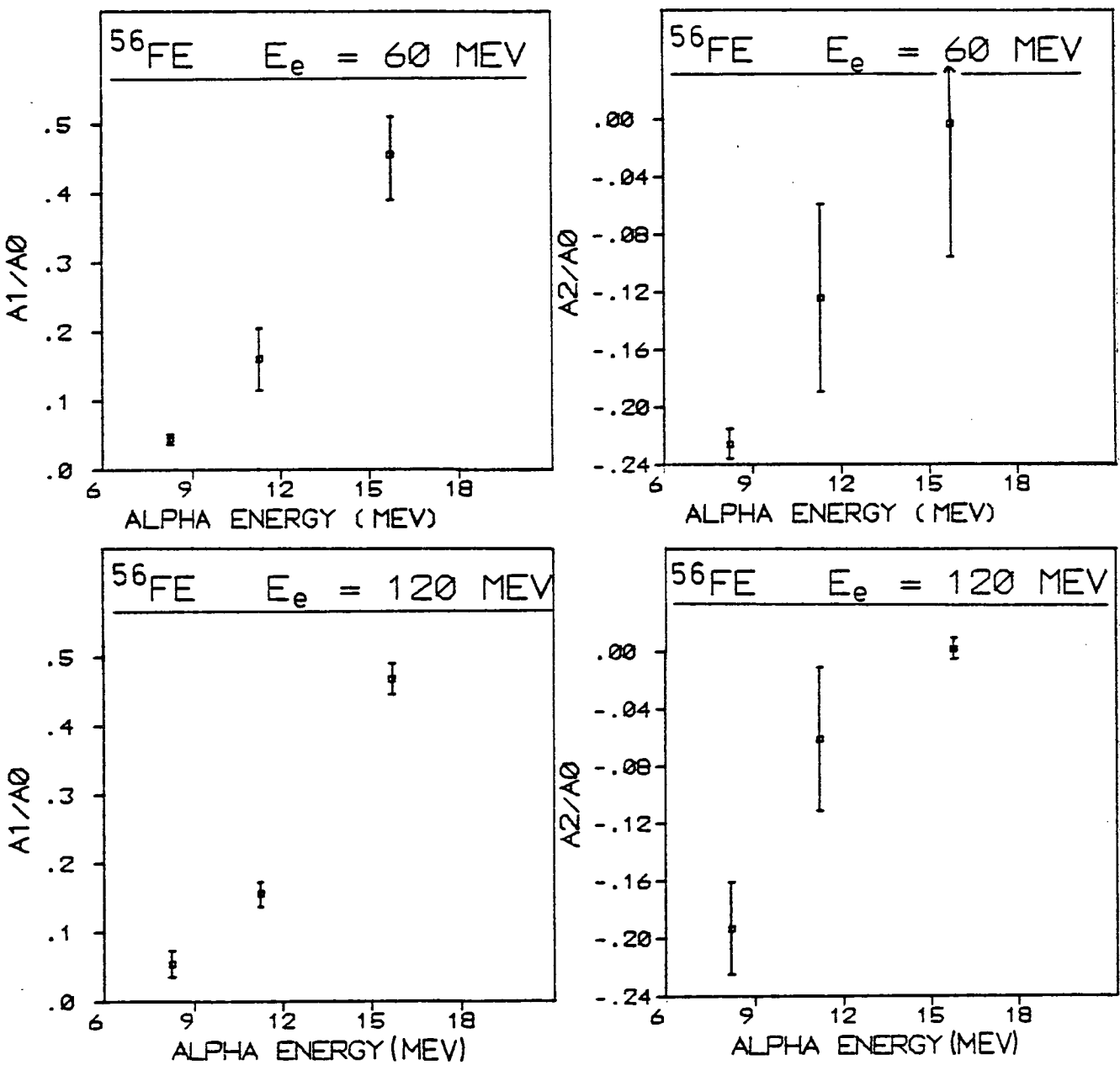

Figure 4.11 Legendre polynomial coefficients for ^{56}Fe alpha angular distributions at 60 MeV and 120 MeV incident electron energies.

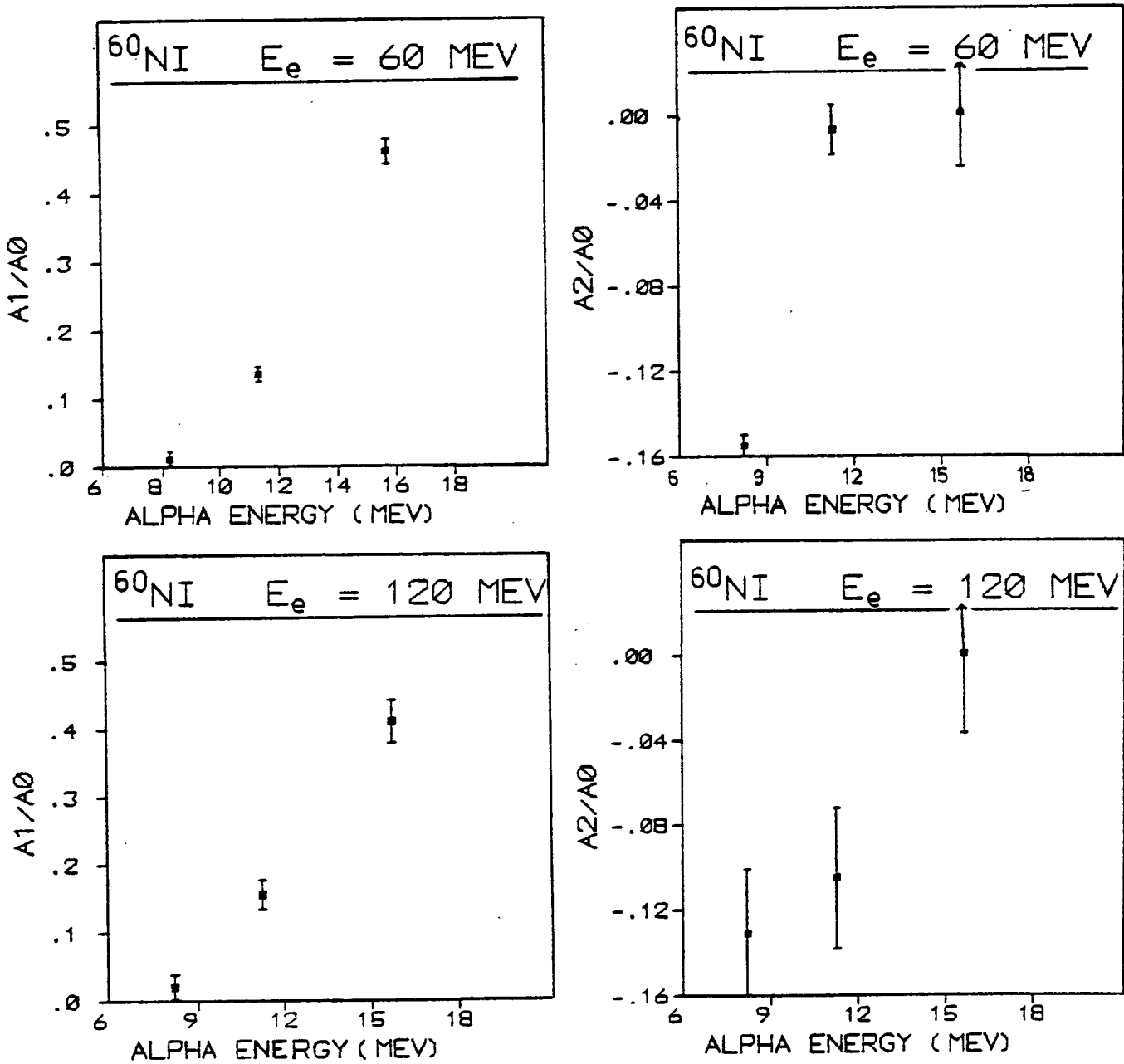

Figure 4.12 Legendre polynomial coefficients for ^{60}Ni alpha angular distributions at 60 MeV and 120 MeV incident electron energies.

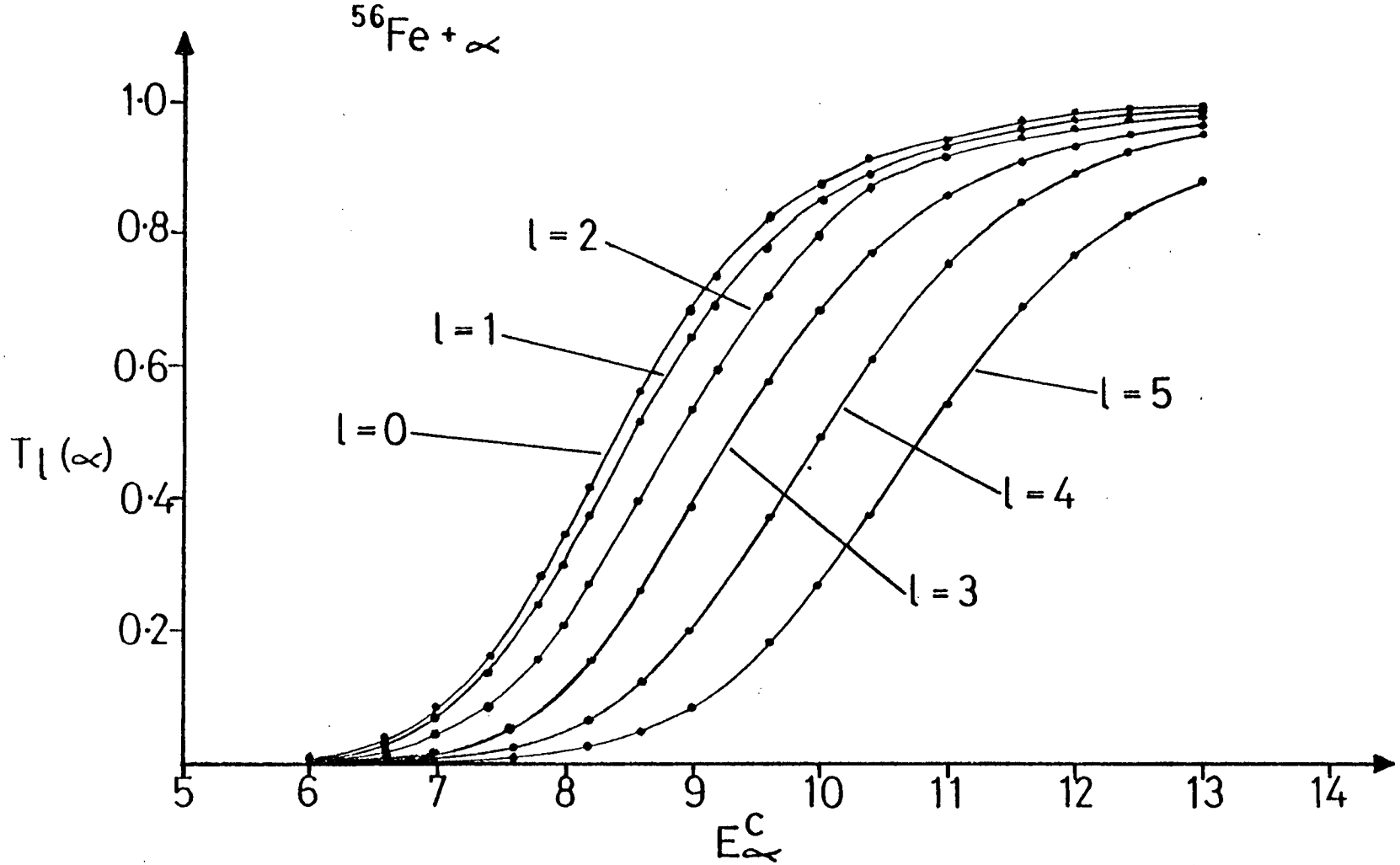

Figure 4.13. Transmission coefficient alpha particle channel energy dependence for partial waves $\ell = 0 \rightarrow 5$ in ^{60}Ni alpha decay.

compound nucleus decay. However, the A_1/A_o ratio dominates the angular distribution at high alpha energies. This can arise from either,

a) Interference between different outgoing alpha particle channels

or,

b) Direct, or few step, alpha particle knock-out.

Interference terms may arise from E1-E2 interference, or interference between different partial waves of the same channel spin. Interference between 1^- and 2^+ states evidently does not occur in the isoscalar GQR region. Alphas of energy, $E_\alpha \sim 8$ MeV, which arise principally from this region, exhibit no interference effects despite the possibility of large interference terms being produced by even a small quadrupole resonance in the presence of the dominant dipole resonance. It is likely that any 1^- or 2^+ states in this region will be strongly overlapping and the average of any interference terms is expected to be close to zero[144]. This conclusion is consistent with $^{56}Fe(\alpha,\gamma_o)^{60}Ni$[126] data which showed essentially zero interference terms over excitation energies $E_x = 15 - 20$ MeV. Similar results should be expected for the broader isovector E2 resonance, likely to be centred around $E_x \sim 33$ MeV, though in this case the E2 strength is relatively greater compared to E1 strength.

The interference terms which arise due to differing partial waves from the same compound nucleus state yield only symmetric (though possibly anisotropic) angular distributions. Only interference between compound nucleus states of differing J^π can yield angular asymmetries in statistical particle decays. The experimental evidence at low alpha particle energies ($E_\alpha \sim 8$ MeV) suggests that such interference is not present. Ideally, a full theoretical treatment of partial wave interference terms should be carried out. However, at the excitation energies

encountered here detailed calculations of interference phase factors, using channel wave functions and reaction matrices, are unrealistic.

The present evidence suggests that compound nucleus states should continue to emit alpha particles with symmetric (though anisotropic) angular distributions, at increasing alpha particle energies, and correspondingly increasing excitation energies. It is questionable, however, whether the excitation mechanisms at these energies lead to a fully equilibrated nucleus prior to alpha emission. The observed forward peaked angular distributions most probably arise from an intranuclear cascade, or few step process, initiated by high energy nucleons from (γ,N) processes (such nucleons themselves being forward peaked). The forward peaked angular distributions are therefore considered to be indicative of the onset of a dominant pre-equilibrium (pre-compound) emission process. Such processes are considered in more detail in Chapter 5.

4.4 Alpha Decay of the Isoscalar GQR

4.4.1 The (e,α) Reaction as a Tool for GQR Studies

The differing response of a GQR to real photon and electron induced excitation leads to the use of the (e,α) reaction as a tool for GQR alpha decay study. The photon-nucleus and electron-nucleus reactions are contrasted in detail in Section 1.3.1. The real photon interaction may be considered as a sum of multipole terms; the strength associated with each term can be inferred from sum rule estimates. These estimates of strength decrease rapidly with increasing multipolarity (see Section 1.4.2) and so real photons only produce observable excitation of the first few multipole resonances. The ratios of the sum rule estimates for isovector E1, and isoscalar E2 and E3 strengths localised at their

expected centroid energies for ^{60}Ni are $1:1.3 \times 10^{-2} : 3.7 \times 10^{-6}$ respectively (Table 1.2). Consequently, real photon absorption proceeds predominantly by dipole excitation.

The electrodisintegration cross sections can also be considered as a sum of multipolarities in the virtual photon spectra, but the strengths of the multipole components will be different. Calculations of virtual photon spectra[66] yield increasing virtual photon intensities with increasing multipolarity. At 16 MeV photon energy (corresponding to the centroid energy for excitation of the ^{60}Ni GQR) the ratio N^{E2}/N^{E1} increases with electron energy to exceed a factor of 10 at 100 MeV electron energy (Fig. 4.14*). Thus the magnitude of GQR excitation relative to GDR excitation increases with electron energy and the (e,α) reaction will result in enhanced yields of alphas from the GQR relative to the GDR decays, at higher electron energies. Alpha decay from a GQR is therefore indicated by a marked departure from the form of (e,α) cross section electron energy dependence predicted for statistical giant dipole resonance decay. To obtain an estimate of the magnitude of the alpha decay from the isoscalar GQR its strength is assumed to be concentrated in a narrow resonance at E_x = 16 MeV,

---

* Here the E2 virtual photon spectra are calculated using a method requiring the summation of large numbers of partial waves in two converging sequences[66]. Over certain kinematic regions the convergence of these sequences is very slow and the calculation is terminated with the convergent sequences still separated by a value outwith the required accuracy. Fig. 4.12 shows this occurrence at E_e = 40 - 55 MeV. A polynomial is fitted through the calculated points to avoid the necessity of unrealistically long computations for the few slowly convergent points. These difficulties have been removed in a recent reformulation of the virtual photon calculations[69].

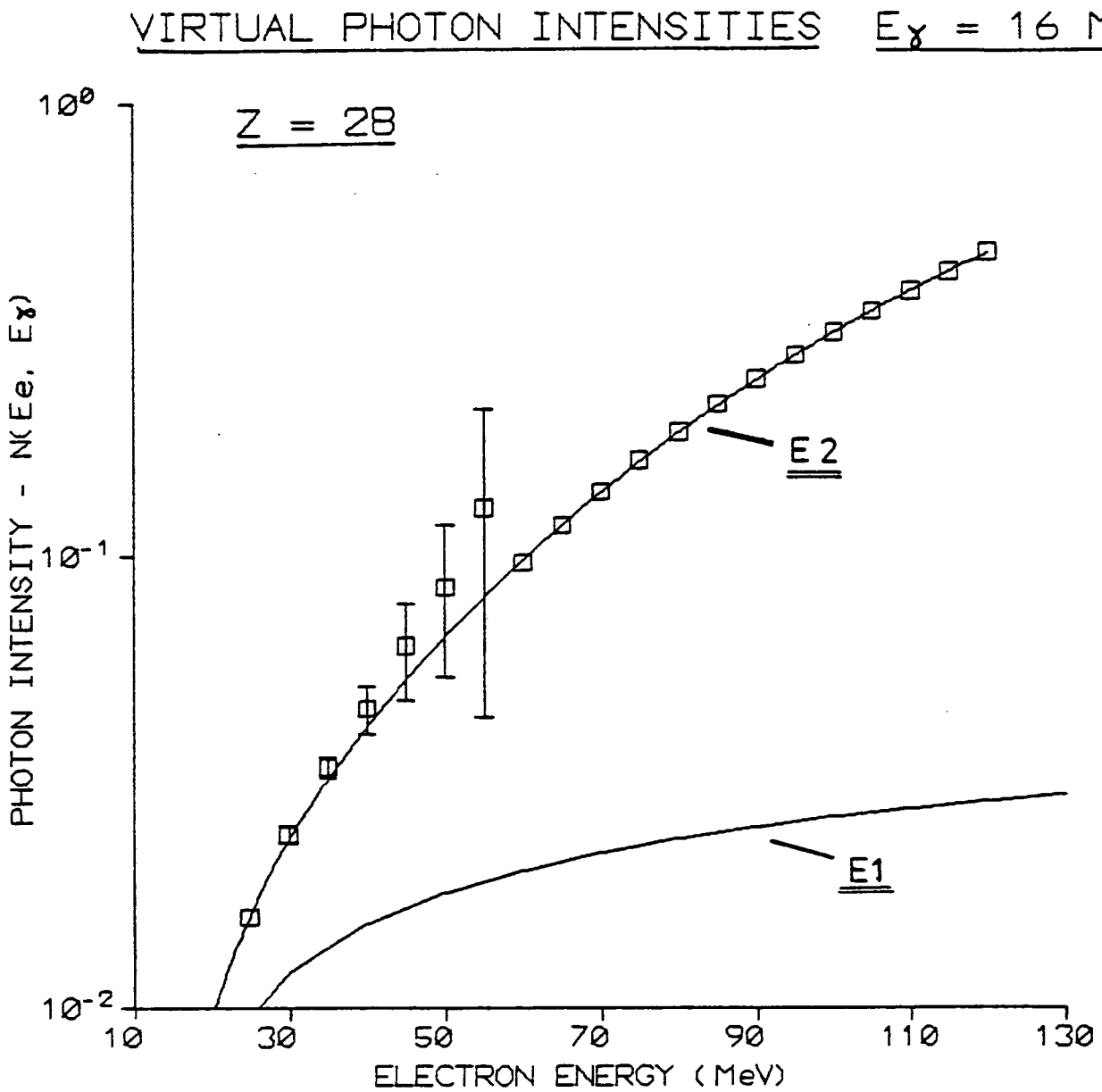

Figure 4.14. Comparison of E2 and E1 virtual photon intensities for Z = 28, at 16 MeV photon energy.

and ^{60}Ni is considered in detail. The assumption of localised GQR strength is consistent with the results of alpha scattering studies[139] which indicate narrow ($\Gamma \sim 4$ MeV) GQRs in medium weight nuclei.

Comparison of the alpha branching from 1^- and 2^+ levels in ^{60}Ni, at $E_x = 16$ MeV (Fig. 4.15) shows that for statistical decay the 2^+ levels will decay predominantly to the first excited state in ^{56}Fe, whereas 1^- levels decay with almost equal probabilities to the ground and first excited states. In both cases $\sim$ 90% of alpha decays from a resonance at $E_x = 16$ MeV will branch between the ground and the first four excited states. Alpha particles from 2^+ states at $E_x = 16$ MeV will predominantly have a laboratory energy of $E_{\alpha_1}^{LAB} \sim 8.2$ MeV (the 50% branch). Thus, the cross section for emission of alphas with this energy from a GQR excited by electrons will exhibit the most marked departure from the electron energy dependence expected for the case of GDR decay. In ^{60}Ni the excitation function for $E_\alpha^{LAB} = 7.7 - 8.7$ MeV (see Fig. 3.13) is therefore a sensitive indicator of the presence of GQR alpha emission.

4.4.2 The ^{60}Ni 8.2 MeV Alpha Decay Excitation Function

The cross section for 8.2 MeV alpha particles decaying statistically from the GDR is calculated using expression (4.4) for electron energies $E_e = 20 - 120$ MeV. The result of this calculation is compared with the experimental data in Fig. 4.16 without any normalisation. The result is presented as a broad band to indicate the inherent uncertainty resulting from the numerical techniques employed in the calculation. Excellent agreement is obtained with the measured absolute cross section, though this may be somewhat fortuitous in view of the expected uncertainties in the absolute magnitude of the statistical

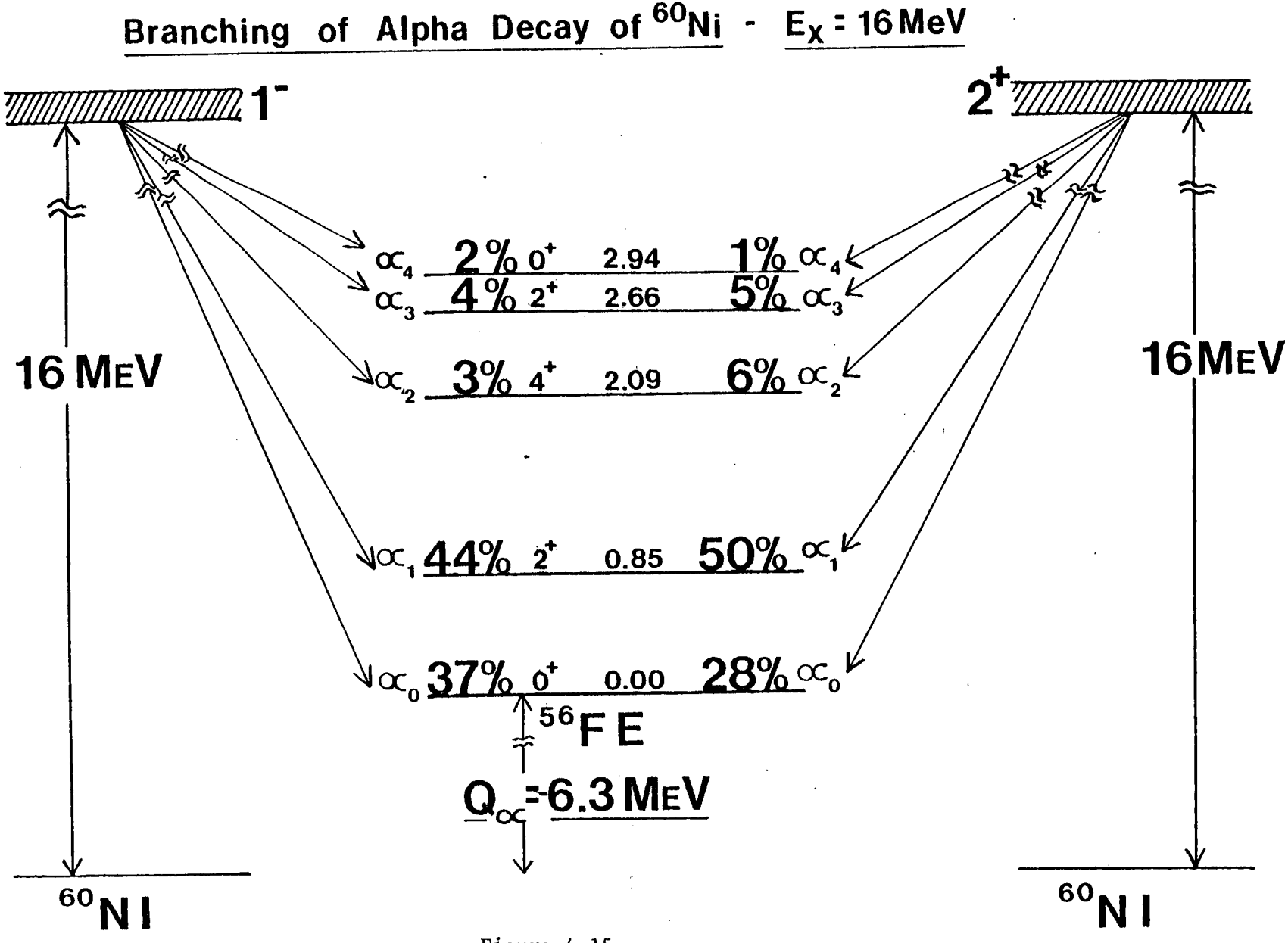
Branching of Alpha Decay of ^{60}Ni - E_X = 16 MeV
1$^-$
2$^+$
16 MeV
16 MeV
α_4 2% 0$^+$ 2.94 1% α_4
α_3 4% 2$^+$ 2.66 5% α_3
α_2 3% 4$^+$ 2.09 6% α_2
α_1 44% 2$^+$ 0.85 50% α_1
α_0 37% 0$^+$ 0.00 28% α_0
^{56}FE
Q_α = -6.3 MeV
^{60}NI
^{60}NI

Figure 4.15

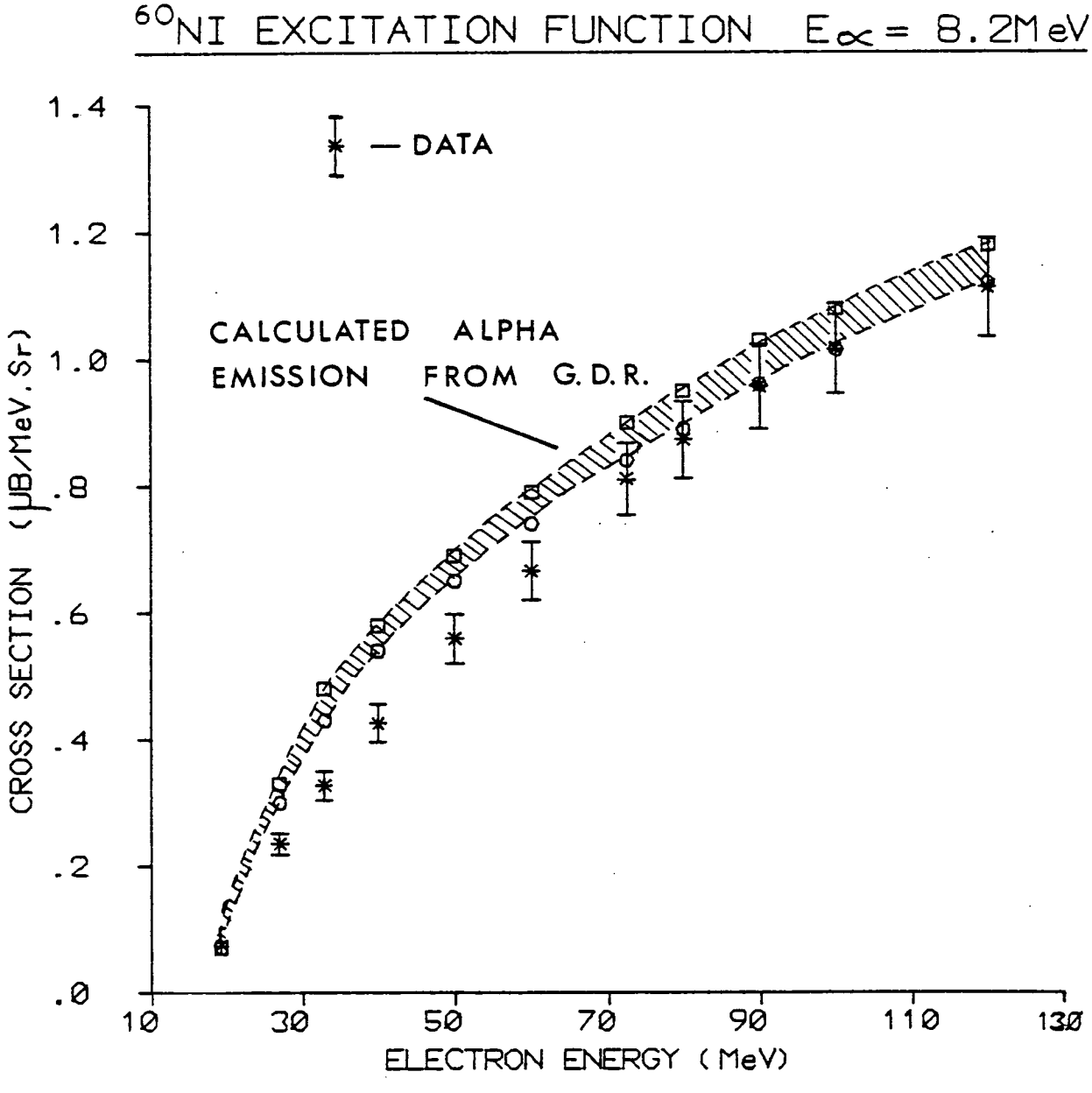
^{60}NI EXCITATION FUNCTION E_α = 8.2MeV
— DATA
CALCULATED ALPHA EMISSION FROM G.D.R.
CROSS SECTION (μB/MeV.Sr)
ELECTRON ENERGY (MeV)
1.4
1.2
1.0
.8
.6
.4
.2
.0
10
30
50
70
90
110
130

Figure 4.16

model cross sections and virtual photon intensities. However, the shape of the excitation function derives from the shapes of $d\sigma_{\gamma,\alpha}(E_\gamma,E_\alpha)$ and $N^{E1}(E_\gamma,E_e)$, which are expected to be reasonably well defined. It is evident that the general form of the (e,α) excitation function is well reproduced on the assumption that alpha decay arises predominantly from the GDR. However, the experimental excitation function does increase slightly more rapidly than that calculated. This can be attributed to:

a) GQR alpha decays.

b) Alphas decaying from states at excitation energies above the resonance region $(E_x > 33$ MeV).

Consideration b) is deferred to Chapter 5. Here, the alpha decay branch from the GQR is calculated assuming that all divergence from the pure GDR decay calculated excitation function is attributed to the GQR decay channel.

The experimental data is fitted with the function,

$$d\sigma_{e,\alpha}^{E1+E2}(E_e,E_\alpha) = C \cdot d\sigma_{e,\alpha}^{E1}(E_e,E_\alpha) + \frac{N^{E2}(E_e,16)}{16} \cdot d\sigma_{\gamma,\alpha}^{E2}(E_\alpha) \qquad (4.13)$$

where $d\sigma_{e,\alpha}^{E1+E2}$ is the summed differential electro-alpha cross section arising from both GQR and GDR alpha decay, and $d\sigma_{e,\alpha}^{E1}$ is the calculated GDR decay component. The treatment of the GQR assumes the strength to be localised at $E_x = 16$ MeV. The parameter C is a normalisation factor which allows the E2 strength to be determined by a fit of the calculated excitation functions to the shape of the measured excitation function. The N^{E2} are E2 virtual photon intensities (Fig. 4.14) calculated in D.W.B.A. These must be used cautiously, in accord with

the conclusions of Section 1.3.2, and it must be recognised that they may be seriously in error, particularly N^{E2} for $E_e \gtrsim 50$ MeV. The analysis and conclusions below are based on the currently best available virtual photon theory and therefore comprise a best estimate of GQR decay using the (e, α) reaction given the available experimental and theoretical techniques.

The best fit of expression (4.13) to the measured excitation function is shown in Fig. 4.17. This yielded a normalisation factor, $C = 0.78$, and $d\sigma^{E2}_{\gamma,\alpha}(E_\alpha = 8.2\ \text{MeV}) = 14.8\ \mu\text{b/MeV.sr}$. The total GQR alpha decay cross section can now be calculated by applying:

i) The assumption of angular isotropy for the GQR alpha emission (since the excitation function is for $\theta_\alpha = 45^\circ$, and the angular distributions have been shown to be symmetric, a detailed consideration of angular effects gives less than 10% increase in the results obtained here).

ii) A calculated alpha branch of 50% (Fig. 4.15) for $E_\alpha = 8.2 \pm 0.5$ MeV.

The total cross section for GQR alpha decay is then $\sigma^{E2}_{\gamma,\alpha} = 370\ \mu\text{b}$, i.e. 3.5% E2 sum rule strength. This figure compares very favourably with the 3.0% sum rule strength obtained in a calculation of statistical decay of a 2^+ state at $E_x \sim 16$ MeV which exhausts the E2 sum rule over all decay channels.

Allowance for the GQR width can be made by considering the form of the observed alpha energy spectra. The calculation above uses an alpha branch for the observed part of the alpha energy spectrum which yields,

$$\sigma^{E2}_{\gamma,\alpha} \sim 2\int_{7.7}^{8.7} \frac{d\sigma^{E2}_{\gamma,\alpha}}{dE_\gamma}\, dE_\alpha$$

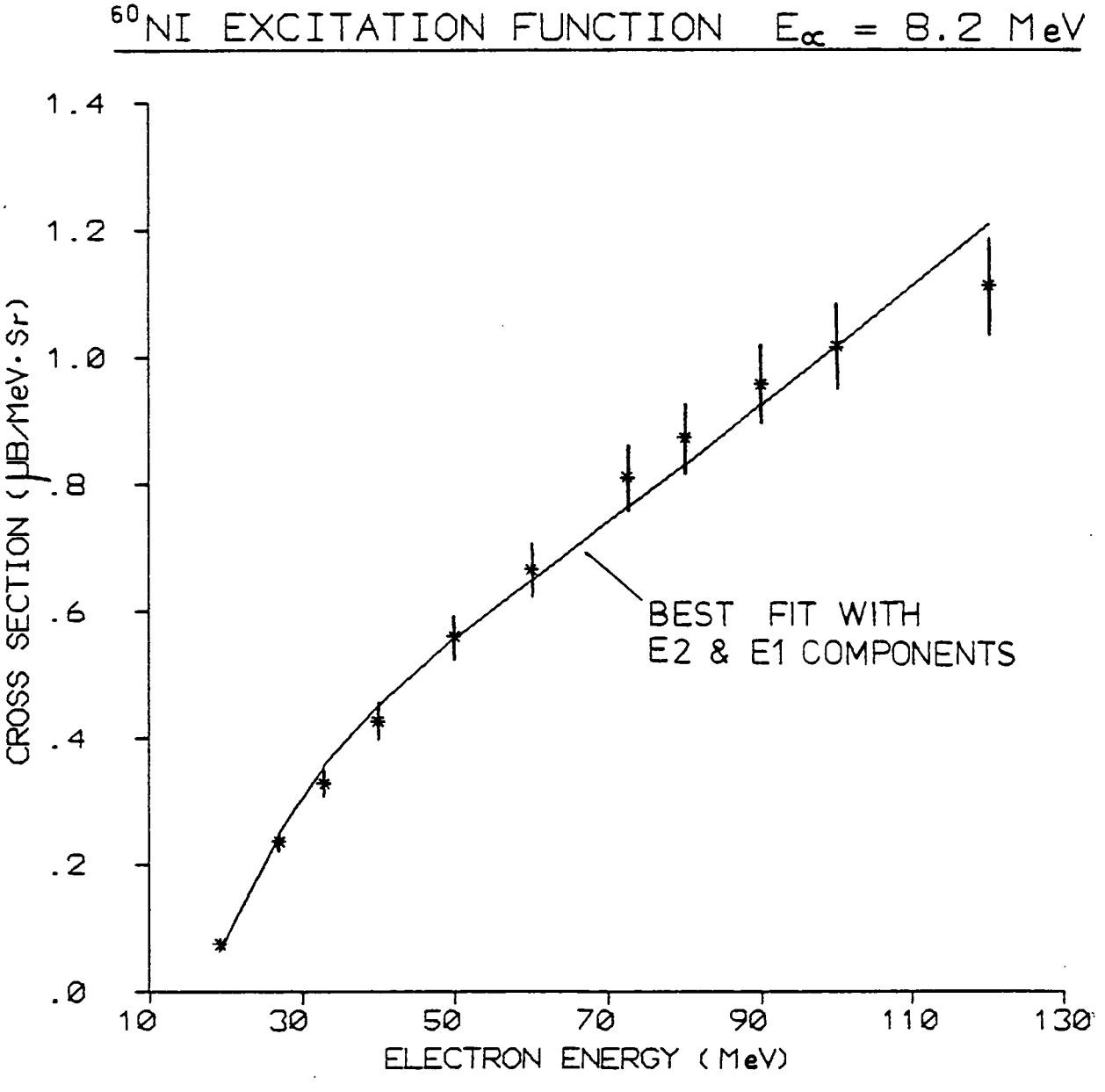
^{60}NI EXCITATION FUNCTION E_α = 8.2 MeV
CROSS SECTION (μB/MeV·Sr)
1.4
1.2
1.0
.8
.6
.4
.2
.0
10
30
50
70
90
110
130
ELECTRON ENERGY (MeV)
BEST FIT WITH
E2 & E1 COMPONENTS

Figure 4.17

whereas the observed spectra indicate,

$$\sigma_{\gamma,\alpha} \sim 3 \int_{7.7}^{8.7} \frac{d\sigma_{\gamma,\alpha}}{dE_\gamma} \, dE_\alpha \quad ,$$

i.e. a lower fraction of observed alphas actually appear in the energy interval E_α = 7.7 - 8.7 MeV, than expected for GQR alpha decay from a level at 16 MeV. The neglect of a finite GQR width may therefore lead to an overestimate of the fraction of GQR alpha decays observed in the E_α = 7.7 - 8.7 MeV energy range included in the excitation function data. To account for this an upper limit is assigned equal to twice the strength quoted above, i.e. $\sigma^{E2}_{\gamma,\alpha} \sim$ 750 μb, or 7% E2 sum rule. At E_e = 33 MeV this figure implies that only ∿ 7.5% of the observed alphas at $E_\alpha \sim 8$ MeV arise from the GQR.

4.4.3 Comparison with other Nickel GQR Alpha Decay Studies

During the course of this thesis work several independent studies of GQR alpha decay have been undertaken. Two independent (α, α' α") coincidence experiments have given ≤ 16% [145], and ∿ 6% [146] of E2 sum rule exhausted by alpha decay of the ^{58}Ni GQR, and Ref. 145 additionally gives $\lesssim$ 7.5% E2 sum rule for the GQR alpha decay channel in ^{62}Ni. All these results were considered consistent with statistical decay of the GQR. No (α, α' α") experiments have been carried out for ^{60}Ni. However the general systematics of the alpha scattering results indicates good agreement with the results and conclusions presented here for ^{60}Ni.

In contrast, an (e,α) and (γ, α) study of the nickel isotopes by a group at N.B.S., Washington[41], has yielded the conflicting results of 56%, 52% and 28% E2 sum rule exhausted by alpha decay from the GQRs in ^{58}Ni, ^{60}Ni and ^{62}Ni, respectively. Taking account of the experimentally

determined total strengths of the ^{58}Ni and ^{60}Ni GQRs (55% and 63% respectively[139]) shows that these results indicate almost a 100% alpha branch from the GQR, i.e. highly non-statistical GQR decay. This conflicting result is derived from (e,α) data in excellent agreement with that presented here (see Figs. 3.17, 3.19) and hence a fundamental disagreement with the N.B.S. analysis technique is evident.

The N.B.S. analysis technique differs from the present analysis in the form of the GDR photoalpha cross section, $\sigma^{E1}_{\gamma,\alpha}(E_\gamma)$, employed in calculating $d\sigma^{E1}_{e,\alpha}(E_e, E_\alpha)$. A Lorentz shape is assumed, with differing upper and lower widths, Γ_1, Γ_2, to account for Coulomb barrier effects on the lower edge of the resonance, i.e.

$$\sigma_{\gamma,\alpha}(E\gamma) = \frac{\sigma_m(\Gamma_i E_\gamma)^2}{(E_\gamma^2 - E_m^2)^2 + (\Gamma_i E_\gamma)^2} \qquad \begin{array}{l} i = 1, \quad E_\gamma < E_m \\ i = 2, \quad E_\gamma > E_m \\ \Gamma_1 < \Gamma_2 \end{array}$$

for a resonance centred at excitation energy E_m, with peak cross section σ_m. This resonance form is also assumed for the GQR and thus between the two resonances a total of eight free parameters must be fitted to excitation function data to derive the relative E1 and E2 strengths. As a check on their fit the N.B.S. group obtains real photon induced excitation function data using bremsstrahlung. If the (γ, α) cross section is correctly decomposed into the components $\sigma^{E1}_{\gamma,\alpha}(E\gamma)$ and $\sigma^{E2}_{\gamma,\alpha}(E_\gamma)$ then the bremsstrahlung yields are given by,

$$Y_{\gamma,\alpha}(E_e) = \int_0^{E_e} [\sigma^{E1}_{\gamma,\alpha}(E_\gamma) + \sigma^{E2}_{\gamma,\alpha}(E_\gamma)] K(E_\gamma, E_e) E_\gamma^{-1} \, dE_\gamma \qquad (4.14)$$

The N.B.S. group does indeed find such yields to be in good agreement

with their data, thus apparently strengthening their conclusion of large GQR alpha decay branches in the nickel isotopes. However bremsstrahlung yield data acquired at the Kelvin Laboratory indicates that the N.B.S. yield data is in error (see Fig. 4.18). Furthermore, serious doubt is cast on the validity of the assumption that $\sigma_{\gamma,\alpha}(E_\gamma)$ is a Lorentz shape. Whilst giant resonance total photon absorption cross sections are expected to have a Lorentz form, individual decay channels may have substantially different forms dependent on the branching ratio excitation energy dependence for these channels. Indeed, the $^{60}Ni(\gamma,\alpha)$ cross section calculated for the statistical emission of $E_\alpha = 8 \pm 0.5$ MeV alpha particles (see Fig. 4.19) differs considerably from a Lorentz shape. (Above the region where the statistical model calculation can reasonably be applied ($E_x \lesssim 30$ MeV) an assumed shape is employed which is found to be consistent with the observed bremsstrahlung induced alpha particle yields.)

Further (e,α) data obtained using ^{NAT}Ni is compared in Fig. 4.18 with N.B.S. data, by deriving a $^{NAT}Ni(e,\alpha)$ excitation function from N.B.S. $^{60}Ni(e,\alpha)$ and $^{58}Ni(e,\alpha)$ data weighted by isotopic content of ^{NAT}Ni. Again, excellent agreement between the two sets of (e,α) data is obtained. Applying the (γ,α) cross section in Fig. 4.19 in expressions (4.13) and (4.14), assuming no E2 contribution, leads to electron induced and bremsstrahlung induced yields for 8.0 ± 0.5 MeV alphas, σ_8 and Y_8 respectively, illustrated by the solid lines in Fig. 4.18. This gives a poor agreement with the (e,α) data, which can only be rectified by normalising the (e,α) calculation to the data (curve A, Fig. 4.18), or including a contribution of $\sim$ 10% E2 sum rule strength for alpha decay of a GQR centred at $E_x = 16$ MeV (curve B, Fig. 4.18). Since only the latter approach retains the good fit to the bremsstrahlung yield data, in a consistent

Figure 4.18.

Figure 4.18 Excitation functions for electron - (open symbols) and bremsstrahlung - (closed symbols) induced yields of 7.5 - 8.5 MeV alpha particles from natural nickel. Statistical uncertainties are shown where larger than the symbols. The triangles show the present data and the circles represent the equivalent data derived from th results of Ref. 41 normalised to the present bremsstrah- lung radiator thickness of 0.169 g cm^{-2}. The solid lines result from folding the bremsstrahlung and E1 virtual photon spectra with the (γ, α) cross section of Figure 4.19. The broken curve A is the result of multiplying the E1 only calculation by a factor of 1.2, while the broken curve B is the result of including a 10% EWSR E2 contribution.

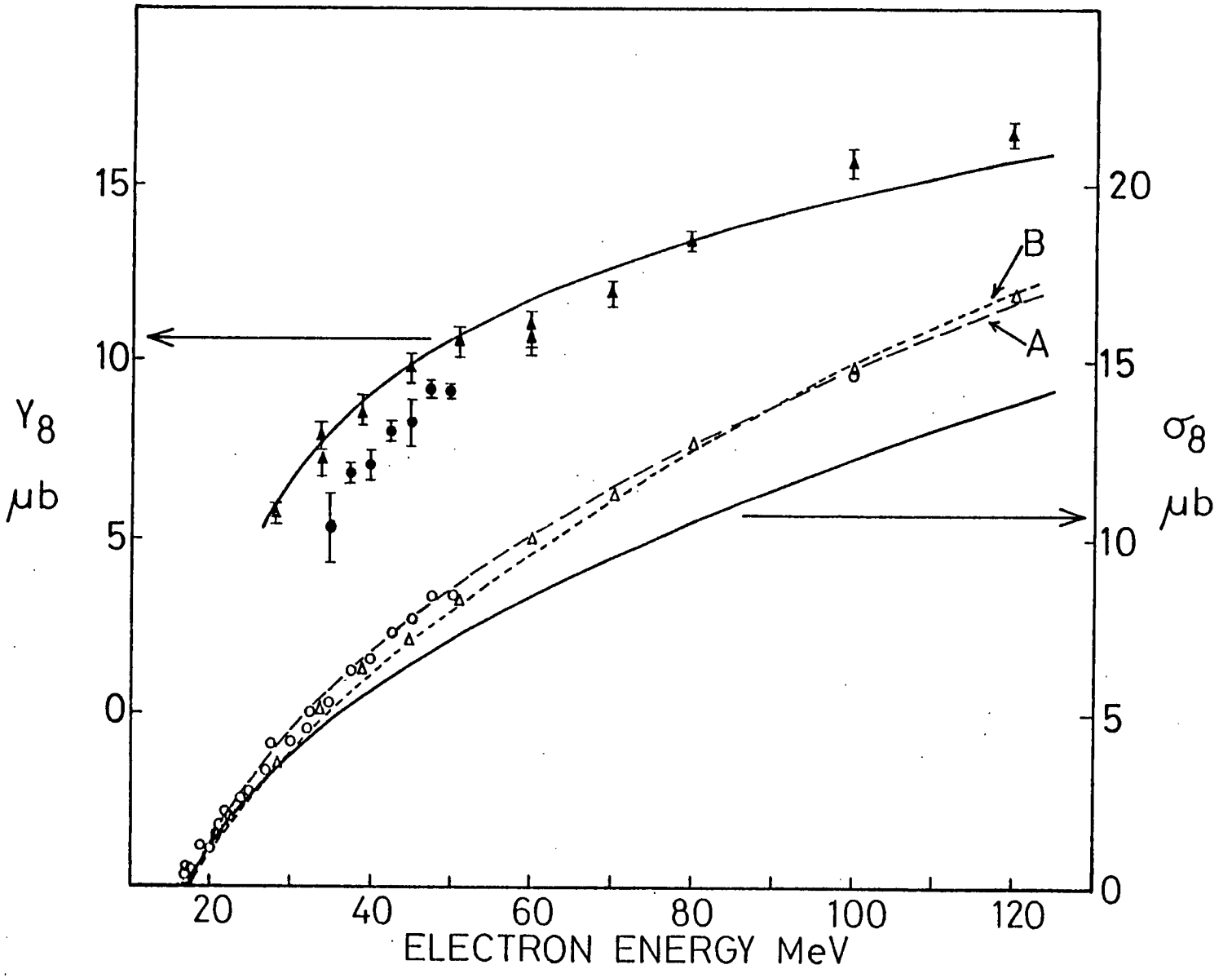
15
10
5
0
20
15
10
5
0
B
A
Y_8
μb
σ_8
μb
20
40
60
80
100
120
ELECTRON ENERGY MeV

Figure 4.18.

Figure 4.19.

Figure 4.19 The ^{60}Ni (γ, α) cross section for emission of 7.5 - 8.5 MeV alpha particles calculated using the statistical model and assuming a constant cross section above 50 MeV. The 'structure' just above threshold results from taking account of discrete states in the ^{56}Fe product nucleus.

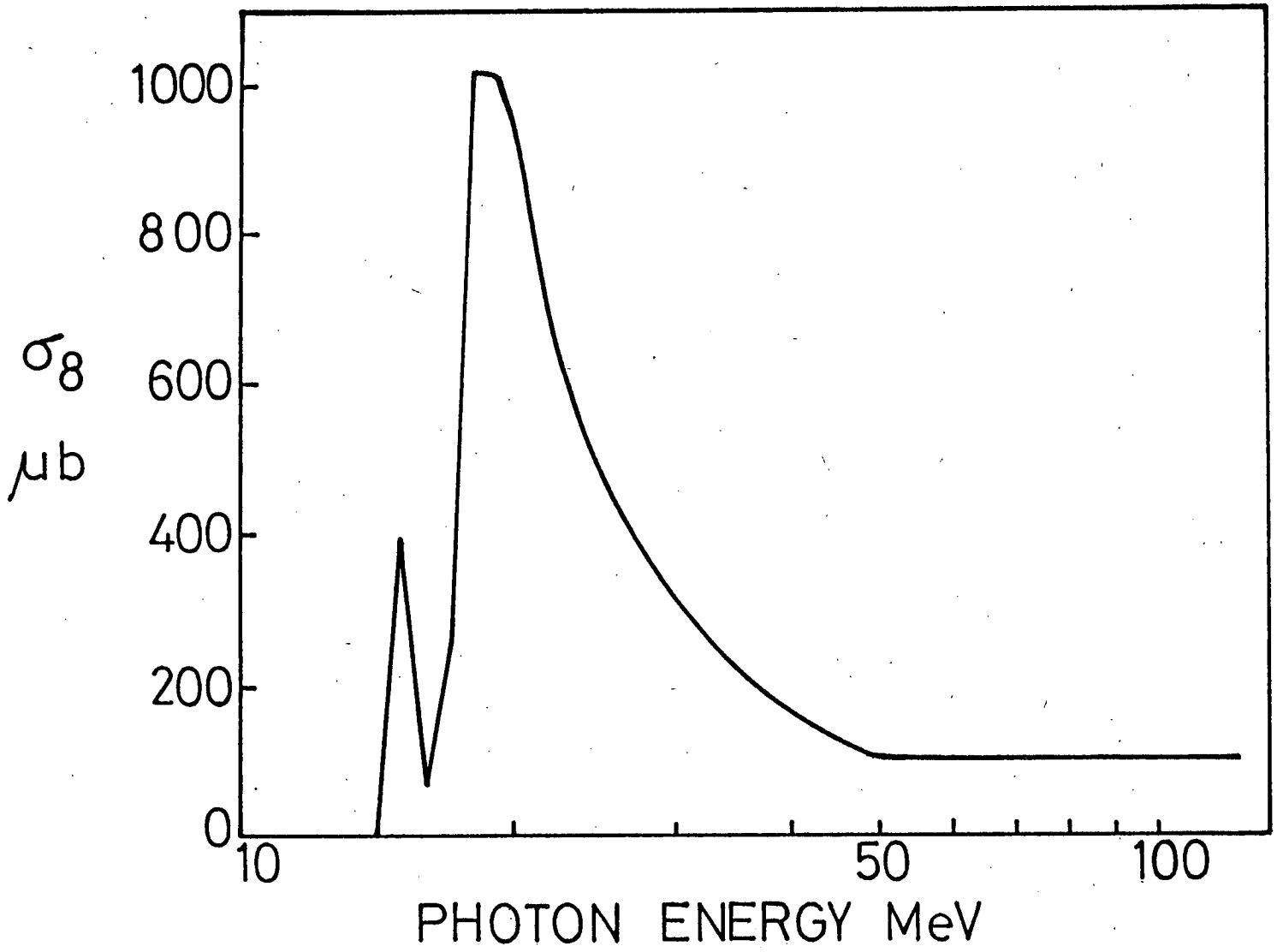

Figure 4.19.

manner, it is evident that this further evaluation of GQR alpha decay of the nickel isotopes supports the conclusions of both Section 4.4.2 and the alpha scattering studies[145),146)].

In summary, the disagreement with the N.B.S. analysis can be traced to two main sources:

i) The (γ,α) cross section of Ref. 41 is assumed to be a Lorentz shape with no high energy tail, yet a statistical model calculation of the dipole resonance alpha decay channel suggests the need to include a high energy tail.

ii) The bremsstrahlung yield data used to support the conclusions of Ref. 41 are in disagreement with the presently extended results (yet the (e,α) data is in good agreement). It is suggested that the disagreement is due to counting losses in the N.B.S. spectrometer focal plane detectors resulting from an enlargement of the beam spot due to multiple scattering in the bremsstrahlung radiator.

CHAPTER 5

ALPHA EMISSION DUE TO PRE-EQUILIBRIUM EFFECTS

5.1 Introduction

A pre-equilibrium process is one for which particle emission arises from a nucleus during equilibration, following localised excitation. This may include particle emission from a localised region in the nucleus for which the nucleons themselves are in equilibrium, i.e. a quasi-equilibrium process. Nuclear reaction models to predict high energy particle spectra similar in form to those observed here have been called both 'precompound' and 'pre-equilibrium'. Feshbach notes[150] a preference for the term 'precompound', suggesting that a rigorous definition of the term 'pre-equilibrium' would exclude the case of quasi-equilibrium. In contrast, Blann[151] notes that the term 'compound nucleus' is not unanimously used to refer to a system in equilibrium and so suggests the use of the term 'pre-equilibrium' in preference to 'precompound'. This preference is followed here, it being noted that the majority of recent literature uses the term 'pre-equilibrium' on the understanding that quasi-equilibrium conditions are included. This clarification of terminology is important since one of the most extensively applied pre-equilibrium models, the exciton model[152], invokes a quasi-equilibrium condition in its formulation[151].

The energy spectra and forward peaked angular distributions for high energy ($E \gtrsim 15$ MeV) alpha particles, observed here for the (e, α) reaction (see Figs. 3.14, 3.15), are qualitatively similar to corresponding (p, α) data[153),154] to which pre-equilibrium particle emission models have been applied extensively with considerable success. This qualitative similarity suggests that the (e, α) spectra and angular distributions may also be well explained by reaction models describing particle emission during the nuclear equilibration process. The success of

intranuclear cascade pre-equilibrium calculations[155] in predicting photon induced nucleon spectra indicates the existence of an equilibration process following high energy ($E_\gamma \gtrsim 35$ MeV) photon absorption. In this chapter the mechanism and extent of alpha emission during equilibration is considered. Consequently, the (e,α) high energy spectra and angular distributions are now examined for quantitative evidence indicative of pre-equilibrium alpha emission processes. The high energy alpha component is initially only tentatively labelled 'pre-equilibrium' to distinguish it in discussion from the component well explained in Chapter 4 as an equilibrium statistical component.

5.2 Energy Spectra

5.2.1 Cross Section Target Mass Dependence

The target mass number dependence of the pre-equilibrium (e,α) cross section differs considerably from that of the evaporative (equilibrium) component. As illustrated in Fig. 1.2 the evaporative component peaks at about mass 60 and then falls off rapidly with increasing mass number. In contrast, Fig. 3.15 indicates that the 'pre-equilibrium' component continues to increase steadily with mass number. The (e,α) double differential cross section for $E_\alpha \sim 29$ MeV and $E_\alpha \sim 50$ MeV, at 120 MeV electron energy, is illustrated in Fig. 5.1, together with fitted curves of the form,

$$\left(\frac{d^2\sigma(A)}{dE_\alpha\, d\Omega} \right)_{\theta_\alpha=30^\circ} = \left(\frac{d^2\sigma_o}{dE_\alpha d\Omega} \right)_{\theta_\alpha=30^\circ} \cdot A^n \quad .$$

These illustrate an $A^{1.5}$ dependence for the (e,α) cross section at $E_\alpha \sim 29$ MeV and $\theta_\alpha = 30^\circ$, increasing to $A^{2.0}$ at $E_\alpha \sim 50$ MeV. The total (e,α) cross section integrated above $E_\alpha = 25$ MeV (obtained by

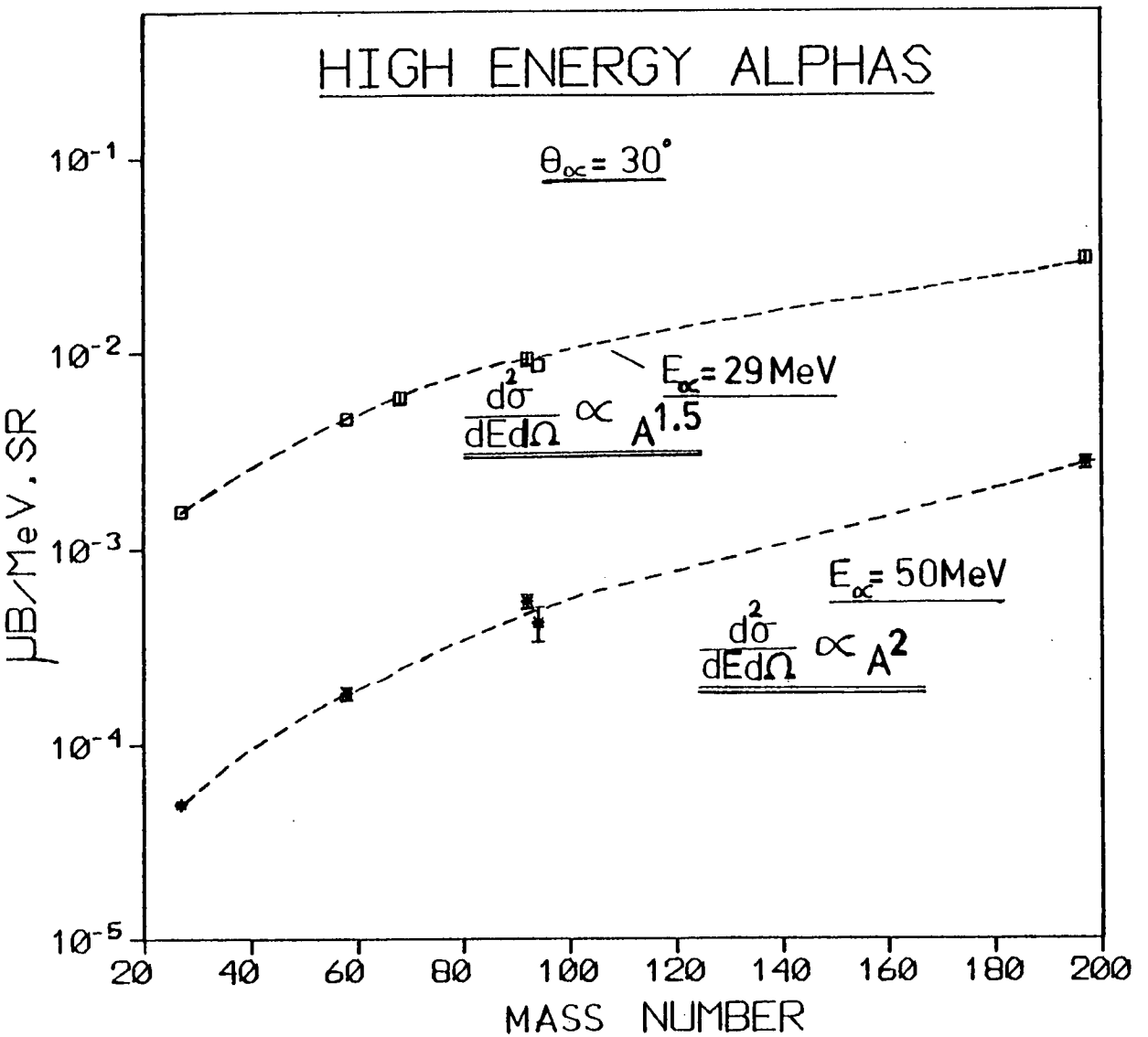

Figure 5.1 Mass number dependence of (e,α) reaction cross sections at 120 MeV electron energy.

consideration of the measured angular distributions) is proportional to $A^{1.5}$.

This mass dependence is in marked contrast with the $A^{1/3}$ dependence found for (p,α) cross sections and suggests at least a two step reaction process. At photon energies above $E_\gamma \sim 35$ MeV the photon absorption mechanism is well explained by a quasi-deuteron process (see Section 5.4), for which the cross section is approximately volume dependent and increases almost linearly with mass number. The quasi-deuteron interaction produces a fast proton and neutron which can then initiate a second stage (N, α) reaction. If this second stage were surface dependent ($\sim A^{2/3}$) or volume dependent ($\sim A$), it would lead to a mass dependence between $A^{5/3}$ and A^2, essentially as observed. A conclusion that the second stage of the process changes from a surface to a volume effect as the nucleon and alpha energies increase, cannot yet be justified in view of the purely qualitative treatment here, neglecting absorption effects. The alpha particle mean free path will increase with particle energy, decreasing the likelihood of an alpha "knocked out" from near the nuclear centre being scattered or broken up on the way out. The alpha particle mean free path can be obtained from the relation[156],

$$\bar{\lambda}(\varepsilon) = \frac{\hbar c}{2W}\left(\frac{2(\varepsilon + V)}{mc^2}\right)^{\frac{1}{2}}, \quad \varepsilon+V >> W$$

where V and W are the real and imaginary optical model volume potentials, ε is the particle energy in the nucleus relative to the top of the potential well, and $\bar{\lambda}$ is the mean free path, $\hbar c \sim 197$ MeV.fm, and here $mc^2 = m_\alpha c^2 = 3728$ MeV. Using $V = 180$ MeV and $W = 23$ MeV, as representative of alpha particle optical potential parameters, we obtain $\bar{\lambda}(E_\alpha \sim 25) \sim 1.42$ fm. and $\bar{\lambda}(E_\alpha \sim 50) \sim 1.5$ fm. Thus the

variation in mean free path with increasing particle energy is unlikely to cause the observed significant change in mass dependence and emitted alpha energy.

It is concluded that the mass dependences indicate a two step or at most few step mechanism for the emission of alpha particles above 25 MeV, implying that the nuclear excitation is shared among relatively few nucleons at this stage of the reaction. An indication of the validity of this picture is obtained by consideration of the form of the alpha energy spectra, and their parameterisation in terms of a nuclear "temperature".

5.2.2 Temperature Parameterisation of Energy Spectra Pre-equilibrium Components

The smooth exponential decrease in cross section exhibited by alpha particles of $E_\alpha \sim 25$ MeV, suggests a parameterisation in terms of a nuclear "temperature". The spectra were parameterised using the expression*,

$$\frac{d^2\sigma}{dE_\alpha d\Omega} \propto \sigma_{inv}(E_\alpha)\cdot E_\alpha \cdot \exp(-\frac{E_\alpha}{T}) .$$

The cross sections for alpha capture by the residual nuclei, σ_{inv}, were calculated using the analytical expressions of Dostrovsky[157] as applied by Gadioli, Erba and Hogan[158]. The resulting temperatures are given in Table 5.1, and exceed the values of 1.0 - 1.5 MeV for the equilibrium component of the (e,α) reaction[27] by a factor of 4. The temperature mass number dependence is illustrated in Fig. 5.2. The temperatures obtained from electrodisintegration experiments are only mean values resulting from all excitations from threshold to the electron energy. However, it is informative to compare these with Fermi Gas

* In Ref. 42 the factor 'E_α' was accidentally omitted from this expression. The expression used to obtain the temperature parameters here, and in Ref. 42 is that given here.

TABLE 5.1

Temperatures corresponding to the pre-equilibrium component of the (e,α) reaction, derived from the energy spectra at $\theta_\alpha = 30^\circ$ for $E_e = 120$ MeV.

Target	Temperature (MeV)[a]
^{27}Al	5.3
^{NAT}Ni	5.5
^{68}Zn	5.4
^{92}Mo	5.6
^{94}Mo	5.4
^{197}Au	6.1

(a) Error on temperature is ±0.2 MeV.

Figure 5.2.

Figure 5.2. Temperature mass number dependence of the (e,α) reaction pre-equilibrium component for 120 MeV energy incident electrons. The temperatures are compared with calculated Fermi gas temperatures (solid lines), those derived from heavy ion reactions (triangles) and low energy photoalpha reactions (squares).

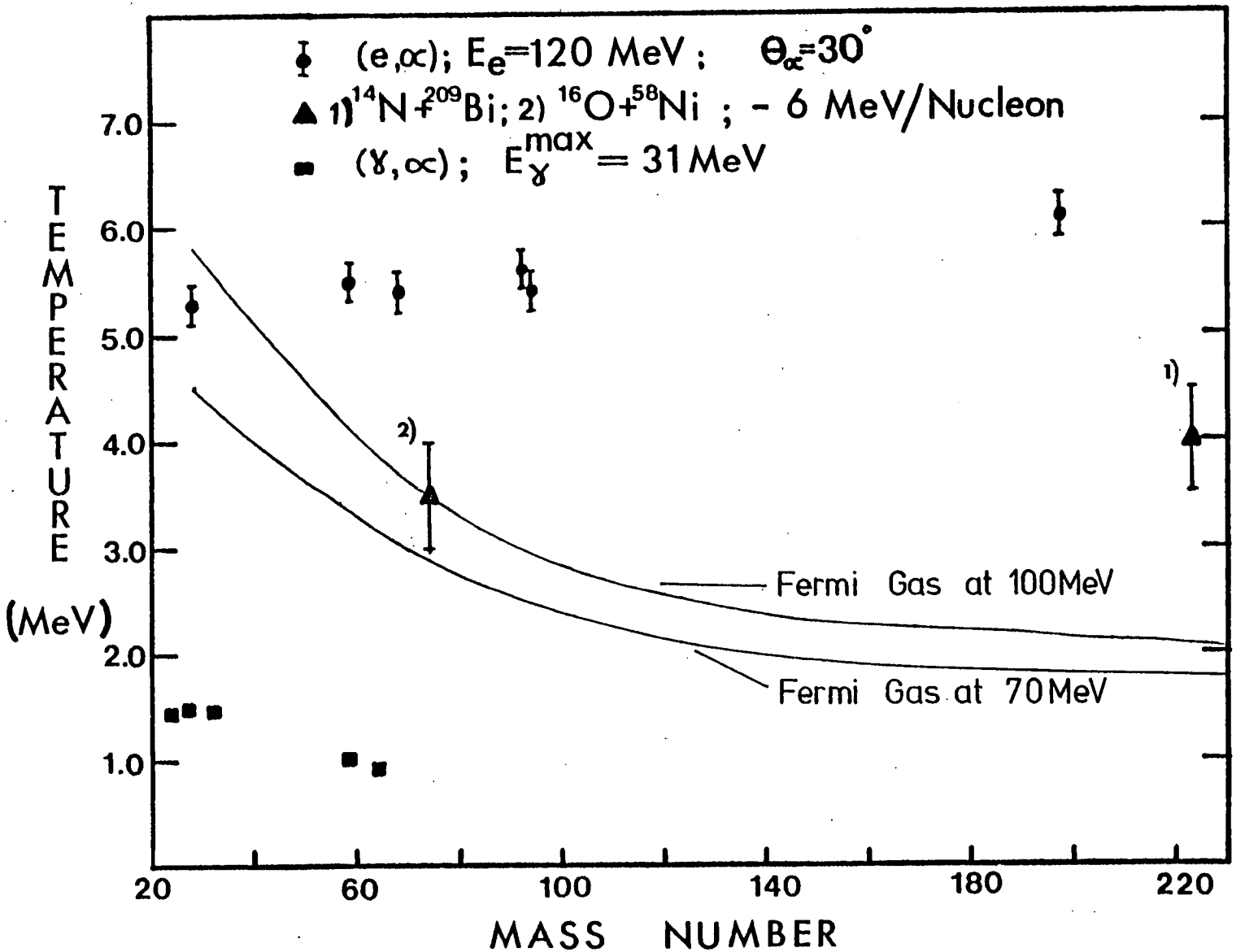
(e,α); E_e=120 MeV ; θ_α=30°
1) $^{14}N+^{209}Bi$; 2) $^{16}O+^{58}Ni$; - 6 MeV/Nucleon
(γ,α); E_γ^{max} = 31 MeV
TEMPERATURE (MeV)
7.0
6.0
5.0
4.0
3.0
2.0
1.0
1)
2)
Fermi Gas at 100MeV
Fermi Gas at 70MeV
20
60
100
140
180
220
MASS NUMBER

Figure 5.2.

temperatures (corresponding to the equilibrium stage) at the likely upper limit of the average excitation energy, E_x, in the reaction process. Here, a generous upper limit of 100 MeV is assigned for 120 MeV electrons. The Fermi Gas temperature, T, is given by (Appendix 7),

$$\frac{1}{T} = \sqrt{\frac{a}{E_x}} - \frac{3}{2E_x}$$

where a is the nucleus level density parameter[132]. This yields the temperature mass number dependences at E_x = 100 MeV and E_x = 70 MeV shown in Fig. 5.2. Only the experimentally derived temperature for ^{27}Aℓ is compatible with alpha emission from a highly excited equilibrated nucleus. The temperatures derived for all other nuclei considered here are factors of 2 to 3 above the upper limit for the equilibrium temperature.

The form of the energy spectra observed at forward angles in medium weight and heavy nuclei indicates a reaction process in which the initial excitation energy is shared by only a few nucleons at the stage when most high energy alpha emission occurs. Such alpha emission may then be considered as arising from some direct alpha emission process (e.g. a quasi-free scattering process) or evaporation of an alpha particle from excited nucleons in quasi-equilibrium.

It is interesting to note that elevated temperatures, in excess of the Fermi Gas equilibrium temperature, have previously been associated[159] with a localised excitation or "hot spot" within the nuclear volume. This concept was originated by Bethe[160] in 1938 and has recently been applied to the analysis of pre-equilibrium alpha emission following deep-inelastic scattering of heavy ions[161),162]. Temperatures of 3.5 - 4.0 MeV were obtained for alpha particles emitted in the forward direction following ∿30 MeV excitation of the compound system (see Fig. 5.2).

It has been recognised[162] that the observed energy spectra may result from direct reaction processes. A parameterisation in terms of a thermodynamic quantity relating to a system in equilibrium (or even 'quasi-equilibrium') may therefore not be valid in these cases and consequently no inferences relating to the (e,α) data are drawn from the heavy ion studies.

Valid use of the temperature parameterisation here requires the alpha emission to arise from a quasi-equilibrated group of nucleons. It has been noted[163] that such a process cannot occur in cases where asymmetric angular distributions are observed, since particles emitted from a quasi-equilibrated group of nucleons should have an angular distribution symmetric about 90° in the centre of mass frame. However, the conversion of angular distributions from the laboratory frame to centre of mass frame, for reactions in which the scattered projectile is not detected, is not well determined due to the unknown centre of mass momentum at the time of particle emission. Prior to any consideration of alpha emission from quasi-equilibrium states it is important to consider under what conditions the pre-equilibrium laboratory frame angular distributions are compatible with symmetric centre of mass angular distributions.

5.3 Angular Distributions

The laboratory frame angular distributions for $\sim$ 30 MeV and $\sim$ 50 MeV alpha particles emitted from nickel and gold at 120 MeV incident electron energy are shown in Fig. 3.16. These distributions are fitted by up to 4th order Legendre Polynomials,

$$\sigma(\theta) = \sum_{L=0}^{4} A_L P_L(\cos\theta) \quad .$$

The coefficient A_4/A_o is zero within experimental uncertainty. The coefficients A_i/A_o ($i = 1,2,3$) are compared with fits to lower alpha energy (e,α) data in Figs. 5.3 and 5.4. The low energy alpha data for nickel is from the present work at $E_e = 120$ MeV, whilst the data for $E_\alpha < 30$ MeV for ^{197}Au is from W.R. Dodge[164], taken at $E_e = 100$ MeV. At alpha energies above the Coulomb barrier ($\sim$ 10 MeV and $\sim$ 20 MeV for nickel and gold respectively) the increasing and dominant positive A_1/A_o ratio is further illustrative of the smoothly varying angular distribution asymmetry at high electron energies. Alpha particles of increasing energy are likely to be emitted following absorption of increased energy photons. The possibility that the observed asymmetry results from the resulting (increasing) centre of mass momentum therefore must be considered.

The relation between the centre of mass and laboratory frame angular distributions (differential only in angle, azimuthal symmetry assumed) is[165],

$$\sigma(\theta) = \frac{(1 + 2\Gamma'\cos\theta' + \Gamma'^2)^{3/2}}{1 + \Gamma'\cos\theta'} \sigma(\theta') \quad . \qquad (5.1)$$

The primed quantities refer to the centre of mass frame, and unprimed quantities refer to the laboratory frame. The kinematic parameter, Γ', for photonuclear reactions in which the momentum transfer is directed forwards (forward scattering approximation) is,

$$\Gamma' = \frac{V_{cm}}{V'} = \frac{q\ m}{p' M_T} \quad .$$

q - photon momentum transferred to target mass, M_T.

p' - momentum of emitted particle, mass, m, in centre of mass frame.

V_{cm} - centre of mass velocity, $V_{cm} = \frac{q}{M_T}$.

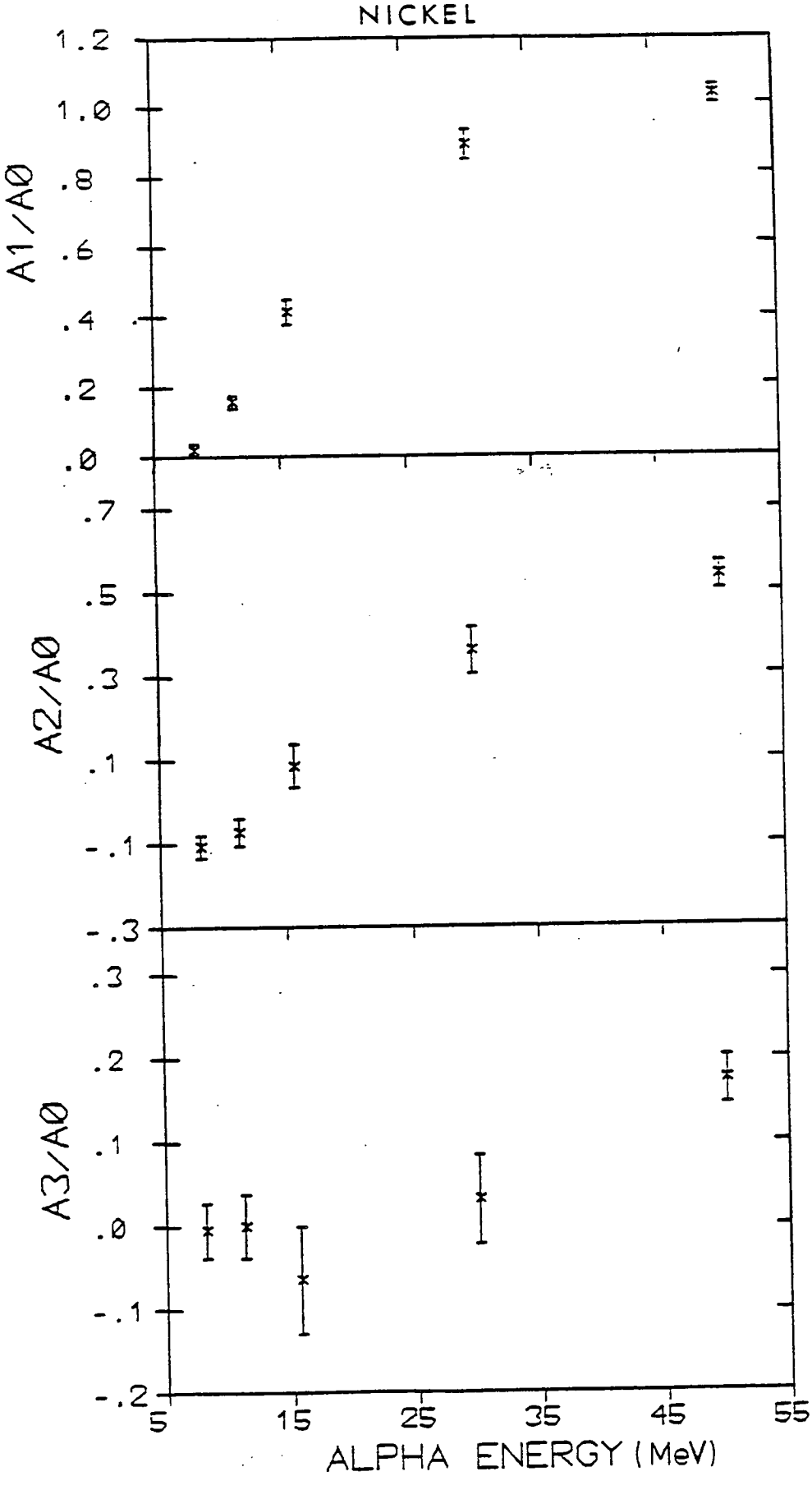

Figure 5.3. Legendre polynomial coefficients for (e,α) angular distributions from 120 MeV electrons incident on nickel.

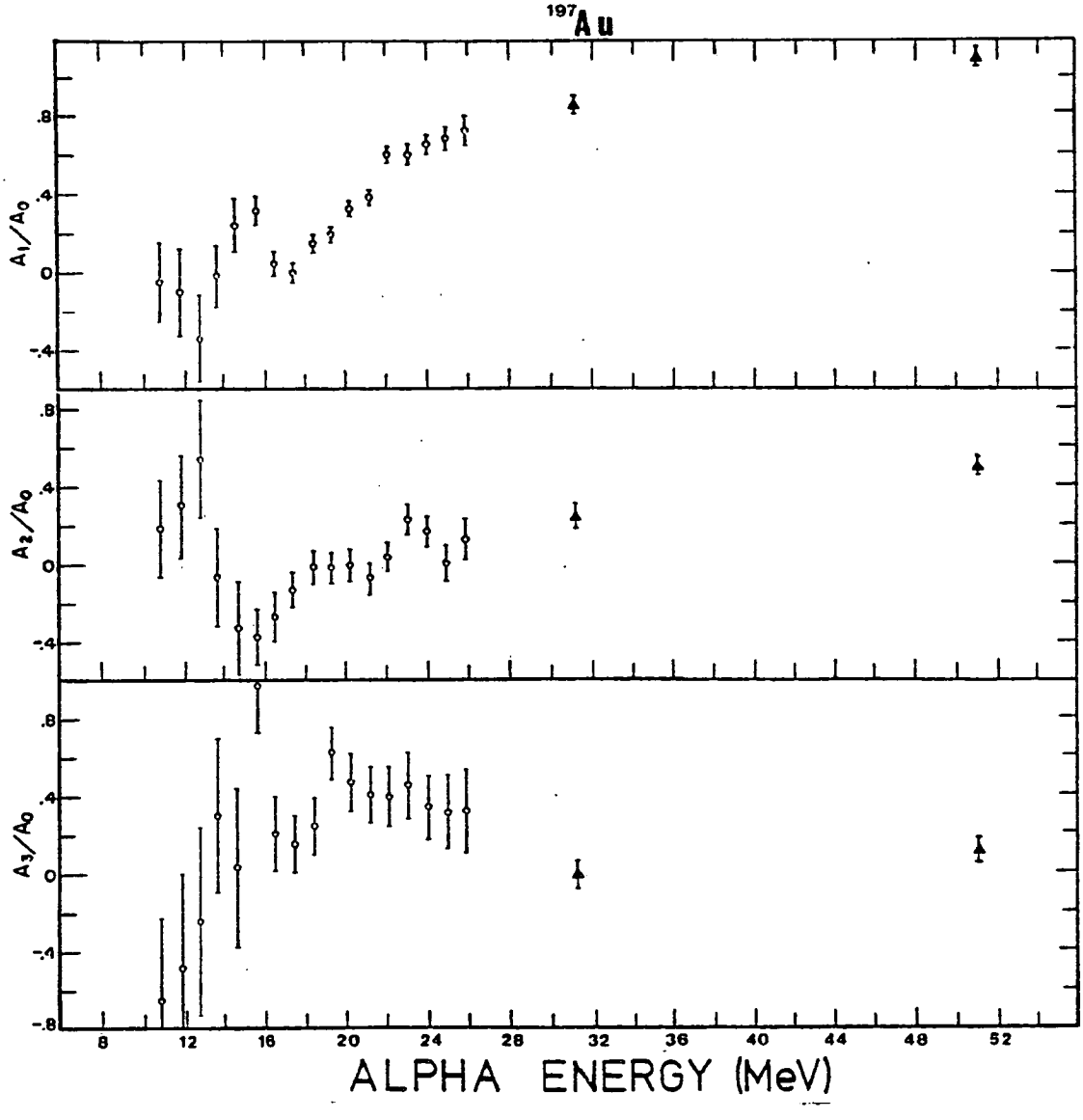

Figure 5.4. Legendre polynomial coefficients for (e,α) angular distributions from 100 MeV electrons (circles) (Ref. 164) and 120 MeV electrons (triangles) (present work) incident on gold.

An alternative version of expression (5.1), employing laboratory frame coordinates, is given by,

$$\sigma(\theta) = \frac{(1 - \Gamma\cos\theta)}{(1 - 2\Gamma\cos\theta + \Gamma^2)^{3/2}} \cdot \sigma(\theta') \quad . \tag{5.2}$$

Alpha particles emitted from nickel following a 100 MeV/c photon momentum transfer yield $\Gamma \sim 0.014$. Expression (5.2) can therefore be approximated for $\Gamma \ll 1$, yielding,

$$\sigma(\theta) = (1 + 2\Gamma\cos\theta)\sigma(\theta') \quad . \tag{5.3}$$

Assuming angular isotropy in the centre of mass frame, i.e. $\sigma(\theta')$ = constant, the laboratory frame angular distribution will then be in the form,

$$\sigma(\theta) = (A_o + A_1 P_1(\cos\theta))$$

where $$\frac{A_1}{A_o} = 2\Gamma \quad .$$

For the case under consideration, this gives $A_1/A_o \simeq 0.03$, i.e. a factor of $\sim$30 lower than that observed for E_α = 30 - 50 MeV for nickel. The discrepancy would be even larger for gold, since in this case Γ is smaller. Furthermore, any reasonable assumption of anisotropy (retaining symmetry about 90°) in the centre of mass frame, would not greatly alter the above asymmetry estimate. It is concluded that either alpha particles are emitted asymmetrically in the centre of mass frame from a compound nucleus, or the emission process has a kinematic factor greater than that estimated for compound nucleus particle emission. Such an increased kinematic factor may result if $M_T < A$, i.e. if the photon momentum is shared by only a few nucleons at the stage when particle emission occurs.

The laboratory frame angular distribution arising from isotropic particle emission in the centre of mass frame, is shown in Appendix 9

to be given by,

$$\frac{d^2\theta}{dE_\alpha d\Omega}(\bar{E}_\alpha,\theta) = \frac{\bar{p}}{p}\frac{d^2\sigma}{dE_\alpha d\Omega}(E_\alpha, \theta_o) \qquad (5.4)$$

where,

$$p = \bar{p}\,\Gamma\cos\theta_o \pm \sqrt{\bar{p}^2\Gamma^2\cos^2\theta_o + \bar{p}^2 - 2\Gamma\bar{p}^2\cos^2\theta}$$

$$\bar{E}_\alpha = \frac{\bar{p}^2}{2m}, \qquad E_\alpha = \frac{p^2}{2m}$$

$\bar{p}$ - emitted particle momentum, in the laboratory frame, at which the laboratory frame angular distribution is obtained.

θ_o - angle to which the laboratory frame energy spectrum data, $\frac{d^2\sigma}{dE_\alpha d\Omega}(E_\alpha, \theta_o)$ applies.

$$\Gamma = \frac{qm}{\bar{p}M_T} .$$

The angular distributions derived from (5.4) for a given emitted particle type, can be fitted to the observed angular distributions by the variation of only one free parameter, q/M_T. Fits to the angular distributions for $\sim$ 30 MeV and $\sim$ 50 MeV alphas from nickel and gold, are illustrated in Figs. 5.5 and 5.6. The calculated angular distribution are very sensitive to the free parameter, and give good fits to the data with $q/M_T \sim 10$ MeV/c/A.M.U. for nickel and $q/M_T \sim 12$ MeV/c/A.M.U. for gold, at both alpha energies considered here. Since the spectrum of nuclear excitation energies $N(E_\gamma)$, includes all excitation energies, E_γ, up to the electron energy (here E_e = 120 MeV), and since a forward scattering approximation is reasonable in view of the pronounced forward peaking of electron scattering angular distributions, then $q = \frac{E_\gamma}{\hbar c}$, and a reasonable upper limit for the average momentum transfer is q = 100 MeV/c. This yields $M_T \sim 8$ A.M.U. and $M_T \sim 10$

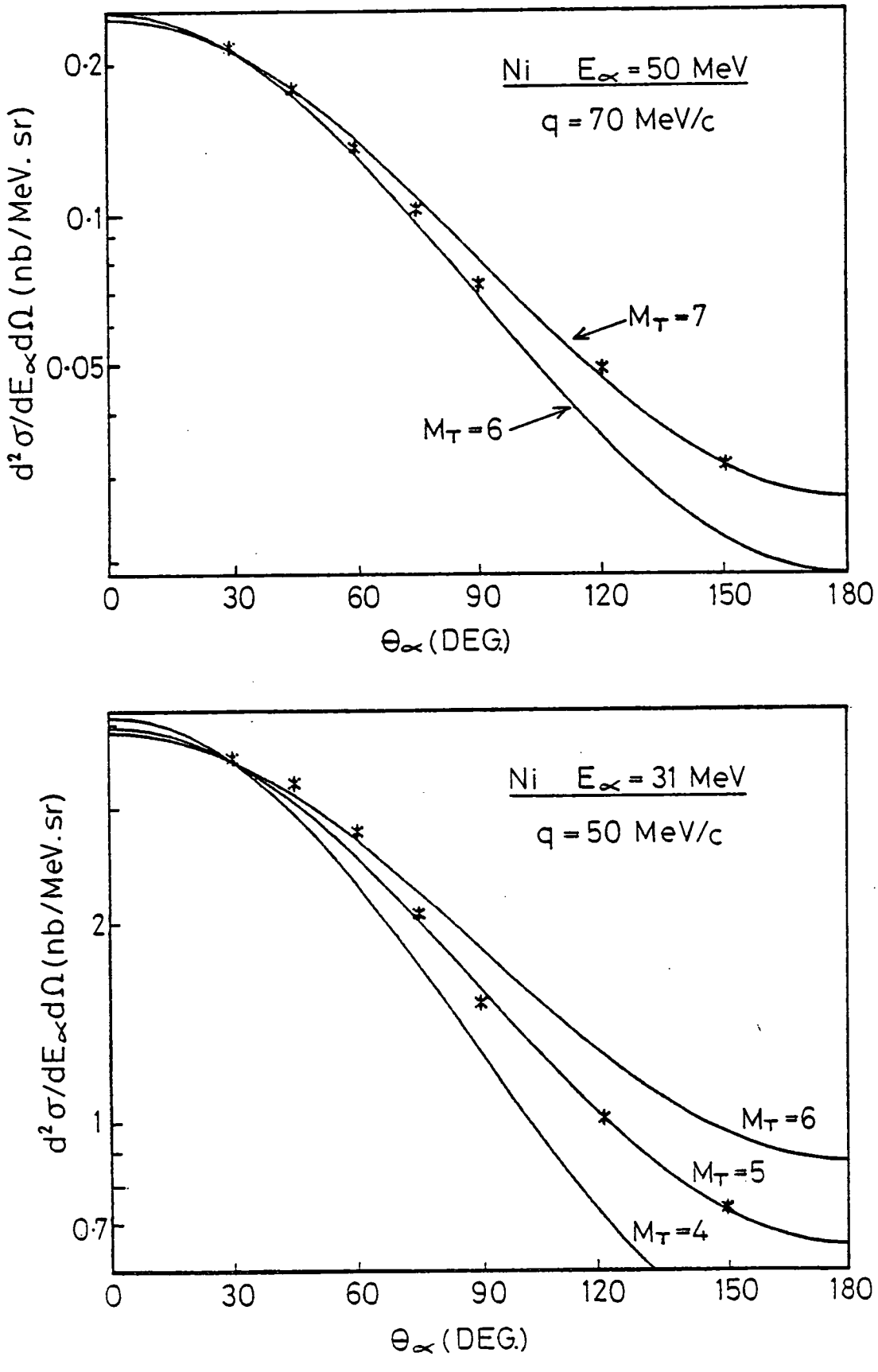

Figure 5.5. Natural nickel (e,α) angular distributions at 120 MeV electron energy. The data are represented by stars, the solid lines are the laboratory frame angular distributions for alpha particles emitted isotropically from a mass M_T system with momentum q.

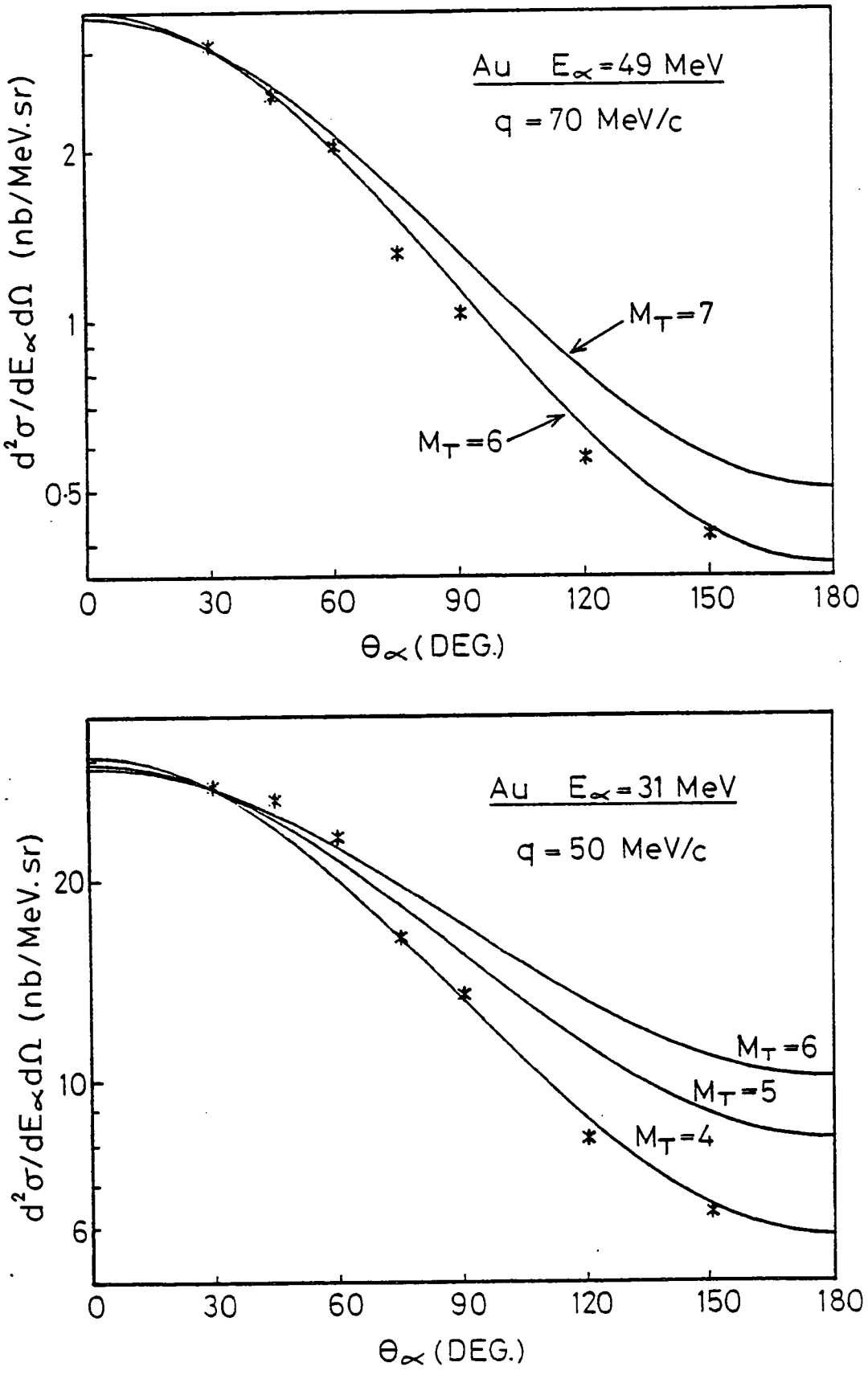

Figure 5.6. Gold (e,α) angular distributions at 120 MeV electron energy. Notation and symbols as in Figure 5.5.

A.M.U. for gold and nickel, respectively. Here M_T is interpreted as the average number of nucleons sharing the incident photon energy at the stage when an alpha particle is emitted from the nucleus. The lower value of M_T for gold may be indicative of a greater probability of alpha formation, or of alpha knock-out, compared to nickel.

It is concluded that the observed laboratory frame angular distributions are compatible with isotropic alpha emission relative to the centre of mass of a few nucleon system. Consequently, it is considered justifiable to apply quasi-equilibrium conditions to the analysis of the particle emission process. The analysis here indicates that if such conditions are valid, substantial alpha emission occurs at an early stage in the equilibrium process when, on average, about 10 target nucleons are excited.

5.4 Pre-equilibrium Reaction Models for the (e,α) Reaction

5.4.1 Direct Alpha Particle Knock-out

Early descriptions of high energy ($E \gtrsim 35$ MeV) photonuclear reactions considered the initial photon absorption process to occur on a correlated neutron-proton pair[166] (quasi-deuteron) and assumed that no further interactions occurred in the nucleus[167),168]. The observation here of high energy alpha emission indicates that either (i) some form of intranuclear interaction must occur after the initial photon absorption process or, (ii) there exists a direct (one step) alpha knock-out mechanism. Such a knock-out process has been proposed by Carver[169] who showed that ratios of $(\gamma,\alpha)/(\gamma,p)$ yields for heavy nuclei were compatible with those estimated for direct alpha and proton knock-out. Here the mass dependence of a direct alpha knock-out process is compared with the present observations.

The (e,α) and (γ,α) cross sections are related by (see Section 1.3.1),

$$\sigma(e,\alpha) = \sum_{\lambda L} \int_{Thr}^{E_o} N^{\lambda L}(E_\gamma, E_o) \cdot \sigma^{\lambda L}(\gamma,\alpha) E_\gamma^{-1} \, dE_\gamma \, . \qquad (5.5)$$

For $E_\gamma/E_o \gtrsim 0.3$, $N^{\lambda L}$ has essentially no mass dependence, hence the mass dependence of $\sigma(e,\alpha)$ is identical to that of $\sum_{\lambda L} \sigma^{\lambda L}(\gamma,\alpha)$. The (γ,α) cross section is given by[169],

$$\sigma^{\lambda L}(\gamma,\alpha) \sim (q_{eff}^{\lambda L})^2 \cdot n \qquad (5.6)$$

where $q_{eff}^{\lambda L}$ is the effective charge[170] for an alpha particle in a radiation field of type λL (e.g. $\lambda L = E1$ for electric dipole) and n is the number of alpha particles in the target nucleus. The small alpha particle mean free paths estimated in Section 5.2.1 ($\bar{\lambda}_\alpha \sim 1.5$ fm for $E_\alpha \sim 30 - 50$ MeV) indicate that most observed alphas originate on the nuclear surface, hence $n \sim A^{2/3}$. The alpha particle effective charges for E1 and E2 multipoles are,

$$q_{eff}^{E1} = \frac{2(N - Z)}{A} \sim A^{2/3}$$

$$q_{eff}^{E2} = 2\left(1 - \frac{2}{A} + \frac{2Z}{A}\right) \approx 2 \, . \qquad (5.7)$$

Hence,

$$\sigma^{E1}(e,\alpha) \sim A^2$$

$$\sigma^{E2}(e,\alpha) \sim A^{2/3} \, .$$

Compared to the total (e,α) mass dependence observed ($A^{1.5}$) the dipole process has a more pronounced mass dependence while the quadrupole process predicts insufficient mass dependence. The observed A^2 mass dependence of the higher energy alpha component ($E_\alpha \sim 50$ MeV) is evidently

compatible with a direct E1 process. However, both E1 and E2 direct processes can be ruled out as independently providing the dominant contribution to the total (e,α) pre-equilibrium cross section. Furthermore, the low sum rule estimate for E2 transitions relative to E1 transitions (see Section 1.4.2) suggests it is unlikely that the components sum to give the observed $A^{1.5}$ mass dependence.

The observed angular distributions do not rule out, on kinematic grounds, the possibility of a direct photoalpha process. Such a process would indicate ratios of transferred forward photon momentum, q, to emitted particle mass, M_T, $q/M_T \sim 12_\Lambda^{MeV/c/AMU.}$ for 50 MeV alphas and $q/M_T \sim 8_\Lambda^{MeV/c/A.M.U.}$ for 30 MeV alphas - close to the values obtained in Section 5.3 (see Figs. 5.5 and 5.6). The existence of some contributions from a direct one step (e, α) process therefore cannot be completely ruled out, given the present data. The experimental determination of the magnitude of such contributions may eventually be possible in future $(e, e'\alpha)$ or $(\gamma,\gamma'\alpha)$ coincidence experiments. For the present, attention is concentrated on the likely contributions from intranuclear interactions.

The inclusion of intranuclear nucleon-nucleon interactions, following a quasi-deuteron absorption process, has been found necessary to explain the observed magnitude of high energy photonucleon spectra. Calculations omitting such interactions overestimate the magnitude of the high energy spectrum components, whereas their inclusion leads to good agreement with experimental results[155),171)]. It is shown in Appendix 10 that an estimate of the (e,α) cross section based on a two step (e,N) - (N,α) reaction, using measured (N,α) cross sections, gives good order of magnitude agreement with the observed cross sections. The second step intranuclear (N,α) reaction may involve one or more of the following mechanisms:

i) Knock-out of a preformed alpha cluster (a quasi-free scattering (Q.F.S.) process).

ii) Formation of an alpha particle after at least two protons and two neutrons are excited in a cascade (a quasi-equilibrium process).

iii) One step three particle cluster pick-up by a nucleon.

These mechanisms are illustrated schematically in Fig. 5.7 and considered in turn in Sections 5.4.3 - 5.4.5. The first step of the reaction process, quasi-deuteron photon absorption, is considered in detail in the next section.

5.4.2 Quasi-deuteron Photon Absorption

In the absence of measured total photon absorption cross sections, $\sigma_\gamma(E_\gamma)$, at $E_\gamma \gtrsim 30$ MeV in medium weight and heavy nuclei, theoretical estimates of these cross sections are necessary. The dominance of the dipole term in high energy photodisintegration led to the consideration by Levinger[166] of photon absorption on a dipole formed by a neutron-proton nucleon pair, or 'quasi-deuteron'. At neutron-proton separation distances, r, within the range of nuclear forces the quasi-deuteron and ground state deuteron wave functions are proportional to each other for a quasi-deuteron with given neutron-proton relative momentum, k, i.e.

$$\frac{\psi_{q.d.}}{\psi_d} = f(k) \quad . \tag{5.8}$$

The relative photon absorption cross sections are then given by Levinger as,

$$\frac{\sigma_{q.d.}}{\sigma_d} = \left(\frac{\psi_{q.d.}}{\psi_d} \right)^2 = \frac{L}{A} \quad , \tag{5.9}$$

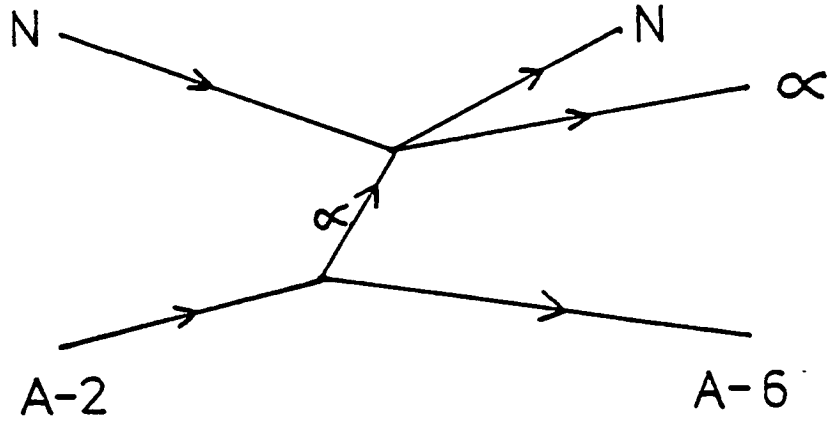

i) QUASI-FREE SCATTERING

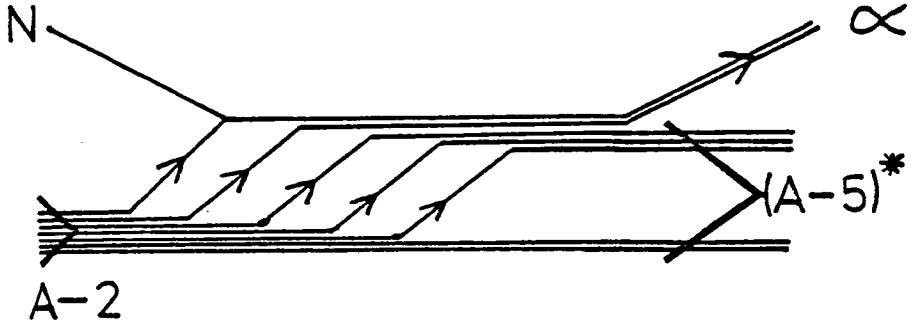

ii) QUASI-EQUILIBRIUM

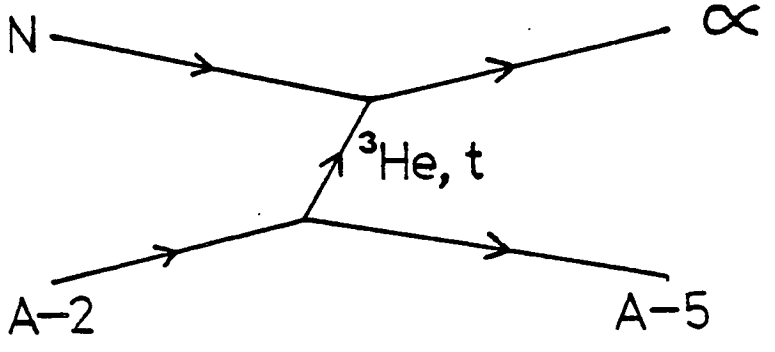

iii) PICK-UP

Figure 5.7. Schematic representation of the most probable pre-equilibrium alpha emission processes following quasi-deuteron photon absorption. In the above it is assumed that one nucleon from the quasi-deuteron escapes from the nucleus and the other interacts with the remaining A-2 nucleons.

where $L = 6.8$ for $kr << 1$ and is now described as the 'Levinger parameter'. The maximum number of neutron-proton pairs which may be formed is NZ, and hence the total photon absorption cross section, allowing only quasi-deuteron photon absorption, is

$$\sigma_\gamma(E_\gamma) = L \left(\frac{NZ}{A}\right) \sigma_d(E_\gamma) \quad . \tag{5.10}$$

However, the assumptions leading to a constant Levinger parameter break down for $E\gamma \lesssim 150$ MeV. The derivation of expression (5.9) assumes that high energy, short wavelength, photons interact with only closely correlated nucleons of separation, r, with low relative momenta, k, i.e. $kr << 1$. Furthermore, as the photon energy approaches the Fermi energy ($\varepsilon_f \sim 35$ MeV), the assumption that all nucleons may form energetically allowed excited nucleon pairs fails dramatically since many final states become blocked by the Pauli exclusion principle (Pauli blocking).

These effects have been accounted for by employing an experimentally determined[172] Levinger parameter ($L = 10.3$) and applying Monte Carlo techniques[155] to obtain the probability of creating two unblocked and energetically allowed excited nucleons, each sampled from a Fermi energy distribution centred about $E_\gamma/2$. Such an approach yields the calculated total photon absorption cross sections shown in Fig. 5.8. The results evidently allow a smooth extrapolation between the experimentally determined region and the region in which quasi-deuteron photon absorption may be expected to dominate. The onset of significant Pauli blocking effects, and the resulting quenching of the quasi-deuteron cross section is evident in Fig. 5.8 for ^{197}Au at $E_\gamma \lesssim 50$ MeV, and for ^{60}Ni at $E_\gamma \lesssim 40$ MeV.

Alternative approaches apply expression (5.10) with a photon energy

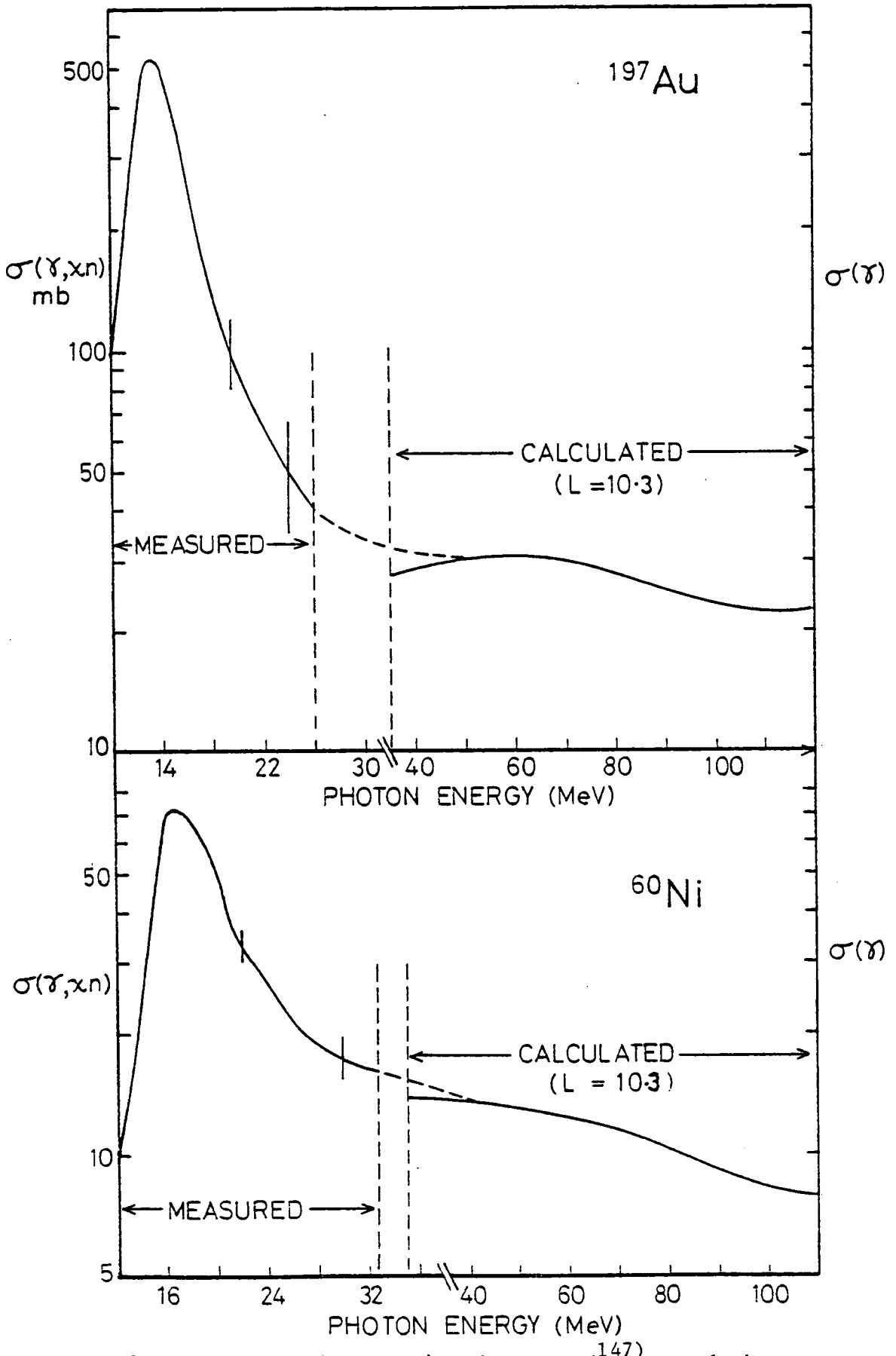

Figure 5.8. Calculated (see text) and measured[147] total photon absorption and photoneutron cross sections for ^{197}Au and ^{60}Ni.

dependent Levinger parameter, $L(E_\gamma)$, to account for quenching. Levinger has suggested $L(E_\gamma) \sim e^{-D/E_\gamma}$ [173], and such a factor has been successfully used[174] with $D = 60$ MeV, to reproduce the form of (γ, xn) cross sections in the range $E_\gamma = 40 - 100$ MeV. Wu and Chang[171] apply a quenching factor,

$$L(E_\gamma) \propto 1 - e^{-0.1(E_\gamma - 40)} \qquad (5.11)$$

in their pre-equilibrium decay calculations for photonuclear reactions. The cut-off at $E_\gamma = 40$ MeV is arbitrary, and unrealistic, since some quasi-deuteron effects can reasonably be expected below 40 MeV, allowing for the Fermi distribution of the energies of the excited quasi-deuteron nucleons.

There is evidently a need for a detailed examination of the photon absorption cross section in medium weight and heavy nuclei for $E_\gamma > 30$ MeV, in order to provide a less arbitrary parameterisation than exists at present.

5.4.3 The Quasi-free Scattering Process

5.4.3.1 Quasi-free Scattering Reaction Models

The quasi-free scattering model assumes that the early stages of the equilibration process can be represented by a series of two-body collisions in the nucleus. This approach was first suggested by Serber[175], and has been successfully applied in Monte Carlo cascade calculations for both nucleon and photon induced nucleon emission[153),155),176),177].

However, these calculations considered alpha emission at only the evaporative stage. Such an omission is of little consequence to the results for single nucleon emission, since nucleon induced alpha

emission (N, α) has a cross section almost two orders of magnitude below that for (N,N) reactions in the pre-equilibrium region[153]. This omission in the only two existing photon induced cascade reaction models - those of Gabriel and Alsmiller[155] and Barashenkov et al.[178] - renders them inapplicable to the present pre-equilibrium (e,α) data. Their calculated evaporative alpha component, is of interest though, being indicative of the magnitude of low energy alpha emission arising from decay of residual compound nuclei following the cascade stage. The extent of this contribution is considered in Section 5.4.3.2.

An alternative approach to the Monte Carlo cascade calculations of quasi-free scattering effects has been developed by Mignerey, Scobel and Blann[179),163]. Here,particle decay rates are calculated by consideration of the available phase space for the decay. The intranuclear cascade is treated using intranuclear transition rates derived from measured elastic scattering cross sections for nucleon - ^{4}He scattering. Unlike the Monte Carlo cascade calculations which geometrically trace out the nucleon paths, no geometry dependence is used. This quasi-free scattering phase space approach has been successfully applied to the prediction of (p,α) data, by use of two free parameters[163]. One free parameter is the probability, ϕ, that an incoming nucleon will interact with an alpha cluster at the first interaction, and the other is a break up factor $\beta(\varepsilon)$, which is the probability that an alpha cluster with energy ε will break up prior to emission or any further collisions. Use is therefore made of the concept of preformed alpha clusters existing as entities immediately prior to any reaction. Fits to (p, α) energy spectra for medium and heavy weight nuclei have been obtained with $\phi \simeq 0.1 - 0.2$ and $\beta = 0.5 - 0.7$. However, this approach has not yet been extended to photonuclear reactions. The conceptual basis of the model is in no way at variance with the two or few step reaction process indicated by

the cross section mass dependences (Section 5.2.1), nor with the inference drawn from the temperature parameters and angular distributions that only a few nucleons are excited at the stage of pre-equilibrium alpha emission. It is therefore concluded that an extension of Q.F.S. models to the (e,α) reaction is meaningful and may prove to be a fruitful approach to pre-equilibrium photonuclear reactions.

5.4.3.2 Post-cascade Alpha Particle Evaporation

A pre-equilibrium reaction process which involves a substantial number of intranuclear interactions will generally lead to an equilibrated compound nucleus which will decay by a statistical (or evaporative) process. In cases where localised particle excitation leads to emission of all the excited particles at the pre-equilibrium stage, a compound nucleus will evidently not be formed. In photonuclear reactions such a situation will pertain if photonucleons are directly knocked out of the nucleus with no further interaction, or if both constituents of an excited proton-neutron pair, as produced in a quasi-deuteron absorption process, are emitted prior to any intranuclear interaction. However, estimated nucleon mean free paths of $\sim$ 4 fm, for the energies of interest here, indicate a significant probability for intranuclear nucleon collisions, particularly for heavy nuclei, and it is evident that if alpha emission is to follow a quasi-deuteron photon absorption process, at least one intranuclear interaction must take place.

The contribution of alpha emission from equilibrated nuclei, produced by an intranuclear cascade, is calculated using the photonuclear cascade and evaporation computer code, 'PICA' [155], written by Gabriel and Alsmillar and based on earlier particle induced cascade calculations by Bertini[176]. The results of calculations using this computer code agree well with a range of photonucleon spectra and photospallation yields

arising from nuclei at excitation energies up to 800 MeV[155),180) - 186)].

The computer code 'PICA' was loaded and tested on the Northumberland Universities' Multi-Access Computer (NUMAC), - an I.B.M. 370/155, which is accessible directly from Edinburgh University. The calculations use Monte Carlo techniques to follow each cascade history, and so require that a large number of cascades be followed to build up emitted particle spectra. The number of cascade histories followed is therefore a compromise between acceptable statistical accuracy on the results, and available computational times. A maximum of 8,000 cascades are followed for any one incident photon energy, for which $\sim$ 14 minutes computational time is required.

Calculations are carried out at nine photon energies for ^{60}Ni, at 10 MeV intervals in the range E_γ = 35 - 115 MeV, and at 27 photon energies for ^{197}Au, at 5 MeV intervals in the range E_γ = 35 - 165 MeV. The lower photon energy limit of E_γ = 35 MeV is set at a limit below which the quasi-deuteron photon absorption process is expected to become negligible compared to giant resonance excitation. The validity of this cut off is supported by the continuity of the measured total photoneutron cross sections $\left(\sum_{x,y} \sigma(\gamma,xn\ yp), x \geq 1, y \geq 0\right)$ up to E_γ = 30 MeV, with the photon absorption cross section calculated using PICA for $E_\gamma \geq$ 35 MeV (Fig. 5.8). In the energy region $E_\gamma \sim$ 30 MeV the total photoneutron cross section is essentially identical to the total photon absorption cross section for cases where $\sigma(\gamma, p)$ and $\sigma(\gamma, f)$ are small, as for the nuclei considered here. The continuity of the measured and calculated cross sections provides a test of the validity of the absolute cross sections derived from 'PICA'.

Two free parameters are input to the calculations. One is the Levinger parameter, L, generally set to L = 10.3 (see Section 5.4.2). The other is the level density parameter, a, required in the evaporation calculations. This parameter was set at a = A/8, as in Ref. 155 ,

and in accord with the general trend of the parameter values obtained from fits of level density formulae to experimentally obtained level schemes. Such a parameterisation omits any shell closure effects.

The probability and kinematics associated with the primary (quasi-deuteron) interaction and secondary (nucleon-nucleon) interactions are determined from experimental free particle scattering cross sections. The Pauli exclusion principle is taken into account by ensuring that no interactions are allowed which leave any nucleon with a kinetic energy below the Fermi energy. Furthermore, no nucleon with a kinetic energy below a certain cut-off value is allowed to escape from the nucleus during the cascade. This value is set at the particle Coulomb barrier energy, for protons, and is zero for neutrons. The cascade stage of the calculation ceases when all excited nucleons have an energy below their respective cut-off energies. The total energy of these nucleons is then considered as the excitation energy of a compound nucleus, and particle evaporation is calculated using a development of Weisskopf's evaporation theory by Dostrovsky[157] and Dresner[187]. As at the cascade stage, Monte Carlo techniques are applied, and the probability of selecting a particular particle type within a certain kinetic energy range is determined from the relative decay widths for the open decay channels. Consequently, a definite evaporative particle decay and residual nucleus is assigned to each cascade which produces a compound nucleus, and a large number of cascades must be followed to construct the required evaporation particle spectra. The average alpha particle evaporation yield is low compared to that for neutrons and protons, (Fig. 5.9). Thus the calculations required to build up alpha particle evaporation spectra using Monte Carlo techniques are particularly time consuming. In particular this technique is evidently inappropriate for the calculation of post-cascade alpha emission in heavy nuclei.

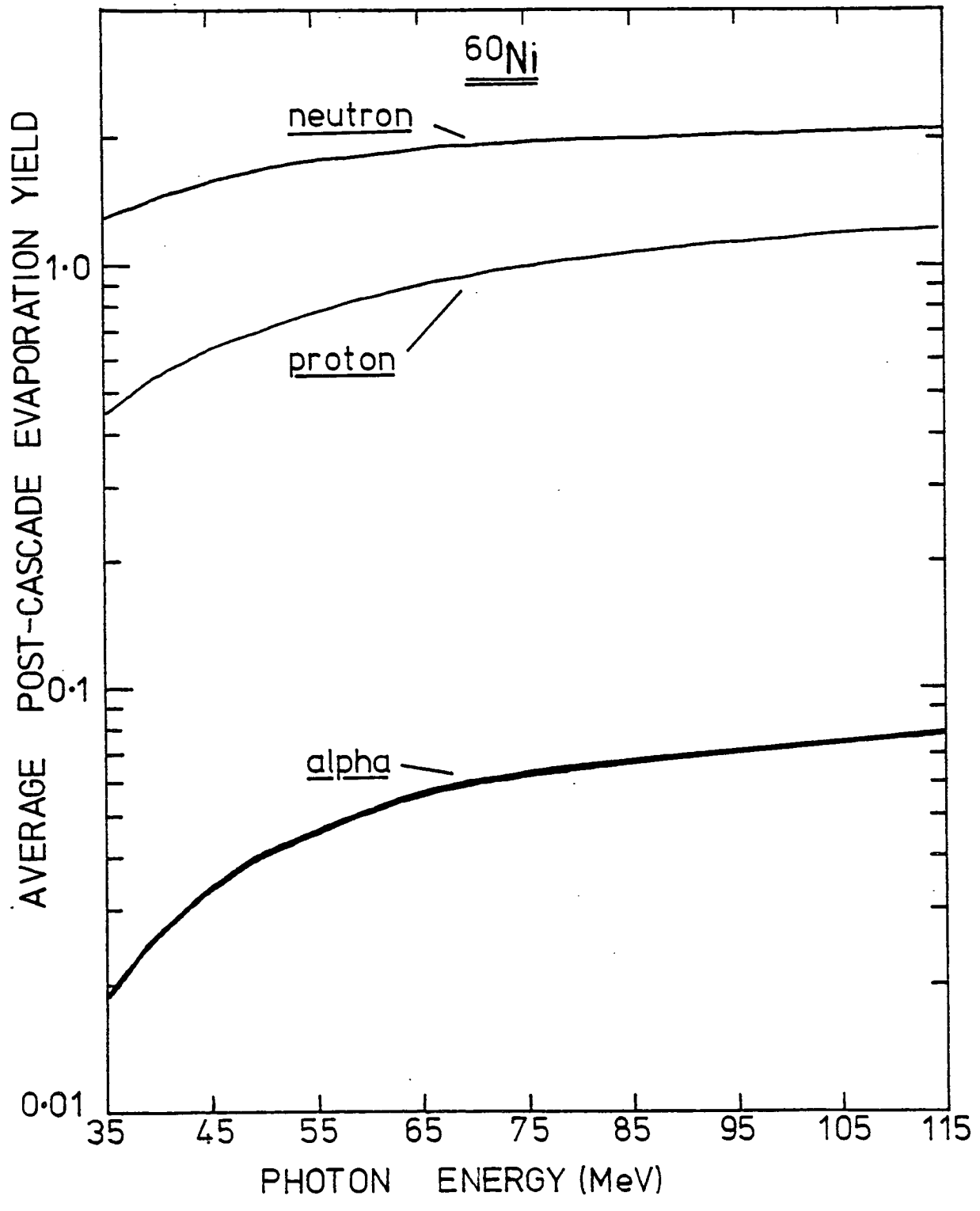

Figure 5.9. Average post-cascade evaporation yields per inelastic event for neutrons, protons and alpha particles emitted from a ^{60}Ni target nucleus. The yields are calculated using the cascade-evaporation code, PICA (see text).

For ^{197}Au at most one alpha evaporation event per 400 cascades is recorded with $E_\gamma < 120$ MeV, and no events are obtained in over 42,000 cascades with $E_\gamma < 70$ MeV. Thus, only an upper limit can be set on this reaction component in gold. In contrast, medium weight nuclei have an average alpha particle evaporation yield of ~ 0.05 alphas per compound nucleus ($E_\gamma = 45 - 95$ MeV) and a spectrum composed of $\sim 2,500$ events is obtained for ^{60}Ni after $\sim 50,000$ cascades.

Alpha evaporation spectra were calculated at nine photon energies ($E_{\gamma,i}$, i = 1-9) spaced at intervals of $\Delta E_\gamma = 10$ MeV, over the range $E_\gamma = 35 - 115$ MeV. The typical spectrum shape obtained is shown in Fig. 5.10 where the spectrum at $E_\gamma = 95$ MeV is compared with the form of spectrum obtained for giant dipole resonance alpha decay at $E_e = 120$ MeV, as described in Section 4.2. In both cases residual nucleus recoil is taken into account, and centre of mass to laboratory frame transformation effects are negligible. The higher energy peak position of the post-cascade alpha spectrum is attributed to both the higher excitation energies associated with that evaporation process, and the differing parameterisation of the Coulomb barrier in the two calculations.

Cross sections for the (e,α) reaction are calculated here, taking account of only quasi-deuteron photon absorption processes with $E_\gamma > 35$ MeV, and by weighting the energy spectrum calculated at each photon energy $\frac{d\sigma}{dE_\alpha}(E_{\gamma,i})$, by the appropriate E1 distorted wave virtual photon spectrum[67], $N^{E1}(E_{\gamma,i}, E_e)/E_{\gamma,i}$. Assuming isotropic particle emission,

$$\frac{d^2\sigma}{dE_\alpha d\Omega} = \frac{1}{4\pi} \sum_{i=1}^{9} \frac{N^{E1}(E_{\gamma,i}, E_e)}{E_{\gamma,i}} \cdot \frac{d\sigma}{dE_\alpha}(E_{\gamma,i}) \cdot \Delta E_\gamma \quad . \qquad (5.12)$$

The calculated spectrum is shown in Fig. 5.11 for $E_e = 120$ MeV, and

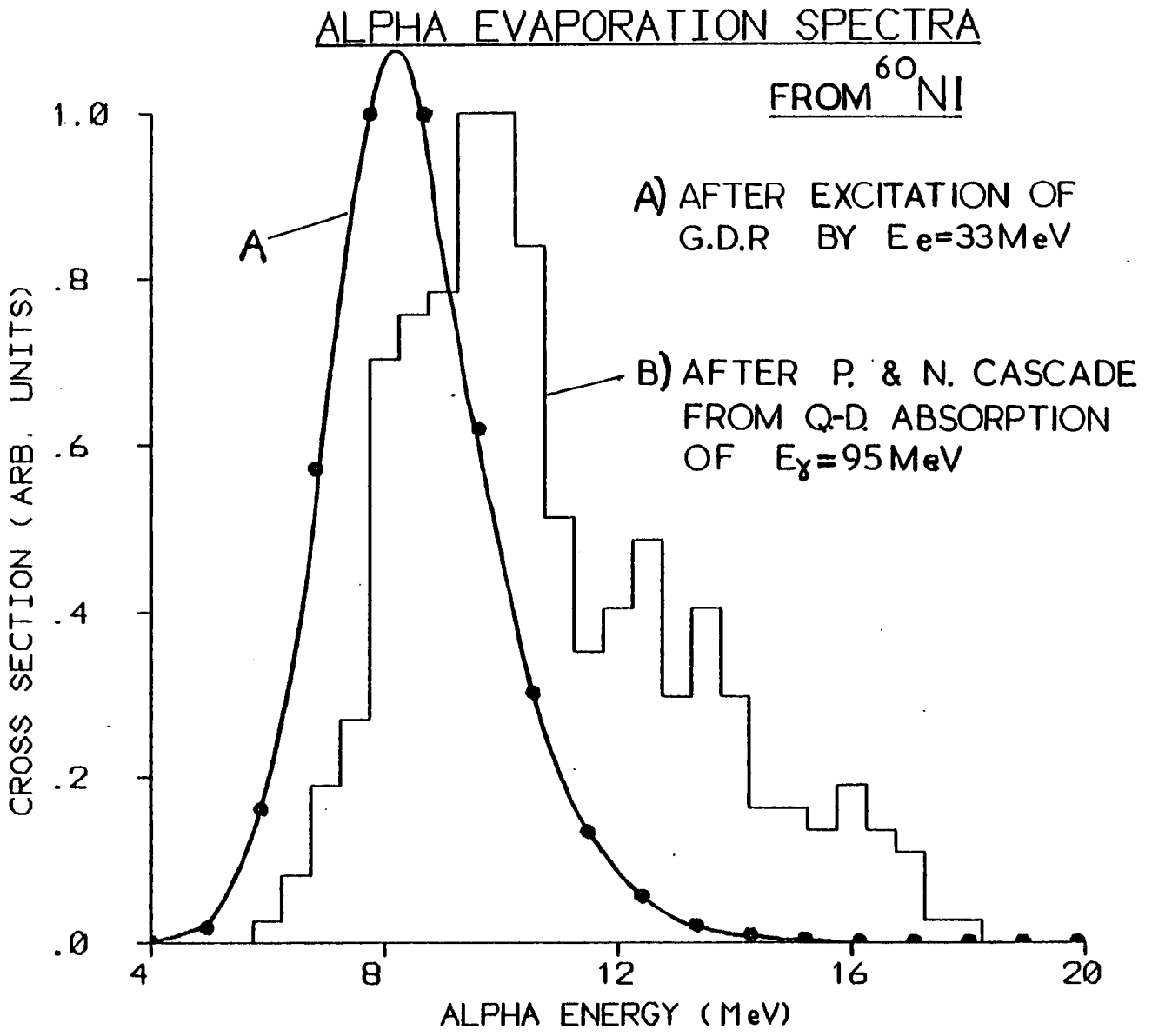
ALPHA EVAPORATION SPECTRA
FROM ^{60}NI
A) AFTER EXCITATION OF G.D.R BY Ee=33MeV
B) AFTER P. & N. CASCADE FROM Q-D. ABSORPTION OF Eγ=95MeV
A
CROSS SECTION (ARB. UNITS)
1.0
.8
.6
.4
.2
.0
4
8
12
16
20
ALPHA ENERGY (MeV)

Figure 5.10.

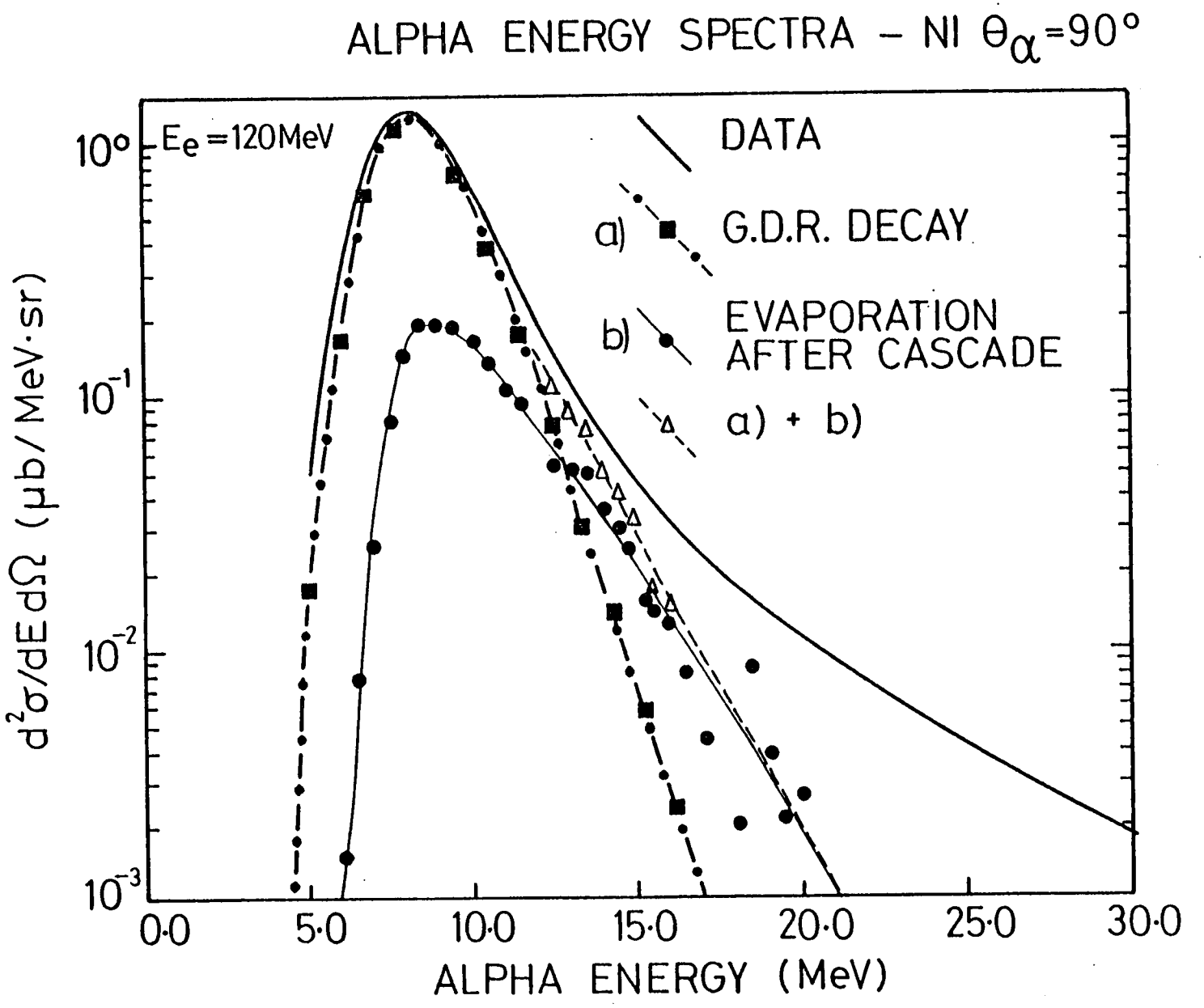

Figure 5.11. Calculated G.D.R. and post-cascade evaporation contributions to (e,α) energy spectra at 120 MeV electron energy.

is up to 50% of the observed cross section for E_α = 10 - 15 MeV. In contrast the upper limit for post-cascade alpha emission from 120 MeV electrons on gold is 10^{-3} μb/MeV.sr at E_α = 21 MeV, amounting to only 1.5% of the observed average cross section for E_α = 20 - 25 MeV.

It is concluded that the extent of intranuclear interactions predicted by the cascade evaporation calculations, and the resulting compound nuclei, produce contributions to the evaporation spectra compatible with the observed spectra. The calculated contributions are a significant component of the observed spectra for medium weight nuclei, but negligible in heavy nuclei. In both the medium and heavy nuclei considered there remains a significant high energy component which must arise from alpha emission before equilibrium is established. In the absence of any quasi-elastic scattering cascade calculations which include alpha emission, and given the non-trivial nature of the adaptation of existing calculations, no assessment is made here of the pre-equilibrium alpha emission component predicted using a Monte Carlo cascade approach.

5.4.4 The Quasi-equilibrium Exciton Model

In recent years the most extensively applied technique for the calculation of pre-equilibrium decay spectra has been the exciton model. Originally formulated by Griffin[152] the model has been extensively developed and refined by many authors[151]. It replaces the geometry dependent approach of the Monte Carlo cascade calculations with phase space considerations for which it is only necessary to follow the energy partitions between excited particles as the cascade proceeds towards equilibrium. The cascade is initiated by creation of a state with p_o excited particles and h_o holes, (p_o, h_o), which sum to give $n_o = p_o + h_o$ excitons. The initial

particle-hole state is determined by the initial interaction. For nucleon induced reactions a (2,1) initial state is generally used. The cascade is considered to proceed only by two body interactions which lead to either the creation of a particle-hole pair ($\Delta p = \Delta h = +1$), the annihilation of a particle-hole pair ($\Delta p = \Delta h = -1$), scattering between excitons ($\Delta p = \Delta h = 0$), or the emission of a particle or cluster of particles from continuum states. A quasi-equilibrium approach is invoked in the determination of the exciton state particle hole distributions. The state densities are calculated using equidistant Fermi gas levels and each possible partition of energy over the n excitons is assumed to have equal probability. Thus a statistical, or quasi-equilibrium, assumption is implied for each exciton state. This statistical assumption and use of an 'equal spacing' model introduces substantial errors into the calculations for light nuclei and nuclei near shell closures.

The transition rates, $\lambda_{nn'}$, between exciton states, are generally calculated using,

$$\lambda_{nn'} = \frac{2\pi}{\hbar} |M|^2 \rho_{n'} , \qquad (5.13)$$

where $\rho_{n'}$ is the number of accessible final states, and $|M|^2$ is an average squared two-body transition matrix, used for all two body transitions during the cascade. Other approaches to the calculation of transition rates have applied free nucleon-nucleon scattering cross sections to calculate an average effective cross section, $\langle\sigma\rangle$ for intranuclear collisions, which then gives,

$$\lambda_{+}^{NN} = \left[\frac{2(\varepsilon + V)}{mc^2}\right]^{\frac{1}{2}} \rho\langle\sigma\rangle \qquad (5.14)$$

where ρ is the density of nuclear matter, V is the real volume optical potential and ε is the channel energy for the nucleons of mass m. The transition rates can also be related to the nucleon scattering volume imaginary optical potential, W. If $\varepsilon + V >> W$, then it can be shown[188],

$$\lambda_+^W = \frac{2W}{\hbar} \quad . \tag{5.14}$$

Here, the approach followed uses an average two-body transition matrix by applying the empirical expression[189],

$$|M|^2 = K E^{-1} A^{-3} ,$$

E - excitation energy

A - nucleon mass number.

A detailed evaluation of the transition matrix elements would require knowledge of the exciton state wave functions and nucleon interaction operators. The absence of this knowledge has led to use of an empirically obtained average matrix element, with the constant 'K' determined by fits to nucleon induced nucleon emission pre-equilibrium spectra. The simplifications introduced into the calculations by this parameterisation of the transition rates, and the resulting ease of application to any nuclei has led to widespread use of this approach. However, its application may result in overestimates of pre-equilibrium components if substantial direct reactions are present in the nucleon induced reactions from which the average matrix elements are derived.

The value, $K \sim 200$ MeV^3, yields nucleon induced nucleon spectra in good agreement with experimental data[189]. Furthermore, this value corresponds to intranuclear transition rates of $\sim 10^{22}$ sec^{-1}, in general agreement with the rates deduced from nucleon optical model parameters (expression 5.14) taken together with nucleon mean free paths, $\bar{\lambda}$,

of 4 fm ($\bar{\lambda} \approx 1/\rho \cdot \langle\sigma\rangle$).

Particle emission rates into the continuum are calculated using the principle of detailed balance, as described in Ref. [190]. Complex particle emission rates have been found to require the addition of a complex particle formation probability in order to reproduce the observed cross sections. This formation probability factor has been set by various authors at either i) a factor proportional to p_β [189], where p_β is the number of particles in the complex particle of type β, or, ii) $\gamma_\beta\ \omega(p_\beta, 0, E)/g_o$ [171], where ω/g_o is the number of configurations of p excitons with total excitation energy, E, and γ_β is the probability that a group of p_β nucleons formed in the nucleus has the right momentum to undergo emission as an entity. The parameters, γ_β, have been obtained for nucleon induced complex particle emission[191] and thus can be tested for applicability to the present data for photonuclear reactions. The extraction procedure for the complex particle formation probabilities assumes that all the observed complex particle emission arises from non-direct reaction components, and thus may result in an overestimate of the calculated pre-equilibrium component.

The formalism and parameters used to calculate particle decay probabilities by the exciton model approach are summarised in Appendix II. The application of the exciton model to photoreactions is considered in the next section.

5.4.4.1 Exciton Model Application to Photonuclear Reactions

The exciton model has had limited application to photonuclear reactions principally due to the shortage of appropriate experimental data. All previous applications have considered only nucleon emission. Luk'yanov et al.[192] compared exciton model results with photoneutron spectra from ^{181}Ta, ^{197}Au and ^{209}Bi irradiated with bremsstrahlung of

20 MeV end point energy. In this energy range a significant pre-equilibrium component was observed in the nucleon spectra, and its shape was reproduced by the exciton model calculations. Since the photon absorption cross section for these reactions was dominated by giant dipole resonance effects a 1 particle - 1 hole doorway state was used to characterise the collective (1p, 1h) dipole excitation states (see Section 1.4.3). Empirical correction factors were applied to the transition probabilities to inhibit transitions to higher exciton number states and thus account for the comparatively long life of the (1p, 1h) giant resonance states. The empirical correction factors are used to enhance the transition probabilities for the $n = 4 \rightarrow n = 2$, and $n = 2 \rightarrow n = 2$ transitions. Once the reaction proceeds past the $n = 4$ state the process is calculated using a normal exciton formalism with no other enhancement of states. The enhanced (1p, 1h) states result in a significant pre-equilibrium nucleon yield in comparison to the negligible alpha emission component, which can only arise from $p > 4$ exciton states. The model is therefore capable of accounting for the absence of an observable high energy (pre-equilibrium) component in alpha decay of the giant resonances, whilst allowing for a substantial pre-equilibrium nucleon component. Pre-equilibrium alpha emission is therefore only significant compared to equilibrium alpha emission for excited states above the giant resonance region.

At excitation energies above the resonance region the doorway exciton state is considered to be $(p_o,h_o) = (2,2)$, in accord with the two particle quasi-deuteron excitation mechanism considered valid for $E_\gamma \gtrsim 35$ MeV. This approach has been followed by Wu and Chang[171] who have obtained exciton model results in excellent agreement with the

shape and magnitude of photoneutron spectra arising from 55 - 85 MeV bremsstrahlung difference photons. No long lifetime collective states are considered to be dominant above $\sim$ 35 MeV, hence no enhancements of transitions to the doorway state are required, and the calculation of nucleon and complex particle emission proceeds as in the case of particle induced reactions, but with a differing initial particle hole state.

In cases where bremsstrahlung or electron induced reactions are considered, the photon energy dependence of the total photon absorption cross section, $\sigma_\gamma(E_\gamma)$, must be included in the calculation since it has an effect on the spectrum shape in addition to the absolute values. In the case of monochromatic photon reactions the spectrum shape is obviously independent of the photon absorption cross section, which could be left as a free parameter, allowing normalisation to the experimental data. The present test of the exciton model uses the Wu and Chang formulation[171] and thus expression (5.10) with the quenching factor of expression (5.11) and a proportionality constant of 10.3. The Wu and Chang parameterisation of the photon absorption cross section could be refined by applying a more rigorous correction for Pauli blocking effects (see Section 5.3.2). However, at the electron energy considered here, such a correction is likely to cause only small changes in the lower energy portion of the calculated pre-equilibrium spectra.

The calculation of emitted particle spectra for the (e,α) reaction requires the folding of a plane wave virtual photon spectrum, $N^{E1}(E_\gamma, E_e)$, (assuming only dipole photon absorption) into the calculated alpha energy spectra, over all photon energies up to the electron energy,

$$\frac{d\sigma}{dE_\alpha}(E_e) = \int_0^{E_e} \frac{N^{E1}}{E_\gamma}(E_\gamma, E_e)\sigma_\gamma(E_\gamma) I_\alpha^{PEQ}(E_\gamma, E_\alpha) dE_\gamma \qquad (5.16)$$

where $I_\alpha^{PEQ}(E_\gamma, E_\alpha)$ is the probability of pre-equilibrium emission of an alpha particle with an energy in the range E_α to $E_\alpha + dE_\alpha$, at excitation energy E_γ. Expressions for I_α^{PEQ} are given in Appendix 11. To reduce computation times the integral in equation (5.16) is obtained using Gaussian quadrature. The use of a plane wave virtual photon spectrum means Coulomb distortion and finite nuclear size effects on the photon spectra are neglected. These effects are expected to cause only small changes (< 10%) to the calculated spectral shape, although absolute magnitudes may be overestimated by up to ∿ 40% due to their omission. However such correction factors are not important here since uncertainties in the determination of the alpha particle formation probabilities and the average two-body transition matrix elements do not allow accurate calculation of absolute cross sections.

5.4.4.2 Exciton Model (e,α) Energy Spectra

Energy spectra calculated using the Wu and Chang exciton model code 'PREQEC' are presented in Fig. 5.12 for ^{60}Ni and ^{197}Au. In both cases the calculated results are normalised to the data. The spectrum shapes are in reasonable agreement with the data, particularly for ^{197}Au; however the spectrum for ^{60}Ni overestimates the high energy component. Such an overestimate is found to be even more pronounced for ^{27}Aℓ. This lends further weight to the suggestion (Section 5.2.2) that light element high energy alpha emission arises primarily from statistical compound nucleus decays. The spectrum shapes obtained from

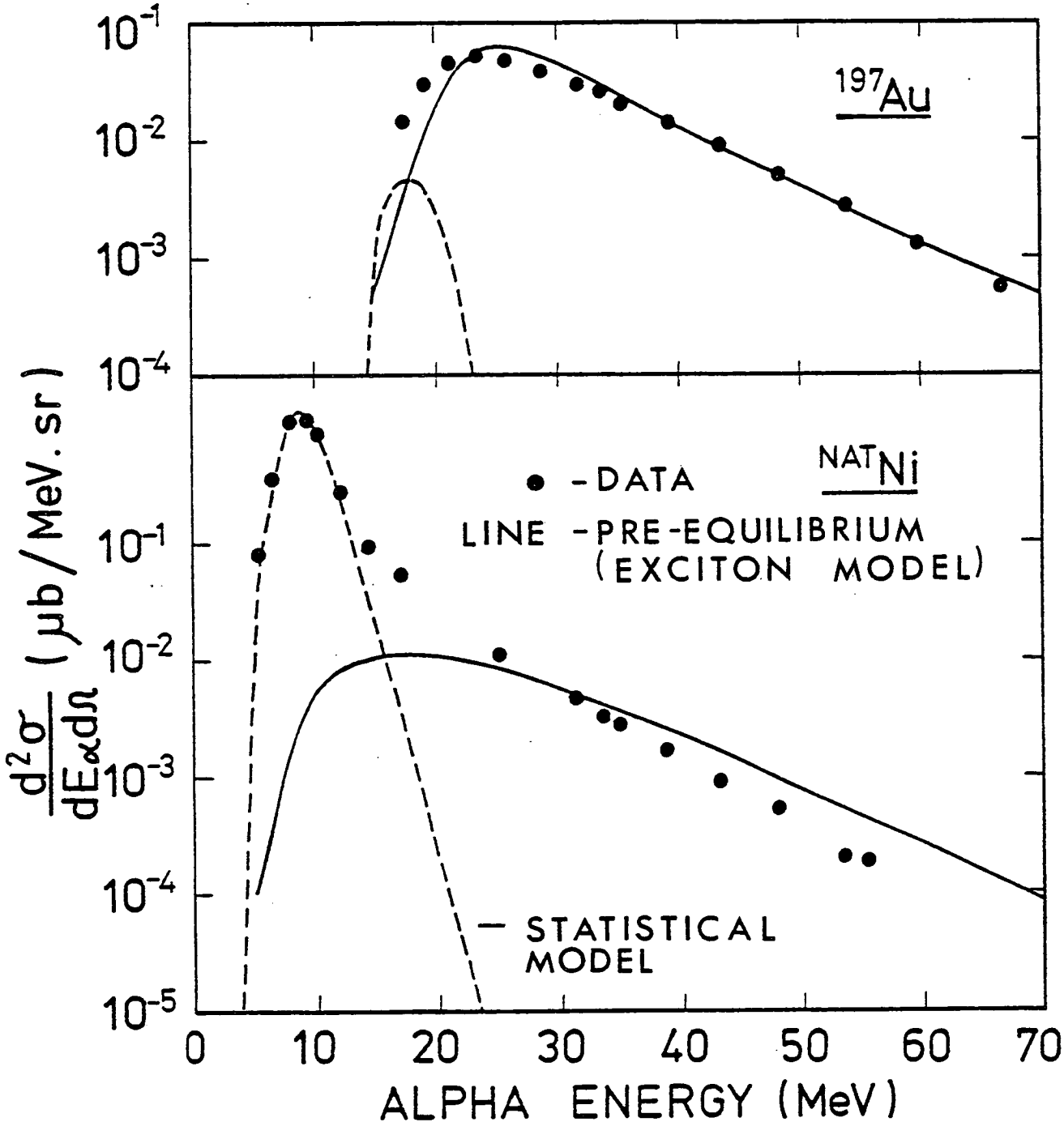

Figure 5.12. Alpha particle energy spectra at $\theta_\alpha = 30^\circ$, for $E_e = 120$ MeV. The solid circles are experimental points. The solid lines are the results of pre-equilibrium exciton model calculations and the dashed lines are the results of statistical calculations neglecting photon absorption above $E_\gamma = 33$ MeV.

exciton model calculations are strongly dependent on the initial exciton number[190]. A lower initial exciton number than used would lead to an even greater discrepancy in the predicted spectrum shapes for light and medium weight nuclei.

The calculations are performed using identical input parameters to those which produced a good reproduction of both the shape and magnitude of (γ, n) spectra in Ref. 171, and the complex particle formation probabilities are obtained from the fits to nucleon induced complex particle spectra in Ref. 191. It might therefore be expected that error in the calculated absolute cross section will arise mainly from the virtual photon intensity and photon absorption cross section. Together these might lead to an overestimate of the absolute magnitude of at most a factor of two. However, the calculated cross sections for $^{27}A\ell$, ^{60}Ni and ^{197}Au were respectively factors of 8, 4 and 10 above the experimental values. This overestimate most probably arises from the (p,α) formation probabilities being inapplicable to (e,α) reactions. The neglect of direct (p,x) components when fitting the nucleon induced data may lead to an overestimate of the formation probabilities, since pick-up and knock-out reactions may be large components in (p,α) spectra[197]. Such an overestimate might be expected to be evident when comparisons are made with photonuclear reactions, since these are volume interactions in comparison to the peripheral nature of nucleon induced reactions which occur in the nuclear region with high alpha cluster probabilities.

It is concluded that the exciton model can reasonably reproduce the shapes of the observed alpha energy spectra. Improvements to the parameterisation of the photon absorption cross section may lead to better fits to the observed spectral shapes in medium weight nuclei. No definite predictions arising from the model are in conflict with

experimental observations in medium weight and heavy nuclei, and therefore it provides a plausible description of the reaction process at high excitation energies in such nuclei. However, the model cannot provide any prediction of absolute cross sections and therefore the possibility of other competing or even dominant reaction mechanisms cannot be ruled out. A necessity to employ different complex particle formation probabilities for (N,α) and (e,α) reactions has been identified. This suggests a lower alpha emission probability relative to nucleon emission, for photonuclear reactions, compared to particle induced reactions.

5.4.5 Three Particle Pick-up Effects

The exciton model is based on sequential two body interactions and hence the only 'direct' effect that it includes, leading to alpha emission, is sequential three particle pick-up. The one step triton pick-up process, or any steps involving two nucleon cluster pick-up processes are excluded in exciton model formulations which permit only nucleon excitons.

Early studies of (p,α) reactions[193] to low lying final states showed that the pick-up reaction dominated knock-out components, and comparison of experimental data with D.W.B.A. calculations provided evidence that pick-up of a quasi-triton is the dominant reaction mechanism for many (p,α) reactions to low lying final states. More recently, semi-microscopic D.W.B.A. calculations, using mass-three cluster wave functions, have successfully reproduced observed reduced transition strengths[194].

The observation that similar single proton states are populated in (p,α) and (t,α) reactions has led to the inference that the (p,α) reaction may be considered as a two step process in which a di-neutron

and single proton are sequentially picked up. Calculations which factor the proton and di-neutron amplitudes are successful for some nuclei[195),196)], and it is evident that the nature of the dominant three nucleon pick-up mechanism is strongly dependent on nuclear structure effects.

It is evident that pick-up processes are important in (p,α) reactions to low lying residual nucleus states, and thus may contribute substantially to the pre-equilibrium continuum arising during a nucleon cascade. Kalbach has attempted to estimate the magnitude of such a component in (p,α) reactions, relative to exciton model and knock-out contributions[197)]. However, all components considered required the use of normalisation factors and thus conclusions were mainly dependent on the spectrum shapes. Kalbach concluded that pick-up effects dominated knock-out effects for incident protons at energies of a few tens of MeV. The knock-out component had the wrong energy dependence to make it the dominant contribution. Furthermore, the form of experimental (p,α) energy spectra for E_p = 29-62 MeV, were well reproduced by Kalbach's calculated (p,α) pick-up spectra. These conclusions contradict the quasi-free scattering calculations of Blann[163)], and Gadioli et al.[199)] (see Section 5.4.3.1), which assume that alpha emission occurs only if a cascade nucleon interacts with a preformed alpha cluster. Such calculations were found to reasonably reproduce the observed emitted alpha particle energy spectra.

It is likely that a direct one step or two step pick-up component contributes to the (N,α) step of the two step (e,N) - (N,α) process suggested here. However, presently available calculations do not yield the absolute magnitude of this component. Evidently a detailed study of the reaction components which contribute to the (N,α) continuum, requires to be undertaken to settle which is the dominant mechanism leading to alpha emission, and to remove the apparent contradictions which

presently exist. Only when that is concluded can realistic calculation be undertaken to ascertain the dominant mechanism in the high energy (e,α) reaction.

5.5 Photon Energy Dependence of the High Energy Alpha Emission Cross Section

The predictions of various photonuclear reaction models should ideally be compared with experimental data obtained for various fixed absorbed photon energies, over the excitation energy region of interest. Such a comparison provides a test of the predicted photon energy dependence of the required particle decay cross sections, and avoids the averaging of the reaction model predictions over excitation energy, which occurs with calculations of electron or bremsstrahlung induced particle emission cross sections. The photon energy dependence of the high energy alpha emission cross section, $\sigma_\alpha(E_\gamma)$, should ideally be obtained using a monochromatic photon source, to avoid the use of bremsstrahlung or virtual photon formulae. However, such a source can only be obtained from high duty cycle ($\sim$ 100%) electron accelerators using photon tagging, or coincidence techniques, or alternatively by positron beam annihilation. In the absence of the availability of these techniques, and noting that the low cross sections encountered in the present studies exclude the use of photon difference techniques to yield a "pseudo" monochromatic photon source, the required photon absorption cross sections are unfolded from electron induced alpha emission excitation functions. This procedure is described in the next section.

The photon energy dependences of the cross sections for the emission of 15, 20 and 25 MeV alpha particles from ^{60}Ni are derived here from the excitation functions presented in Fig. 3.13. The derived cross sections

are then compared with the predictions of the exciton model and a simple one step particle emission statistical model.

The unfolding technique employed to derive the cross sections, $\sigma_\alpha(E_\gamma)$, requires either, (i) only one contributing multipole component, or (ii) a reasonable prediction to be made of the relative contributions of different multipoles. Since the electric dipole (E1) sum rule strength considerably exceeds all other multipole sum rules, multipolarities other than E1 are neglected. As long as no high multipolarity narrow resonances are present in the energy range considered, the presence of higher multipolarity components will not alter conclusions made about the form of $\sigma_\alpha(E_\gamma)$ since higher multipolarity virtual photon spectra are of a similar form over the energy ranges considered here. Only the presence of electric monopole, or unexpectedly large high multipolarity contributions would change the cross section forms resulting from the unfolding procedure. The assumption made for the present analysis, of a pure E1 absorption process, can be tested in future work by the comparison of bremsstrahlung and electron induced reaction cross sections.

5.5.1 Unfolding of Excitation Functions

The excitation functions comprise a series of (e,α) cross section measurements at electron energies E_i. Assuming that only electric dipole excitation need be considered, the (e,α) cross section is given in terms of the E1 virtual photon intensity, N/E_γ, and the photon absorption cross section $\sigma(E_\gamma)$, by

$$\sigma_{e,\alpha}(E_i) = \int_{\text{Thr.}}^{E_i} \sigma(E_\gamma) \frac{N(E_i,E_\gamma)}{E_\gamma} dE_\gamma \quad . \qquad (5.17)$$

Alternatively, by dividing the integration range into n intervals from

$E_{j-1} \rightarrow E_j$, and letting E_o be the threshold energy,

$$\sigma_{e,\alpha}(E_i) = \sum_{j=1}^{n} \int_{E_{j-1}}^{E_j} \sigma(E_\gamma) \frac{N(E_i,E_\gamma)}{E_\gamma} dE_\gamma \quad . \qquad (5.18)$$

If the virtual photon intensity $N(E_i,E_\gamma)/E_\gamma$ is slowly varying over each energy division then,

$$\sigma_{e,\alpha}(E_i) \approx \sum_{j=1}^{n} \frac{2 \cdot N\left[E_i, (E_{j-1} + E_j)/2\right]}{E_{j-1} + E_j} \int_{E_{j-1}}^{E_j} \sigma(E_\gamma) dE_\gamma \qquad (5.19)$$

or more simply,

$$\sigma_{e,\alpha}(E_i) = \sum_{j=1}^{n} N_{ij} \, \bar{\sigma}_j \, \Delta E_j \qquad (5.20)$$

where

$$N_{ij} = \frac{2 \cdot N\left[E_i, (E_{j-1} + E_j)/2\right]}{E_{j-1} + E_j}$$

is the 'central' virtual photon intensity over the photon energy range, $E_{j-1} \rightarrow E_j$, for electron energy E_i. The average photon absorption cross section, $\bar{\sigma}_j$, in the interval $E_{j-1} \rightarrow E_j$ is related to the photon absorption cross section $\sigma(E_\gamma)$ by

$$\bar{\sigma}_j \, \Delta E_j = \int_{E_{j-1}}^{E_j} \sigma(E_\gamma) dE_\gamma$$

where $\Delta E_j = E_j - E_{j-1}$.

Equation (5.20) can be re-written to give an expression yielding

$$\bar{\sigma}_j = \frac{1}{\Delta E_j} \sum_{i=1}^{n} N_{ij}^{-1} \, \sigma_{e,\alpha}(E_i) \quad . \qquad (5.21)$$

Thus, if n measurements of the (e,α) cross section are made at intervals ΔE_j an average photonuclear cross section $\bar{\sigma}_j$ can be derived for each such interval. In general the intervals ΔE_j must be considerably smaller than the interval over which any structure might be observed. Studies of photon absorption cross sections over the giant resonance region, where resonances of width 4 - 6 MeV are encountered, require $\Delta E_j \lesssim 1$ MeV. In this thesis work the only excitation functions unfolded relate to particle emission following excitation to energies above the peak energy of the giant resonance. In this region it is assumed that the photon absorption cross section is smooth and structureless, thus, values of $\Delta E_j \gtrsim 5 - 10$ MeV were used for $j \neq 0$. The size of the first interval, ΔE_o, is dependent on the lowest electron energy at which data could be obtained within reasonable run times and with a tolerable peak to background ratio. The difference between that electron energy, and the threshold for emission of alpha particles of the energy under consideration, yields ΔE_o. The excitation functions for $E_\alpha \sim 15$ MeV and $E_\alpha \sim 20$ MeV have $\Delta E_o \sim 6$ MeV, whereas for $E_\alpha \sim 25$ MeV, $\Delta E_o = 23$ MeV is employed. Consequently, only an average cross section is obtained for the production of 25 MeV alpha particles up to 23 MeV above threshold.

The unfolding of excitation function data with random statistical error, $\delta\sigma(E_i)$, generally leads to large fluctuations between neighbouring values of $\bar{\sigma}_j$ when derived according to expression (5.21). Such fluctuations are found to arise with the present excitation function data, as illustrated by the solid histograms in Figs. 5.13 - 5.15. The fluctuations can be considerably reduced, and the unphysical negative cross section solutions removed, if an unfolding technique is applied which finds the smoothest set of $\bar{\sigma}_j$ compatible with the data allowing for the experimental errors. Such a technique is Cook's Method of Least

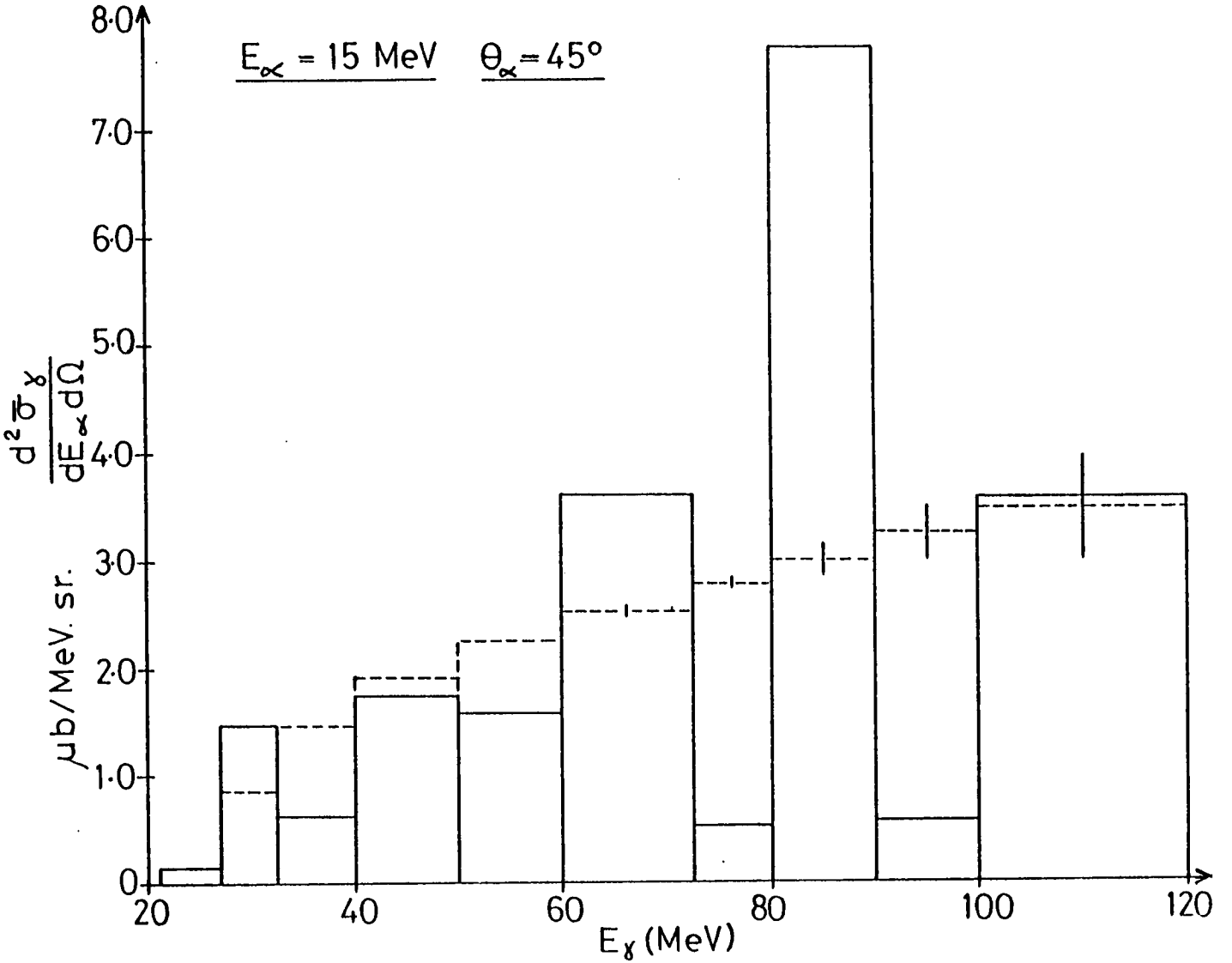

Figure 5.13. Photoalpha cross sections unfolded from the ^{60}Ni, $E_\alpha \sim 15$ MeV (e,α) excitation function. The solid histograms are the unsmoothed results and the dashed histograms are derived using Cook's Method of Least Structure (see text).

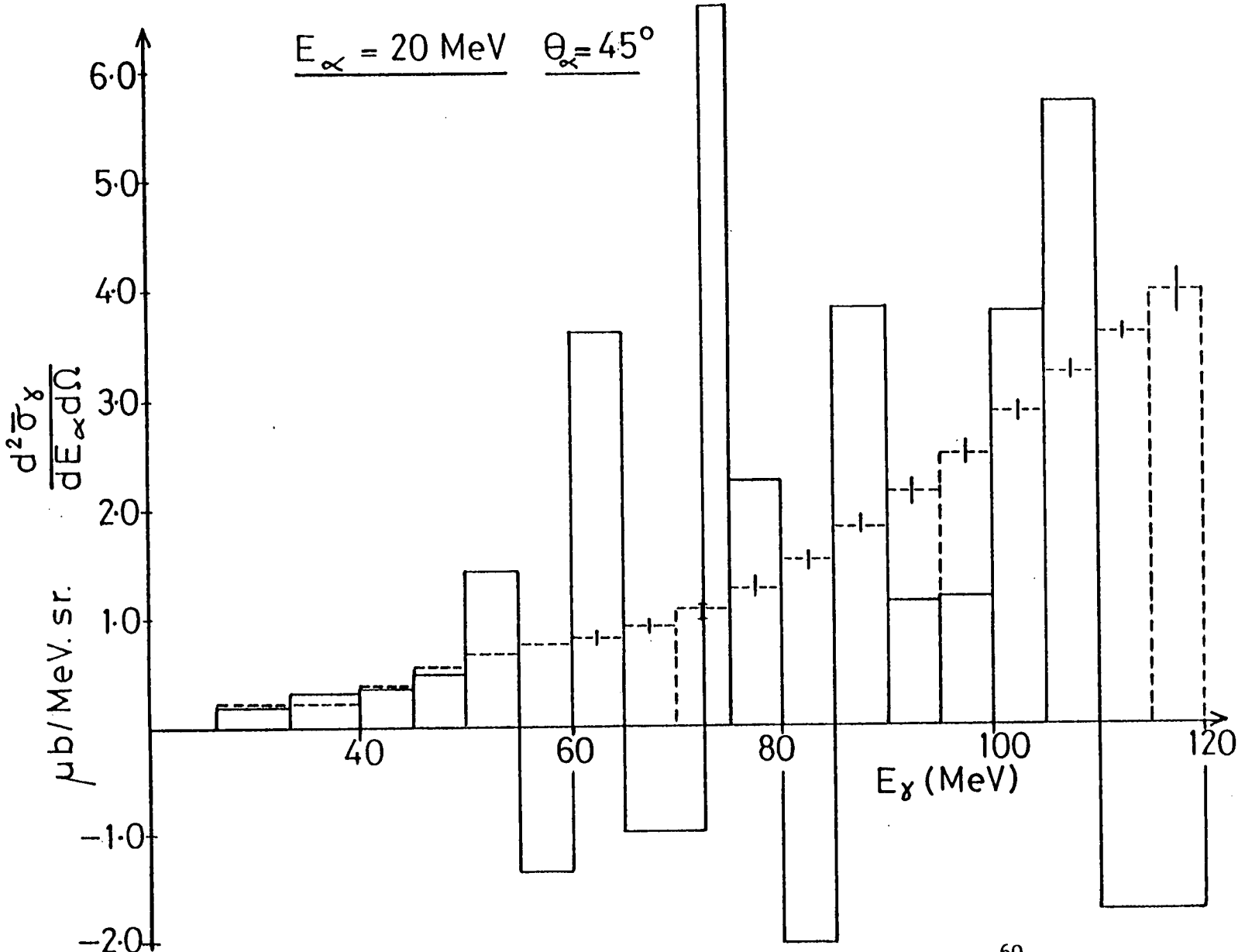

Figure 5.14. Photoalpha cross sections unfolded from the ^{60}Ni, $E_\alpha \sim 20$ MeV (e,α) excitation function. Histograms

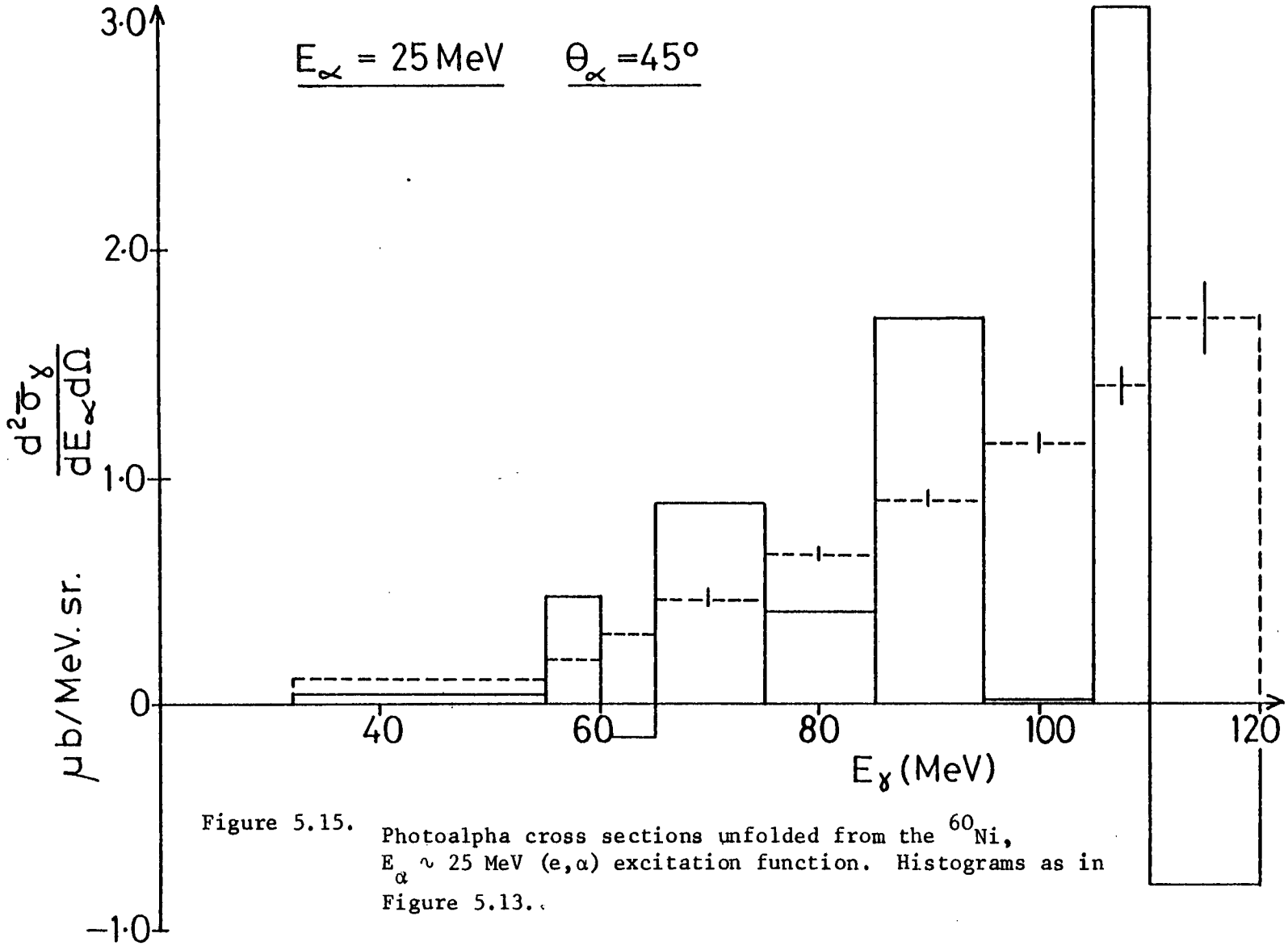

Figure 5.15. Photoalpha cross sections unfolded from the ^{60}Ni, $E_\alpha \sim 25$ MeV (e,α) excitation function. Histograms as in Figure 5.13.

Structure[198].

A structure function, $S(\bar{\sigma}_j)$, is defined, where

$$S(\bar{\sigma}_j) = \sum_{j=2}^{n-1} (\bar{\sigma}_{j+1} - 2\bar{\sigma}_j + \bar{\sigma}_{j-1})^2 \qquad (5.22)$$

and solutions of $\bar{\sigma}_j$ are sought which minimise $S(\bar{\sigma}_j)$ within the constraint that $\chi^2(\bar{\sigma}_j) = n$, with

$$\chi^2 = \sum_{i=1}^{n} \left\{ \frac{(\sum_{j=1}^{i} N_{ij}\,\bar{\sigma}_j) - \sigma_{e,\alpha}(E_i)}{\delta\sigma_{e,\alpha}(E_i)} \right\}^2 . \qquad (5.23)$$

A totally smoothed solution set of $\bar{\sigma}_j$ has $S(\bar{\sigma}_j) = 0$, and yields $\bar{\sigma}_j(E_j)$ in the form of a straight line of some constant gradient. Solutions which yield $\chi^2 > n$ are oversmoothed, and those with $\chi^2 < n$ are undersmoothed. To obtain optimum smoothing $|\chi^2 - n|$ is minimised.

The values of $\bar{\sigma}_j$ obtained using the above smoothing technique are illustrated in Fig. 5.13 - 5.15 by the dashed histograms. The validity of the smoothed solution is simply checked by applying expression (5.20) to yield the values of $\sigma_{e,\alpha}(E_i)$, corresponding to the derived $\bar{\sigma}_j$, which can be compared with the original experimental values, $\sigma_{e,\alpha}(E_i) \pm \delta\sigma_{e,\alpha}(E_i)$.

The compatibility of the smooth solution of $\bar{\sigma}_j$ with the experimental data indicates that no physical significance can be ascribed to the fluctuations obtained in the unsmoothed solutions of expression (5.21). The necessity of applying a smoothing technique in order to obtain physically reasonable cross section dependences on photon energy illustrates the difficulties inherent in unfolding excitation functions of even the moderate ($\sim$ 7%) statistical accuracy obtained here.

Improved experimental accuracy, data acquired nearer the thresholds, and more closely spaced excitation function data would all contribute to a reduction in the extent of smoothing required. However, since it is reasonable to assume that the alpha emission cross sections, $\sigma_\alpha(E_\gamma)$ are smooth, the derived smoothed cross sections are likely to be an adequate indication of the form of $\sigma_\alpha(E_\gamma)$ for comparison with the predictions of reaction models.

5.5.2 Comparison of $\sigma_{\gamma,\alpha}(E_\alpha,E_\gamma)$ with Equilibrium and Pre-equilibrium Reaction Models

The alpha emission cross section, derived using Cook's Least Structure Method, exhibits a steady increase with increasing photon energy, for each of the three alpha energies considered. In particular, for both 20 MeV and 25 MeV alpha particles, the cross section increases almost linearly above 70 MeV, with the cross section for 20 MeV alpha emission becoming comparable with that for 15 MeV alpha emission when $E_\gamma \sim 110$ MeV. Although the total photon absorption cross section is essentially constant in the energy range under consideration, since the integrated cross section for emission of alpha particles of energies between E_α = 15 MeV - 25 MeV, is at most 3% of the total photon absorption cross section, it is evident that sufficient phase space is available to allow for an alpha emission cross section which increases with photon energy. Indeed, such a cross section dependence is indicated by the form of Γ_α/Γ for one step particle evaporation.

At high excitation energies ($E_x \gtrsim 10$ MeV), total decay widths for a particle β, at excitation energy, E_x, can be approximated using a Fermi Gas level density by the expression,

$$\Gamma_\beta = C\, m_\beta\, (2S_\beta + 1)(E_x - B_\beta)\exp(2a_\beta^{\frac{1}{2}}(E_x - B_\beta)^{\frac{1}{2}})/a_\beta \ , \qquad (5.24)$$

where m, S, B and a, are the mass, spin, emission threshold energy and level density parameter associated with particle β and its decay to the residual nucleus. The parameter, C, is a constant for the given target nucleus, and excitation energy. The decay width for alpha particles of energy ε can be approximated by a similar expression,

$$\Gamma_\alpha(\varepsilon)d\varepsilon = C\, m_\alpha(2S_\alpha + 1)\varepsilon\, \exp(2a_\alpha^{\frac{1}{2}}(E_\alpha - B_\alpha - \varepsilon))d\varepsilon \ . \qquad (5.25)$$

Neglecting those particles with high Q-values, only neutron, proton, and alpha particle channels are considered here for the case of ^{60}Ni, and the appropriate level density parameters[132] and threshold energies are,

$$a_\alpha = 6.75 \ ; \qquad a_n = 5.97 \ ; \qquad a_p = 8.04$$
$$B_\alpha = 6.3 \ ; \qquad B_n = 11.3 \ ; \qquad B_p = 9.53 \ ,$$

The alpha emission cross section is given by,

$$\frac{d\sigma_{\gamma,\alpha}}{d\varepsilon}(\varepsilon, E_x) = \sigma_{CN}(E_\gamma)\ \frac{\Gamma_\alpha(\varepsilon)}{\sum_\beta \Gamma_\beta} \ ,$$

where the total photon absorption cross section $\sigma_{CN}(E_\sigma)$, is that employed in the Oak Ridge photonuclear cascade evaporation calculation (see Fig. 5.8). The values of $\sigma_{CN}(E_\gamma)$ are only slowly decreasing, over the photon energy range considered here, and for simplicity were approximated to a constant 10 mb for nickel. The resulting estimated alpha emission cross sections are shown in Fig. 5.16. Comparison with the experimentally derived alpha emission cross sections indicate that the photon energy dependence is reasonably reproduced, but could be

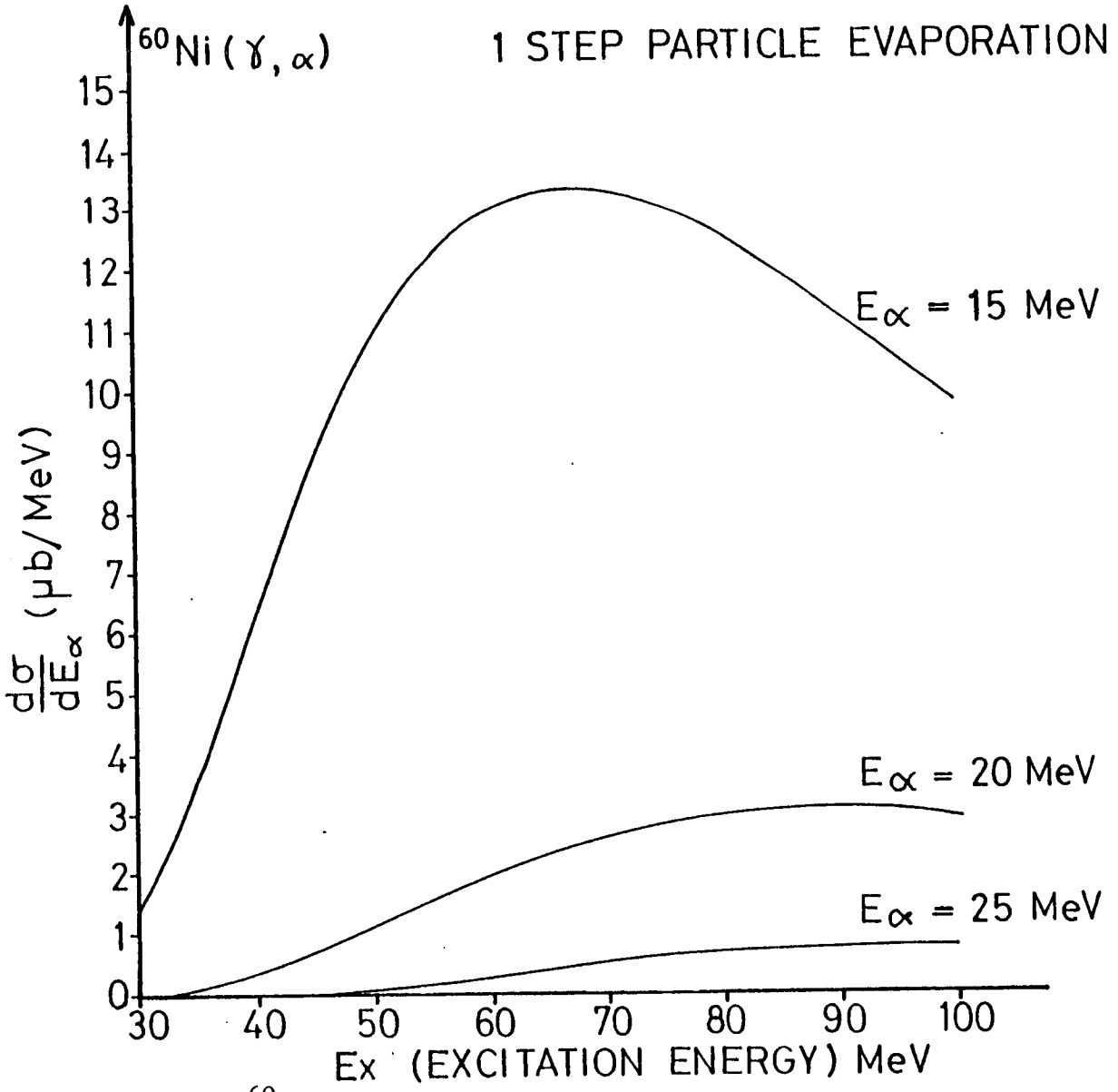

Figure 5.16. ^{60}Ni photoalpha cross sections calculated assuming one step alpha particle evaporation from a compound nucleus excited to the incident photon energy.

improved by the inclusion of mechanisms leading to cross section enhancement at high excitation energies, e.g. multistep alpha evaporation. The estimated magnitudes are in all cases below those observed. Assuming isotropic alpha emission, and even making the assumption of compound nucleus formation prior to any particle emission, the estimated cross sections for $E_\alpha \sim 20 - 25$ MeV are a factor of ten low. At $E_\alpha \sim 15$ MeV, however, the estimated cross section improves to 30-50% of that observed. Since (γ,p) and (γ,n) pre-equilibrium effects are well known, it is evident that the assumption here of 100% compound nucleus formation with excitation energy equivalent to the absorbed photon energy must lead, if anything, to evaporation cross section overestimates. Thus, a further indication is provided of the decline in the evaporation component with increasing particle energy, and the need to include pre-equilibrium reaction components for the alpha emission channel in medium weight nuclei. Additionally, the calculated equilibrium component fails to reproduce the form of the energy spectra deduced for high excitation energies - a shortcoming not rectified by the inclusion of multistep effects, which preferentially enhance lower energy particles.

The exciton model pre-equilibrium formulation, which was applied with some success to electron induced alpha particle spectra in Section 5.4.4.2, yields the photoalpha cross sections for ^{60}Ni presented in Fig. 5.17, using $\sigma_{CN}(E_\gamma) = 10$ mb $(30 < E_\gamma < 100)$. In contrast to the statistical model cross sections, the exciton model results lead to an overestimate of the photoalpha cross section. This overestimate necessitated the normalisation used in Section 5.4.4.2, though this normalisation can be eliminated by a reduction of the alpha particle formation probability employed in the model. However, the form of the photoalpha cross section predicted by the exciton model differs markedly

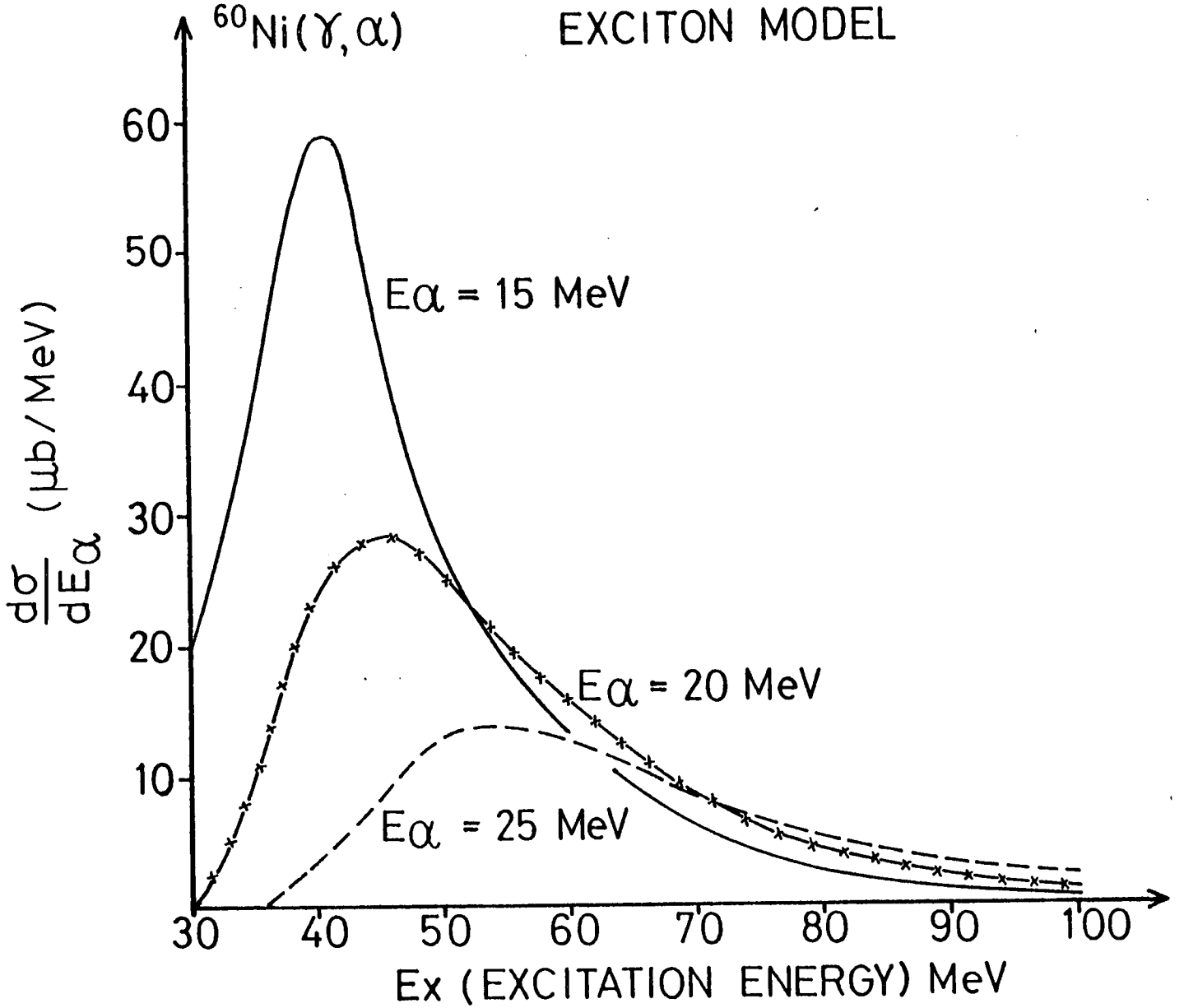

Figure 5.17. Exciton model photoalpha cross sections for ^{60}Ni.

from that derived from the excitation function data. It is important to note that the photoalpha cross sections derived from the excitation functions contain much more reaction information than an energy spectrum taken at one electron energy. Calculations of energy spectra require the reaction model photoalpha cross section to be folded into a virtual photon spectrum. Although the magnitude of the calculated photoalpha cross section must be correct in order to yield absolute agreement with the observed $d\sigma(e,\alpha)/dE_\alpha$, the functional form of $d\sigma_{\gamma,\alpha}(E_\gamma)/dE_\alpha$, required to provide agreement with the observed (e,α) energy spectra at a given electron energy, is not unique. Thus, the agreement of model cross sections with energy spectra obtained at only one electron energy is necessary, but not sufficient to establish the validity of the model's description of the (γ,α) reaction process over a range of electron energies. In the present analysis, the exciton model evidently fails the more rigorous test of comparison with excitation function data. The most encouraging aspect of the exciton model is the form of the energy spectra obtained for $60\ \text{MeV} \lesssim E_\gamma < 100\ \text{MeV}$. In that energy region comparable cross sections are obtained for 15-25 MeV alpha particles, and the peaking of the alpha energy spectrum in that region, at high excitation energy, is qualitatively reproduced. It is primarily the success of the model in predicting the forms of high energy particle spectra, in the excitation energy 60-100 MeV, which has led to its wide acceptance and application. The present work indicates a probable failure of the model to yield the observed excitation energy dependence of the particle emission probabilities, particularly for lower energy ($\sim$ 20 MeV) emitted particles. The present conclusions, however, are dependent on the assumptions that either (i) dipole photon absorption dominates the (e,α) reaction process or, (ii) that if other multipoles are present, they are

non-localised, and their corresponding virtual photon spectra are of similar form (two assumptions which are likely, but respectively await experimental and theoretical justification). The conclusions stated here must therefore be accepted tentatively at present.

A likely cause of any failure of the present exciton model formulation is the omission of multi-chance particle emission. The present formalism allows only one particle to escape at the pre-equilibrium stage. However, the inclusion of multi-chance processes in the exciton model[158] still leaves several serious shortcomings[199]. It must be noted that the exciton model is not a fundamental nuclear reaction theory, but contains only crude estimates of two-body interaction transition probabilities, and a somewhat ad hoc treatment of complex particle emission. In an attempt to remove these latter two difficulties, and place pre-equilibrium reaction models on a more rigorous quantum mechanical basis, Feshbach[200] has recently developed a generalised pre-equilibrium formulation which includes the treatment of quasi-equilibrium systems. The present data will enable future strict tests of this model when applied with an incident photon channel.

CHAPTER 6

SUMMARY

6.1 Conclusions

This study of the (e,α) reaction over a range of nuclei $A = 27 - 197$ using electrons of energies $E_e = 19$ MeV - 120 MeV has yielded new information on alpha particle emission following photon absorption at energies below the pion threshold. In the medium weight nuclei studied the (e,α) reaction proceeds predominantly by statistical decay of the GDR, with full isospin mixing. In ^{60}Ni a component of the observed alpha emission is consistent with GQR alpha decay. This decay branch exhausts $\lesssim$ 7% of the E2 sum rule, in accord with the expectations for GQR statistical decay. There is no evidence that either the GDR or GQR have observable direct alpha decay branches in medium weight nuclei, i.e. $\Gamma_\alpha^\uparrow \sim 0$.

All the nuclei studied exhibit a high energy ($E_\alpha > 25$ MeV) alpha decay component with a magnitude varying as $A^{1.5}$ at 120 MeV electron energy. There is some evidence that in the lightest nucleus studied, ^{27}Al, statistical alpha decay dominates even up to $\sim$ 100 MeV excitation energy. In medium weight nuclei a significant component arises from statistical decay of the residual excited nucleus after pre-equilibrium (or intranuclear cascade) particle emission. Pre-equilibrium alpha decay channels in heavy nuclei dominate the negligible giant resonance and 'post-cascade' alpha decay channels. The pre-equilibrium alpha decay process in medium and heavy nuclei is consistent with isotropic alpha emission from a small number of nucleons ($\sim$ 10) sharing the incoming photon momentum. This is consistent with the physical picture employed

in both the exciton model and quasi-free scattering model. Exciton model calculations yield reasonable agreement with the shape of the observed pre-equilibrium alpha energy spectra at 120 MeV electron energy. However, this may be fortuitous since at lower electron energies there is poorer agreement. This is likely to be due to either invalid application of a quasi-equilibrium condition, or shortcomings in the presently applied model, in particular, the omission of multi-chance processes. The possibility cannot be ruled out that a significant direct (one step) alpha particle knock-out component is present towards the high energy end of the energy spectrum observed at 120 MeV electron energy.

Publications comprising parts of the work in this thesis are contained in Appendix 12.

6.2 Future Work

The present study indicates several likely fruitful extensions to the data and analysis described in this thesis:

i) A study of other pre-equilibrium decay channels, i.e. p, d, t, ^{3}He emission. In particular, surprisingly little (e,p) or (γ,p) data exists for the energy region E_{γ} = 30 - 140 MeV. The acquisition of such data would provide a much needed test of models for photon absorption and pre-equilibrium nucleon emission. An extension to complex particle emission would then be possible, based on more firmly founded reaction models than those presently available.

ii) A study of the multipole components present in the resonance region. The present study has indicated, at most, small effects in this region from resonances other than the GDR. Present experimental techniques are inadequate for studying the decay

of resonances other than the GDR or GQR, and some studies of the GQR have yielded confusing results. Future (e, e'x) coincidence experiments are likely to yield more definite information on giant resonances and their decay properties.

iii) The unexplained low energy 'cusp' in the ^{60}Ni alpha spectrum should be further investigated to determine its true origin.

iv) Direct alpha cluster knock-out should be searched for by extending the present data to the kinematic limit of the energy spectra. If found, detailed information on alpha cluster momentum functions could be obtained. Initially, light nuclei with well separated ground and first excited states can be examined using presently available electron accelerators providing continuous bremsstrahlung beams.

v) Pre-equilibrium models for photonuclear reactions require various modifications and refinements. The exciton model should be refined with an improved photon absorption cross section parameterisation and the inclusion of multi-chance pre-equilibrium decays. Present quasi-free scattering (QFS) models with complex particle decay channels should be modified to include a photon absorption ingoing channel. A comparison of such modified models with the exciton model may then indicate whether the existence of quasi-equilibrium configurations(assumed in the exciton model) is a valid or necessary hypothesis.

APPENDIX 1 Electron Beam Energy Measurement and Calibration

The electron beam energy is derived directly from a measurement of the magnetic field in the first bending magnet of the energy analysis system. Thus an energy calibration requires the determination of the constant, k, such that

$$p = kB$$

where p is the momentum of the electrons in the beam, and B is the measured magnetic field. A Spectromagnetics N.M.R. Gaussmeter Model 5300 is used to provide a precision measurement of the magnetic field. The field can be reasonably assumed to be uniform, and linearly related to the N.M.R. frequency, since the magnet pole gap is small compared to the pole pieces, and the fields are below the expected saturation region for the magnet. Hence, the determination of one momentum and the corresponding bending magnet field provides the calibration constant.

This calibration used the magnetic spectrometer with its field set near to that at which 5.499 MeV calibration alphas from a ^{239}Pu source are observed in the central counters. These doubly charged alphas have momenta per unit charge of 101.25 MeV/c, and thus provide the spectrometer field setting at which 101.25 MeV/c electrons are momentum analysed and observed on the optic axis. An alpha particle calibration of the spectrometer (Appendix 4) gives the relationship between detected particle momentum and magnetic field for $p \sim 100$ MeV/c, thus it is not essential that the detected electrons' momentum is precisely that of the alpha calibration momentum.

Electrons of energy $\sim$100 MeV were scattered from a thin aluminium foil and detected in one of the two central detectors on the spectrometer focal plane at a field R_e. The spectrometer alpha calibration is

used to give the detected electron momentum, p'_e, and thence by consideration of electron energy losses between the target and detectors, and application of the nuclear recoil correction, the electron beam momentum, p_e, is derived.

The present calibration is derived from an earlier calibration[201] which was carried out as described above, and yielded a calibration constant, $k_{N.M.R.}$, which related N.M.R. probe resonance frequency to analysed electron momentum. This earlier calibration constant was found to be (Ref. (201)):

$$k_{N.M.R.} = \frac{f_{N.M.R.}}{p} = 233.67 \pm 0.07 \ {}^{kc}/_{s} \ /^{MeV}/_{c}.$$

This calibration constant can be related to the required constant, k, using

$$f_{N.M.R.} = \frac{g\,q\,B}{(2\pi)2m_p} = k_{N.M.R.}\ p$$

hence,

$$k = \frac{g\,q}{(2\pi)2m_p\ k_{N.M.R.}} \quad \text{MeV/c per gauss}$$

where g, q and m_p are the proton spin gyromagnetic ratio (g = 5.5855), charge and mass respectively. The calibration constant, k, is thus found to be,

$$k = (1.8199 \pm 0.0005) \times 10^{-2} \ \text{MeV/c / gauss.}$$

APPENDIX 2 Toroid Charge Monitor Calibration

The response of the toroid charge monitor is compared to that of an evacuated Faraday Cup of 99.6% efficiency, placed in beam after the scattering chamber. Charge collected by the Faraday Cup is monitored by a Brookhaven (Model 1000) current integrator, calibrated to give one output logic pulse for 2×10^{-7} coulombs charge. Logic pulses are accumulated in a similar fashion for the toroid charge monitor. The relative response of the toroid and Faraday Cup is obtained by taking the ratios of the corresponding total logic pulses. These ratios are shown in Fig. A2.1. The relative response of the toroid is stable to within 0.5% up to $\sim$19μa mean current. In practice currents over $\sim$16μa were avoided, to ensure a linear toroid response.

The toroid calibration is obtained from the ratio of toroid to Faraday Cup integrated charge, and the current integrator calibration, i.e.

$$1 \text{ Toroid Monitor Count} = \frac{(1.555 \pm 0.008)}{0.996} \times 2 \times 10^{-7} \text{ coulombs.}$$

The number of electrons incident on the target during a standard experimental run, in which 10^5 toroid monitor counts are accumulated is,

$$N_e = (1.95 \pm 0.01) \times 10^{17} \text{ electrons.}$$

The efficiency of the toroid charge monitor, ε_T, is found by obtaining the ratio of the charge collected on the Brookhaven current integrator connected to the toroid, to that collected by the Faraday Cup. This ratio is found to be $\varepsilon_T = 0.2025 \pm 0.001$, in agreement with the value, $\varepsilon_T = 0.2025 \pm 0.0001$ of Ref. (106).

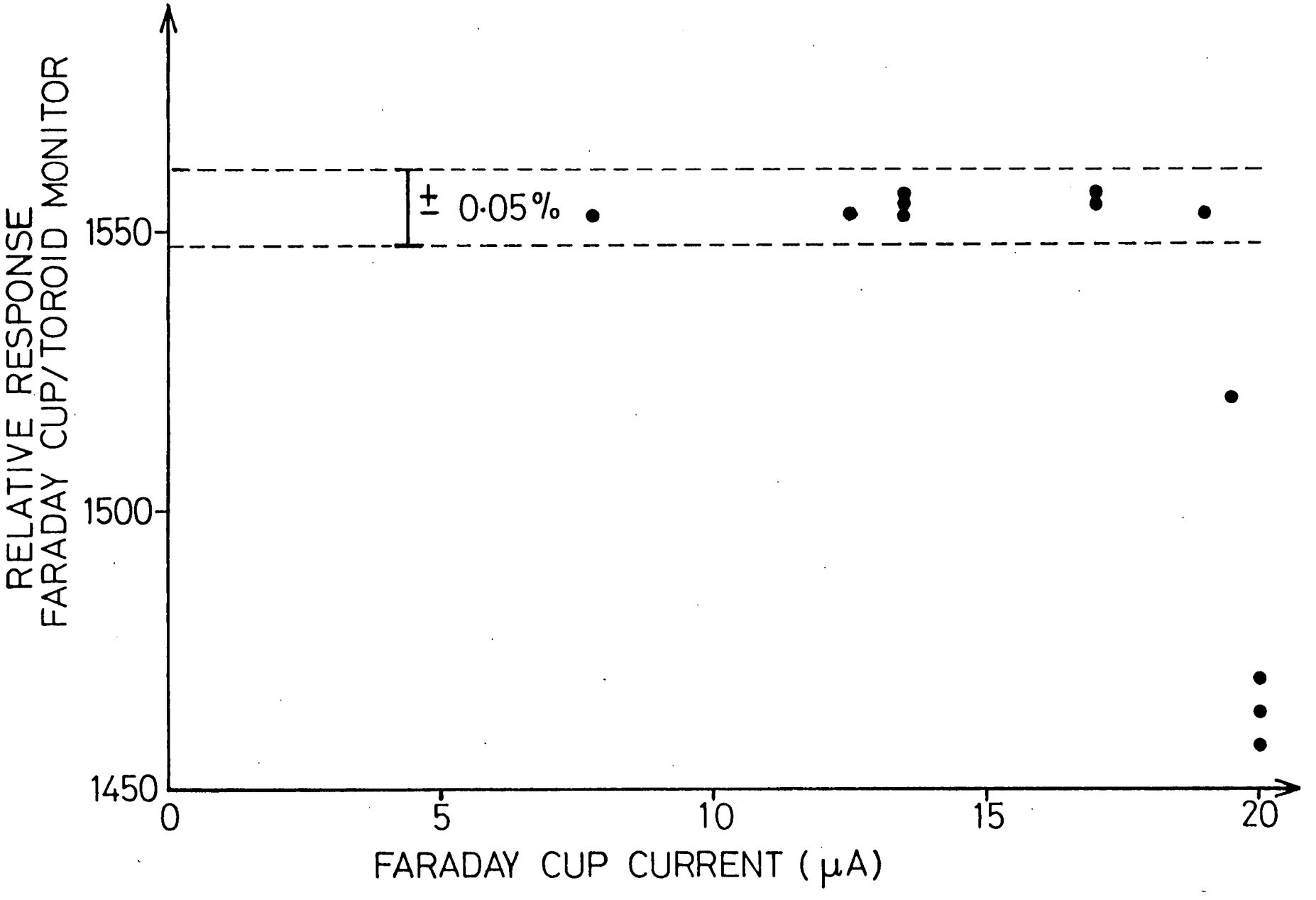

Figure A2.1 Toroid Monitor Calibration and Stability.

APPENDIX 3 Detector Relative Efficiencies

The detector relative efficiencies, r_J, are determined by comparing the alpha particle count rates obtained in different detectors over a small range of spectrometer field settings, using a target which yields a smooth particle spectrum. If the field settings are chosen such that the energy spectra obtained for each detector cover overlapping energy regions, then sets of spectra will be obtained as shown in Fig. A3.1. The raw spectra have the same form for each detector, but differ by a normalisation factor, from which can be obtained the efficiency of a given detector relative to the mean efficiency of the two central detectors (J = 4,5).

The counts, C_{jJ}, in each detector (J = 0, 9) are obtained for a series of N spectrometer field settings (j = 1, N). Taking logarithms of expression 3.4.1 and inserting expression 3.4.3 yields

$$\ell n \left(\frac{C_{jJ}}{\bar{E}_j \frac{(1 + \frac{\bar{E}_j}{2mc^2})^2}{(1 + \frac{E_{jJ}}{mc^2})}} \right) = \ell n \left(\frac{d^2\sigma}{dE_{jJ} d\Omega} \right) + \ell n(r_J) + \text{constant}$$

$$= y_i \qquad (i = 10(j-1) + J) \qquad \text{(A3.1)}$$

$\bar{E}_j$ = energy of particle along spectrometer optic axis for field setting j.

E_{jJ} = energy of particle seen in detector J, at field setting j.

The left-hand expression is calculated directly from any chosen particle's pulse height spectrum peak areas, and the spectrometer energy calibration as a function of spectrometer field (Appendix 4). In the right-hand expression r_J is the only variable to change as J varies. The spectra obtained are fitted by an L^{th} degree polynomial, hence

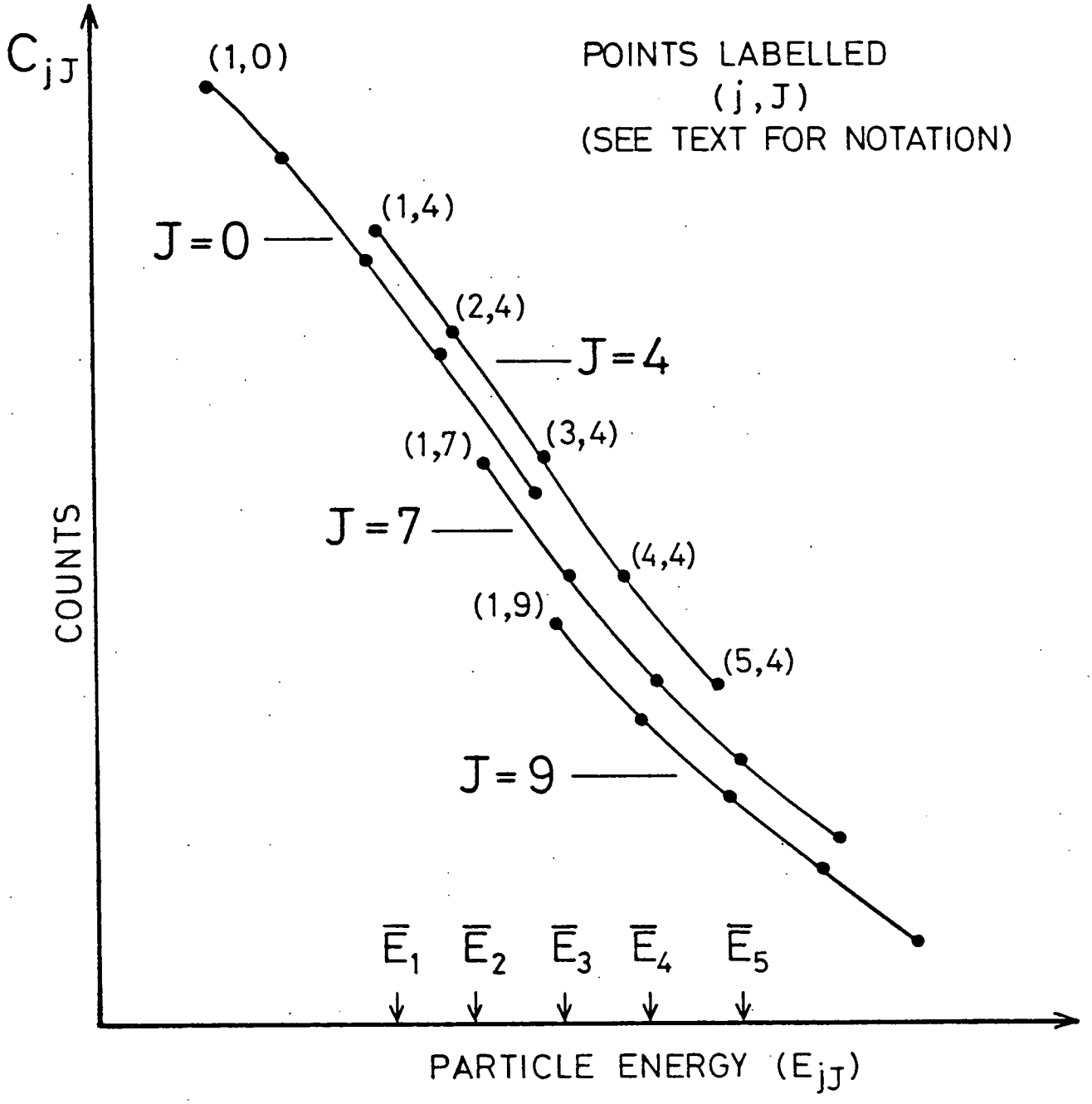

Figure A3.1 Raw data acquired for detector relative efficiency calibration. Here, five different spectrometer field settings are employed, each placing alpha particles of energy $\bar{E}_j$ along the optic axis. Spectra from detectors J = 1,2,3,5,6 and 8 have been omitted for clarity.

$$\ell n\left(\frac{d^2\sigma}{dE_{jJ}d\Omega}\right) + \ell n(r_J) + \text{constant} = a_J + \sum_{n=1}^{L} a_{9+n} E^n$$

$$= \sum_{k=0}^{9+L} a_k f_k$$

$$f_k = \delta_{Jk} \quad k = 0,9$$

$$f_k = E_{jJ}^{k-9} \quad k = 10,9+L$$

and the coefficients a_k are determined by the result of minimising the quantity,

$$\sum_{i=0}^{10N-1} \left(\frac{\sum_{k=1}^{9+L} a_k f_k - y_i}{\sigma_i} \right)^2 . \qquad (\sigma_i = \text{error in } y_i)$$

The coefficients a_k $(k = 10, L+9)$ are identical for each detector "raw spectrum", only the coefficients a_k $(k = 0,9)$ differ for each detector. Hence, from (A3.1),

$$a_J - a_{J'} = \ell n(r_J) - \ell n(r_{J'}) \quad J,J' = 0 \to 9.$$

The relative efficiencies are normalised to $r_{4.5} = 1$, where

$$r_{4.5} = \frac{(e^{a_4} + e^{a_5})}{2} .$$

The relative efficiency of detector J with respect to a detector on the spectrometer optic axis is thus given directly from the coefficients a_J $(J = 0 \to 9)$ by

$$r_J = \frac{e^{a_J}}{\frac{1}{2}(e^{a_4} + e^{a_5})} .$$

The relative efficiencies obtained in two determinations carried out

for different detector configurations are listed in Table A3.1 and A3.2 and plotted in Fig. A3.2.

The general functional form of the relative efficiencies across the counter ladder, can be understood in terms of the various spectrometer effects which they embody. The varying energy bite across the focal plane causes r_J to be a decreasing function of J. This is most evident near the centre of the counter ladder. Detectors at the ends of the focal plane have a reduced effective solid angle due to particles hitting the spectrometer vacuum box or experiencing irregular field distributions. This is reflected by the low relative efficiencies derived for the detectors at the ends of the focal plane. Fluctuations from detector to detector reflect different geometries of the sensitive detector region, particularly evident for the case in which some detectors were collimated and others not, leading to substantially differing detector widths.

Relative Efficiencies

J	r_J	±	Δr_J
0	0.7449		0.0069
1	0.7643		0.0073
2	0.8377		0.0074
3	0.9957		0.0074
4	1.0002		0.0078
5	0.9998		0.0081
6	0.9584		0.0087
7	0.7661		0.0098
8	0.8593		0.0098
9	0.6941		0.0110

$$\Delta J_{4.5} = 0.75$$

TABLE A3.1 - Detector Relative Efficiencies obtained using ∿11 MeV α's from Natural Nickel in May 1978. Detectors 0, 2, 7 and 9 are collimated.

J	r_J	±	Δr_J
0	0.9264		0.011
1	0.97765		0.011
2	1.0608		0.010
3	1.0480		0.010
4	1.0099		0.006
5	0.9901		0.006
6	0.9854		0.011
7	0.9605		0.012
8	0.9417		0.013
9	0.8984		0.013

$$\Delta J_{4.5} = 0.64$$

TABLE A3.2 - Detector Relative Efficiencies obtained using ∿9 MeV α's from BeO in September 1976. All detectors are collimated.

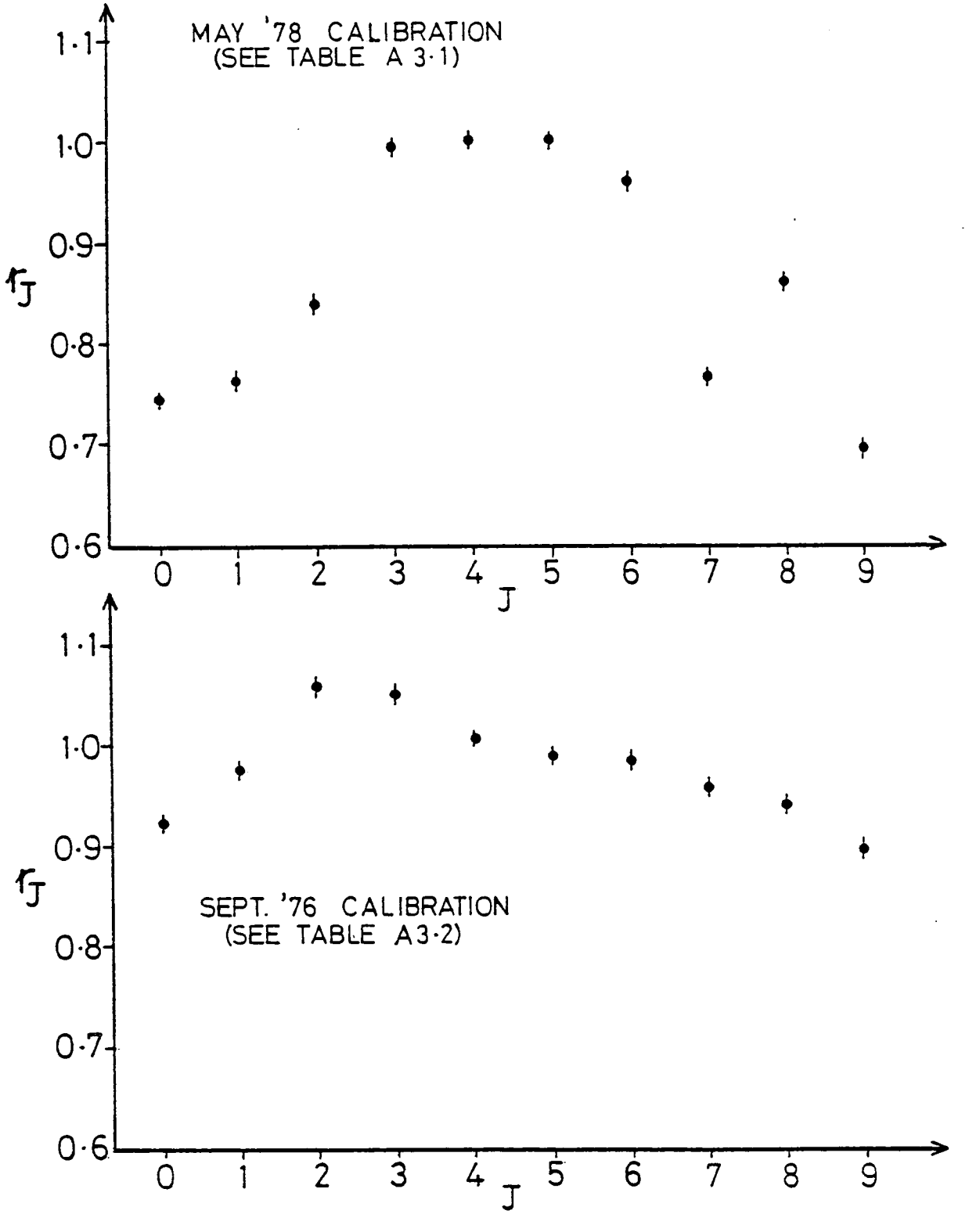

Figure A3.2 Relative efficiencies for two different sets of spectrometer focal plane detectors.

APPENDIX 4 Spectrometer Momentum Calibration

The spectrometer is calibrated in two stages. The first determines the momentum of a particle on the spectrometer optic axis, as a function of spectrometer field setting, $\bar{p}(R)$. The second stage determines the momentum of particles incident on each detector, $p(R, J)$, given $\bar{p}(R)$, i.e. we determine the parameters $F(J)$, where,

$$p(R, J) = F(J)\,\bar{p}(R), \qquad F(4.5) = 1 \qquad \text{(A4.1)}$$

by this definition.

The $F(J)$ parameters are related to the spectrometer dispersion, D_L (cms/% momentum), where D_L is the positional change (in cms) per percentage change in momentum. A change in momentum from $\bar{p}(R)$ to $p(R,J)$ will result in a positional change of the detected particles, for a given spectrometer field of Δx, where

$$\Delta x = D_L \frac{\Delta p}{p}, \qquad \Delta p = p(R,J) - \bar{p}(R) .$$

Consequently, the spectrometer dispersion can be expressed as,

$$D_L = \frac{\Delta x}{(F(J) - 1)} \cdot \frac{1}{100} \ (\text{cms}/\%) .$$

The spectrometer dispersion can be expressed dimensionlessly using,

$$D = \frac{D_L}{R} ,$$

where R is the spectrometer radius. It is the quantity, D, which is tabulated in Table 2.2 as the spectrometer dispersion.

The spectrometer focal plane detectors are arranged symmetrically on the focal plane with detectors, $J = 4$ and $J = 5$ on either side of the optic axis, hence the precise determination of $F(J)$ and $\bar{p}(R)$ can only be made by a series of iterative determinations of these quantities in turn. However, the approximation,

$$\bar{p}(R) \quad = \quad p(R,\ 4.5) \quad = \quad \frac{p(R,4) + p(R,5)}{2} \qquad (A4.2)$$

is accurate to within 1 part in 10^4, since we find

$$\Big(F(4.5 - F(4)\Big) \ - \ \Big(F(5) - F(4.5)\Big) \quad \equiv \quad 10^4,$$

thus an initial determination of $\bar{p}(R)$ can easily be made, if particles of known momenta are incident on the central detectors. This is achieved using a calibrated alpha particle source.

A thin ^{238}Pu α-source is used with decay alpha particle energies and intensities, $E_{\alpha_o} = 5.4992 \pm 0.0002$ MeV, $I_{\alpha_o} = 71.6 \pm 0.6\%$ and $E_{\alpha_1} = 5.4565 \pm 0.0004$ MeV, $I_{\alpha_1} = 28.3 \pm 0.6\%$ (Ref. 202). This is placed on the target ladder in the centre of the scattering chamber, which is coupled to the spectrometer. The ^{238}Pu alpha particles pass unimpeded from the source to the detectors in the focal plane. Measurement of the total number of alphas incident on each detector, over a unit time interval, is obtained as a function of spectrometer field setting, yielding the functional form shown in Fig. A4.1. This form derives from the two principal ^{238}Pu alpha lines, which are "swept" across each detector as the spectrometer field varies. These functional forms are fitted with either two gaussians, or two trapezoids with gaussian edges, depending on detector resolution. The fits yield a magnetic field setting, $R(p_\alpha, J)$ for which a given alpha momentum p_α, is incident at the centre of detector J.

The alpha calibration provides the primary calibration point for the energy analysis system (see Appendix 1). Given the calibration of the energy analysis system, proton end points and elastic electron scattering peaks provide further calibration points which determine the functional form of $\bar{p}(R)$, resulting from a fit through these points. A 3rd degree polynomial is used, which meets the physical requirement of

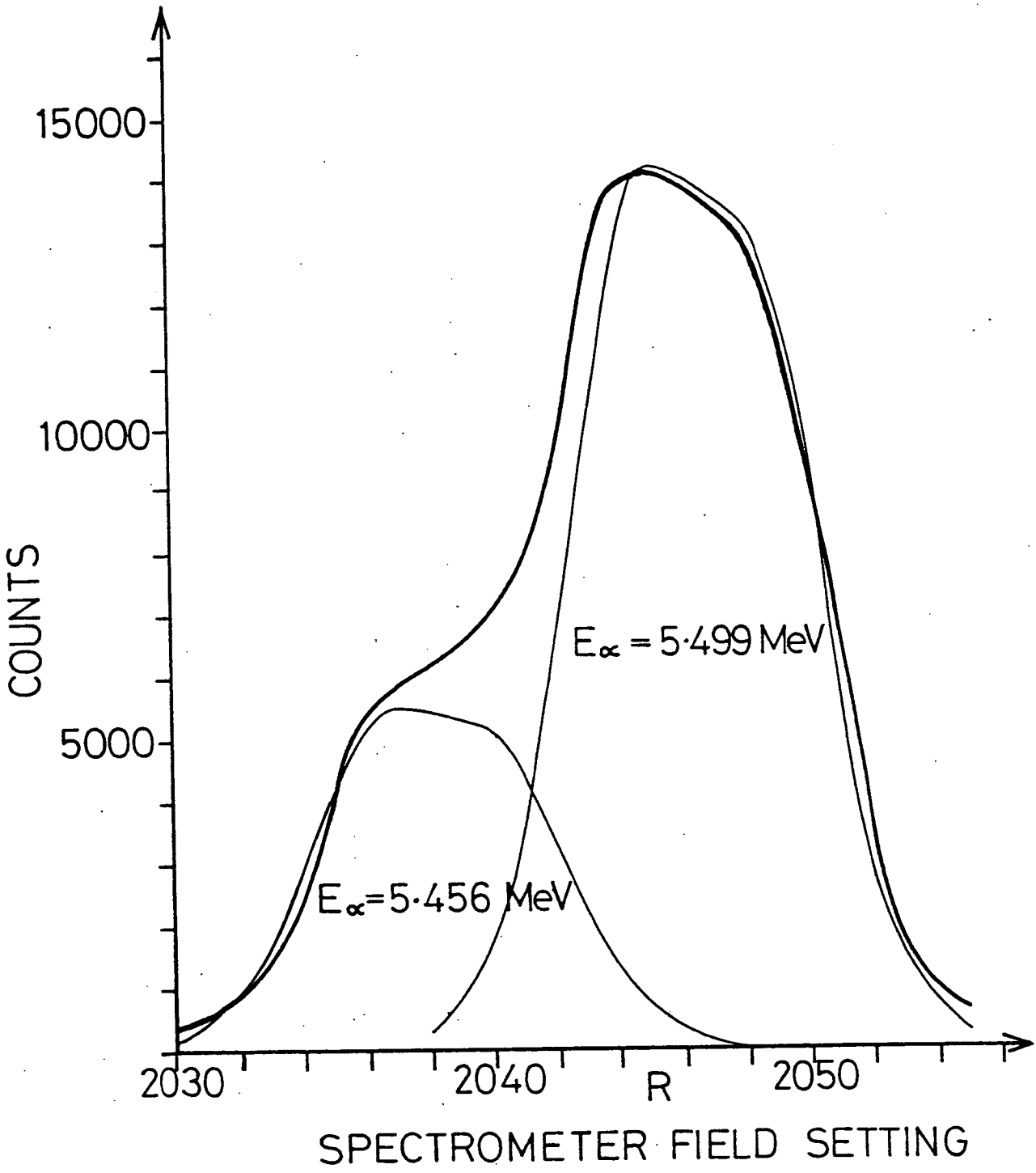

Figure A4.1 The solid line shows the functional form of the counts obtained in a given detector (J=9) from a ^{238}Pu alpha calibration source as the spectrometer magnetic field is varied. The fine lines are the result of fitting two trapezoids with gaussian edges. The tw principal ^{238}Pu lines are thus resolved and can each be assigned to a centroid spectrometer field setting for the detector.

a zero constant term (i.e. $\bar{p}(0) = 0$),

$$\bar{p}_1(R) = a_1 R + a_2 R^2 + a_3 R^3$$

$$a_1 = 5.2269 \times 10^{-2}$$

$$a_2 = -6.3410 \times 10^{-7}$$

$$a_3 = 1.2249 \times 10^{-10}$$

$$R \approx \frac{\text{Spectrometer field in gauss}}{2}$$

$\bar{p}_1(R)$ = momentum of singly charged particle on spectrometer optic axis.

Momenta of particles of charge Z along the spectrometer optic axis are obtained from,

$$\bar{p}_Z(R) = Z\,\bar{p}_1(R) \quad .$$

Although the particle momentum is evidently non-linear with respect to the measured magnetic field, (R), the effect is small, the deviation from linear being only $\sim 4\%$ at $\bar{p}_2 = 700$ MeV/c - the largest alpha particle momentum analysed. The effect of this non-linearity on the $F(J)$ parameters is negligible.

If the spectrometer momentum calibration is considered linear with respect to measured magnetic field, the $F(J)$ parameters are trivially related to the $R(p_\alpha, J)$ measured in the alpha calibration, since,

$$\bar{p}(R(p_\alpha, J)) = c\,R(p_\alpha, J), \qquad c \text{ - constant}$$

and

$$p_\alpha = p(R(p_\alpha, J), J) = c\,R(p_\alpha, 4.5).$$

From expression (A4.1),

$$F(J) = \frac{p(R(p_\alpha, J), J)}{\bar{p}(R(p_\alpha, J))} = \frac{R(p_\alpha, 4.5)}{R(p_\alpha, J)} \quad .$$

The parameter, F(J), for each detector is thus obtained by dividing the magnetic field setting which places the calibration alphas along the optic axis, by the field setting which places the calibration alphas at the centre of the given detector.

Non-linearity effects can be included in the F(J) determination by introducing a small non-linear correction term, which is zero for $R(p_\alpha, 4.5)$, then

$$\bar{p}(R(p_\alpha, J)) = c(R(p_\alpha, J) + \varepsilon(R(p_\alpha, J))) \quad .$$

The F(J) parameters must then be obtained using the function obtained in the momentum calibration $\bar{p}(R)$, i.e.

$$F(J) = \frac{\bar{p}(R(p_\alpha, 4.5))}{\bar{p}(R(p_\alpha, J))} \quad .$$

The F(J) parameters obtained are presented in Fig. A4.2. Use of F(4) and $\Delta x = 1$ cm, yields $D_L = 3.2$ cms/%, or $D = 4$, - the theoretical spectrometer dispersion.

The gradient of F(J) at the optic axis is required for the calculation of cross section in expression (3.4.3) . The differential of a fourth degree polynomial fitted to the F(J) yields,

$$\frac{\partial F}{\partial J}(4.5) = 0.00621 \quad .$$

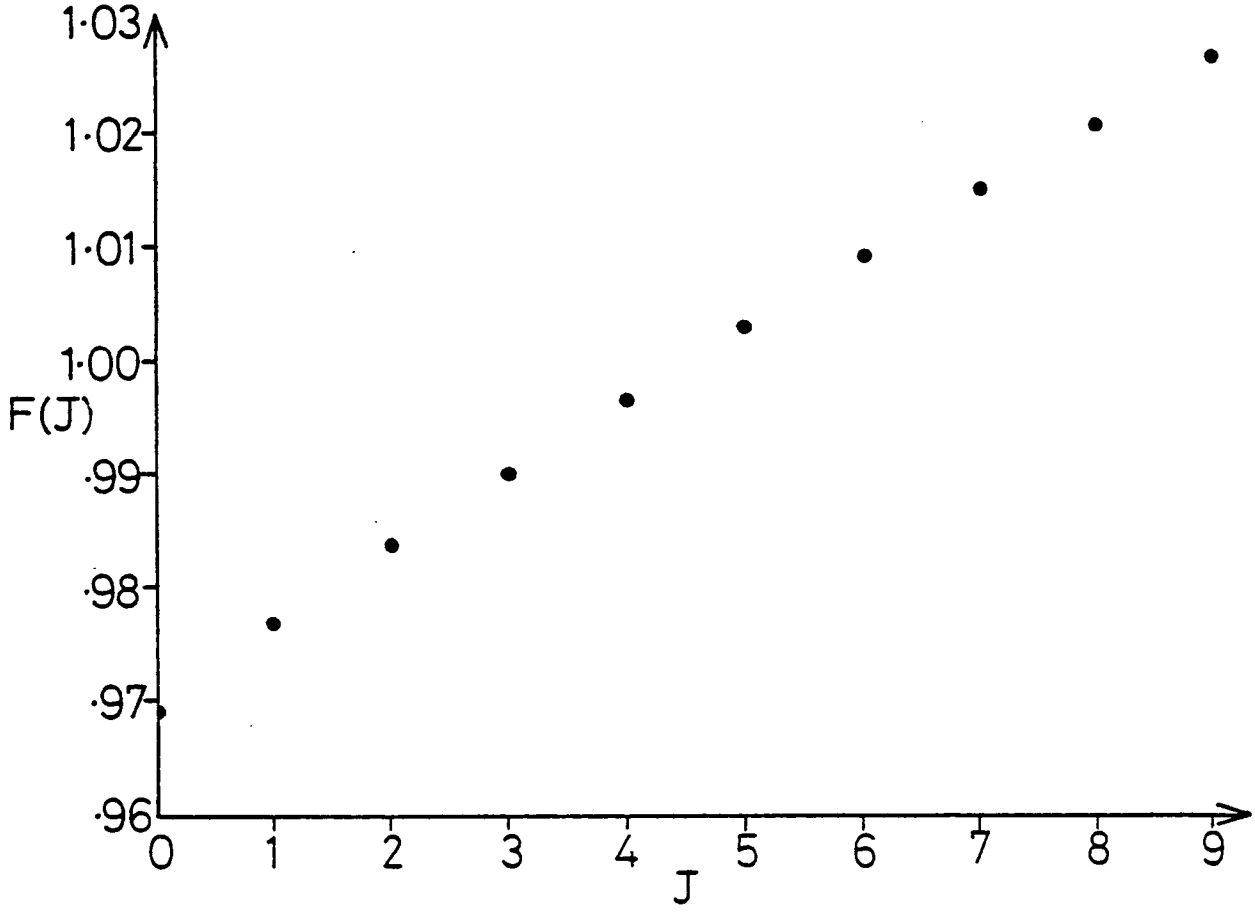

J	F(J)
0	0.9693
1	0.9769
2	0.9839
3	0.9903
4	0.9968
5	1.0031
6	1.0092
7	1.0152
8	1.0209
9	1.0269

Figure A4.2. Spectrometer Momentum Calibration F(J) Parameters.

APPENDIX 5 Detector Absolute Efficiency

The absolute efficiency of a detector relates the total number of particles incident on the detector to the area of the particle peak in the detector pulse height spectrum. It is a function of particle type and energy, comprising components due to inelastic nuclear interactions and multiple scattering in the detector. Both these effects produce a low energy tail below the particle peak. The peak integration procedure will lose all particles with energy $E < c\, E_{PEAK}$, where E_{PEAK} is the particle energy corresponding to the pulse height spectrum peak, and c is a constant defining the peak integration limits. Here $c = 0.85$. If ε_L% particles are lost, the detector absolute efficiency is $\varepsilon = 100 - \varepsilon_L$.

The multiple scattering loss was evaluated by calculating the root mean square displacement, $d_{r.m.s.}$ [203),204)] of an alpha particle from its plane of incidence, after passing through a thickness of detector corresponding to the range of a particle with the fraction 'c' of the incident particle energy. An alpha particle incident on a detector within $d_{r.m.s.}$ of the edge is considered to be lost due to its scattering out of the sensitive detector volume. The calculation of $d_{r.m.s.}$ is simplified by using the thin foil multiple scattering formula[205)] with an energy equal to the geometric mean of the incident particle energy and the energy of the particle when it leaves the sensitive volume. This is equivalent to assuming a constant stopping power $\frac{dE}{dx}$, with a value corresponding to the 'geometric mean' energy.

The estimated multiple scattering and nuclear interaction losses for alpha particles incident on a fully depleted 500 μm silicon detector, are shown in Fig. A5.1. The fractional nuclear interaction loss, f_N,

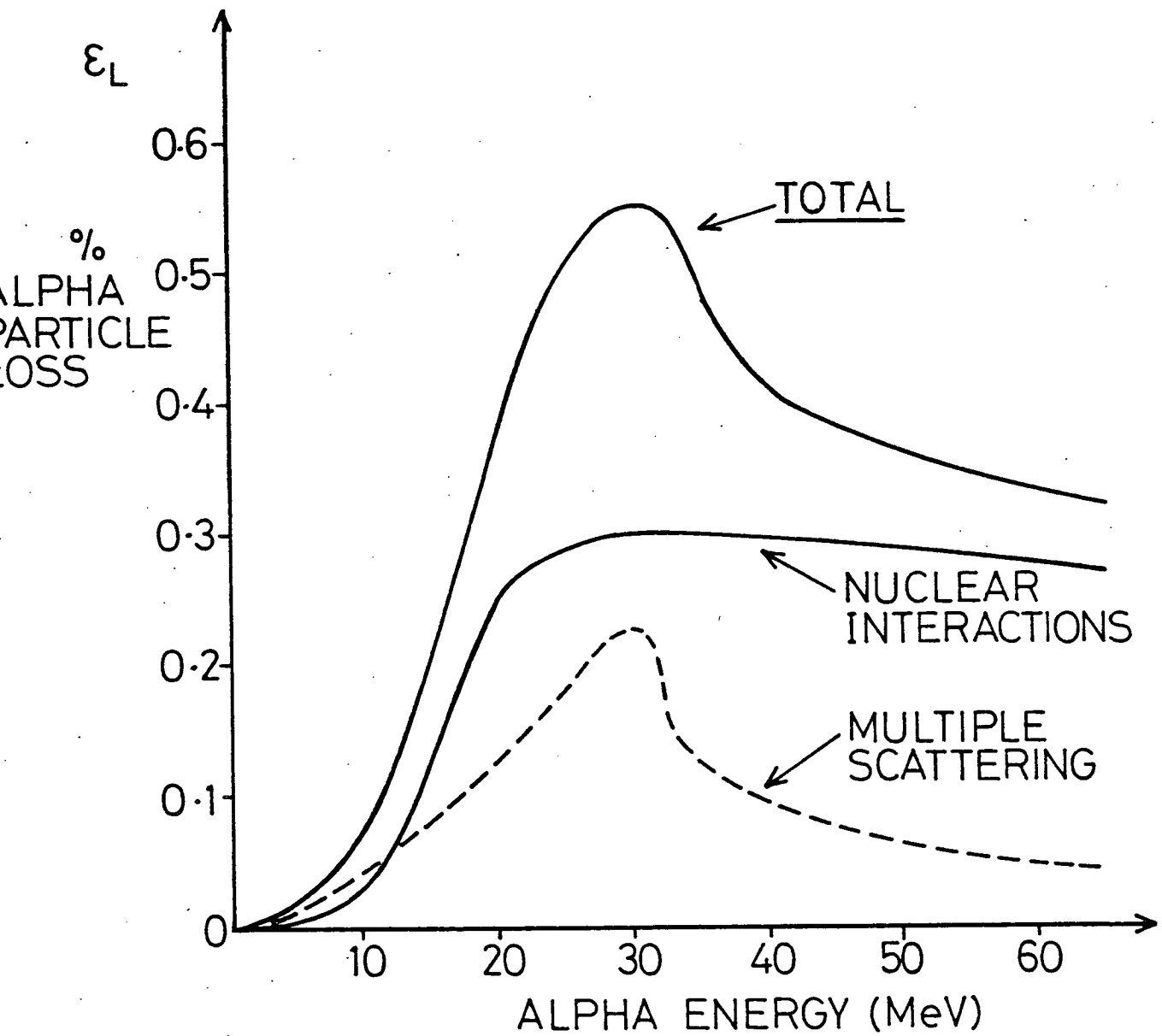

Figure A5.1 Multiple scattering and nuclear interaction losses for alpha particles on a fully depleted 500 μm silicon detector.

is calculated using,

$$f_N = \int_o^R \left(\frac{N_o}{A}\right) \sigma_R(E)\,dx = \int_o^R \left(\frac{N_o}{A}\right) \sigma_R(x)\,dx,$$

where R is the distance traversed by the particle in the detector, N_o is Avogadro's number and A is the atomic weight of the detector material. The total reaction cross section $\sigma_R(E)$ is expressed as a function of particle position from the front face of the detector, x, using the appropriate stopping power, $\frac{dE}{dx}(E)$ [205]. The reaction cross section was calculated, using an analytic form[157] normalised to experimental measurements[206),207)]. The multiple scattering losses are most significant for particles which just stop in the detector, and total particle losses are consequently largest at the corresponding particle energy. The approximations used to calculate the particle losses give an upper estimate of these losses. It is therefore concluded that these losses are negligible, since the alpha particle absolute efficiency for the thin, large area detectors used here is greater than 99.4%, over the entire particle energy range considered.

APPENDIX 6 Energy Loss Effects and Corrections

Particles incident on an absorber of thickness t have their energy spectrum, $\frac{dN}{dE}(N)$, modified to $\frac{dN'}{dE'}(E')$ after passing through the absorber. If $s(E, t, E')$ describes the energy loss distribution of particles passing through the absorber, then,

$$\frac{dN'}{dE'}(E') = \int \frac{dN}{dE}(E)\, s(E, t, E')dE \quad .$$

The energy loss distribution (or straggling function), $s(E, t, E')$ is a Landau distribution for very low energy loss $(\overline{\Delta E} \lesssim 0.01E)$ and a Gaussian distribution for higher energy loss. In general dN'/dE' is known and dN/dE must be obtained by deconvolution using $s(E, t, E')$. However, when the mean energy loss is small $(\overline{\Delta E} \lesssim 0.05E)$, the energy spectrum smooth, and resolution better than $\overline{\Delta E}$ not required, straggling effects may be neglected and $s(E, t, E')$ taken to be the Dirac δ-function,

$$s(E, t, E') = \delta(E' - E''), \qquad E'' = E - \Delta E(E,t)$$

ΔE - energy loss for particles of energy E, in thickness t,

and

$$\frac{dN'}{dE'}(E') = \int \frac{dN}{dE}(E'' + \Delta E)\delta(E' - E'')dE$$

$$dE = \left(1 + \frac{d(\Delta E)}{dE''}\right)dE'' \quad .$$

Thus

$$\frac{dN'}{dE'}(E') = \left[1 + \frac{d(\Delta E)}{dE''}\right] \frac{dN}{dE}(E'' + \Delta E)$$

$$= D(E,t)\, \frac{dN}{dE}(E) \quad .$$

The term $D(E,t)$ is a spectrum dilatation factor. It can be obtained alternatively by considering ΔN particles in the energy interval E to $E + dE$ being transformed into the interval $E'' + dE''$ after passing through an absorber (neglecting straggling). Then,

$$\Delta N = \frac{dN}{dE}(E)\,dE = \frac{dN'}{dE'}(E'')\,dE''$$

hence

$$\frac{dN'}{dE'}(E'') = \frac{dN}{dE}(E)\cdot\frac{dE}{dE''} = \frac{dN(E)}{dE}\cdot\frac{d(E''+\Delta E)}{dE''} = \left(1 + \frac{d(\Delta E)}{dE''}\right)\cdot\frac{dN(E)}{dE}\,.$$

The spectrum dilatation factor can be related to the stopping power, $\frac{dE}{dx}$, for the absorber, by considering,

$$t = \int_{E''}^{E''+\Delta E} \frac{1}{\frac{dE}{dx}(z)}\,dz \qquad z \text{ - dummy energy variable} \qquad \text{(A6.1)}$$

$$\text{or} \qquad t = \int_{o}^{E''+\Delta E} \frac{1}{\frac{dE}{dx}(z)}\,dz - \int_{o}^{E''} \frac{1}{\frac{dE}{dx}(z)}\,dz\,.$$

Differentiating both sides gives,

$$\frac{dt}{dE''} = 0 = \frac{d(E''+\Delta E)}{dE''}\cdot\frac{d}{d(E''+\Delta E)}\int_{o}^{E''+\Delta E}\frac{1}{\frac{dE(z)}{dx}\cdot dz}\,.$$

$$-\frac{d}{dE''}\int_{o}^{E''}\frac{1}{\frac{dE(z)}{dx}\cdot dz}$$

$$= \left(1 + \frac{d(\Delta E)}{dE''}\right)\left[\frac{dE}{dx}(E''+\Delta E)\right]^{-1} - \left[\frac{dE}{dx}(E'')\right]^{-1}$$

yielding,

$$1 + \frac{d(\Delta E)}{dE''} = D(E,t) = \frac{\frac{dE}{dx}(E''+\Delta E)}{\frac{dE}{dx}(E'')} = \frac{\frac{dE}{dx}(E)}{\frac{dE}{dx}(E-\Delta E(E,t))}\,.$$

The dilatation factor is therefore given by the ratio of the incident particle stopping power to the emergent particle stopping power. Since the stopping power is an exponentially decreasing function of particle energy (in the region of interest) $D(E,t) < 1$.

Particles incident on the spectrometer focal plane detectors suffer energy losses in the target and in the thin ($\sim$200 $\mu gm/cm^2$) aluminium vacuum isolator at the spectrometer entrance aperture. The detected particle energy and energy spectrum is corrected by considering particles which arise from half-way through the target.

Energy loss curves for alpha particles are obtained from Ref. (205) and fitted with the function,

$$\frac{dE}{dx} = a\,E^{b}$$

which can be applied in A6.1 to show

$$E = \left[a \cdot t(1-b) + (E'')^{1-b}\right]^{\frac{1}{1-b}} \qquad (A6.2)$$

Relation (A6.2) must be applied twice, firstly to correct for energy loss in the aluminium isolator, and secondly to correct for half target thickness energy loss. For a detected particle energy, E", the derived energies are written as E and E_α respectively. The aluminium isolator and target are parameterised by stopping power parameters and thicknesses, a_1, b_1, t_1 and a_2, b_2, t_2 respectively. The overall spectrum dilatation factor is then given by,

$$D(E'', E_\alpha, t_1, t_2) = \left[\frac{\frac{dE}{dx}(E)}{\frac{dE}{dx}(E'')}\right]_{Al} \times \left[\frac{\frac{dE}{dx}(E_\alpha)}{\frac{dE}{dx}(E)}\right]_{Target}.$$

Using the analytic stopping power expression,

$$D(E'', E_\alpha, t_1, t_2) = \left(\frac{E}{E''}\right)^{b_1} \left(\frac{E_\alpha}{E}\right)^{b_2} .$$

APPENDIX 7 LEVEL DENSITY FORMULAE

The Hauser-Feshbach statistical model calculations described in Section 4.2 use level density formulae, as parameterised by Gilbert and Cameron[132], in order to estimate the properties of the experimentally undetermined levels in the residual nuclei. These formulae have been extensively applied in many statistical calculations with some considerable success (e.g. refs. 112, 126).

Two formulae are used, relating to different regions of excitation energy, E. At high excitation energies, $E > E_x$, the formula is derived assuming a Fermi gas model for the nucleus [208]. The expression used is essentially no different from that given by Bethe over forty years ago[209]

$$\rho_>(E,J) = \frac{1}{12\sqrt{2}} \cdot \frac{\exp(2\sqrt{aU})}{\sigma\, a^{\frac{1}{4}} U^{5/4}} \cdot \rho_J(J) \quad ,$$

where

$$\rho_J(J) = \frac{(2J+1)}{2\sigma^2} \cdot \exp\left(\frac{-(J+\frac{1}{2})^2}{2\sigma^2}\right) \quad .$$

The level density and spin cut-off parameters, a and σ, determine the excitation energy and spin dependences of the level density. The excitation energy factor, U, is related to the actual excitation energy, E, by,

$$U = E - P(Z) - P(N) \quad ,$$

where P(N) and P(Z) are pairing energy corrections to the excitation energy related to the nucleus proton, Z, and neutron, N, numbers. These correction factors are fully tabulated in ref. (132). The spin density function $\rho_J(J)$ gives the proportion of levels which have spin (of either parity), and hence, $\sum_{J=0}^{\infty} \rho_J(J) = 1.0$. Calculated spin

distributions for 4 residual excitation energies in ^{56}Fe, are shown in Fig. A7.1.

Below the excitation energy E_x, given in ref. (132), a constant nuclear temperature formula is applied

$$\rho_<(E,J) = \frac{1}{T} \exp\left(\frac{(E - E_o)}{T} \right) \rho_J(J) \quad .$$

The nuclear temperature, T, is determined by matching $d(\log \rho_<)$ and $d(\log \rho_>)$ at the pairing energy corrected excitation energy U_x, corresponding to E_x. This yields (noting that σ is energy dependent),

$$\frac{1}{T} = \sqrt{\frac{a}{U_x}} - \frac{3}{2U_x} = \left(\frac{d}{dU} (\log \rho_>) \right)_{E_x}$$

and E_o is determined by fitting $\rho_<$ and $\rho_>$ at $E = E_x$, hence,

$$E_o = E_x - T \log T \, \rho_>(U_x) \quad .$$

The spin cut-off parameter, σ, is related to the nuclear temperature and moment of inertia, I, of the nucleus by,

$$\sigma^2 = \frac{TI(E)}{h^2} \quad , \qquad E \leq E_x$$

and so varies as I varies with increasing excitation energy. Here, σ^2 is set to $0.3.I_{rig}$ at zero excitation energy, where,

$$I_{rig} = \frac{2}{5}MR^2, \quad - \quad M, \text{ mass of nucleus}$$

$$R, \text{ radius of nucleus}$$

and is increased linearly up to a value $\sigma^2(U_x)$, given by

$$\sigma^2(U) = 0.0888 \cdot \sqrt{aU} \cdot A^{2/3} \quad . \qquad \text{(A7.1)}$$

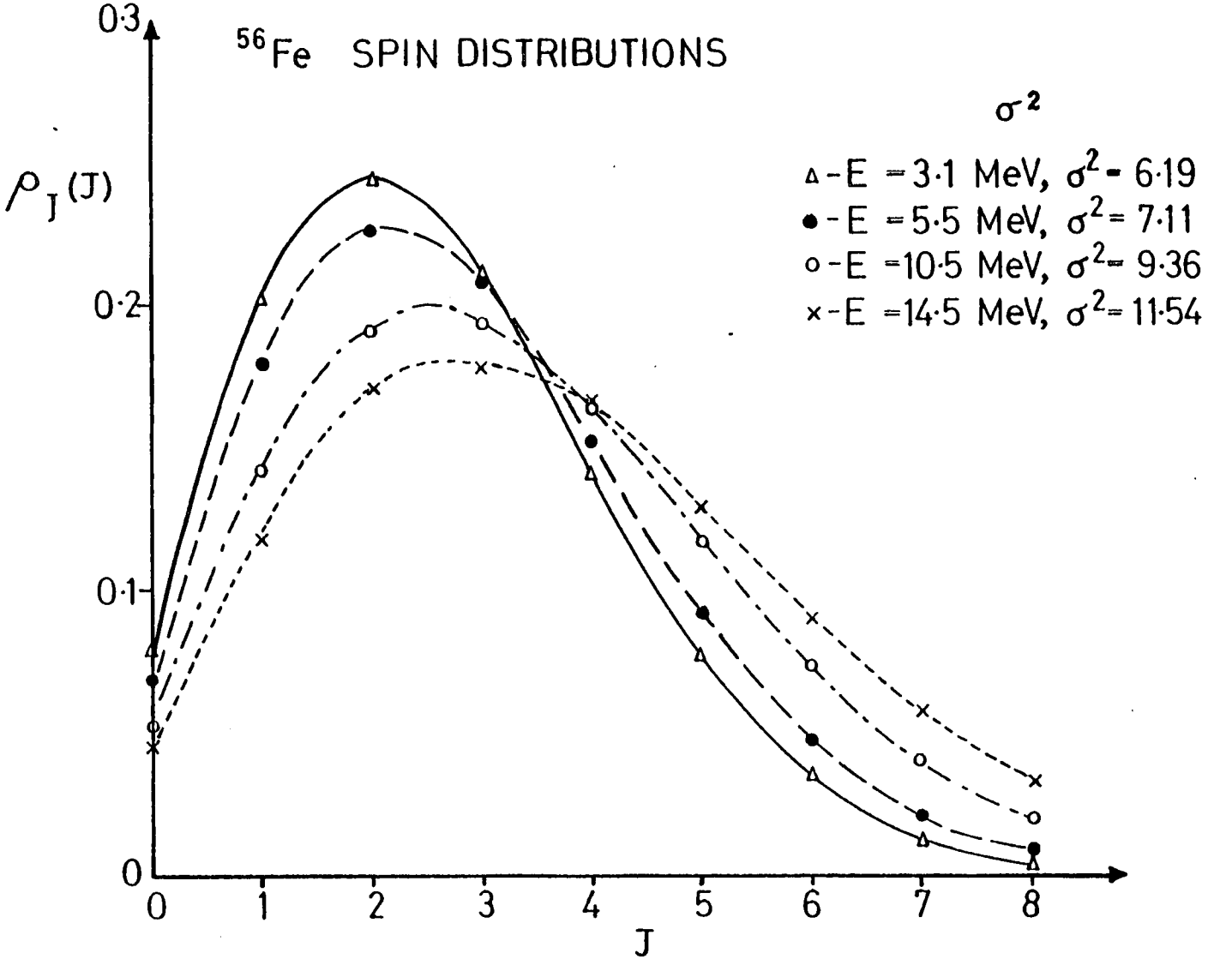
^{56}Fe SPIN DISTRIBUTIONS
σ^2
Δ - E = 3·1 MeV, σ^2 = 6·19
● - E = 5·5 MeV, σ^2 = 7·11
○ - E = 10·5 MeV, σ^2 = 9·36
× - E = 14·5 MeV, σ^2 = 11·54
$\rho_J(J)$
0·3
0·2
0·1
0
0 1 2 3 4 5 6 7 8
J

Figure A7.1.

At $E > E_x$, σ^2 increases as given by expression (A7.1) above. The effect of a spin cut-off parameter which increases with excitation energy is evident in Fig. A7.1. At higher excitation energies the spin distributions become flatter and shift gradually to higher spins since the maximum of the spin distribution is given by

$$J_{max} = \sigma - \tfrac{1}{2} \quad .$$

The values of the parameters used in the level density calculations are given in Table A7.1. Given a, E_x, P(N) and P(Z), the remaining parameters T, E_o and σ^2 are derived using relationships given in this appendix.

Level Density Parameters

	P(Z)	P(N)	a	E_x
^{52}Cr	1.35	1.30	6.15	10.1
^{55}Fe	1.54	0.0	5.76	9.8
^{56}Fe	1.54	1.27	6.75	9.2
^{59}Ni	1.20	0.0	5.97	9.7
^{195}Ir	0.0	0.0	19.56	5.0
^{196}Au	0.0	0.79	18.31	4.06

Table A7.1

APPENDIX 8 ANGULAR DISTRIBUTION COEFFICIENTS

The description of nuclear reaction angular distributions in terms of Z coefficients was introduced by Blatt and Biedenharn[141]. These coefficients were later developed to include photon channels[142] and to include a phase factor omitted in the early formalism[210),211)]. Allowing, initially, for interference terms between different reaction channels t_1 and t_2, the Z coefficients are, for particles:

$$Z(\ell_1\ J_1\ \ell_2\ J_2;\ sL) = i^{L-\ell_1+\ell_2}\left[(2\ell_1+1)(2\ell_2+1)(2J_1+1)(2J_2+1)\right]^{\frac{1}{2}} \times W(\ell_1 J_1 \ell_2 J_2; sL)(\ell_1 0 \ell_2 0 | L0)\ , \qquad (A8.1)$$

and for photons:

$$Z_\gamma(\lambda_1\ J_1\ \lambda_2\ J_2;\ J_A L) = \left[(2\lambda_1+1)(2\lambda_2+1)(2J_1+1)(2J_2+1)\right]^{\frac{1}{2}} \times W(\lambda_1 J_1 \lambda_2 J_2; J_A L)(\lambda_1 -1\ \lambda_2 1 | L0)\ . \qquad (A8.2)$$

Here, the usual notation is used for Racah and Clebsch-Gordon coefficients. The symbols are defined in Fig. A8.1. They refer to the two interfering channels, each specified by $t = (p, \lambda, J^\pi, \ell, s)$ for an ingoing photon and outgoing particle. When interference terms are omitted the subscripts 1 and 2 are dropped since then $\ell_1 = \ell_2$, $J_1 = J_2$ and $\lambda_1 = \lambda_2$.

A coefficient C_{tL} can be introduced which contains all the information on the form of the angular distribution resulting from a particular channel, t. Including interference terms the coefficient

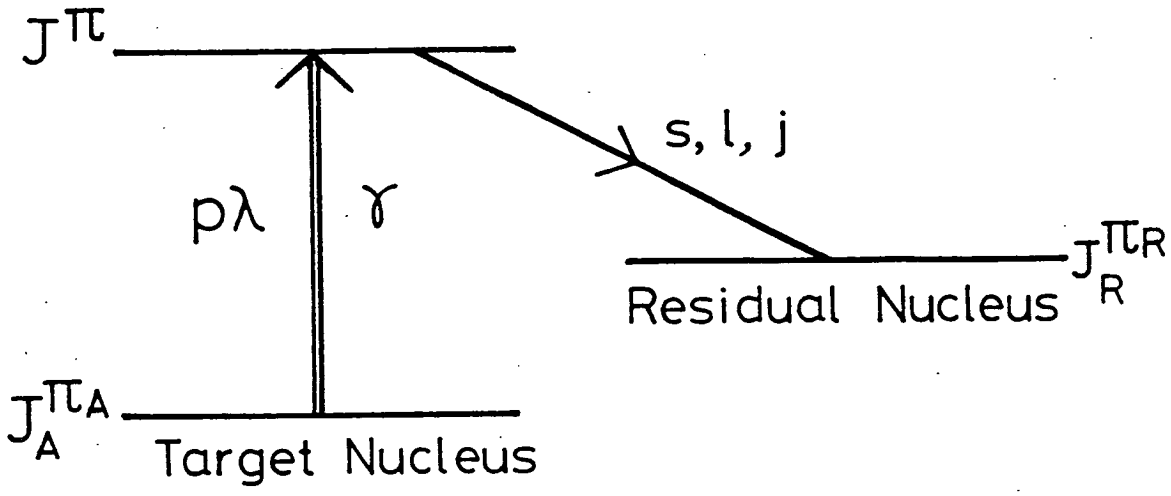

$J_A^{\pi_A}$ Spin and parity of target nucleus.

P Nature of transition; p = 0 for magnetic, p = 1 for electric.

λ Multipolarity of transition.

J^{π} Spin and parity of the excited state reached by the pλ photon transition.

ℓ Decay particle orbital angular momentum.

j Spin of the decay particle (parity assumed positive).

$J_R^{\pi_R}$ Spin and parity of residual nucleus level.

s Outgoing particle channel spin, $\underline{s} = \underline{j} + \underline{J}_R$

$$|J_R - j| \leq s \leq J_R + j.$$

L Integer parameter defining order of Legendre polynomial.

For interfering channels 1 and 2:

$$\text{Max}(|\ell_1 - \ell_2|, |\lambda_1 - \lambda_2|, |J_1 - J_2|)$$

$$\leq L \leq \text{Min}(\ell_1 + \ell_2, \lambda_1 + \lambda_2, J_1 + J_2)$$

and $\ell_1 + \ell_2 + L$ must be even.

For no interfering channels:

$$0 \leq L \leq \min(2\ell, 2\lambda, 2J)$$

and L must be even.

Figure A8.1 Definition of notation employed in Appendix 8.

$C_{t_1 t_2 L}$, relating to channels t_1 and t_2 is,

$$C_{t_1 t_2 L} = (-1)^{s-J_A-1} \cdot (-1)^{p_1+p_2} \cdot Z_\gamma \cdot Z \cdot i^{-\ell_2+\ell_1-L} \qquad (A8.3)$$

and C_{tL} is trivially obtained for $t_1 = t_2$ by setting $p_1 = p_2$, $\ell_1 = \ell_2$.

The coefficient C_{t0} is of particular interest since this describes the isotropic part of the angular distribution and relates the angle integrated and angle differential cross section expressions. Employing an expression given by Biedenharn et al.[212],

$$Z(\ell_1\ J_1\ \ell_2\ J_2;\ s0) = \delta_{\ell_1\ell_2}\ \delta_{J_1J_2}(-1)^{J_1-s}(2J_1+1)^{\frac{1}{2}}, \qquad (A8.4)$$

it is evident that the C_{t0} isotropic term only arises when $\ell_1 = \ell_2$ and $J_1 = J_2$, i.e. from the non-interfering channels. The equivalent expression for the photon Z_γ coefficient is,

$$Z_\gamma(\lambda_1 J_1 \lambda_2 J_2; J_A 0) = \delta_{\lambda_1\lambda_2}\ \delta_{J_1J_2}(-1)^{J_1-J_A-1}(2J_1+1)^{\frac{1}{2}}\ . \qquad (A8.5)$$

Applying (A8.4) and (A8.5) in (A8.3) yields

$$C_{t0} = (-1)^{s-J_A-1)}\ (-1)^{J-s}\ (-1)^{J-J_A-1}\ (2J+1)$$

$$\text{i.e.}\quad C_{t0} = 2J+1\ .$$

Values of C_{tL} are tabulated in Tables A8.1 and A8.2. These values are required for the calculation of alpha particle angular distributions following E1 or E2 excitation of 0^+ ground state nuclei. Residual nucleus spins of up to $J_R = 7$ were considered, with both parities allowed. Thus, decays from 1^- states to, say, $J_R = 6$ levels, are allowed by 3 channels, - $\ell = 5$, 6 and 7. The channels with $\ell = 5$ and 7 are transitions to a 6^+ level, and

the channel with $\ell = 6$ is a transition to a 6^- level. Similarly, alpha decay of 2^+ states has 5 allowed channels for all $J_R > 1$.

Tables A8.1 and A8.2 may be compared with those of Carr and Baglin[213] in which the $C_{t_1 t_2 L}$ coefficients are given only up to $J_R \leq \frac{5}{2}$. The present tabulations are the result of an independent calculation and agree with ref. 213 for all $t_1 = t_2$ cases where comparisons can be made. The need to obtain C_{tL} for residual nucleus spins up to $J_R \sim 7$ led to the extended tabulation given here.

Several properties of the C_{tL} coefficients are reflected in the tables,

a) $C_{tL} = 0, \quad L > 2\lambda$

b) $C_{tL} = 0, \quad L$ - odd

c) $\sum_{\ell} C_{tL} = 0, \quad L > 0$ and $J_R > 1$ if $p\lambda = E2$

$L > 0$ and $J_R > 0$ if $p\lambda = E1$.

Thus, with no interference terms included alpha particle angular distributions will be described by up to second order Legendre polynomials, if only dipole radiation produces compound nuclear states, and by up to fourth degree Legendre polynomials if quadrupole excitation is present. No odd Legendre polynomials will be present, hence the angular distributions will be symmetric about 90°. In the continuum small angular anisotropies will arise from the lower residual spins $J_R = 0, 1$.

t = 0^+ Target Nucleus, 0^+ Emitted Particle, pλ = E1

$J_R^{\pi_R}$	ℓJs	C_o	C_1	C_2	C_3	C_4
0^+	110	3.000	0.0	-3.000	0.0	0.0
1^-	011	3.000	0.0	0.0	0.0	0.0
1^+	111	3.000	0.0	1.500	0.0	0.0
1^-	211	3.000	0.0	-1.500	0.0	0.0
2^+	112	3.000	0.0	-0.300	0.0	0.0
2^-	212	3.000	0.0	1.500	0.0	0.0
2^+	312	3.000	0.0	-1.200	0.0	0.0
3^-	213	3.000	0.0	-0.429	0.0	0.0
3^+	313	3.000	0.0	1.500	0.0	0.0
3^-	413	3.000	0.0	-1.071	0.0	0.0
4^+	314	3.000	0.0	-0.500	0.0	0.0
4^-	414	3.000	0.0	1.500	0.0	0.0
4^+	514	3.000	0.0	-1.000	0.0	0.0
5^-	415	3.000	0.0	-0.545	0.0	0.0
5^+	515	3.000	0.0	1.500	0.0	0.0
5^-	615	3.000	0.0	-0.955	0.0	0.0
6^+	516	3.000	0.0	-0.577	0.0	0.0
6^-	616	3.000	0.0	1.500	0.0	0.0
6^+	716	3.000	0.0	-0.923	0.0	0.0
7^-	617	3.000	0.0	-0.600	0.0	0.0
7^+	717	3.000	0.0	1.500	0.0	0.0
7^-	817	3.000	0.0	-0.900	0.0	0.0

TABLE A8.1 C_{tL} Coefficients

Table 8.2

t = 0^+ Target Nucleus, 0^+ Emitted Particle, pλ = E2

$J_R^{\pi_R}$	ℓJs	C_o	C_1	C_2	C_3	C_4
0^+	220	5.000	0.0	3,571	0.0	-8.571
1^-	121	5.000	0.0	2.500	0.0	0.000
1^+	221	5.000	0.0	1.786	0.0	5.714
1^-	321	5.000	0.0	2.857	0.0	-2.857
2^+	022	5.000	0.0	0.0	0.0	0.0
2^-	122	5.000	0.0	-2.500	0.0	0.0
2^+	222	5.000	0.0	-0.765	0.0	-2.449
2^-	322	5.000	0.0	0.714	0.0	4.286
2^+	422	5.000	0.0	2.551	0.0	-1.837
3^-	123	5.000	0.0	0.714	0.0	0.0
3^+	223	5.000	0.0	-2.041	0.0	0.612
3^-	323	5.000	0.0	-1.310	0.0	-2.857
3^+	423	5.000	0.0	0.255	0.0	3.673
3^-	523	5.000	0.0	2.381	0.0	-1.429
4^+	224	5.000	0.0	1.020	0.0	-0.068
4^-	324	5.000	0.0	-1.786	0.0	0.952
4^+	424	5.000	0.0	-1.507	0.0	-3.006
4^-	524	5.000	0.0	0.0	0.0	3.333
4^+	624	5.000	0.0	2.273	0.0	-1.212
5^-	325	5.000	0.0	1.190	0.0	-0.130
5^+	425	5.000	0.0	-1.623	0.0	1.169
5^-	525	5.000	0.0	-1.603	0.0	-3.077
5^+	625	5.000	0.0	-0.162	0.0	3.117
5^-	725	5.000	0.0	2.198	0.0	-1.079
6^+	426	5.000	0.0	1.299	0.0	-0.180
6^-	526	5.000	0.0	-1.511	0.0	1.319
6^+	626	5.000	0.0	-1.656	0.0	-3.117
6^-	726	5.000	0.0	-0.275	0.0	2.967
6^+	826	5.000	0.0	2.143	0.0	-0.989

t = 0^+ Target Nucleus, 0^+ Emitted Particle, pλ = E2

$J_R^{\pi_R}$	ℓJs	C_o	C_1	C_2	C_3	C_4
7^-	527	5.000	0.0	1.374	0.0	-0.220
7^+	627	5.000	0.0	-1.429	0.0	1.429
7^-	727	5.000	0.0	-1.689	0.0	-3.142
7^+	827	5.000	0.0	-0.357	0.0	2.857
7^-	927	5.000	0.0	2.101	0.0	-0.924

TABLE A8.2 C_{tL} Coefficients

APPENDIX 9 Kinematic Construction of Laboratory Frame Angular Distributions

The laboratory and centre of mass reference frame double differential cross sections are related by,

$$\frac{1}{p'} \frac{d^2\sigma}{dE'd\Omega'} (E',\theta') = \frac{1}{p} \frac{d^2\sigma}{dEd\Omega} (E,\theta) \qquad (A9.1)$$

for a particle of momentum, p, energy, E, emitted at an angle θ in the laboratory frame. Primed quantities relate to the centre of mass reference frame.

If the centre of mass angular distributions are isotropic, over the range of centre of mass particle energies sampled in the laboratory frame angular distribution, they are related to the laboratory frame energy spectrum, as measured at a fixed angle θ_o, by,

$$\frac{d^2\sigma}{dE'd\Omega'} (E', \theta') = \frac{p'}{p} \frac{d^2\sigma}{dEd\Omega} (E,\theta_o) = C(E') \qquad (A9.2)$$

where $C(E')$ is the centre of mass frame energy spectrum (independent of θ'). The parameters p' and p are related as shown in Fig. A.9.1 by use of the quantities θ_o and q'. Assuming the incident photon momentum is directed forwards, then for a photonuclear reaction with an incident photon momentum q shared by a group of nucleons of mass M_T, a particle of mass m emitted from the group will have a momentum $q' = \frac{mq}{M_T}$, due to the centre of mass motion.

To obtain the laboratory frame angular distribution of particles of laboratory momenta $\bar{p}$, emitted from the mass M_T at an angle θ, the corresponding centre of mass momentum p' must be obtained, as shown in Fig. A.9.2. The corresponding value of p follows from Fig. A.9.1,

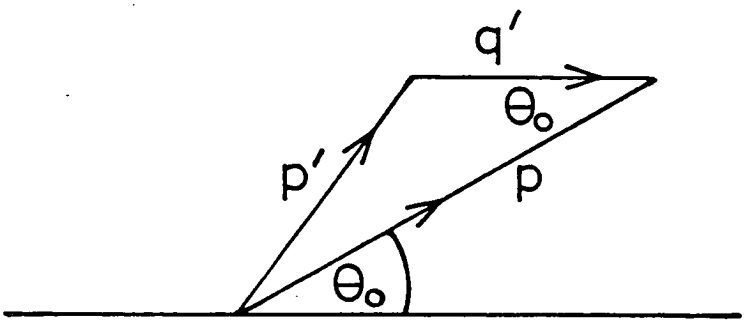

$$q' = \frac{mq}{M_T}$$

$$p'^2 = p^2 + q'^2 - 2pq' \cos\theta_0$$

Figure A.9.1.

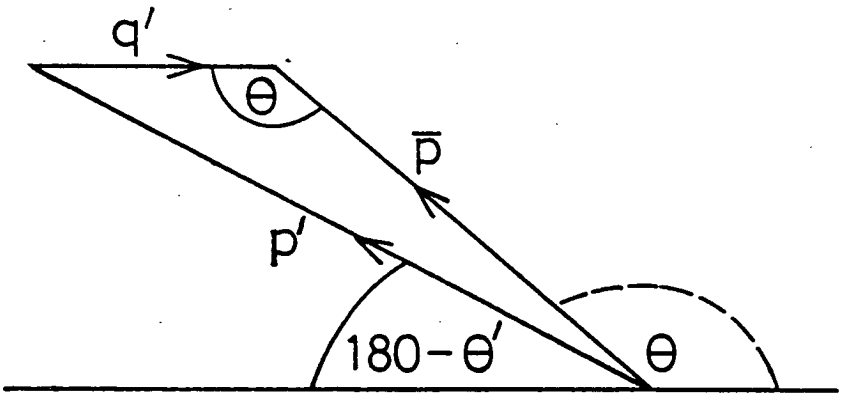

$$p'^2 = \bar{p}^2 + q'^2 - 2\bar{p}q' \cos\theta$$

Figure A.9.2.

and thus $d^2\sigma(E',\theta')/dE'd\Omega'$ can be derived. Application of (A.9.1) at momentum $\bar{p}$, together with (A.9.2) yields,

$$\frac{d^2\sigma}{dEd\Omega}(\bar{E},\theta) = \frac{\bar{p}}{p'}\frac{d^2\sigma}{dE'd\Omega'}(E',\theta') = \frac{\bar{p}}{p}\frac{d^2\sigma}{dEd\Omega}(E,\theta_o). \quad (A.9.3)$$

The momenta p and $\bar{p}$ are related by,

$$p(\theta,q',\theta_o,\bar{p}) = q'\cos\theta_o \pm \sqrt{q'^2\cos^2\theta_o + \bar{p}^2 - 2q'\bar{p}\cos\theta} \quad (A.9.4)$$

- positive sign chosen if $p' > q'\sin\theta_o$, otherwise negative sign selected.

This expression can be written in terms of the kinematic parameter, $\Gamma = \frac{mq}{\bar{p}M_T}$ by noting $q' = \bar{p}\Gamma$.

The form of $p(\theta)$, for q', θ_o, $\bar{p}$ fixed, is illustrated in Fig. A.9.3, for $\theta_o = 30^o$, and q', $\bar{p}$ derived for 50 MeV laboratory frame energy alpha particles, from a mass 6 A.M.U. system with $q = 70$ MeV/c, - parameters found to yield a fit to the angular distributions of 50 MeV alpha particles from nickel, using 120 MeV electrons. The laboratory frame angular distribution is principally dependent on the energy spectrum variation with $p(\theta)$. Since at backward angles, higher values of p are sampled, an energy spectrum decreasing with increasing particle momentum, will yield a backward angle cross section lower than the forward angle cross section, and pronounced forward peaking will be observed in the laboratory frame, for a fixed laboratory frame particle energy.

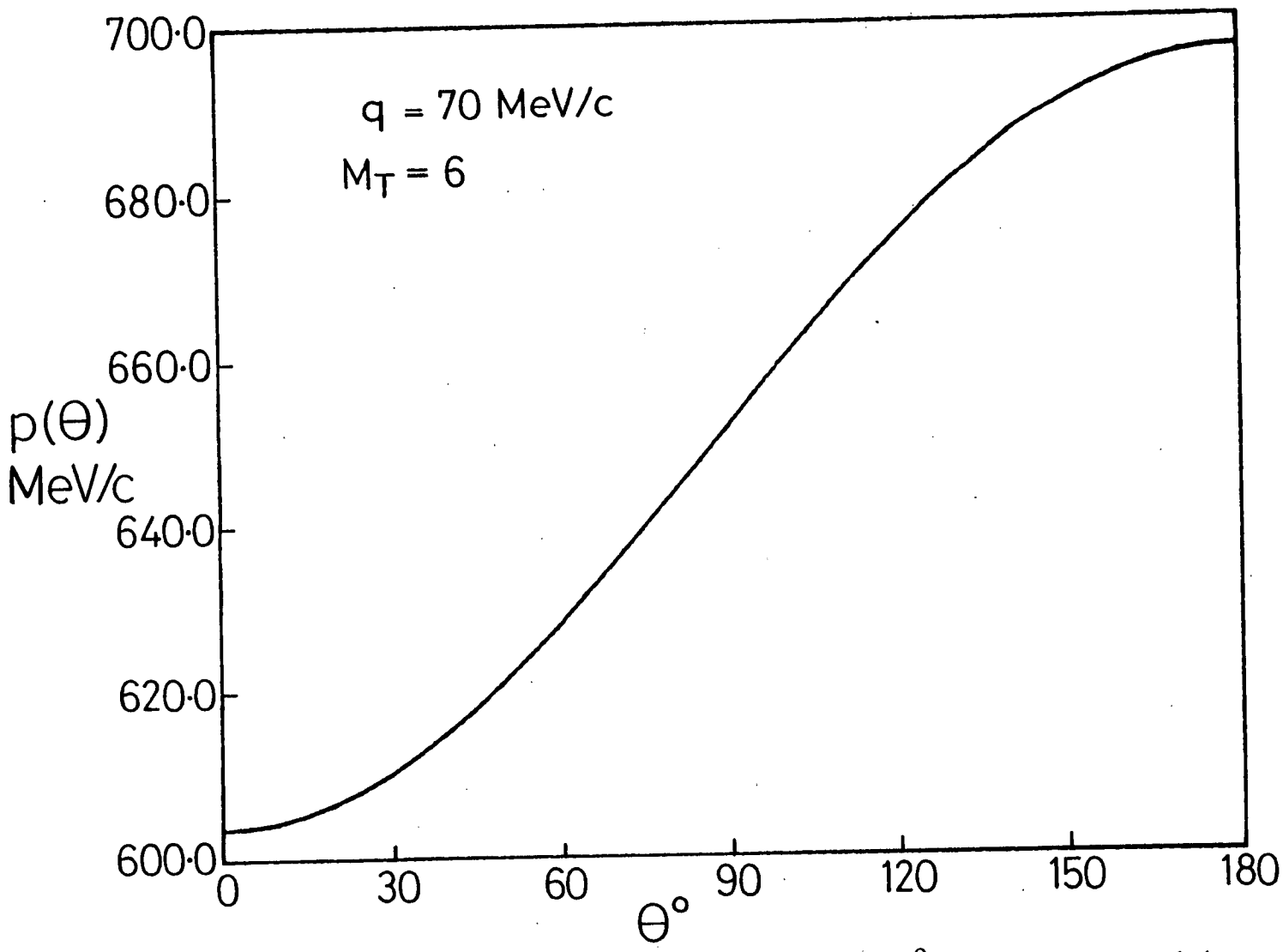

Figure A.9.3 The laboratory frame "equivalent momentum" at $\theta_\alpha = 30^\circ$ sampled when acquiring a laboratory frame angular distribution for 50 MeV alpha particles assuming q = 70 MeV/c and $M_T = 6$ (see text for notation).

APPENDIX 10 Estimation of (e,α) Cross Sections for a Two Step (γ,N) - (N,α) Process

The pre-equilibrium component in the (e,α) reaction is considered to arise from a two step process. Firstly a quasideuteron absorption process occurs with cross section $\sigma_\gamma(E_\gamma)$. This leads to the creation of a fast neutron and proton within the nuclear volume. These each have a probability $P(E_N,E_\gamma)dE_N$ of having an energy in the interval E_N to $E_N + dE_N$. A fraction, $f_{INT}(E_N)$ of these nucleons interact with the nucleus prior to escape. A fraction, $\phi_\alpha(E_\alpha,E_N)dE_\alpha$, of these interactions lead to the emission of an alpha particle of energy in the interval E_α to $E_\alpha + dE_\alpha$. Accounting for the creation of two fast nucleons by each absorbed photon, the cross section for emission of an alpha particle of energy E_α, following absorption of a photon of energy E_γ given by,

$$\frac{d\sigma_{\gamma,\alpha}}{dE_\alpha}(E_\alpha) \simeq \sigma_\gamma(E_\gamma) \int_{Thr}^{E_{max}} 2 \cdot P(E_N,E_\gamma) \cdot f_{INT}(E_N) \times \phi_\alpha(E_\alpha,E_N)dE_N \qquad (A10.1)$$

and the (e,α) cross section (assuming only dipole photon absorption) is then,

$$\frac{d\sigma_{e,\alpha}}{dE_\alpha}(E_e) \sim \int_{Thr}^{E_o} \frac{N^{E1}(E_e,E_\gamma)}{E_\gamma} \cdot \frac{d\sigma_{\gamma,\alpha}(E_\gamma)}{dE_\alpha} \cdot dE_\gamma. \qquad (A10.2)$$

It is the purpose of this appendix to obtain estimates of $d\sigma_{e,\alpha}/dE_\alpha$, using approximations to (A10.1) and (A10.2), to provide comparison with data obtained in this thesis.

Consideration of the (N,α) mechanism is avoided by estimating the quantity $\phi_\alpha(E_\alpha,E_N)$ using measured[153), 191)] (p, α) cross

sections, $d\sigma_{p,\alpha}/dE_\alpha$, and calculated nucleon capture cross sections, σ_R, thus

$$\phi_\alpha(E_\alpha,E_N)dE_\alpha \sim \frac{d\sigma_{p,\alpha}(E_N)}{\sigma_R} . \qquad (A10.3)$$

The calculation of (A10.2) and (A10.1) is simplified by using an average $\bar{\phi}_\alpha(E_\alpha,\bar{E}_N)$ calculated for an average energy, $\bar{E}_N$, for a nucleon created in the quasideuteron process, over the photon energy range for which an alpha of energy, E_α, may be emitted.

The intranuclear interaction probability, f_{INT}, is estimated using a nucleon mean free path, $\lambda = 4$ fm (here taken to be a constant for all nucleon energies considered), and an assumed average nucleon path length, prior to escape, equal to the radius of the nucleus, $R = 1.4\ A^{1/3}$fm. Thus

$$f_{INT} \sim (1 - \exp^{-R}/\lambda). \qquad (A10.4)$$

The factor $P(E_N,E_\gamma)$ is derived from the Oak Ridge cascade-evaporation code, PICA, (see Section 5.4.3.2). This yields photonucleon energy spectra for photon energies $E_\gamma \gtrsim 30$ MeV. These spectra give the probability, $\bar{P}(\bar{E}_N,\bar{E}_\gamma)$, that one of the initial fast nucleons has an energy sufficient to remove an alpha particle of the particular energy under consideration.

Over the photon energy range applicable for the present estimates (i.e. $E_\gamma \sim 30 - 120$ MeV) a constant photon absorption cross section can be assumed. Applying all the approximations and taking (A10.1) and (A10.2) together yields

$$\frac{d\bar{\sigma}_{e,\alpha}}{dE_\alpha}(E_e) \sim \left(\int_{Thr}^{E_e} \frac{N^{E1}}{E_\gamma}(E_e,E_\gamma)dE_\gamma\right) \cdot f_{INT} \cdot \sigma_\gamma \times 2\cdot\bar{P}(\bar{E}_N,\bar{E}_\gamma)\cdot \frac{d\bar{\sigma}_{p,\alpha}}{dE_\alpha} \cdot \frac{1}{\sigma_R} . \qquad (A10.5)$$

The values of the parameters employed in (A10.5) to yield four estimated (e,α) cross sections, are given in Table A10.1, together with a comparison of the estimated and experimental cross sections. The evident success of the approximate calculation employed here indicates likely fruitful results from a more detailed and rigorous approach using the proposed reaction process.

E_e = 120 MeV

	Nickel		Gold	
	E_α = 30 MeV	E_α = 50 MeV	E_α = 30 MeV	E_α = 50 MeV
$\int_{Thr}^{E_e} \frac{N^{E1}}{E_\gamma}(E_e,E_\gamma)dE_\gamma$	0.013	0.0058	0.026	0.0081
σ_γ (mb)	10	10	25	25
$\overline{P}(\overline{E_N},\overline{E_\gamma})$	0.35	0.2	0.4	0.25
f_{INT}	0.75	0.75	0.87	0.87
$\frac{d\overline{\sigma}_{p,\alpha}}{dE_\alpha}$ $(\frac{mb}{MeV})$	0.8	0.1	1.0	0.2
σ_R (mb)	900	900	1800	1800
ESTIMATE				
$\frac{d\overline{\sigma}_{e,\alpha}}{dE_\alpha}$ $(\frac{\mu b}{MeV})$	0.06	0.002	0.26	0.01
DATA				
$\frac{d\sigma_{e,\alpha}}{dE_\alpha}$ $(\frac{\mu b}{MeV})$	0.023	0.0012	0.19	0.016
$\frac{\text{ESTIMATE}}{\text{DATA}}$	2.6	1.7	1.4	0.62

TABLE A10.1 Estimated (e,α) cross sections and required parameters assuming a (γ,N) - (N,α) process.

APPENDIX 11 Exciton Model Formalism

The expressions used to calculate pre-equilibrium alpha particle emission in the Wu and Chang exciton model formalism are summarised in this appendix. The expressions presented here are discussed in further detail in Refs. 171 and 191.

A nucleus with initial excitation energy E, proceeding through states of p excited particles and h holes, will yield a pre-equilibrium energy spectrum for particles of type β and energy ε, given by,

$$\frac{d\sigma_\beta}{d\varepsilon}(E,\varepsilon) = \sigma_R \sum_{\substack{p=p_o \\ \Delta p=+1}}^{\bar{p}} \frac{\Gamma_\beta(p,h,E,\varepsilon)}{\Gamma(p,h,E)} \cdot P(p,h,E) \quad . \qquad (A11.1)$$

The partial and total branching widths are derived from particle-hole state densities, $\omega(p,h,E)$, calculated using an equal level spacing model, and from empirically determined average two body matrix elements $|M|^2$.

The particle-hole state density is

$$\omega(p,h,E) = \frac{g(gE - A_{p,h})^{p+h-1}}{p!\ h!\ (p+h-1)!} \qquad (A11.2)$$

where g is the single particle state density, and is related to the level density parameter, a, by $g = 6a/\pi^2$. $A_{p,h}$ is a correction term to take account of the reduction of possible particle-hole excitations due to the Pauli exclusion principle,

$$A_{p,h} = \frac{1}{4}(p^2 + h^2 + p - 3h). \qquad (A11.3)$$

The widths for transitions $(p,h) \rightarrow (p+1, h+1)$, $(p,h) \rightarrow (p-1, h-1)$ and $(p,h) \rightarrow (p,h)$ are given respectively by,

$$\Gamma_+(p,h,E) = \pi \cdot |M|^2 \cdot \frac{g(gE - C_{p+1,h+1})^2}{(p + h + 1)} \qquad \text{(A11.4)}$$

$$\Gamma_-(p,h,E) = \pi\ |M|^2\ gph(p + h - 2) \qquad \text{(A11.5)}$$

$$\Gamma_o(p,h,E) = \pi\ |M|^2 \cdot g \cdot (gE - C_{p,h}) \cdot \left\{\frac{p(p-1) + 4ph + h(h-1)}{p + h}\right\} \qquad \text{(A11.6)}$$

where $C_{p,h}$ is a further Pauli correction term,

$$C_{p,h} = \frac{1}{2}(p^2 + h^2) \ ,$$

and

$$|M|^2 = K_\gamma\ A^{-3}\ E^{-1}$$

where K_γ is an empirically determined constant. Here $K_\gamma = 200$ is used.

The expression for the decay width for a particle β with channel energy ε from a state with p excited particles and h holes to a residual nucleus with excitation energy U is,

$$\Gamma_\beta(p,h,E,\varepsilon) = \frac{2S_\beta + 1}{\pi^2\hbar^2}\ \mu_\beta\ \sigma_\beta(\varepsilon)\varepsilon \cdot \times \frac{\omega(p - p_\beta,\ h,\ U)}{\omega(p,\ h,\ E)} \times \frac{\omega(p_\beta,\ 0,\ E-U)}{g_\beta} \times R_\beta(p)\gamma_\beta \ . \qquad \text{(A11.7)}$$

The factor $R_\beta(p)$ [214] is a combinatorial probability giving the probability that p_β nucleons, chosen at random from among the p excited particles, has the right combination of protons and neutrons to form the outgoing complex particle β. γ_β is a complex particle formation

probability, considered to account for the probability of emission of the complex particle. The factor γ_β is obtained from fits to (p,x) data, or may be treated as a free parameter.

The total particle decay width is trivially given by,

$$\Gamma_\beta(p,h,E) = \int_0^{E-B_\beta} \Gamma_\beta(p,h,E,\varepsilon)d\varepsilon \qquad \text{(A11.8)}$$

and hence the total particle-hole state width is,

$$\Gamma(p,h,E) = \Gamma_+(p,h,E) + \Gamma_-(p,h,E) + \Gamma_o(p,h,E) + \sum_\beta \Gamma_\beta(p,h,E) \quad . \qquad \text{(A11.9)}$$

The probability of reaching a given particle-hole state (p,h) is

$$P(p,h,E) = \left\{ \prod_{\substack{p'=p_o \\ \Delta p'=+1}}^{p-1} \frac{\Gamma_+(p',h',E)}{\Gamma(p',h',E)} \right\} \cdot \left\{ 1 + \frac{\Gamma_+(p,h,E)}{\Gamma(p,h,E)} \cdot \frac{\Gamma_-(p+1,h+1,E)}{\Gamma(p+1,h+1,E)} \right\} \qquad \text{(A11.10)}$$

The last term in the second bracket of (A11.10) accounts for the 'backwards' transition of the (p+1, h+1) state into the (p,h) state. Since $\Gamma_- << \Gamma_+$ this term is generally neglected in order to simplify the calculation of P(p,h,E).

Expressions (A11.1 - A11.10) contain all the relations required to calculate particle induced pre-equilibrium exciton model angle integrated energy spectra. The extension to electron induced reactions is, in principle, trivial. The total reaction cross section, σ_R, is replaced in (A11.1) by a total photon absorption cross section $\sigma_\lambda^{p\lambda}(E)$ of appropriate multipolarity $p\lambda$. The resulting pre-equilibrium energy spectrum is then used to yield,

$$\frac{d\sigma_{e,\beta}}{d\varepsilon}(E_e,\varepsilon) = \sum_{\lambda} \int_{E_{thr}}^{E_o} \frac{d\sigma_{\beta}^{p\lambda}}{d\varepsilon}(E_\gamma) \cdot N^{p\lambda}(E_e,E_\gamma) E_\gamma^{-1}\, dE_\gamma . \quad \text{(A11.11)}$$

For $140 \gtrsim E_\gamma \gtrsim 40$ MeV electric dipole transitions are expected to dominate the reaction process, and hence only $p\lambda \equiv E1$ is generally applied in (A11.11).

APPENDIX 12 Publications

The following publications comprise parts of the work presented in this thesis:

1. 'New Evidence for a Direct Process in the (e,α) Reaction'
   A.G. Flowers, A.C. Shotter, D. Branford, J.C. McGeorge and R.O. Owens,
   Phys. Rev. Lett. 40, 709 (1978).

2. 'Electron-Induced Preequilibrium Alpha Emission'
   A.G. Flowers, D. Branford, J.C. McGeorge, A.C. Shotter, P. Thorley, C.H. Zimmerman, R.O. Owens and J.S. Pringle,
   Phys. Rev. Lett., 43, 323 (1979).

These papers are contained in the following pages.

New Evidence for a Direct Process in the (e, α) Reaction

A. G. Flowers, A. C. Shotter, and D. Branford
Department of Physics, University of Edinburgh, Edinburgh, United Kingdom

and

J. C. McGeorge and R. O. Owens
Kelvin Laboratory, Department of Natural Philosophy, The University, Glasgow, United Kingdom

(Received 12 December 1977)

Alpha-particle energy and angular distributions have been measured for the reaction ^{60}Ni$(e,\alpha)e'X$ using electrons of energies 33, 60, and 120 MeV. Statistical-model calculations give good quantitative agreement in the region of the peak of the α energy spectra. Higher-energy α particles exhibit a forward-peaked angular distribution and a cross section several orders of magnitude above the statistical-model predictions, indicating the presence of a direct-reaction component.

Alpha particles emitted by medium-weight nuclei which have been excited by real or virtual photons originate mainly from the statistical decay of the excited nucleus.[1-4] In heavy nuclei there is some evidence of a direct-reaction process,[2,5] but such a process has not been observed

in medium-weight nuclei. In this Letter we present unambiguous evidence for the presence of both a direct-reaction (pre-equilibrium) component and an evaporation component in the $(e, \alpha)e'$ reaction on the medium-weight nucleus ^{60}Ni.

We have studied the α energy spectra and angular distributions of α particles emitted in the reaction ^{60}Ni$(e, \alpha)e'X$ at electron energies up to 120 MeV, using the University of Glasgow electron linear accelerator. The α particles were momentum analyzed with an $n = \frac{1}{2}$ double-focusing spectrometer,[6] of energy resolution 0.1%, and detected in an array of ten silicon surface-barrier detectors. Shielding around the detectors reduced the background to negligible proportions over most of the α energy range. The target was isotopically enriched ^{60}Ni, of 99.6% purity. Its thickness was found by α energy-loss measurement to be 696 ± 42 μg/cm^2. The total error in cross section due to uncertainties in the values of target thickness, electron current, spectrometer solid angle, and dispersion is $< 7\%$.

Spectra of α particles emitted following electron bombardment at 33, 60, and 120 MeV are presented in Fig. 1. The solid lines in the figure are the results of a statistical-model calculation which relates the (γ, α) cross section to the (γ, n) cross section:

$$d\sigma_{\gamma,\alpha}(E_\gamma, E_\alpha) = \frac{\sigma_{\gamma,n}(E_\gamma)\,\Gamma_\alpha(E_\gamma, E_\alpha)\,dE_\alpha}{\int \Gamma_n(E_\gamma, E_n)\,dE_n}. \quad (1)$$

Here the (γ, n) cross section has been approximated by using the measured[7] single-photoneutron cross section $[\sigma(\gamma, n) + \sigma(\gamma, pn)]$. This approximation is reasonable since in the region of our calculation $\sigma(\gamma, pn)$ is small compared with $\sigma(\gamma, n)$. The $(e, \alpha)e'$ cross section was then computed on the assumption that the $E1$ virtual-photon spectrum provides the dominant contribution to the excitation process:

$$d\sigma_{e,\alpha}(E_e, E_\alpha) = \int_{12}^{33} d\sigma_{\gamma,\alpha}(E_\gamma, E_\alpha) N^{E1}(E_e, E_\gamma) E_\gamma^{-1}\,dE_\gamma, \quad (2)$$

where N^{E1} is the electric-dipole virtual-photon intensity spectrum calculated from the analytical expression of Wolynec, Onley, and Nascimento[8] which results from a fit to the distorted-wave calculations of Gargaro and Onley.[9] The neutron- and α-channel exit widths (Γ_n and Γ_α) were calculated with a modified version[10] of the computer code HAUSER,[11] based on conventional Hauser-Feshbach theory.[12] The optical-model parameters are taken from Wilmore and Hodgson[13] and Lemos.[14] The method of level-density calculation, and the parameters used, were those of Gilbert and Cameron.[15] The calculation takes no account of photon absorption above $E_\gamma = 33$ MeV, yielding only that part of the α energy spectrum which results from excitation of the target in the region of the giant dipole resonance.

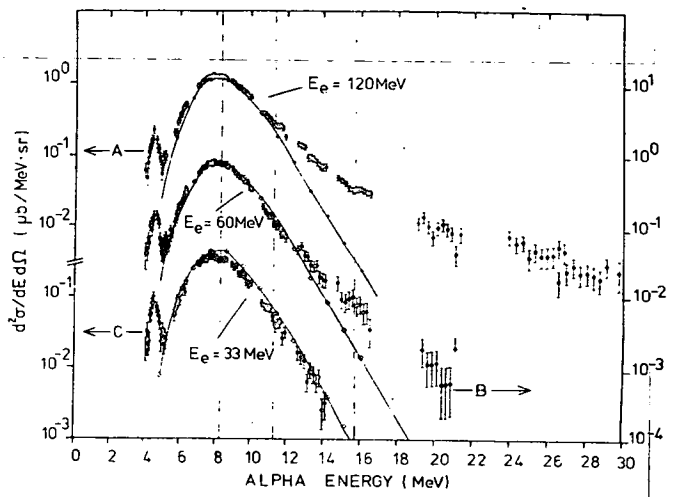

FIG. 1. Alpha-particle energy spectra at $\theta_\alpha = 90°$, for $E_e = 120$ MeV (curve A, upper left-hand scale), $E_e = 60$ MeV (curve B, right-hand scale), and $E_e = 33$ MeV (curve C, lower left-hand scale). Errors shown are absolute. The solid lines are the results of a statistical calculation assuming photon absorption below $E_\gamma = 33$ MeV. The dashed lines mark the mean energies at which angular distributions were taken.

This method of calculating the $(e, \alpha)e'$ cross section can be used only in regions above the neutron threshold. The sudden drop in observed cross section above 4.3 MeV is due to the onset of neutron emission: α particles of lower energy doubtlessly result almost entirely from the compound-nuclear excitations below the neutron separation energy of 11.4 MeV.

The statistical-model calculations are seen to give good agreement with the magnitude and position of the peak of the α spectrum at all three electron energies. For E_α in the range 6–12 MeV the discrepancies do not exceed ±50%, which is within the inherent uncertainty of our evaporation calculation. Above $E_\alpha = 12$ MeV, comparison of the measured and calculated energy spectra shows dramatic differences; a high-energy tail in the spectrum becomes systematically larger compared to the evaporation calculation as the electron energy is increased. Whereas the observed spectrum agrees with the calculation at $E_e = 33$

MeV, it exceeds it by several orders of magnitude at $E_e = 120$ MeV. Although slight changes in the calculation input parameters could improve agreement in the absolute magnitude of the cross section in the 6–12-MeV region, it is unlikely that such a procedure would improve the fit significantly above $E_\alpha = 12$ MeV.

Clearly there exists a further component in the $(e, \alpha)e'$ reaction, in addition to the evaporative part resulting from excitation of the target by photons of $E_\gamma \lesssim 33$ MeV. Further evidence on the nature of this component has been obtained by measuring α-particle angular distributions. Data obtained at $E_e = 120$ MeV are presented in Fig. 2; similar results have been obtained at $E_e = 60$ MeV.

The angular distribution for α energy, 8.2 MeV, in the peak of the evaporation spectrum is symmetric about 90°, as expected of particle emission proceeding through compound-nucleus states. However, at higher α-emission energies the angular distributions become increasingly forward peaked, suggesting that a larger fraction of the α-emission process is associated with a direct-reaction process. Angular distributions similar to those for ^{60}Ni have been obtained by us for ^{56}Fe. These distributions show, for the first time in medium-weight nuclei, the smooth change from a symmetric to an asymmetric angular distribution as the α-emission energy increases.

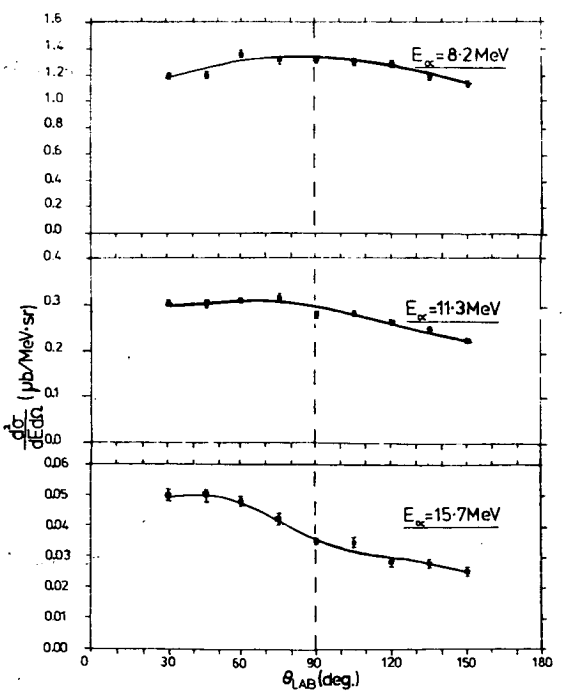

FIG. 2. Alpha-particle angular distributions at $E_e = 120$ MeV averaged over the α energy ranges 7.7–8.7 MeV, 10.6–11.9 MeV, and 14.8–16.4 MeV. Errors shown are relative. The solid lines are merely to guide the eye.

The evaporative component of our α energy spectra is well explained in terms of $E1$ virtual-photon absorption to a compound giant resonance state which undergoes statistical decay. It has been claimed[16] that in heavy nuclei, at least, the α-emission process proceeds dominantly through $E2$ transitions. It is possible that the evaporative component observed here can be explained entirely in terms of photon absorption to the $E2$ isoscalar resonance, positioned[17] at about $E_x = 16$ MeV in ^{60}Ni. The magnitude of our cross sections would then require the α-emission channel to exhaust 75% of the $E2$ energy-weighted sum rule.[18] The $E2$ virtual-photon intensity was obtained from the computer code of Gargaro and Onley, as used in Ref. 9. However, such a process still would fail to reproduce the high-energy tail seen in the α-energy spectra. Consideration of the angular distributions makes it unlikely that the $E2$ isovector resonance contributes to the high-energy α spectrum. The overlap of the $E1$ resonance centered at 20 MeV and the predicted $E2$ isovector resonance at ~33 MeV would probably not be sufficient to produce the necessary interference terms required to explain the observed forward-peaked angular distributions.

It has been assumed previously that an evaporative process would dominate α emission following the absorption of high-energy photons; for example, an attempt has been made to fit α energy spectra from targets irradiated by 450-MeV bremsstrahlung with calculated evaporation spectra.[19] However, there are several inherent difficulties with such a calculation. Above ~30 MeV photon energy a pre-equilibrium cascade becomes increasingly probable, leading to a final compound-nucleus energy below the initial excitation energy. The cross section for photon absorption leading to compound-nucleus formation is uncertain above ~30 MeV, and even if we assume knowledge of this cross section, difficulties arise with the validity of level-density formulas at high excitation energies. Therefore the questionable validity of evaporation calculations based on a compound nucleus at excitation energies above ~30 MeV led us to cut off the statistical-model calculations at 33 MeV excitation. Since such calculations predict angular distributions symmetric about 90°, the observed forward-peaked angular distributions for high-energy α's will not

be reproduced, even at high-excitation energies. It seems more probable that an intranuclear cascade initiated by high-energy nucleons from (γ, N) processes (such nucleons themselves being strongly forward peaked) is responsible for the high-energy α emission. The cascading nucleons could then eject α particles in a similar reaction mechanism to the (n, α) and (p, α) reactions. Recent work[20] on these (N, α) reactions has yielded a satisfactory explanation of the observed energy spectra, which are similar in form to those observed here. Currently an attempt is being made to interpret our $(e, \alpha)e'$ data in terms of the (N, α) results.

It can be seen from Fig. 1 that the increase in electron energy from 60 to 120 MeV causes an order of magnitude increase in the observed cross section for high-energy α particles ($E_\alpha \sim 18$ MeV). The ratio of virtual-photon intensity at these two energies, for $E_\gamma = 30$ MeV, is 1.6. The high-energy α particles are therefore unlikely to result from a single-step direct reaction mechanism involving the virtual photon.

The authors are grateful to Dr. D. J. S. Findlay for supplying data-acquisition programs and for assistance with the experimental work. We acknowledge the support of the work by the Science Research Council. One of us (J. C. M.) acknowledges the support of the Central Electricity Generating Board; another (A. G. F.) acknowledges receipt of an Edinburgh University Postgraduate Scholarship. We thank Professor W. Cochran for his support and encouragement in this work.

[1]M. Kregar and B. Povh, Nucl. Phys. 43, 170 (1963).

[2]L. Meneghetti and S. Vitale, Nucl. Phys. 61, 316 (1965).

[3]H. Hoffman, B. Prowe, and H. Ullrich, Nucl. Phys. 85, 631 (1966).

[4]N. A. Keller and D. B. McConnell, Can. J. Phys. 50, 1554 (1972).

[5]J. J. Murphy, II, H. J. Gehrhardt, and D. M. Skopik, Nucl. Phys. A277, 69 (1977).

[6]J. L. Matthews, D. J. S. Findlay, S. N. Gardiner, and R. O. Owens, Nucl. Phys. A267, 51 (1976).

[7]S. C. Fultz, R. A. Alverez, B. L. Berman, and P. Meyer, Phys. Rev. C 10, 608 (1974).

[8]I. C. Nascimento, E. Wolynec, and D. S. Onley, Nucl. Phys. A246, 210 (1975).

[9]W. W. Gargaro and D. S. Onley, Phys. Rev. C 4, 1032 (1971).

[10]N. Shikazono and T. Terasawa, Nucl. Phys. A250, 260 (1975).

[11]P. J. Dallimore, Australian National University Report No. ANU-P/512, 1970 (unpublished).

[12]W. Hauser and H. Feshbach, Phys. Rev. 87, 366 (1952).

[13]D. Wilmore and P. E. Hodgson, Nucl. Phys. 55, 673 (1964).

[14]O. F. Lemos, Institute of Nuclear Physics, Université de Paris XI, Orsay, France, Internal Report, Ser. A, No. 136, 1972 (unpublished).

[15]A. Gilbert and A. G. W. Cameron, Can. J. Phys. 43, 1446 (1965).

[16]E. Wolynec, M. N. Martins, and G. Moscati, Phys. Rev. Lett. 37, 585 (1976).

[17]D. H. Youngblood *et al.*, Phys. Rev. C 13, 994 (1976).

[18]V. L. Telegdi and M. Gell-Mann, Phys. Rev. 91, 169 (1953).

[19]P. David, J. Debrus, F. Lübke, H. Mommsen, R. Schoenmackers, and G. Stein, Nucl. Phys. A221, 145 (1974).

[20]M. Blann and A. Mignerey, Nucl. Phys. A287, 301 (1977).

Electron-Induced Preequilibrium Alpha Emission

A. G. Flowers, D. Branford, J. C. McGeorge, A. C. Shotter, P. Thorley, and C. H. Zimmerman
Department of Physics, University of Edinburgh, Edinburgh EH9 3JZ, United Kingdom

and

R. O. Owens and J. S. Pringle[a]
Kelvin Laboratory, Department of Natural Philosophy, The University, Glasgow G12 8QQ, United Kingdom

(Received 9 May 1979)

This paper presents energy spectra of α particles emitted following the bombardment of ^{27}Al, ^{nat}Ni, ^{92}Mo, ^{94}Mo, and ^{197}Au with 120-MeV electrons, together with α-particle angular distributions from ^{197}Au and ^{nat}Ni for $E_\alpha = 30$ and 50 MeV. The data are compared with preequilibrium exciton-model and statistical-model calculations. It is concluded that few-step processes are dominant in the production of α particles with energies above 20 MeV.

There have been few studies of preequilibrium particle decay in photonuclear reactions compared to the extensive effort made to acquire and interpret data on preequilibrium effects arising from nucleon-induced reactions. There is some evidence that photon-induced preequilibrium complex-particle emission is observable in heavy nuclei,[1,2] and in a previous paper[3] we concluded that a preequilibrium component occurs in the (e,α) reaction for medium-weight nuclei. In this paper, we present measurements undertaken to determine the systematics of preequilibrium α emission from electron-induced reactions corresponding to excitations up to 120 MeV.

Targets of ^{27}Al, ^{nat}Ni, ^{68}Zn, ^{92}Mo, ^{94}Mo, and ^{197}Au were bombarded with 120-MeV electrons from the University of Glasgow electron linear accelerator. The α-particle detection system has been described previously.[3] The target thicknesses were determined by weighing, and were selected to give a maximum energy loss $\Delta E_\alpha < 0.05 E_\alpha$.

Spectra of α particles emitted at 30° in the laboratory frame are presented in Fig. 1. Previously we have shown the success of conventional statistical-model calculations in predicting the low-energy region ($E_\alpha \lesssim 12$ MeV) of the α-particle spectra from medium-weight nuclei[3] (see Fig. 2). In heavy nuclei the statistical component is considerably reduced since the Coulomb bar-

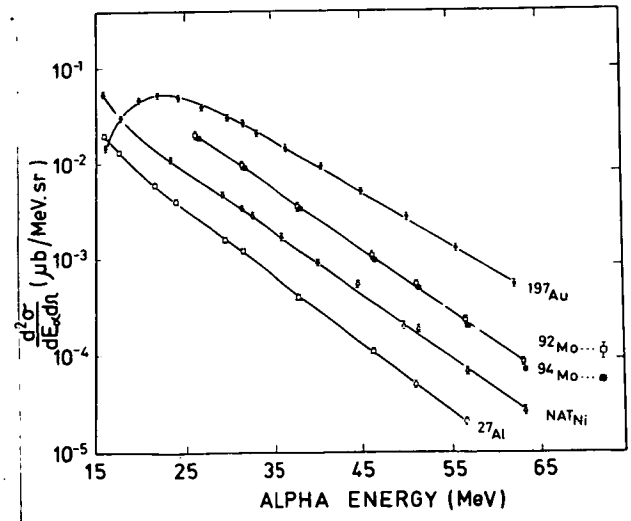

FIG. 1. α-particle energy spectra at $\theta_\alpha = 30°$, for $E_e = 120$ MeV. Errors shown are the sum of statistical and systematic contributions. The solid lines are a guide to the eye.

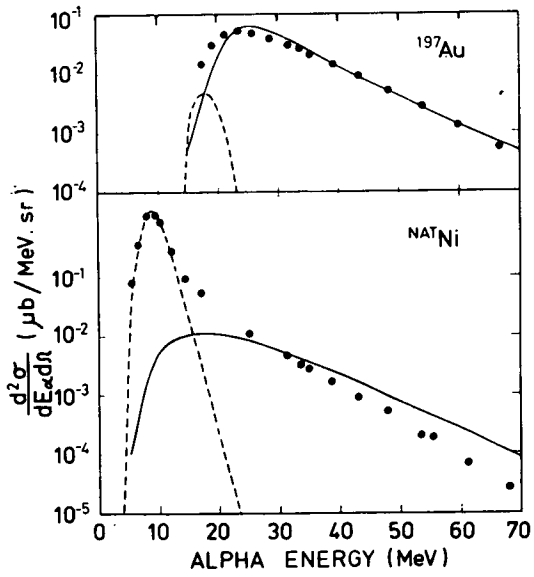

FIG. 2. α-particle energy spectra at $\theta_\alpha = 30°$, for $E_e = 120$ MeV. The solid circles are experimental points. The solid lines are the results of preequilibrium exciton-model calculations and the dashed lines are the results of statistical calculations neglecting photon absorption above $E_\gamma = 33$ MeV.

rier height exceeds the energy of α particles emitted following giant-resonance excitation. The expected position and magnitude of the ^{197}Au evaporation peak has been calculated here with use of the conventional Hauser-Feshbach approach described in Ref. 3. The neutron optical-model parameters were taken from Wilmore and Hodgson.[4] α-particle optical-model parameters were estimated from those for α scattering on gold and tungsten.[5] An optical potential $(V+iW)f(r_0,a)$ was employed, with $V=192$ MeV and $W=30$ MeV. The Saxon-Woods function $f(r_0,a)$ had a radius parameter $r_0=1.42$ fm and diffuseness parameter $a=0.55$ fm. The required values of $\sigma(\gamma,n)$ for ^{197}Au were taken from Veyssiere *et al.*[6] All other parameters employed are given in Ref. 3. The predicted evaporation component is shown in Fig. 2. The peak position is in agreement with the calculations of Meneghetti and Vitale.[1] It is evident that in heavy nuclei the α emission arises almost entirely from preequilibrium effects. This contrasts with medium-weight nuclei for which the Coulomb barrier is lower, and consequently a large evaporative component is observed, in close agreement with the statistical calculation.

The mass-number dependence of the evaporative (equilibrium) and preequilibrium contributions to the (e,α) cross section differ considerably. While the evaporative component peaks at about mass 60 and then falls off rapidly with increasing mass number, the preequilibrium component continues to increase steadily. The total (e,α) cross section integrated above $E_\alpha=25$ MeV is proportional to $A^{1.5}$ and this dependence becomes $A^{2.0}$ at $E_\alpha=50$ MeV. This mass dependence is in marked contrast with the $A^{1/3}$ dependence found for (p,α) cross sections,[7] and suggests a two-stage process. Such a process is likely to be initiated by a quasideuteron interaction,[8] for which the cross section is volume dependent and increases almost linearly with mass number. The second stage would then be an (N,α) reaction which if it were surface dependent ($\sim A^{2/3}$) or volume dependent ($\sim A$) would lead to a mass dependence between $A^{5/3}$ and A^2, as observed. A conclusion that the second stage of the process changes from a surface to a volume effect as the nucleon and α energies increase cannot yet be justified in view of the purely qualitative treatment here, neglecting absorption effects. Definite conclusions must await further calculations.

The apparent importance of a two-step, or at most few-step, mechanism in the emission of α particles above 25 MeV implies that the nuclear excitation is shared among relatively few nucleons at this stage of the reaction. An indication of the validity of this picture is obtained from the energy dependence of the spectra in Fig. 1. Since each of the spectra exhibits a smooth exponential decrease in cross section with increasing α energy an interpretation in terms of a nuclear temperature is suggested. The spectra were parametrized, therefore, by use of the expression $d^2\sigma/dE_\alpha d\Omega \propto \sigma_{\text{inv}}(E_\alpha)\exp(-E_\alpha/T)$. The cross sections for α capture by the residual nuclei, σ_{inv}, were calculated by Gadioli, Erba, and Hogan.[9] The resulting temperatures are given in Table I and exceed the values of 1.0–1.5 MeV for the equilibrium component of the (e,α) reaction[10] by about a factor of 4. The temperatures obtained from electrodisintegration experiments are only a mean value resulting from all excitations from threshold to the electron energy, and hence only general comparisons can be made with other reactions exhibiting preequilibrium effects. In the case of other preequilibrium spectra an elevated temperature has been associated[11] with a localized excitation, or "hot spot" within the nuclear volume. The concept of a "hot spot" has been applied to the analysis of preequilibrium α emission following deep-inelastic scattering of heavy ions.[12,13] This yielded temperatures of 3.5–4.0 MeV for α particles emitted in the forward direction following ~30-MeV excitation of the compound system. The higher temperatures observed in the present work reflect higher excitation energies, and possibly greater localization of the "hot spot."

A quantitative treatment of the process of sharing the initial excitation among an increasing number of nucleons is provided by the exciton model and calculations with this model have proved to be successful at predicting numerous

TABLE I. Temperatures corresponding to the preequilibrium component of the (e,α) reaction, derived from energy spectra at $\theta_\alpha=30°$ for $E_e=120$ MeV.

Target	Temperature[a] (MeV)
^{27}Al	5.3
^{nat}Ni	5.5
^{68}Zn	5.4
^{92}Mo	5.6
^{94}Mo	5.4
^{197}Au	6.1

[a]Error is ± 0.2 MeV.

preequilibrium reaction spectral shapes, e.g., Ref. 9 and Wu and Chang.[14] We have therefore compared typical spectra with results from the exciton model as applied to photonuclear reactions by Wu and Chang.[14] The only amendment to the technique employed in Ref. 14 was the substitution of a plane-wave, $E1$, virtual-photon spectrum in place of the bremsstrahlung spectrum. Coulomb distortion and finite-nuclear-size effects[15] on the photon spectra were neglected. These effects are expected to cause only small changes ($<10\%$) to the calculated spectral shape, although the absolute magnitude may only be accurate to $\sim 40\%$ when they are neglected. Such correction factors are not important here since the preequilibrium calculations only yield relative cross sections. Uncertainties in the determination of the α-particle formation probabilities and the average two-body matrix elements used to calculate exciton-state decay rates do not allow the calculation of absolute cross sections. In Fig. 2 the calculated spectral shapes are compared with our data. The exciton-model calculations yield angle-integrated spectra, and these have been normalized to the data taken at $\theta_\alpha = 30°$. These spectra are in reasonable agreement with the data, particularly for ^{197}Au. The peak of the ^{197}Au(e,α) energy spectrum clearly arises from a preequilibrium component and not the equilibrium component as suggested by Murphy, Skopik, and Asai[16] who arbitrarily fit an evaporation-model shape to such data.

The spectral shapes obtained from exciton-model calculations are strongly dependent on the initial exciton number.[17] The initial exciton number used here was $n_0 = 4$, corresponding to the quasideuteron process in which a two-particle, two-hole state is formed. A lower initial exciton number would result in an increased high-energy component, and thus a flatter energy spectrum. It is evident that use of a lower initial exciton number would not improve the fits obtained here and in Ref. 14.

α angular distributions obtained for 30- and 50-MeV α particles from ^{nat}Ni and ^{197}Au are shown in Fig. 3. The form of the angular distributions for each α-particle energy exhibits no marked difference between the two nuclei considered. In both cases the asymmetry increases with increasing α energy. Although some calculations of preequilibrium nucleon angular distributions have been carried out,[18-20] we are unaware of any preequilibrium model which calculates complex-particle angular distributions, although

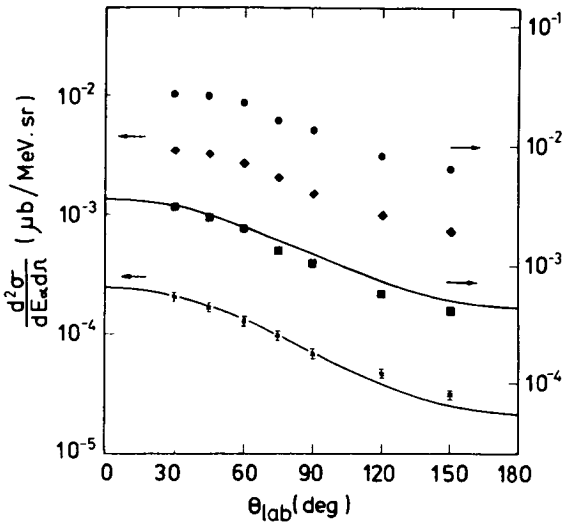

FIG. 3. α-particle angular distributions at $E_e = 120$ MeV for ^{197}Au (shown as circles for $E_\alpha = 30$ MeV and squares for $E_\alpha = 50$ MeV) and ^{nat}Ni (shown as diamonds for $E_\alpha = 30$ MeV and stars for $E_\alpha = 50$ MeV). The solid lines are the result of simple kinematic calculations described in the text. The sum of statistical and systematic errors is shown where it exceeds the size of the points.

work is in progress on this problem.[21,22] In the spirit of the exciton model we have been able to reproduce the distribution shown in Fig. 3, using crude kinematic considerations. α emission occurs when two neutrons and two protons with the proper momenta combine in an exciton state. Only the excited nucleons take part in the reaction, and the rest of the nucleus can be considered to act as a spectator. Hence the incoming photon momentum is shared by only a few nucleons at the preequilibrium stage, and a complex particle formed from these nucleons will have a large fraction of the incoming momentum transferred to it. Therefore the angular distribution obtained for particles of a fixed energy in the laboratory frame will arise from a range of particle energies in the center-of-mass frame of the excited nucleons. At forward angles the observed complex particles are at a lower energy in the center-of-mass frame than in the laboratory frame and conversely for backward angles. If the cross section falls rapidly with increasing particle energy, as is observed for the preequilibrium (e,α) reaction, then a forward-peaked angular distribution will be obtained for particles of a fixed energy in the laboratory frame (even if the emission is isotropic in the center-of-mass frame). To estimate the importance of this ef-

fect we have assumed that the average momentum transferred to the nucleus prior to the emission of a 50-MeV α particle is $k_\gamma = 70$ MeV/c. The number of nucleons, p, sharing the momentum at the time of α emission was varied to obtain the best fit to the angular distribution data. With use of the experimentally determined slopes for $\sigma(E_\alpha)$ the fits shown in Fig. 3 are obtained with $p = 6$. Similar fits can be obtained for $E_\alpha = 30$ MeV by varying k_γ and p in a qualitatively reasonable way. In view of the fair agreement observed, it seems plausible that the exciton model could describe the α-particle angular distributions.

In conclusion, we have observed a significant preequilibrium component in the (e,α) reaction which may be described by a two-step or few-step process in which only a few nucleons share the initial excitation energy prior to particle emission.

We are grateful to J. R. Wu and C. C. Chang for providing us with their exciton-model code PREQEC, and for carrying out calculations on our behalf. We wish to thank the U. K. Science Research Council for supporting this work.

---

[a]Present address: Radiation Centre, University of Birmingham, P. O. Box 363, Birmingham, U. K.

[1]L. Meneghetti and S. Vitale, Nucl. Phys. 61, 316 (1965).

[2]J. J. Murphy, II, H. J. Gehrhardt, and D. M. Skop Nucl. Phys. A277, 69 (1977).

[3]A. G. Flowers *et al.*, Phys. Rev. Lett. 40, 709 (19

[4]D. Wilmore and P. E. Hodgson, Nucl. Phys. 55, 6 (1964).

[5]M. Makowska-Rzeszutko, A. Dubek, and A. Drzyn la, Institute of Nuclear Physics, Cracow, Poland, R port No. 735/PL, 1970 (unpublished).

[6]A. Veyssiere *et al.*, Nucl. Phys. A159, 561 (1970)

[7]A. Chevarier *et al.*, Phys. Rev. C 11, 886 (1975).

[8]J. S. Levinger, Phys. Rev. 84, 43 (1951).

[9]E. Gadioli, E. Gadioli Erba, and J. J. Hogan, Phy Rev. C 16, 1404 (1977).

[10]H. Hoffmann, B. Prowe, and H. Ullrick, Nucl. Ph 85, 631 (1966).

[11]R. Weiner and M. Weström, Phys. Rev. Lett. 34, 1523 (1975), and Nucl. Phys. A286, 282 (1977).

[12]H. Ho *et al.*, Z. Phys. A 283, 235 (1977).

[13]T. Nomura *et al.*, Phys. Rev. Lett. 40, 694 (1978)

[14]J. R. Wu and C. C. Chang, Phys. Rev. C 17, 1540 (1978).

[15]A. C. Shotter, J. Phys. G 5, 371 (1979).

[16]J. J. Murphy, II, D. M. Skopik, and J. Asai, Phys Rev. C 18, 736 (1978).

[17]C. K. Cline and M. Blann, Nucl. Phys. A172, 225 (1971).

[18]G. Mantzouranis, D. Agassi, and H. A. Weidenmü ler, Phys. Lett. 57B, 220 (1975).

[19]G. Mantzouranis, D. Agassi, and H. A. Weidenmü ler, Z. Phys. A 278, 145 (1976).

[20]J. M. Akkermans, Phys. Lett. 82B, 20 (1979).

[21]C. Kalbach, private communication.

[22]E. Gadioli, private communication.

REFERENCES

1) J. Chadwick and M. Goldhaber, Nature 134, 237 (1934).

2) L. Szilard and T.A. Chalmers, Nature 134, 494 (1934).

3) M.S. Livingstone and H.A. Bethe, Rev. Mod. Phys. 9, 351 (1936).

4) H. Hanni, V.L. Telegdi and W. Zunti, Helv. Phys. Acta, 21, 203 (1948).

5) D.W. Kerst, Rev. Sci. Instr. 13, 387 (1942).

6) H.F. Kaiser, J. App. Phys. 18, 1 (1947).

7) W.F. Westendorp and E.E. Charlton, J. App. Phys. 16, 58 (1945).

8) G.C. Baldwin and G.S. Klaiber, Phys. Rev. 70, 259 (1946).

9) F.K. Goward and J.J. Wilkins, Proc. Roy. Soc. A228, 376 (1955).

10) P. Erdös, P. Scherrer and P. Stoll, Helv. Phys. Acta 30, 639 (1957).

11) L.H. Greenberg, J.G.V. Taylor and R.N.H. Haslam, Phys. Rev. 95, 1540 (1954).

12) J.D. Walecka, S. Penner and J.R. Calarco, Nuclear Physics with Electromagnetic Interactions, p. 484, p. 99 and p. 114 respectively, Proc. Mainz 1979, Lecture Notes in Physics 108, eds. H. Arenhovel and D. Drechsel (Springer Verlag).

13) E.G. Fuller, H.M. Gerstenberg, H. Vander Molen and T.C. Dunn, Photonuclear Reaction Data, 1973, N.B.S. Special Publication 380, and supplement 1 (1977).

14) M.E. Toms and John McElhinney, Phys. Rev. 111, 561 (1958).

15) C.H. Millar and A.G.W. Cameron, Phys. Rev. 78, 78 (1950).

16) R.N.H. Haslam and H.M. Skarsgard, Phys. Rev. 81, 479 (1951).

17) R.N.H. Haslam, L.A. Smith and J.G.V. Taylor, Phys. Rev. 84, 840 (1951).

18) R.N.H. Haslam, A.G.W. Cameron, J.A. Cooke and E.H. Crosby, Can. J. Phys. 30, 349 (1952).

19) L. Katz and A.G.W. Cameron, Can. J. Phys. 29, 518 (1951).

20) F. Heinrich, H. Wäffler and M. Walter, Helv. Phys. Acta, 29, 3 (1956).

21) C.H. Millar, Can. J. Phys. 31, 262 (1953).

REFERENCES (Contd.)

22) J. Blatt and V.F. Weisskopf, Theoretical Nuclear Physics, John Wiley and Sons, Inc., New York (1952).

23) J.H. Carver, Proc. Phys. Soc. 77, 417 (1961).

24) M. Kiegar and B. Povh, Nucl. Phys. 43, 170 (1963).

25) J.A. Scheer, K. Schlüpmann and F.Triantafyllidis, Nucl. Phys. 56, 113, (1964).

26) M. Meneghetti and S. Vitale, Nucl. Phys. 61, 316 (1965).

27) H. Hoffmann, B. Prowe and H. Ullrich, Nucl. Phys. 85, 631 (1966).

28) G. Kraft, R. Kosiek, R. Mundhenke and J. Winter, Nucl. Phys. A118, 25 (1968).

29) N.A. Keller and D.B. McConnell, Can. J. Phys. 50, 1554 (1972).

30) W.R. Dodge and H.V. Molen, Proceedings of 2nd International Conference on Clustering Phenomena in Nuclei, College Park, Maryland, U.S.A., p. 325 (1975).

31) D.M. Skopik, Y.M. Shin and J.J. Murphy II, Can. J. Phys. 53, 1398 (1975).

32) M. Sugawara, T.Terasawa, T. Tamae, N. Kawamura, H. Saito and H. Tsubota, Nucl. Phys. A248, 477 (1975).

33) E. Wolynec, M.N. Martins and G. Moscati, Phys. Rev. Lett. 37, 585 (1976).

34) J.J. Murphy II, H.J. Gehrhardt and D.M. Skopik, Nucl. Phys. A277, 69 (1977).

35) S. Oikawa and K. Skoda, Nucl. Phys. A277, 301 (1977).

36) A.G. Flowers, A.C. Shotter, J.C. McGeorge and R.O. Owens, Phys. Rev. Lett. 40, 709 (1978).

37) J.C. McGeorge, A.G. Flowers, A.C. Shotter and C.H. Zimmerman, J. Phys. G4, L145 (1978).

38) J.J. Murphy II, D.M. Skopik, J. Asai and J. Uegaki, Phys. Rev. C18, 736 (1978).

39) D.H. Dowell, P. Axel and L.S. Cardman, Phys. Rev. C18, 1550 (1978).

REFERENCES (Contd.)

40) W. Dodge, E. Hayward, G. Moscati and E. Wolynec, Phys. Rev. C18, 2435 (1978).

41) E. Wolynec, W.R. Dodge and E. Hayward, Phys. Rev. Lett. 42, 27 (1979).

42) A.G. Flowers, D. Branford, J.C. McGeorge, A.C. Shotter, P. Thorley, C.H. Zimmerman, R.O. Owens and J.S. Pringle, Phys. Rev. Lett., 43, 323 (1979).

43) Y.M. Volkov et al., Pis'ma V. Zh, Eksp. and Theor. Fiz. (USSR) 30, 67 (1979), translation to be published in J.E.T.P. Letters.

44) J.C. McGeorge, A.G. Flowers, D. Branford, C.H. Zimmerman, R.O. Owens and J.M. Reid, Nature, 280, 724 (1979); and to be published in J. Phys. G.

45) E. Wolynec, W. Dodge and E. Hayward, private communication (1979).

46) G.B. Collins, B. Waldman and E. Guth, Phys. Rev. 56, 876 (1939).

47) M.L. Wiedenbeck, Phys. Rev. 69, 235 (1946).

48) L.S. Skaggs, J.S. Laughlin, A.O. Hanson and J.J. Orlin, Phys. Rev. 73, 420 (1948).

49) K.L. Brown and R. Wilson, Phys. Rev. 93, 443 (1954).

50) D.W. Scott, A.O. Hanson and D.W. Kerst, Phys. Rev. 100, 209 (1955).

51) R.L. Hines, Phys. Rev. 105, 1534 (1957).

52) W.C. Barber, Phys. Rev. 111, 1642 (1958).

53) W.C. Barber and T. Wiedling, Nucl. Phys. 18, 575 (1960).

54) W.R. Dodge and W.C. Barber, Phys. Rev. 127, 1746 (1962).

55) E. Wolynec, G. Moscati, J.R. Moreira, O.D. Goncalves, and M.N. Martins, Phys. Rev. C11, 1083 (1975).

56) K.F. von Weizsäcker, Z. Phys. 88, 612 (1934).

57) E.J. Williams, K. Danske Videnskab. Selskab, Mat-fys. Medd. 13, 4 (1935).

58) A.J.F. Siegert, Phys. Rev. 52, 787 (1937).

59) G.C. Wick, Riceria Sci. 11, 49 (1940).

60) B. Peters and C. Rickman, Phys. Rev. 59, 804 (1941).

61) I.N. Sneddon and B.F. Touscheck, Proc. Roy. Soc. A193, 344 (1948).

REFERENCES (Contd.)

62) E. Guth and C.J. Mullin, Phys. Rev. 76, 234 (1949).

63) C.J. Mullin and E. Guth, Phys. Rev. 82, 141 (1951).

64) J.A. Thie, C.J. Mullin and E. Guth, Phys. Rev. 87, 962 (1952).

65) D.F. Herring, I.C. Nascimento, R.B. Walton and R.E. Sund, Phys. Rev. 139, B562 (1965).

66) W.W. Gargaro and D.S. Onley, Phys. Rev. C4, 1032 (1971).

67) I.C. Nascimento, E. Wolynec and D.S. Onley, Nuc. Phys. A246, 210 (1975).

68) M.N. Martins, E. Wolynec and G. Moscati, Phys. Rev. C16, 613 (1977).

69) C.W. Soto Vargas, D.S. Onley and L.E. Wright, Nucl. Phys. A288, 45 (1977).

70) A.C. Shotter, J. Phys. G5, 371 (1979).

71) R.H. Helm, Phys. Rev. 104, 1466 (1956).

72) L.E.H. Trainor, Phys. Rev. 85, 962 (1952).

73) L.A. Radicati, Phys. Rev. 87, 521 (1952).

74) M. Gell-Mann and V.L. Telegdi, Phys. Rev. 91, 169 (1952).

75) G. Morpurgo, Phys. Rev. 110, 721 (1958).

76) G.C. Baldwin and G.S. Klaiber, Phys. Rev. 73, 1156 (1948).

77) M. Goldhaber and E. Teller, Phys. Rev. 74, 1046 (1948).

78) W.D. Myers, W.J. Swiatecki, T. Kodama, L.J. El-Jaick and E.R. Hilf, Phys. Rev. C15, 2032 (1977).

79) R. Pitthan and T. Walcher, Phys. Lett. 36B, 563 (1971).

80) S. Fukuda and Y. Torizuka, Phys. Rev. Lett. 29, 1109 (1972).

81) M.B. Lewis and F.E. Bertrand, Nucl. Phys. A196, 337 (1972).

82) M.B. Lewis, Phys. Rev. Lett. 29, 1257 (1972).

83) H. Tyren, T.A.J. Maris, Nucl. Phys. 4, 637 (1957).

84) N. Marty, M. Morlet, A. Willis, V. Comparat and R. Frascaria, Nucl. Phys. A238, 93 (1975).

85) C.C. Chang, F.E. Bertrand and D.C. Kocher, Phys. Rev. Lett. 34, 221 (1975).

REFERENCES (Contd.)

86) D.J. Horen, J. Arvieux, M. Buenerd, J. Cole, G. Perrin and P. de Saintignon, Phys. Rev. C11, 1247 (1975).

87) L.L. Rutledge and J.C. Hiebert, Phys. Rev. Lett. 32, 551 (1974).

88) J.M. Moss, C.M. Rozsa, J.D. Bronson and D.H. Youngblood, Phys. Lett. 53B, 51 (1974).

89) L.W. Fagg, Rev. Mod. Phys. 47, 683 (1975).

90) J.D.T. Arruda Neto, S.B. Herdade, B.S. Bhandari and I.C. Nascimento, Phys. Rev. C18, 863 (1978).

91) J.D.T. Arruda Neto, B.L.B. Berman, S.B. Herdade, and I.C. Nascimento, Lett. Nuovo Cimento 26, 487 (1979).

92) G.F. Bertoch, Nature 280, 639 (1979).

93) R. Bergère, in Lecture Notes in Physics No. 61, Vol. 1, p. 275, edited by S. Costa and C. Schaerf (Springer-Verlag, 1977).

94) R. Pitthan, H. Hass, D.H. Meyer, J.N. Dyer and F.R. Buskirk, Phys. Rev. Lett. 41, 1276 (1978).

95) M.N. Harakeh, K. van der Borg, T. Ishimatsu, H.P. Morsch, A. van der Woude and F.E. Bertrand, Phys. Rev. Lett. 38, 676 (1977).

96) H.P. Morsch, M. Rogge, P. Turek, C. Sükösd, and C. Mayer-Böricke, contribution 5.10 to Int. Conf. on Nuclear Physics with Electromagnetic Interactions, Mainz, 1979.

97) R.A. Broglia, C.H. Dasso, G. Pollarolo and A. Winther, Phys. Rev. Lett. 41, 25 (1978).

98) M.A. Kovask, S.L. Blatt, R.N. Boyd, T.R. Donoghue, H.J. Hausman and A.D. Backer, Phys. Rev. Lett. 42, 700 (1979).

99) J.P. Elliott and B.H. Flowers, Proc. Roy. Soc. A242, 57 (1957).

100) G.E. Brown and M. Bolsterli, Phys. Rev. Lett. 3, 472 (1959).

101) V.K. Luk'yanov, V.A. Seliverstov and V.D. Toneev, Sov. J. Nuc. Phys. 21, 508 (1976).

102) F.A. Zhivopistsev, B.S. Ishkhanov, V.N. Orlin, and V.I. Shvedunov, Sov. J. Nucl. Phys. 26, 397 (1977).

REFERENCES (Contd.)

103) A. Faessler, D.J. Millener, P. Paul and D. Strottman, Nucl. Phys. A330, 333 (1979).

104) G.R. Hogg, A.G. Slight, T.E. Drake, A. Johnstone and G.R. Bishop, Nuc. Inst. Meth. 101, 203 (1972).

105) K.H. Kaiser, Ph.D. Thesis, University of Mainz, 1973, unpublished; and H. Herminghaus and K.H. Kaiser, Nuc. Inst. Meth. 113, 189 (1973).

106) S.N. Gardiner, J.L. Mathews and R.O. Owens, Nuc. Inst. Meth. 87, 285 (1970).

107) L.C. Northcliffe and R.F. Shilling, Nucl. Data Tables A7, 233 (1970).

108) J.F. Ziegler, Helium Stopping Powers and Ranges in All Elemental Matter, Pergamon Press (1977).

109) S.N. Gardiner, Ph.D. Thesis, University of Glasgow, 1971.

110) E.P. Wigner, Phys. Rev. 73, 1002 (1948).

111) F.M. Mann, R.A. Dayras and Z.E. Switkowski, Phys. Lett. 58B, 420 (1975)

112) Z.E. Switkowski, J.C.P. Heggie and F.M. Mann, Aust. J. Phys. 31, 253 (1978).

113) M.R. Anderson, S.R. Kennett, Z.E. Switkowski and D.G. Sargood, Nucl. Phys. A318, 471 (1979).

114) J.L. Zyskind, J.M. Davidson, M.T. Esat, M.H. Shapiro and R.H. Spear, Nucl. Phys. A331, 180 (1979).

115) T.R. Ophel, A.D. Frawley, P.B. Treacy and K.H. Bray, Nucl. Phys. A273, 319 (1976).

116) D. Woods (Harwell), private communication, 1978.

117) P. Thorley, private communication, 1979.

118) P. David, J. Debrus, F. Lübke, H. Mommsen, R. Schoenmackers and G. Stein, Nucl. Phys. A221, 145 (1974).

119) J.-O. Adler, G. Anderson and H.-Å. Gustapson, Nucl. Phys. A223, 145 (1974).

REFERENCES (Contd.)

120) J.H. Carver, Proc. Phys. Soc. 57, 417 (1960).

121) E. Hayward, N.B.S. Monograph 118 (1970).

122) E.W. Vogt, D. McPherson, J.A. Kuehner and A. Almqvist, Phys. Rev. 136, B99 (1964).

123) S.N. Ghoshal, Phys. Rev. 80, 939 (1950).

124) S.M. Grimes, J.D. Anderson, A.K. Kerman and C. Wong, Phys. Rev. C5, 85 (1972).

125) W.A. Fowler, Proc. 4th Conf. on Applications of Small Accelerators (Eds. J.L. Duggan and I.L. Morgan), p. 11 (I.E.E.E., New York, 1976).

126) G.S. Foote, D. Branford, R.A.I. Bell and R.B. Watson, Nucl. Phys. A220, 505 (1974).

127) L. Meyer-Schutzmeister, R.E. Segel, K. Raghunathan, P.T. Debevec, W.R. Wharton, L.L. Rutledge and T.R. Ophel, Phys. Rev. C17, 56 (1978).

128) P.J. Dallimore, Australian National University Report No. ANU-P/512, 1970 (unpublished).

129) D. Wilmore and P.E. Hodgson, Nucl. Phys. 55, 673 (1964).

130) C.M. Perey and F.G. Perey, Atomic Data and Nuclear Data Tables 13, 293 (1974).

131) O.F. Lemos, Institute of Nuclear Physics, Université de Paris XI, Orsay, France, Internal Report, Ser. A, No. 136, 1972, (unpublished).

132) A. Gilbert and A.G.W. Cameron, Can. J. Phys. 43, 1446 (1965).

133) H.E. Jackson, Proc. Int. Conf. on Photonuclear Reactions and Applications, Asilomar, Ed. B.L. Berman, Vol. 2, 817 (1973).

134) T. Suzuki, Nucl. Phys. A217, 182 (1973).

135) J. Martorell, O.Bohigas, S.Fallieros and A.M. Lane, Phys. Lett. 60B, 1386 (1974).

136) A. Bohr and B. Mottelson, Nuclear Structure, p. 389, pub. W.A. Benjamin, New York, 1969.

REFERENCES (Contd.)

137) P. Ring and J. Speth, Nucl. Phys. A235, 315 (1974).

138) P. Ring and J. Speth, Phys. Lett. 44B, 477 (1973).

139) D.H. Youngblood, J.M. Moss, C.M. Rozsa, J.D. Bronson, A.D. Backer and D.R. Brown, Phys. Rev. C13, 994 (1976).

140) W. Hauser and H. Feshbach, Phys. Rev. 87, 366 (1952).

141) J. Blatt and L.C. Biedenharn, Phys. Rev. 86, 399 (1952).

142) M. Morita, A. Sugie and S. Yoshida, Prog. of Theor. Phys. 12, 713 (1954).

143) M.E. Rose, Phys. Rev. 91, 610 (1953).

144) R.B. Watson, D. Branford, J.L.Black and W.J. Caelli, Nucl. Phys. A203, 209 (1973).

145) K.T. Knopfle, Proc. Int. Conf. on Nuclear Physics with Electromagnetic Interactions, Lecture Notes in Physics 108, 311, Springer-Verlag, 1979.

146) M.T. Collins, C.C. Chang, S.L. Tabor, G.J. Wagner and J.R. Wu, Internal Report NSF-2-79, University of Maryland, U.S.A. (1979).

147) B.L. Berman and S.C. Fultz, Rev. Mod. Phys. 47, 713 (1975).

148) A. Molinari, Photon Induced Nuclear Processes, CERN preprint, TH. 2820-CERN, (1980).

149) S. Costa, F. Ferrero, C. Manfredotti, L. Pasqualini and G. Piragino, Nuovo Cimento 51B, 199 (1967).

150) H. Feshbach, Rev. Mod. Phys. 46, 1 (1974).

151) M. Blann, Ann. Rev. Nuc. Sci. 25, 123 (1975).

152) J.J. Griffin, Phys. Rev. Lett. 17, 478 (1966).

153) F.E. Bertrand and R.W. Peele, Phys. Rev. C8, 1045 (1973).

154) A. Chevarier, N. Chevarier, A. Demeyer, G. Hollinger, P. Pertosa and Tran Minh Duc, Phys. Rev. C11, 886 (1975).

155) T.A. Gabriel and R.G. Alsmiller, Jr., Phys. Rev. 182, 1035 (1969).

156) M. Blann, Nucl. Phys. A213, 570 (1973).

157) I. Dostrovsky, Z. Fraenkel and G. Friedlander, Phys. Rev. 116, 683 (1959).

REFERENCES (Contd.)

158) E. Gadioli, E. Gadioli Erba and J.J. Hogan, Phys. Rev. C16, 1404 (1977).

159) R. Weiner and M. Weström, Phys. Rev. Lett. 34, 1523 (1975); and Nucl. Phys. A286, 282 (1977).

160) H.A. Bethe, Phys. Rev. 53, 675 (1938).

161) T. Nomura, H. Utsunomiya, T. Motobayashi, T. Inamura and M. Yanokura, Phys. Rev. Lett. 40, 694 (1978).

162) H. Ho, R. Albrecht, W. Dünnweber, G. Graw, S.G. Steadman, J.P. Wurm, D. Disdier, V. Rauch and F. Scheibling, Z. Phys. A283, 235 (1977).

163) W. Scobel, M. Blann and A. Mignerey, Nucl. Phys. A287, 301 (1977).

164) W.R. Dodge, unpublished data, private communication (1978).

165) L.I. Schiff, Quantum Mechanics, Sec. 18 (McGraw-Hill, New York, 1949).

166) J.S. Levinger, Phys. Rev. 84, 43 (1951).

167) K.G. Dedrick, Phys. Rev. 100, 58 (1955).

168) Kurt Gottfried, Nucl. Phys. 5, 557 (1958).

169) J.H. Carver, Proc. Phys. Soc. 77, 417 (1961).

170) J.M. Eisenberg and W. Greiner, Nuclear Theory, Vol. 2, p. 93, pub. North-Holland (1976).

171) J.R. Wu and C.C. Chang, Phys. Rev. C16, 1812 (1977).

172) J. Garvey, B.H. Patrick, J.G. Rutherglen and I.L. Smith, Nucl. Phys. 70, 241 (1965).

173) J.S. Levinger, Proc. Int. Conf. on Low and Intermediate Energy Electromagnetic Interactions (Acad. Sci. U.S.S.R., Moscow) Vol. 3, 411 (1967).

174) R. Bergère, Proc. Int. Conf. on Nuclear Physics with Electromagnetic Interactions, Lecture Notes in Physics 108, 138, Springer-Verlag, 1979.

175) R. Serber, Phys. Rev. 72, 1114 (1947).

176) H.W. Bertini, Phys. Rev. 131, 1801 (1963).

177) H.W. Bertini, G.D. Harp and F.E. Bertrand, Phys. Rev. C10, 2472 (1974).

REFERENCES (Contd.)

178) V.S. Barashenkov, F.G. Gereghi, A.S.Iljinov, G.G. Jonsson and V.D. Toneev, Nucl. Phys. A231, 462 (1974).

179) A. Mignerey, M. Blann and W. Scobel, Nucl. Phys. A273, 125 (1976).

180) P. Dougan and W. Stiefler, Z. Phys. A269, 105 (1974).

181) B. Bülow, M. Eriksson, G.G. Jonsson and E. Hagebo, Z. Phys. A275, 261 (1975).

182) M. Eriksson and G.G. Jonsson, Nucl. Phys. A242, 507 (1975).

183) I. Blomquist, P. Janecek, G.G. Jonsson, R. Petersson, H. Dinter and K. Tesch, Z. Phys. A278, 83 (1976).

184) B. Bülow, B. Johnsson, M. Nilsson and B. Forkman, Z. Phys. A278, 89 (1976).

185) K. Lindgren, Z. Phys. A276, 359 (1976).

186) J.S. Pringle, A.G. Flowers, D. Branford, J.C. McGeorge and C.H. Zimmerman, Nucl. Phys. A325, 63 (1979).

187) L. Dresner, Oak Ridge National Laboratory Report No. ORNL-CF-61-12-30 (1961) (unpublished).

188) M. Blann, Nucl. Phys. A213, 570 (1973).

189) C.K. Cline, Nucl. Phys. A210, 590 (1973).

190) C.K. Cline and M. Blann, Nucl. Phys. A172, 225 (1971).

191) J.R. Wu and C.C. Chang, Phys. Rev. C17, 1540 (1978).

192) V.K. Luk'yanov, V.A. Seliverstov and V.D. Toneev, Sov. J. Nucl. Phys. 21, 508 (1976).

193) C.B. Fulmer and J.B. Ball, Phys. Rev. 140, B330 (1965).

194) J.W. Smits and R.H. Siemssen, Nucl. Phys. A261, 385 (1976).

195) J.W. Smits, R.J. de Meijer, R.H. Siemssen, S.Y. van der Werf and A. van der Woude, p. 696 and p. 698, Clustering Aspects of Nuclear Structure and Nuclear Reactions, A.I.P. Conference Proceedings No. 47, edited by W.T.H. Van Oers et al. (1978).

196) M.A.M. Shahabuddin, J.C. Waddington and D.G. Burke, Nucl. Phys. A307, 239 (1978).

REFERENCES (Contd.)

197) C. Kalbach, Z. Phys. A283, 401 (1977).

198) B.C. Cook, N.I.M.s 24, 256 (1963).

199) A. Ferrero, E. Gadioli, E. Gadioli Erba, I. Iori, N. Molko and L. Zetta, Z. Phys. A293, 123 (1979).

200) H. Feshbach, A. Kerman and S. Koonin, Ann. Phys. 125, 429 (1980).

201) D. Gibson, Ph.D. Thesis, University of Glasgow (1979).

202) S.A. Baranov, V.M. Kulakov, V.M. Shatinskii and Z.S. Gladkikh, Sov. J. Nuc. Phys. 12, 604 (1971).

203) B. Rossi and K. Greisen, Rev. Mod. Phys. 13, 262 (1941).

204) J.B. Marion and F.C. Young, Nuclear Reaction Analysis, p. 30, pub. Amsterdem (1958).

205) J.F. Ziegler, Helium Stopping Powers and Ranges in All Elements, Pergamon Press (1977).

206) M. Makino, R. Eisberg, K. Ritchie, R. Carlson and C. Waddell, Nuc. Inst. Meth. 80, 299 (1970).

207) M.Q. Makino, C.N. Waddell and R.M. Eisberg, Nuc. Inst. Meth. 60, 109 (1968).

208) T. Ericson, Philosophical Magazine Supplement 9, 425 (1960).

209) H.A. Bethe, Rev. Mod. Phys. 9, 69 (1937).

210) R. Huby, Proc. Phys. Soc. A67, 1103 (1954).

211) F. Coester, Phys. Rev. 89, 819 (1953).

212) L.C. Biedenharn, J.M. Blatt and M.E. Rose, Rev. Mod. Phys. 24, 249 (1952).

213) R.W. Carr and J.E.E. Baglin, Nuclear Data A10, 144 (1971).

214) C.K. Cline, Nucl. Phys. A193, 417 (1972).